AD-A076 769 GENERAL ELECTRIC CO PHILADELPHIA PA RE-ENTRY AND ENV--ETC F/G 17/5
MILLIMETER WAVE HARDENED ANTENNA WINDOW MATERIALS DEVELOPMENT.(U)
AUG 79 J P BRAZEL , R FENTON , J A ROETLING DAAG46-79-C-0047
UNCLASSIFIED AMMRC-TR-79-45 NL

1 OF 3
AD A076769

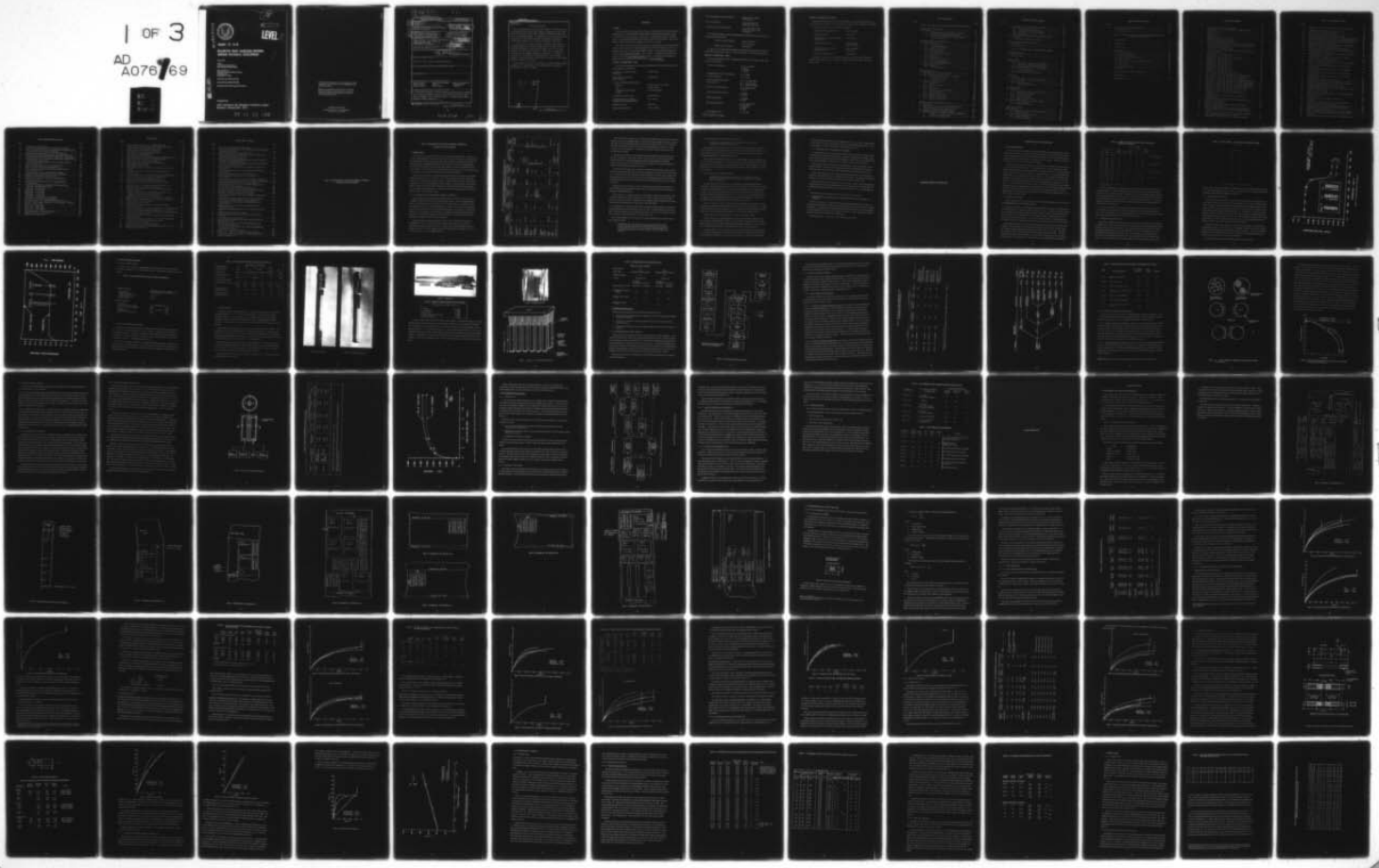

10

AD

LEVEL II

AMMRC TR 79-45

MILLIMETER WAVE HARDENED ANTENNA WINDOW MATERIALS DEVELOPMENT

August, 1979

Authors:
James P. Brazel, Richard Fenton,
John Roetling, and Richard Tanzilli

General Electric Co.,
Re-Entry & Environmental Systems Division
3198 Chestnut St.,
Philadelphia, PA. 19101

Final Report, July 1978 to April 1979

Contract Number DAAG46-79-C-0047

Approved for public release; distribution unlimited

Prepared for

ARMY MATERIALS AND MECHANICS RESEARCH CENTER
Watertown, Massachusetts 02172

The findings in this report are not to be construed as an official Department of the Army position, unless so designated by other authorized documents.

Mention of any trade names or manufacturers in this report shall not be construed as advertising nor as an official indorsement or approval of such products or companies by the United States Government.

DISPOSITION INSTRUCTIONS

Destroy this report when it is no longer needed.
Do not return it to the originator.

(19) TR-79-45

UNCLASSIFIED

SECURITY CLASSIFICATION OF THIS PAGE (When Data Entered)

REPORT DOCUMENTATION PAGE

READ INSTRUCTIONS BEFORE COMPLETING FORM

(18) 1. REPORT NUMBER: AMMRC TR79-45

2. GOVT ACCESSION NO.

3. RECIPIENT'S CATALOG NUMBER

4. TITLE (and Subtitle)

(6) Millimeter Wave Hardened Antenna Window Materials Development.

(9) 5. TYPE OF REPORT & PERIOD COVERED: Final Report, Jul 1978- Apr 1979

6. PERFORMING ORG. REPORT NUMBER

7. AUTHOR(s)

(10) James P. Brazel, Richard Fenton, John Roetling, Richard Tanzilli

(15) 8. CONTRACT OR GRANT NUMBER(s): DAAG46-79-C-0047

9. PERFORMING ORGANIZATION NAME AND ADDRESS

General Electric Co., Re-Entry & Environmental Systems Division, 3198 Chestnut St., Philadelphia, PA 19101

10. PROGRAM ELEMENT, PROJECT, TASK AREA & WORK UNIT NUMBERS

(16) D/A Project: 8X363304D215

AMCMS Code: 633304.21500.07

Agency Accession:

11. CONTROLLING OFFICE NAME AND ADDRESS

Army Materials and Mechanics Research Center, Watertown, Massachusetts 02172

(11) 12. REPORT DATE: Aug 1979

13. NUMBER OF PAGES: 254

14. MONITORING AGENCY NAME & ADDRESS (if different from Controlling Office)

(12) 283

15. SECURITY CLASS. (of this report): Unclassified

15a. DECLASSIFICATION/DOWNGRADING SCHEDULE

16. DISTRIBUTION STATEMENT (of this Report)

Approved for public release; distribution unlimited.

17. DISTRIBUTION STATEMENT (of the abstract entered in Block 20, if different from Report)

18. SUPPLEMENTARY NOTES

19. KEY WORDS (Continue on reverse side if necessary and identify by block number)

Antenna windows	Silica-silica composites	Raytran Zinc Selenide
Silicon nitride	Sialons	Hardened Radar
Aluminum nitride	Boron nitride	Materials

20. ABSTRACT (Continue on reverse side if necessary and identify by block number)

A materials development and characterization program has been conducted with the goal of developing hardened antenna window materials for application to millimeter wave and infrared sensors for ballistic missile defense interceptor (BMDI) applications.

DD FORM 1 JAN 73 1473 EDITION OF 1 NOV 65 IS OBSOLETE

UNCLASSIFIED

SECURITY CLASSIFICATION OF THIS PAGE (When Data Entered)

404 884

Block No. 20

ABSTRACT (Continued)

Three distinct classes of materials were studied. The ADL-4D6 multidirectionally reinforced silica-silica composite developed in previous BMD work was tested for particle erosion resistance and dielectric properties in the mm wavelength region. A comprehensive study was also performed on the effects of constituent properties and weaving and composite densification variations on the mechanical properties of this material.

A second class of refractory dielectrics, ultrahigh purity nitrides of silicon and aluminum, were also examined for their ultimate potential in the BMDI environment. Specimens were prepared by chemical vapor deposition and hot pressing of powders. These were variously tested for mechanical and thermal properties, chemical purity and dielectric properties in X and millimeter wavelength bands. The CVD Si_3N_4 material in particular showed a decade lower loss tangent than previously reported versions of this ceramic.

A third material, "Raytran" zinc selenide, an infrared window material candidate, was characterized for its thermophysical and mechanical properties from -150°C to 1000°C.

FOREWORD

GENERAL

The work described in this report was carried out at General Electric Re-Entry and Environmental Systems Division (GE-RESD) Advanced Materials Development Laboratories, Valley Forge Space Center, King of Prussia, Pennsylvania. Technical supervision was provided for the U.S. Army Materials and Mechanics Research Center by Mr. John Dignam. The program manager for the General Electric Company was Mr. James P. Brazel.

This program was comprised of three major tasks, distinguished by the technical discipline involved. The first of these, "Multidirectional Reinforced Fibrous Composites," was a continuation of work done in previous RESD/AMMRC contracts. The principal investigators for this task were J. Brazel and R. Fenton. The second task, "Ultrahigh Purity Nitride-Based Ceramics" was led by Dr. Richard A. Tanzilli. Task 3, "Thermophysical and Mechanical Characterization of Raytran Zinc Selenide" was led by John A. Roetling.

PRINCIPAL CONTRIBUTORS: TASK I

The principal contributors to the "Multidirectional Reinforced Fibrous Composites" task of the program are listed below:

Fiber Studies, Omniweave Design and Weaving	Richard Fenton
Fiber, Matrix and Composite Chemical Analysis	Kenneth Bleiler
Composite Formulation and Fabrication	
ADL-4D6	Richard Fenton, James Brazel
BNQ	Richard Fenton
CVD methods for BN matrix in BNQ	Dr. Joseph Gebhardt
Scanning Electron Microscopy	Joseph D'Andrea
Characterization Plan, Program Management and Final Report Editor	James Brazel
Mechanical Testing	Robert Kreitz
Ultrasonic Measurements	John A. Roetling

Shock Testing (plate and particle impact)	Marlyn Graham, Effects Technology, Inc.*
Dielectric Properties	Jack Hanson (GE) and William Westphal, MIT*
Composite Micromechanical Analysis	Dr. John J. Kibler, Eddy A. Derby, Materials Science Corporation*

The report contributors also wish to acknowledge in particular the contributions of the following technician personnel:

Omniweave Preform Weaving	Vincent Arcidiacono, Bryce S. Kennedy
Mechanical Measurements	Jordan Konell

In addition, the computer-generated graphs and data reduction presented in this report, notably in the mechanical test section, were the work of John A. Roetling and Robert Kreitz.

PRINCIPAL CONTRIBUTORS: TASK II

The principal contributors to the "Ultrahigh Purity Nitride Based Ceramics" task of the program are listed below:

CVD Process Development	Dr. J. J. Gebhardt C. Farley J. Yodsnukis J. Axelson
Aluminum Nitride Process Development	Dr. C. Dulka
β'-Sialon Specimens	A. Gatti (SD)
Cubic Boron Nitride Specimens	Dr. F. Corrigan (SMD)
Vapor Grown AlN	Dr. G. Slack (C-R&D) Dr. T. McNelly (C-R&D)
Radar Property Measurements	W. B. Westphal (MIT) J. Hanson
Thermal and Optical Properties	J. Hanson B. Kennedy
Mechanical Properties	J. Roetling R. Kreitz
Microstructural Analyses	Dr. E. Feingold (SD) B. Faust (SD) J. D'Andrea W. Staley
Laser Simulation Tests	Dr. D. Smith

*Under subcontract to GE/RESD

PRINCIPAL CONTRIBUTORS: TASK III

Immediate technical supervision for this "Thermophysical and Mechanical Characterization of Raytran Zinc Selenide" task of the program was supplied by Dr. Anton Hofman of AMMRC.

The principal contributors of GE-RESD are listed below:

Technical Planning & Supervision	John A. Roetling
Mechanical Testing	Robert Kreitz
Thermal Expansion, Flexure & Tensile Measurements	Jordan Konell
Ultrasonic Measurements	Roland W. Driver John A. Roetling
Thermal Conductivity & Specific Heat Measurements	Bryce S. Kennedy Jack Hanson
TGA & DTA Measurements	Kenneth Bleiler

In addition, we would like to acknowledge the helpful advice of Mr. Robert Donadio of Raytheon Research Division. Mr. Donadio also supplied additional "Raytran" ZnSe flexure test specimens.

TABLE OF CONTENTS

TABLE OF CONTENTS (Continued)

TABLE OF CONTENTS (Continued)

LIST OF ILLUSTRATIONS

LIST OF ILLUSTRATIONS (Continued)

LIST OF TABLES

LIST OF TABLES (Continued)

PART I: MULTIDIRECTIONAL REINFORCED FIBROUS COMPOSITES

1. INTRODUCTION AND SUMMARY

PART I: MULTIDIRECTIONAL REINFORCED FIBROUS COMPOSITES

1. INTRODUCTION AND SUMMARY

1.1 INTRODUCTION

The purpose of this program has been to develop hardened antenna window or radome materials for potential ballistic missile interceptor applications, with emphasis on the achievement and demonstration of high transmission quality in the millimeter wavelength band under the anticipated thermal, mechanical and particle erosion environments of the "Endo Non-Nuclear Kill" (ENNK) Ballistic Missile Defense Interceptor (BMDI). This environment includes velocities as high as 12,000 feet per second, and heat fluxes sufficient to drive silica-based materials to melting, and most nitride-based materials to sublimation temperatures.

This work was performed in the Advanced Materials Development Laboratory of GE-RESD in the period from July 3, 1978 to April 20, 1979. Three subcontracts were let: Materials Sciences, Inc. performed microstructural analyses of the ADL-4D6 composite system; Effects Technology, Inc. performed exploding foil impact, equation of state and particle impact testing on two variations of ADL-4D6; and the Laboratory for Insulation Research of MIT performed dielectric property measurements on two variations of ADL-4D6 and ultrahigh purity monolithic nitride ceramics of aluminum and silicon.

1.1.1 MULTIDIRECTIONAL-REINFORCED FIBROUS COMPOSITES

This "Millimeter Wave Hardened Antenna Window Materials Study" is the fifth in a series of AMMRC/GE-RESD programs with the stated general objective. In the preceding program (Ref. 1), the ADL-4D6 silica-silica composite process was developed. A "standard" form of the material, based on J. P. Stevens Astroquartz 20 end fibers woven in a 4D cubic configuration by the Omniweave process, and densified with a purified version of Dupont LUDOX AS colloidal silica, was characterized for design data on mechanical, thermophysical and dielectric properties. Its resistance to weapons effects was measured by exploding foil tests and some initial data was gathered on particle impact resistance.

This testing program showed the material to have a tensile strength, as measured by flexural MOR, in excess of 5000 psi for all observations (mean value of 6610 psi) and an extremely high strain to failure-in excess of 1.0 percent. The relevant properties of the material as developed in 1976 are summarized in Table 1 and compared to the other S.O.A. conventional and hardened antenna window materials.

TABLE 1. ANTENNA WINDOW MATERIALS FOR RV AND BMDI APPLICATIONS (ALL PROPERTIES AT ROOM TEMPERATURE UNLESS NOTED)

	Transparent Fused Silica (E.G. Corning 7940)	Slip Cast Fused Silica (E.G. Corning 7941)	Silica Omniweave/ SR-350 Resin (ADL-10)	3-D Silica/Colloidal Silica (AS3DX)	Silica Omniweave/ Colloidal Silica (ADL-4D6)	Silica Omniweave Glass Bonded BN (BNQ) Type V	Type 2	3-D BN/BN Matrix (BN-3DX)
Tensile Strength (psi)	6,800	5,400-9,000	10,000-20,000	5,000 min. (flexural) 4,400 tensile	5,000 min. (flexural	4,000	5,000	8,400 (flexure) 3,600 (tensile)
Tensile Modulus (10^6 psi)	10.5	8.4	1-2	4	2 (flexural)	0.1	1.5	2.2
Failure Strain (%)	0.01		1-2	0.2	1	2 (7-8% for 1.3 gm/cc)	0.4	0.2
Hardening Threshold (taps) (thickness)	500-1,500	500-1,500	5,000 (3/8" thickness)	4,000-5/8" 6,000-1"	4,000-3/8" 8,000-1"	4,000 (1/2")		3,000-1"
Dielectric Constant	3.8	3.3	3 - 3.3	2.9	2.8 - 3.1	2		2.86 - 3.19
Loss Tangent (Heating Limit)	0.0016	0.0002	0.002-0.005 (100 BTU/ft^2-sec. 2800°F surface temp.)	0.008	0.006	0.005		.003
Thermal Conductivity (150°F) (10^{-5} Btu/ ft-sec-F°)	22	15	10	11	11	4.5		140
Q-Star (Btu/lb)	3,000-5,000	3,000-5,000		4,200-11,000	6,000-11,000	6,000		24,000 (Qcw)
Density (gm/cc)	2.2	1.9-2.1	1.8	1.7	1.6	1.3 (prototype) 1.8 (goal)	1.4	1.5-1.6
Relative Cost	Low	Lowest	Moderate-High	High	High	Moderate-High	Moderate	Highest

GE Developmental Material

Ford Aeronutronic Developmental Material

The strength achieved at that time is equivalent to conventional fused silica, but the strain to failure is two orders of magnitude higher. This extreme fracture toughness correlates with the high value for shock hardening threshold as measured by exploding foil tests. This "baseline ADL-4D6" has the highest spall threshold of any known antenna window material: 8000 taps or more for a one inch thickness. Conventional fused silicas and boron nitride fail at one-tenth this level of impulse.

The electrical properties of the high purity fiber and colloidal silica constituents of the ADL-4D6 composite are intrinsically excellent. However, the very porous and permeable composite matrix freely absorbs atmospheric moisture which hydrolyzes on the high surface area matrix silica and raises the effective loss tangent of the unmodified material to well above the acceptable benchmark level of 0.01.

A "water densensitization process" based on treatment of the thermally cleaned and dried densified composite with silane vapor succeeded in eliminating the effects of this water absorption. The baseline ADL-4D6 material described in Reference 1 and summarized in Table 1 has a maximum loss tangent at 250 MHz of 0.006 at room temperature and showed less than three (3) decibels transmission loss at 10 GHz when driven to surface melting in a CO_2 laser heating environment.

The work described in Reference 1 can be considered to have brought this material to a level of characterization adequate for BMDI or RV design and showed it to have superior properties for the BMDI application.

It was, however, soon realized that a more comprehensive data base was required for the critical new performance category of particle erosion. Also, in the interim between the two programs, emphasis was placed by BMDATC on use of higher frequency millimeter wave band radar for the unprecedented fuzing requirements of the ENNK BMDI.

The definition of the work to be performed in this program began with plans to do particle erosion measurements on and model the erosion resistance of standard ADL-4D6, and to measure its dielectric properties in the millimeter wave band. This work would complete the data base required for design studies on the new interceptor mission.

The "Recommendations" section of Reference 1 outlined additional work on the 4D silica-silica composite system:

1. Development of the ADL-4D6 silica-silica composite hardened antenna window materials system should be continued with the goal of achieving the extremely high (10,000 - 30,000 psi) ultimate tensile strength levels which micromechanical analysis of the materials system has shown to be achievable.

Two specific approaches were outlined. The first was:

> Fabrication using finer texture silica Omniweave, thereby yielding smaller unit cell densified composites.

This approach was motivated by the similar experience with carbon-carbon composites, where studies had been conducted to optimize particle erosion and ablation performance versus weave spacing. The effects of weave "coarseness" - too large a fiber-to-fiber spacing on mechanical properties of C/C had also been observed.

The tensile test anomalies of Reference 1 also suggested that a specimen strength versus unit cell size effect was operative. A finer weave tensile specimen or window thickness might then show further improvement in structural properties over the standard material. The complexity and cost of introducing this new weave would also have to assessed against any performance advantages.

The second specific recommendation was a:

> Detailed study of firing temperature and sintering variations to realize the improved strengths indicated in the studies undertaken in this program. (Ref. 1, page 197)

The ADL-4D6 process development work of Reference 1 had indicated that flexural strength was significantly improved by addition of the silane coupler step and that heat treatment variations from the standard process could affect the elastic modulus, and prospectively the strength. There was also experimental evidence from the initial work done on ADL-4D6 in Reference 2 that flexural strengths in the range of 30,000 to 40,000 psi could be achieved with this material. Micromechanical analysis of the system had also allowed for a theoretical strength this high if the optimum fiber-matrix interaction were achieved.

The work of Reference 1 had in fact not achieved this strength level, although the 5000 psi minimum was considered more than adequate for conventional size antenna windows. The application of the material to large radome use or to a structural role in a high performance BMDI large aperture antenna window would be enhanced if such strengths could be achieved.

The ADL-4D6 studies of this program were organized around this outline.

Further development of the BNQ hybrid (boron nitride/fused quartz) composite was also recommended. Excellent spall resistance, tensile properties and an even greater strain to failure capability (7-8%) than ADL-4D6 had been demonstrated in Reference 2. These properties recommended the material for extreme particle impact or blast environments.

The work of Reference 1 was directed toward developing an acceptable manufacturing process for making BNQ composites in window-sized samples. The effort progressed as far as the development of a high BN solids content prepreg Astroquartz silica yarn, and densified/

rigidized flexure specimens with 5000 psi strength were made. But a more "manufacturable" process was still desired, particularly in regard to cost and handling characteristics of the rigidized BNQ. The effort of this program continued along these lines.

1.1.2 ULTRAHIGH PURITY NITRIDE-BASED CERAMICS

A second general class of materials was introduced into this program, in addition to the multidirectional-reinforced fibrous ceramics. These are ultrahigh purity monolithic nitride-based ceramics, principally silicon nitride and aluminum nitride. This class of materials has two principal advantages for the ENNK class of ballistic missile defense interceptors.

The monolithic nature assures that no scattering effects need be considered for even the highest frequencies of interest for this application, whereas composite windows may show some beam optics effects due to the intrinsic inhomogeneity of the fiber/matrix unit cell.

Second, these materials are intrinsically mechanically hard and can be expected to have excellent erosion characteristics in a small particle environment. The multidirectional fibrous composites such as ADL-4D6 however would be superior in large particle impact.

The two prime questions to be answered for the use of these nitrides in the NNK application is whether they have the required high millimeter wave radar transparency at temperatures up to sublimation and whether than can ever be made in the required sizes in a manufacturing process.

The development of these materials is discussed in Part II of this report.

1.1.3 THERMOPHYSICAL AND MECHANICAL CHARACTERIZATION OF RAYTRAN ZINC SELENIDE

Raytran Zinc Selenide is a commercially available high optical quality polycrystalline zinc selenide infrared transparent material made by the chemical vapor deposition process at Raytheon Corporation. Its thermophysical and mechanical properties were characterized in this program over the temperature range from -250°F to 1800°F to confirm the vendor data and to extend it for design use in infrared sensor alternative BMDI designs.

The characterization program is discussed in Part III of this report.

2. COMPOSITE DESIGN AND FABRICATION

2. COMPOSITE DESIGN AND FABRICATION

2.1 SILICA FIBER STUDIES

One of the primary goals of the multidirectional-reinforced composite portion of this program is to explore process variations which would enable the silica-silica ADL-4D6 composite to more closely approach its theoretical mechanical strength, and to realize micromechanical property performance benefits such as mechanical erosion resistance. This section describes the study of the silica fiber component of the composite.

Chemical analyses, breaking strengths, and TGA data were obtained on five different lots of J. P. Stevents Astroquartz roving. The results of the arc emission and atomic absorption analyses and the average roving breaking strengths are shown in Table 2. The sodium contamination data, based on 0.2 gram sampling sizes, are higher than J. P. Stevens data published as typical (Table 3), while data based on larger sampling sizes (1.0 gram) agree reasonably well with the vendor typical data. The data obtained on the larger sample sizes in considered more accurate. The breaking strength data on the as-received Astroquartz roving agrees very well with J. P. Stevens published values (Refs. 3 and 4). TGA data was generated on teflon-finished Astroquartz both in air and N_2 to check on the adequacy of woven preform heat cleaning conditions prior to densification processing. The weight loss versus temperature curves are shown in Figures 1 and 2. Based on this data, the standard 16 hours at 510°C heat cleaning cycle is sufficient to remove the teflon finish.

2.1.1 CHEMICAL ANALYSIS

Atomic absorption and arc emission analyses were the analytical methods used to determine the contamination levels in the Astroquartz fibers.

Arc emission analysis is a good qualitative/semi-quantitative technique for determining the broad range of species of impurities and their approximate levels. The atomic absorption method is an extremely accurate specific quantitative method and was used to accurately determine the level of sodium and iron contamination in the Astroquartz samples. Sodium and iron were selected for atomic absorption analysis, since our prior experience (Ref. 5) indicated high levels of these two elements in Astroquartz roving. The results of these analyses are shown in Table 2.

The following procedure was used in preparing the quartz roving samples for impurity determinations. The Astroquartz roving sample was washed with deionized water, then the teflon was removed by heating the samples in platinum crucibles at 538°C for 16 hours. The samples were allowed to cool to room temperature and again washed with deionized water. The quartz roving was then divided into two samples, one for arc emission analysis and one for atomic absorption analysis. These analyses were then performed using standard analytical procedures.

TABLE 2. CHEMICAL ANALYSES AND BREAKING STRENGTHS OF ASTROQUARTZ ROVING

Astroquartz Roving: Type	Lot Number	Finish	Finish Removal Temperature (°C)	Sample Size (grams)	Chemical Analyses: Arc Emission Major* Impurities (ppm)	Atomic Absorption Na (ppm)	Atomic Absorption Fe (ppm)	Average Breaking Strength Per End** (psi)	Remarks
20 End	92789	Teflon	538	0.2	140	20	--	1.4	• Used in Reflective H/S and #423 Weave
20 End	94891	Teflon	538	0.2	145	30	12		
20 End	94891	Teflon	538	0.2	--	20	--		
20 End	94891	Teflon	550	1.0	--	6.0	--	1.5	• Used in Reflective H/S and #426
20 End	94891	Teflon	650	1.0	--	6.0	--		
20 End	94891	Teflon	750	1.0	--	5.6	--		
12 End	15962-1	Teflon	538	0.2	100	16	59	1.5	• Used in #424 and 425
12 End	15962-2	Teflon	538	0.2	118	19	24	1.4	• Used in #425 and 426
20 End	173-3053	Silane	538	0.2	20	<2	<15		
20 End	173-3053	Silane	550	1.0	--	5.1	--	2.5	• Used in #427
20 End	173-3053	Silane	650	1.0	--	4.5	--		
20 End	173-3053	Silane	750	1.0	--	4.6	--		

*Major Elements: Na, K, Fe, Al, Mg, Ti, Ca

**End = 300-2/0 Yarn

The types and total levels of impurities as determined by the arc emission analyses agrees generally with the J. P. Stevens data published as typical impurities in Astroquartz (Table 3). The sodium levels determined by atomic absorption using 1.0 gram samples also agree with J. P. Stevens data (approximately 5 ppm Na). Sodium and iron levels determined by atomic absorption using the smaller (0.2 gram) sampling sizes are higher than "typical values". The former data (larger sample) are considered more accurate and the contamination levels appear to be about "normal" for Astroquartz.

In one series of analyses, the Astroquartz samples were heat cleaned at 550°, 650°, and 750°C to remove the fiber finish as a check on contaminant levels versus degree of finish removal. (The TGA data had not been completed at this point.) No significant difference in sodium levels was evident between any of the heat cleaning temperatures.

2.1.2 FIBER BREAKING STRENGTH

The breaking strength of roving samples taken from each lot of Astroquartz was determined per ASTM D-578. A minimum test series of five replications was done to determine the average breaking strength of each lot of material. This breaking strength data is also shown in Table 2. The breaking strength of the silane-finished Astroquartz roving is approximately 60 percent higher than the teflon finished Astroquartz, and is most probably due to the silane being a better binder material than the teflon and, therefore giving better load transfer between filaments. As such, the difference in breaking strength is not significant for the purposes of this

TABLE 3. TYPICAL CHEMICAL ANALYSIS ON ASTROQUARTZ® FIBER*

SiO_2 = 99.95%

	Impurities (ppm)
Fe	3
Ti	12
Al	100
Mg	2.5
Ca	2.3
Li	1
Na	5
K	9
P	3
Mn	2
Cu	0.1
Sb	0.5
Cd	0.5
B	10

* J. P. Stevens and Company, Astroquartz® Bulletin #310-7.

process study. The measured breaking strengths for all lots of Astroquartz tested agree with J. P. Stevens advertised data (Refs. 3 and 4) of 1.5 pounds/end and 2.5 pounds/end for teflon-finished and silane-finished Astroquartz, respectively.

2.1.3 FINISH REMOVAL STUDIES

The standard teflon finish removal condition used during this work for Astroquartz Omni-weave preforms was 510°C for 16 hours in an air circulating oven. Since residual teflon finish on the Astroquartz fibers could affect the contamination level and the ultimate composite properties, TGA data on teflon-finished Astroquartz was generated in air and in nitrogen to check on the adequacy of the standard removal conditions. For completeness, the nitrogen run was included to simulate conditions in the interior of the woven preform even though theoretically the air and N_2 TGA curves should be the same since teflon degrades by depolymerization rather than oxidation. The TGA curves obtained are shown in Figure 1 and indicate that the teflon begins to decompose above 450°C when heated at 10°C per minute.

The question still remained, however, of the rate and completeness of decomposition in this temperature range. To determine this, an isothermal TGA at 510°C was run to determine the rate of teflon decomposition under "standard" removal conditions. This curve is shown in Figure 2. Based on this isothermal TGA data, the standard preform heat cleaning cycle of 16 hours at 510°C is sufficient to remove the teflon finish.

The TGA residual mass data are tabulated as insets in Figures 1 and 2.

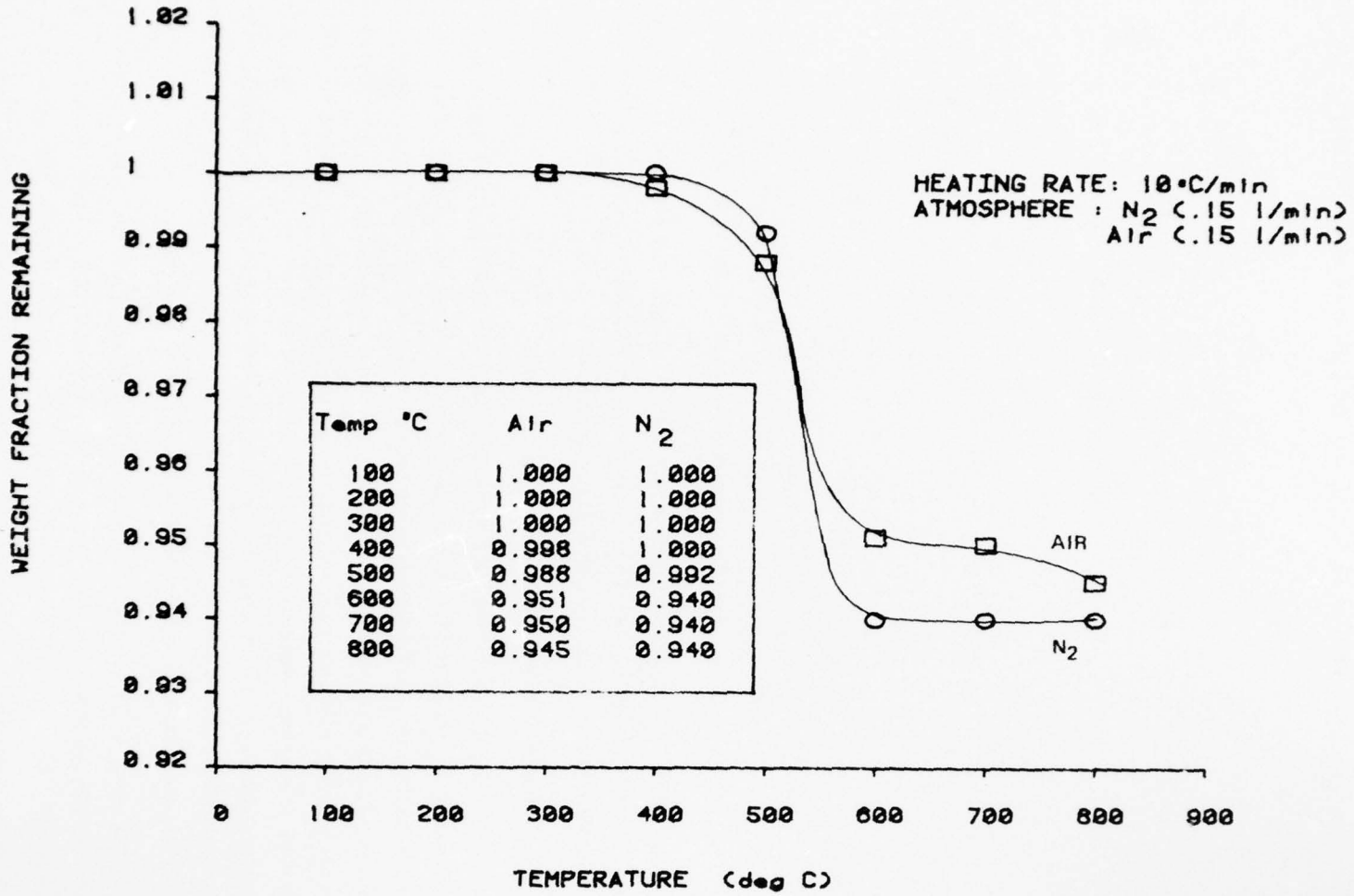

Figure 1. TGA of 20 End Teflon Coated Astroquartz

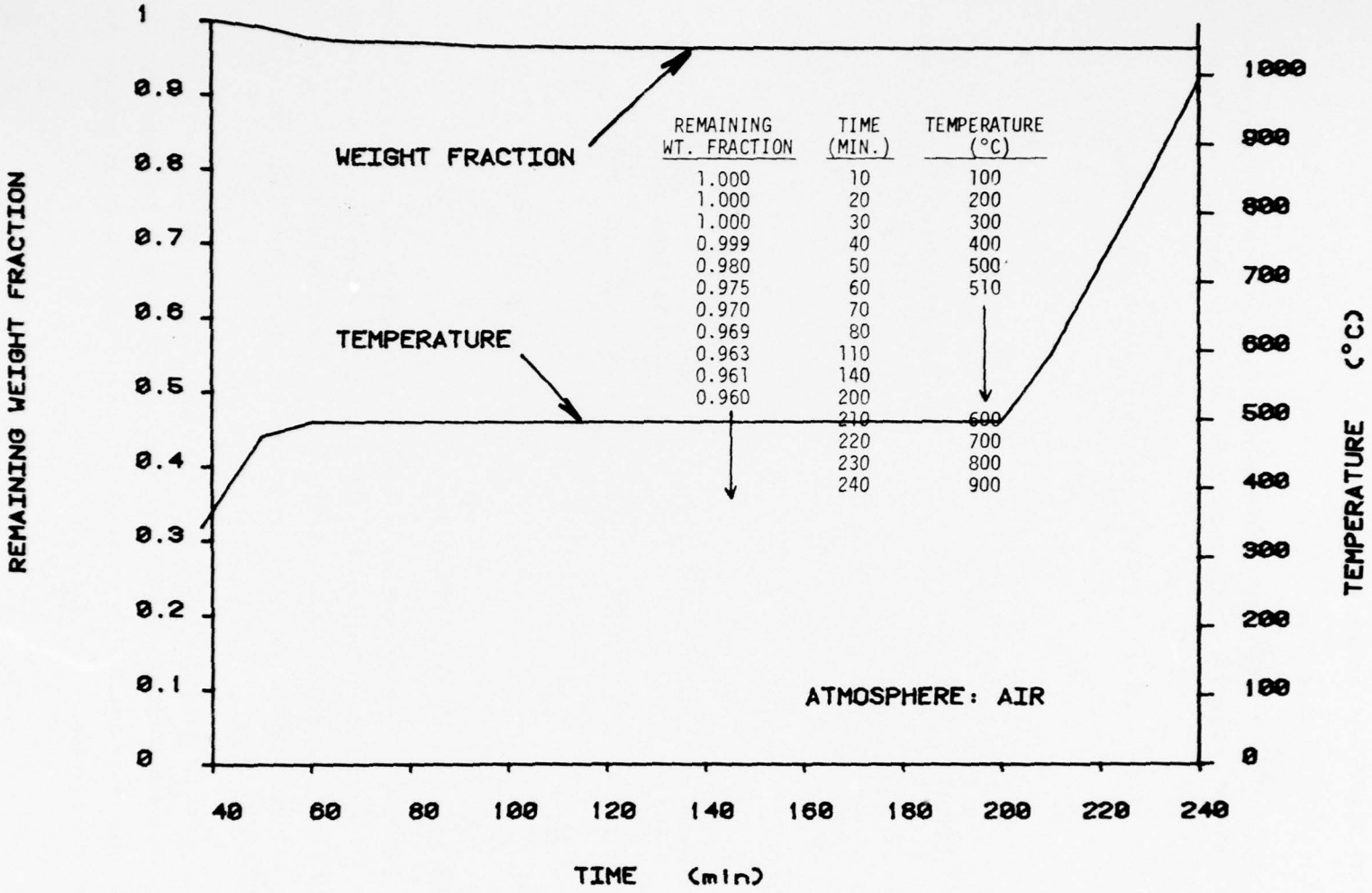

Figure 2. Isothermal TGA of 20 End Teflon Finished Astroquartz Roving

2.2 SILICA PREFORM FABRICATION

2.2.1 SILICA FIBER SYSTEM

The quartz fiber system used in fabricating the Omniweave fabrics for this program was J. P. Stevens Astroquartz, 552 12 end and 20 end roving. The basic fiber properties are shown in Table 4.

TABLE 4. CHARACTERISTICS OF QUARTZ FILAMENTS AND ROVING

Filament Properties	
Designation	Astroquartz (Brazilian Quartz source, fused and drawn into filaments).
Filament Diameter, in.	3.55×10^{-4}
Filament Density, g/cm^3	2.2
Young's Modulus, psi	1×10^7
Poisson's Ratio	0.17
Roving Properties	
Designation	← Astroquartz 552 →
End Count (#300-2/0 Yarns)	20 / 12
No. of Filaments (nominal)	4800 / 2880
Finish	← 5% Teflon →
Yards/Pound	750 / 1250
Breaking Strength, pounds	28.30 / 16-18

2.2.2 ADL-4D6 OMNIWEAVE PREFORMS

Four quartz Omniweave preforms were woven for ADL-4D6 development and characterization. These were preform numbers 423, 424, 425, and 426. Table 5 lists the characteristics of each of these preforms. Preform 423 (Figure 3) is the standard 4D cubic construction using 20 end roving. Preforms 424 and 425 are fine weave versions (12 end roving) of the 4D cubic construction. Figure 4 is a photograph of preform 425.

Preform 426 (see Figure 5) consists of a standard 4D and two 5D sections. The 4D section (426-A) consists of 20 end Astroquartz. In the 5D sections, 426-B has 12 end Astroquartz roving added in the transverse direction and section 426-C has 20 end Astroquartz roving added in the transverse direction.

TABLE 5. ADL-4D6 QUARTZ PREFORM CHARACTERIZATION DATA

PARAMETER	OMNIWEAVE PREFORM NO. 423	424	425	426 A	426 B 5D	426 C 5D
Weave Design	← 4D →					
Fiber Type	← ASTROQUARTZ R TYPE 552 ROVING →					
Roving End Count	20	12	12	20	20/12	20/40
Fiber Finish	← TEFLON →					
Unit Cell Size (MM)	3	2	2	3	-	-
Woven Dimensions (in.)	1.2 x 4.6 x 30 (165)	1.4 x 3.5 x 26 (127)	1.4 x 3.5 x 26 (127)	1.3 x 4.5 x 12 (70)	1.6 x 4.5 x 10 (72)	1.8 x 4.5 x 4 (32)
As-Woven Bulk Density (gm/cc)	1.05	0.94	0.96	1.05	1.04	0.98
Avg. Weave Face Half Angle (Deg.)	40°	40°	40°	38°	31°	30°

2.2.3 BNQ PREFORMS

The preform (427) designated for BNQ process studies consisted of twelve "finger weaves" each approximately 0.6" x 0.8" x 28") woven simultaneously. The fiber used was silane-finished Astroquartz 552, 20 end roving. Six of the "finger weaves" utilized boron nitride/Astroquartz roving prepreg, while the remainder were woven using plain silane-finished Astroquartz. This was done to provide various boron nitride/quartz fiber volume ratios in the preforms.

The formula of the boron nitride emulsion used for prepregging is shown in Table 6. This formulation was selected because the previous antenna window study (Ref. 1) indicated it provided the best prepreg in terms of penetration and uniformity of the boron nitride in the quartz roving with sufficient flexibility of the prepregged quartz to allow weaving in the Omniweave loom. The prepreg process is described in Section 2.1.3.2 of Reference 1.

In order to provide some high boron nitride content preforms, a 12 percent boron nitride (0.5 micron mean particle diameter) in distilled water emulsion was injected into the preform as it was woven. This injection operation was conducted for the first 15 inches of each finger weave, after which weaving continued without these BN additions.

A photograph and sketch of preform 427 appear in Figures 6 and 7. Woven preform characterization data is shown in Table 7.

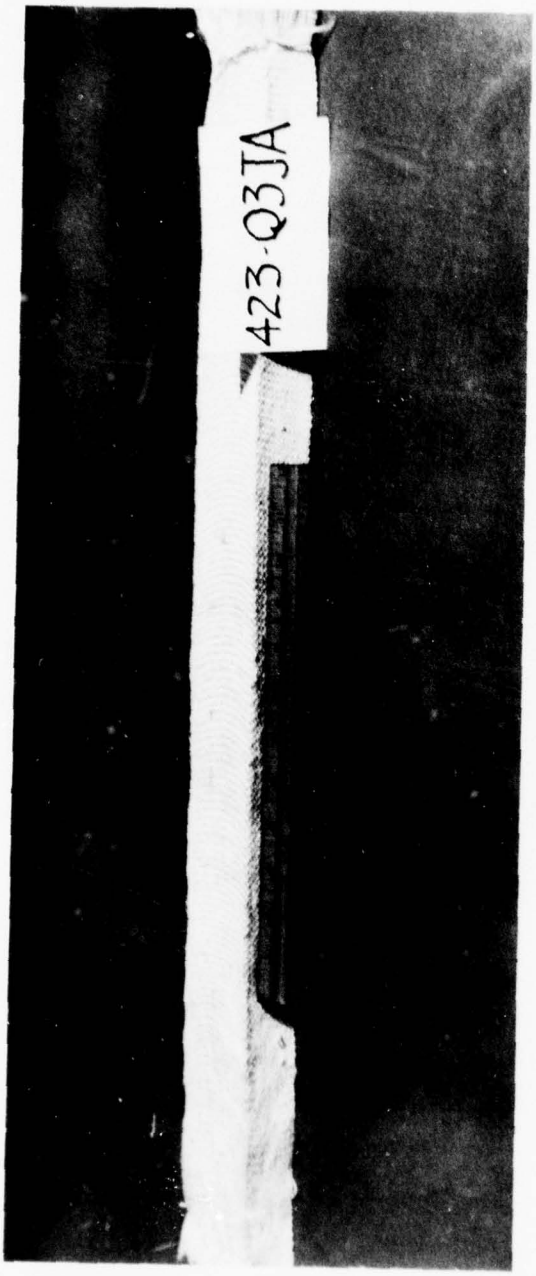

Figure 3. Preform 423

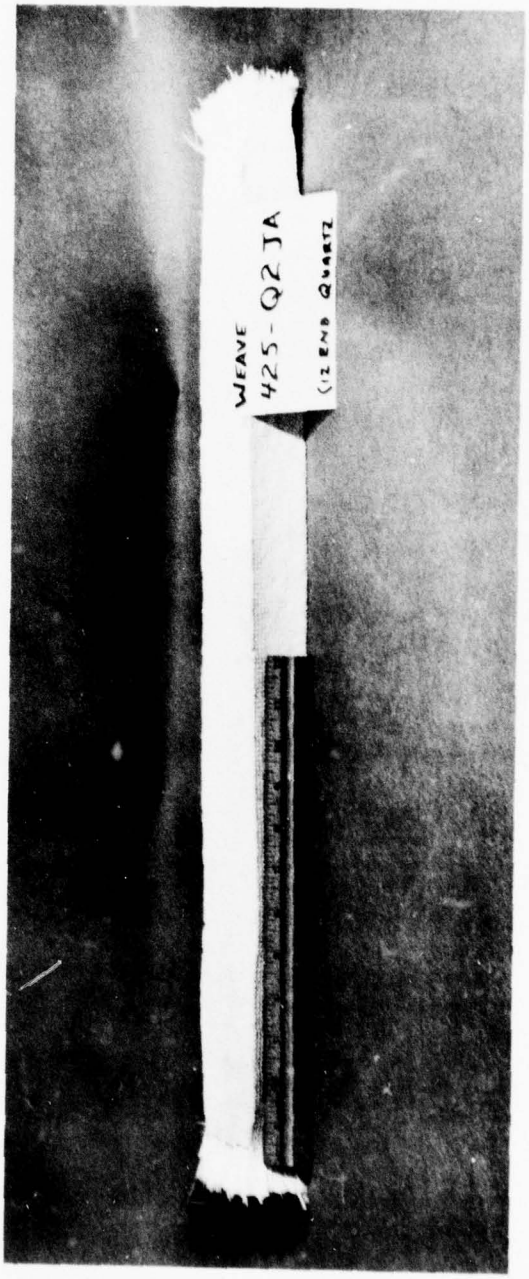

Figure 4. Fineweave Preform 425

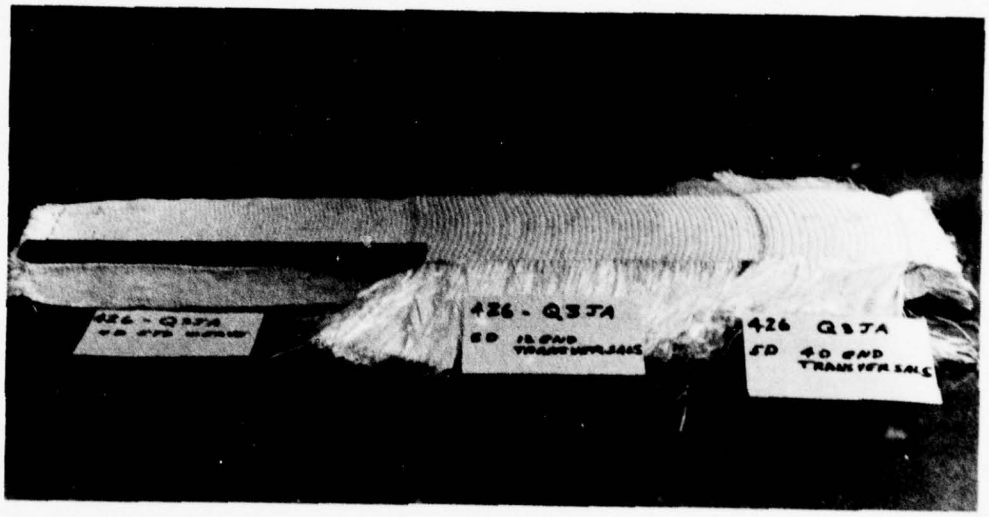

Figure 5. Preform 426

TABLE 6. BORON NITRIDE PREPREGGING EMULSION

(Formulation #8, Table 3, Ref. 1)

Toluene	36 PBW
Isopropanol	49 PBW
Butvar B98	4 PBW
Boron Nitride (0.5 micron)	6 PBW
Dibutyl Sebacate	5 PBW

A review of the boron nitride-fiber volume data in Table 7 shows that the addition of boron nitride either by prepregging or by injection reduces the quartz fiber volume in the preform. It is felt that this is due to the lubricity of boron nitride coupled with the Omniweave preform fabrication process. In the Omniweave process, some friction between fibers is necessary so that previously woven stitches remain tightly packed until subsequent weave motions lock them in place. The addition of the boron nitride prior to or at this point reduces this friction and, therefore, some weave relaxation occurs, thereby reducing the fiber volume of the woven preform.

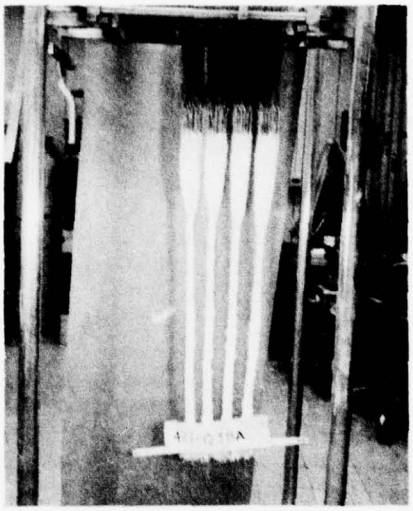

Figure 6. BNQ Preform #427

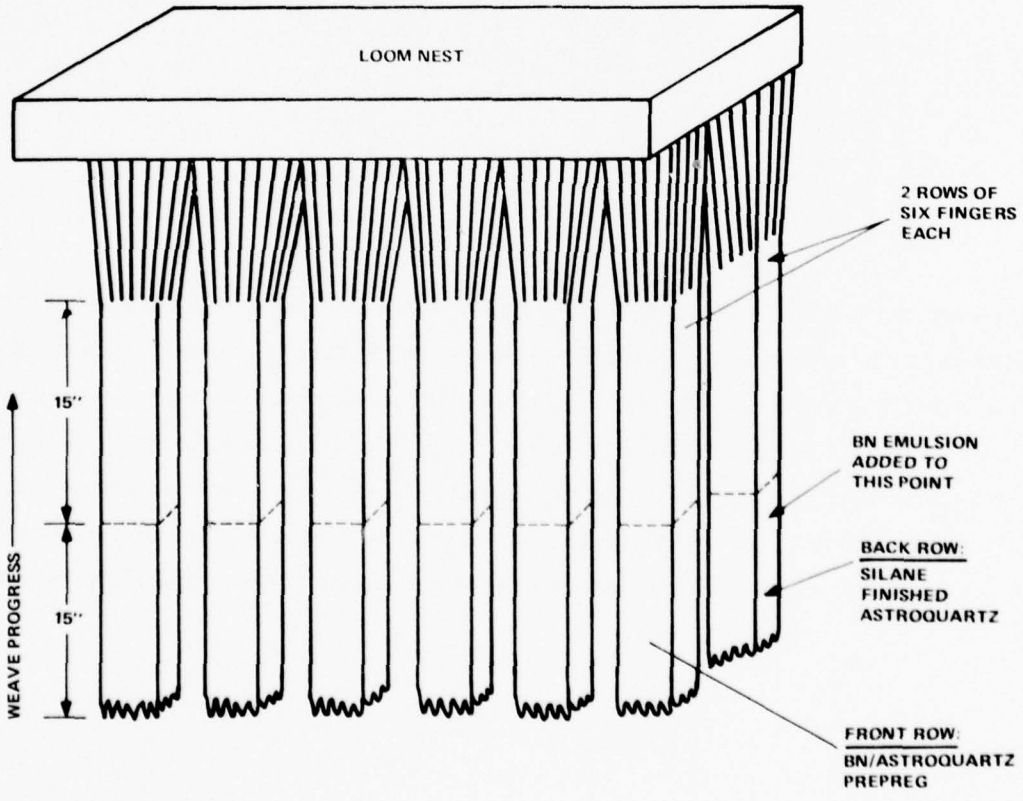

Figure 7. Sketch of #427 Finger Weave Preforms

TABLE 7. BNQ PREFORM CHARACTERIZATION DATA

	Number 427 Series Preforms			
Weave Design:	4D		4D	
Fiber Type:	Astroquartz® 552 Roving		Astroquartz® 552 Roving	
Roving End Count:	20		20	
Finish:	BN Prepreg (6)		Silane (6)	
	BN Added In Situ (3)	Plain (3)	BN Added In Situ (3)	Plain (3)
Woven Dimensions (in)	0.6x0.8x15	0.6x0.8x15	0.6x0.8x14	0.6x0.8x12
Average Woven Density (g/cm^3)	0.8	0.6	0.8	0.9
Average Fiber Volume (%)	19	22	25	42
Average BN Volume (%)	12	1	12	0

2.3 COMPOSITE Ddensification

The three major objectives under the ADL-4D6 densification task are:

1. To fabricate ADL-4D6 material by the "standard" process for further characterization of the baseline material
2. To produce a "fine weave" variation of ADL-4D6 and compare its properties to the standard material
3. To investigate densification process variations which may lead to improved composite properties

2.3.1 STANDARD DENSIFICATION PROCESS

A flow diagram of the standard ADL-4D6 densification process is shown in Figure 8. Prior work on this silica-silica system under a NASA contract (NAS 2-9361, Ref. 5) aimed at producing very high purity silica-silica composites for reflective heat shield applications showed that the contamination level in ADL-4D6 composites is reduced by: 1) washing the Omniweave preform prior to infiltration with colloidal silica (reduces Na+ level in preform from approximately 200 ppm to approximately 100 ppm); and 2) ion-exchanging the colloidal silica sol prior to use (reduces Na+ in silica solids from approximately 220 ppm to approximately 125 ppm).

These two steps have been incorporated into the ADL-4D6 densification process originally reported in Reference 1.

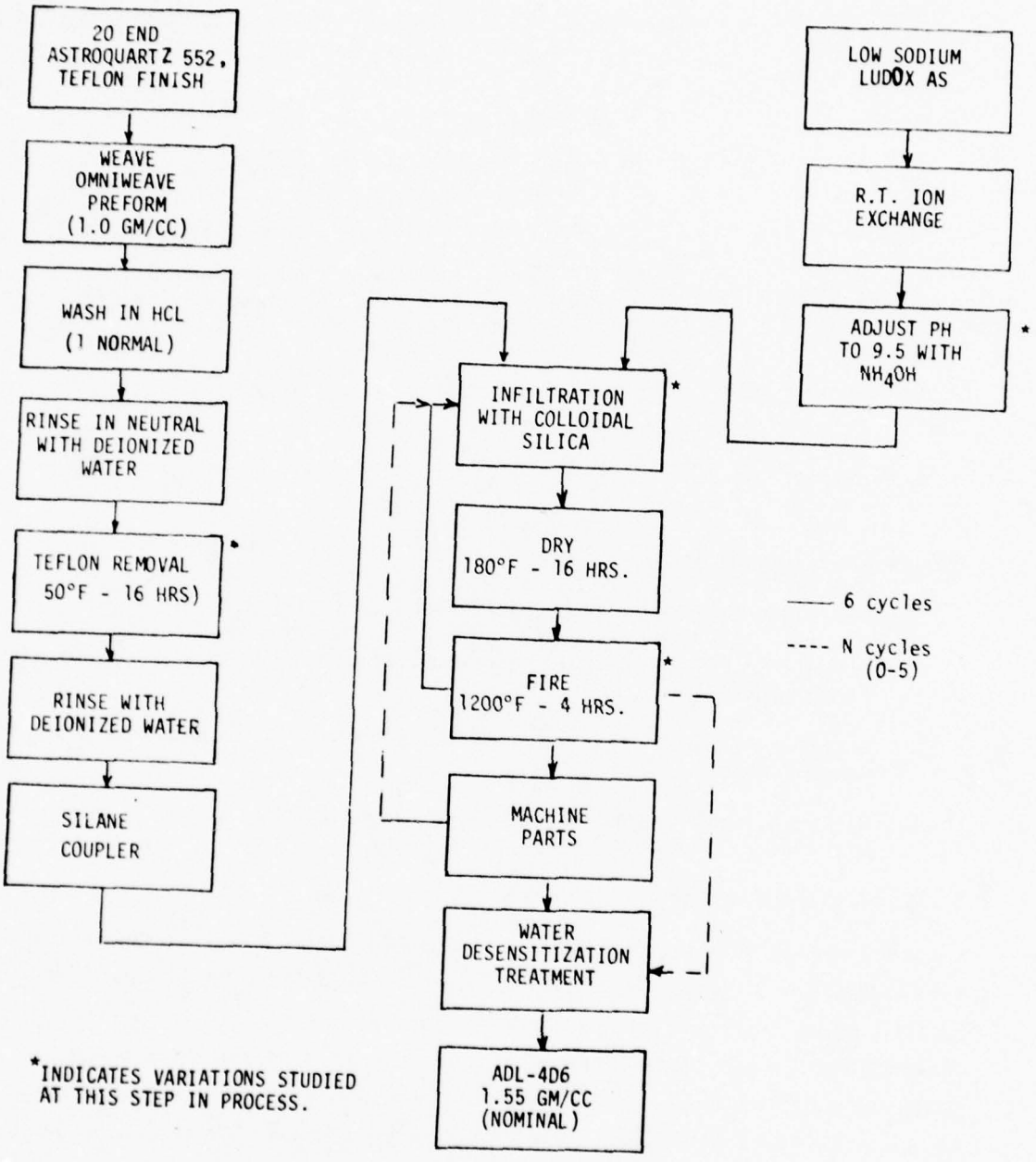

Figure 8. ADL-4D6 Standard Fabrication Process

In this study four ADL-4D6 plates have been densified by this baseline process: two standard preforms (418-2 and 423-3) and two fine weave preforms (424-1 and 424-2). Characterization data on these densified parts is shown in Table 8.

2.3.2 PROCESS VARIATION STUDIES

The goal of this task was to improve ADL-4D6 composite properties by evaluating the effect of certain modifications to the standard densification process. A tree diagram of the densification process variations evaluated is shown in Figure 9. Table 9 lists the bulk panel characterization data for all panels fabricated in this process variation study. Each process variation evaluated is described in the following subsections (2.3.2.1 through 2.3.2.4). The flexure test results for each process variation are given in subsection 3.2.1.2.2.

2.3.2.1 Preform Heat Cleaning Variations

This process variation was intended to evaluate the effect of residual teflon finish on the quartz filaments (prior to initial densification) on the ultimate composite properties through alterations at the fiber/matrix interface.

2.3.2.1.1 Delete Heat Cleaning (Teflon Removal) Step - The purpose of this modification was to prevent thorough penetration of the colloidal silica particles into the fused quartz roving bundles during preform densification. It was felt that this condition might result in higher composite strengths and failure strains due to relatively "soft" (partially impregnated) fiber bundles in the final composite. By allowing the teflon to remain on the fibers during the first two colloidal silica impregnations, it would block the colloidal particles from penetrating the fiber bundles and lead to a buildup of deposited silica around each bundle. This silica coating would inhibit colloidal silica penetration into the fiber bundles during subsequent infiltrations, although the teflon would be removed after the first firing cycle during densification. Panel number 423-1 was fabricated using this modified process. No silane coupler was applied -- it would not bond to the teflon, and minimal silica coupling to the fiber bundles during first infiltrations was the parameter under investigation. Flexural test results for this process variation are shown in Table 14 in Section 3.

2.3.2.1.2 Higher Heat Cleaning Temperature - One preform, #423-6, was initially heat cleaned at 650°C, then densified using the standard procedure. This higher temperature initial heat clean (650°C versus standard 510°C) insured complete removal of the teflon finish prior to silane treatment and infiltration with colloidal silica. With the addition of the silane coupler, this condition provided the maximum possible penetration and bonding between the matrix and fiber. Flexural test results for this process variation are shown in Table 14 in Section 3. This experiment completed the heat cleaning variation studies: no heat clean (423-1), standard heat clean (418-2 and 423-3) and high temperature heat clean (423-4).

However, the relatively high temperature required to form boron nitride from B-trichloroborazole ($B_3N_3H_{30}Cl_3$), i.e., 1100-1200°C had a deleterious effect on the fiber strength although it

TABLE 8. ADL-4D6 PANEL CHARACTERIZATION DATA
(STANDARD DENSIFICATION PROCESS)

Panel ID	Preform ID	Preform Type	Preform Density (g/cm^3)	Surface Fiber Pitch Angle	Densified Panel Bulk Density (g/cm^3)	Densified Panel Fiber Volume	Densified Panel Porosity	End Use
418-2	418*	Standard	1.07	50°	1.59	49%	28%	- Electrical Test - Mechanical Test - Particle Impact - French Solar Furnace
423-3	423	Standard	1.05	40°	1.50	48%	32%	- Mechanical Test - Particle Impact
424-1	424	Fine Weave	0.94	40%	1.57	43%	29%	- Mechanical Test - Spall Test - Electrical Test
424-2	424	Fine Weave	0.96	40°	1.50	40%	32%	- Mechanical Test - Spall Test - French Solar Furnace

*Unused section of preform 418 woven under previous AMMRC contract (Ref. 1, Table 2).

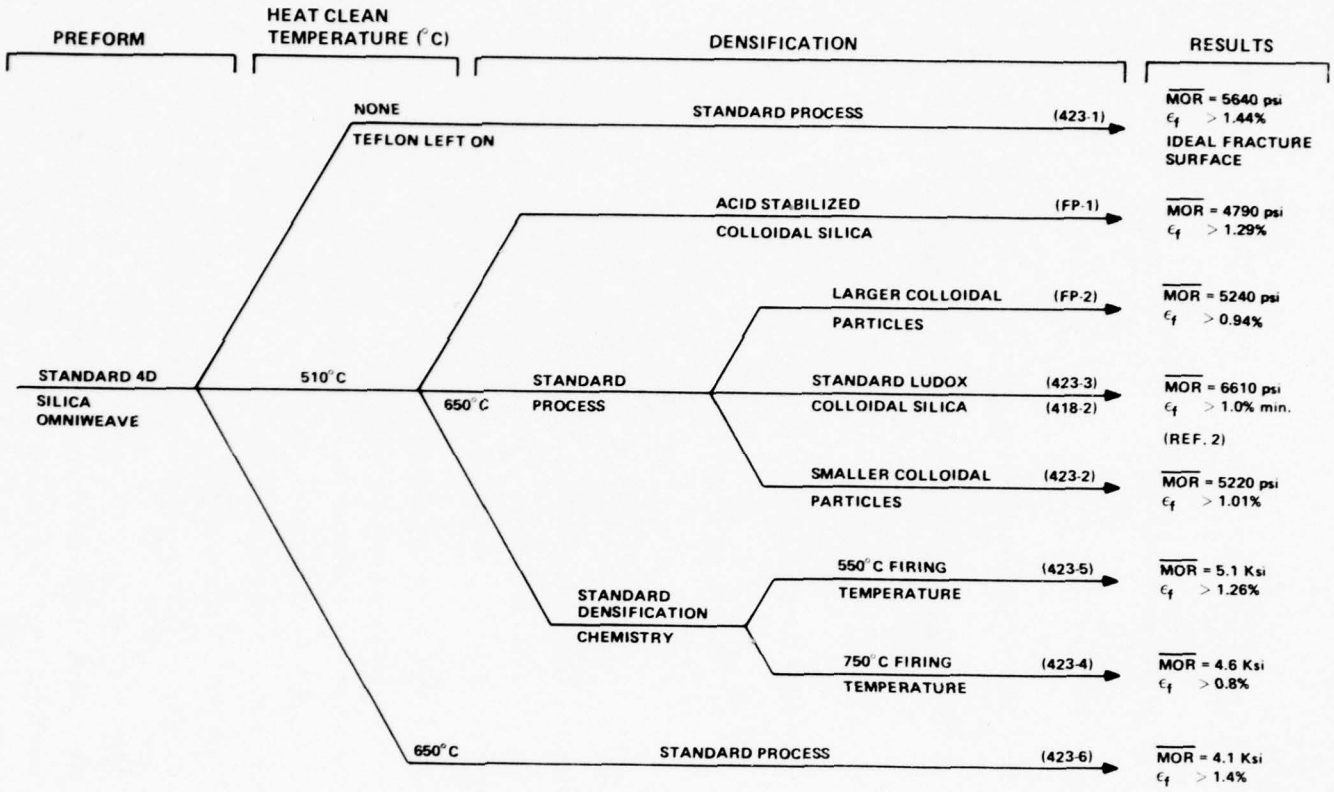

Figure 9. ADL-4D6 Densification Process Variations

TABLE 9. CHARACTERIZATION DATA ON PROCESS VARIATION STUDY PANELS

Panel ID	Process Variation	Bulk Density (g/cm^3)	Fiber Volume	Porosity
423-1	Delete Heat Cleaning	1.57	48	29
423-6	650°C Heat Clean	1.51	43	31
423-2	Smaller Colloidal Silica	1.51	48	31
FP-2	"Aggregated" Colloidal Silica	1.45	41	34
423-4	750°C Firing Temperature	1.54	48	30
423-5	550°C Firing Temperature	1.59	43	28
FP-1	Acid Stabilized Colloidal Silica	1.64	45	25

2.3.2.2 Variation of Colloidal Silica Particle Size

This process modification provided an evaluation of ADL-4D6 composite properties versus size of the colloidal silica particles used during densification. Parts were densified with both smaller and larger (effective) sized colloidal particles than low-sodium Ludox AS.

2.3.2.2.1 Smaller Colloidal Silica Particles - Panel 423-2 was densified using Nalco 2326 colloidal silica which is reported (vendor literature*) to have an average particle size of 5 millimicrons compared to 21 millimicrons for low-sodium Ludox AS. The Nalco 2326 colloidal silica was given one room temperature ion exchange before use since previous work (Ref. 5) had shown that after one ion exchange purification, the Nalco 2326 and low-sodium Ludox AS have comparable purity levels (approximately 100 ppm Na^+ in the silica solids). Flexural test results for this process variation are shown in Table 14 in Section 3.

2.3.2.2.2 Larger Colloidal Silica Particles - Since large particle ammonia-stabilized colloidal silica sols are not readily available, it was decided to use "aggregated" colloidal silica sol in place of a large particle sol. Allowing the colloidal silica particles in low-sodium Ludox AS to aggregate increases the effective particle size, at least for infiltration purposes, as shown below in Figure 10.

*Nalco Chemical Company, Product Technical Data Bulletin, K-2326, November 1975.

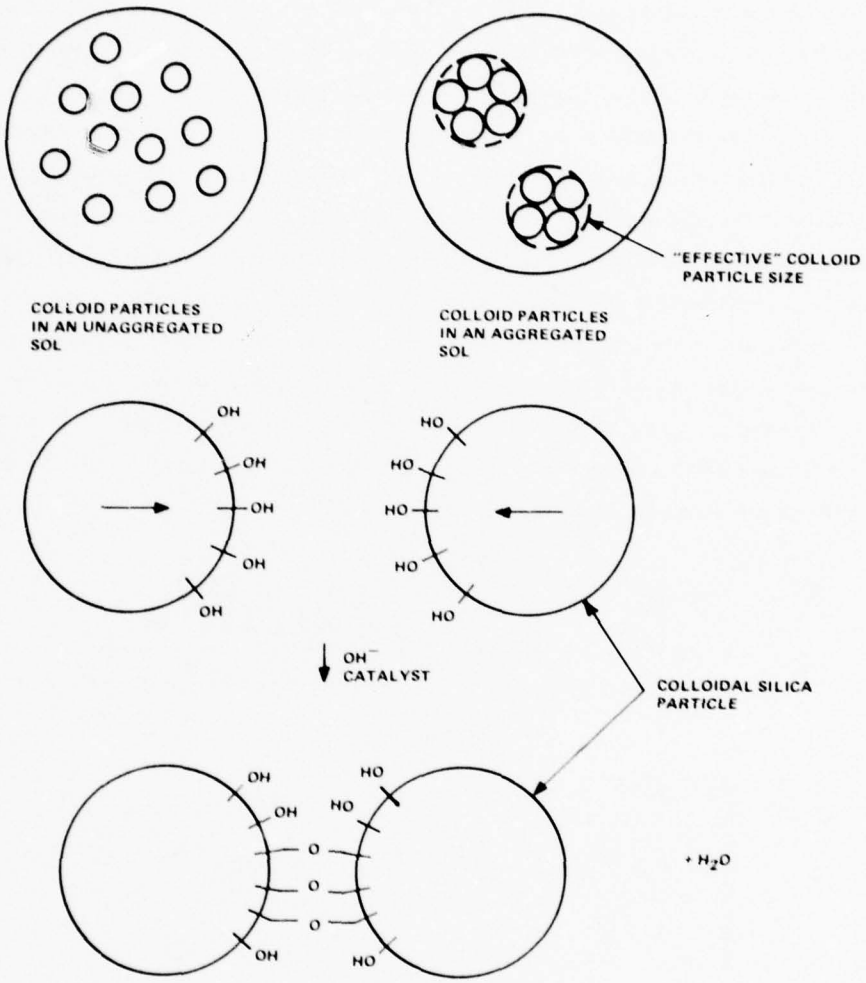

Figure 10. Mechanism of Colloidal Silica Aggregation by Siloxane Bond Formation (Ref. 6, Figure 12)

The layouts for fineweave plates 424-1 and 424-2 are shown in Figures 23 and 24. Spall

The colloidal particles aggregate by forming siloxane bonds between each other. The formation of these siloxane linkages is a function of the surface charge on the colloidal particle and hydroxyl ion content (Ref. 7). This aggregation mechanism is depicted in Figure 11. In the neutral pH region, the colloidal silica particle surface charges are minimized, thereby allowing contact and subsequent siloxane linkage formation. To determine the relative degree of aggregation of a colloidal silica sol a DuPont procedure (Ref. 7) was used. This procedure determines the percent silica in the dispersed phase of a silica sol through viscosity measurements under standard conditions of concentration, purity level and pH. As the percent silica in the dispersed phase decreases, the degree of particle aggregation increases (water becomes occluded in the particle network). Preliminary work showed that low-sodium Ludox AS with pH adjusted to 5-6 with HCL would gel within eight hours. For the degree of aggregation determinations, we adjusted the pH of low-sodium Ludox AS to 5.5 with HCL. The percent silica in the dispersed phase versus time data is shown in Figure 11 for standard low-sodium Ludox AS and Ludox AS. DuPont literature (Ref. 7) notes that particle aggregation has been initiated when the percent silica in the dispersed phase falls below 75 percent. For densification processing, sodium Ludox AS with pH of 5.5 was used after aging 4 hours at room temperature. Part number FP-2 was densified via this technique. Flexural test results for this process variation are shown in Table 15 in Section 3.

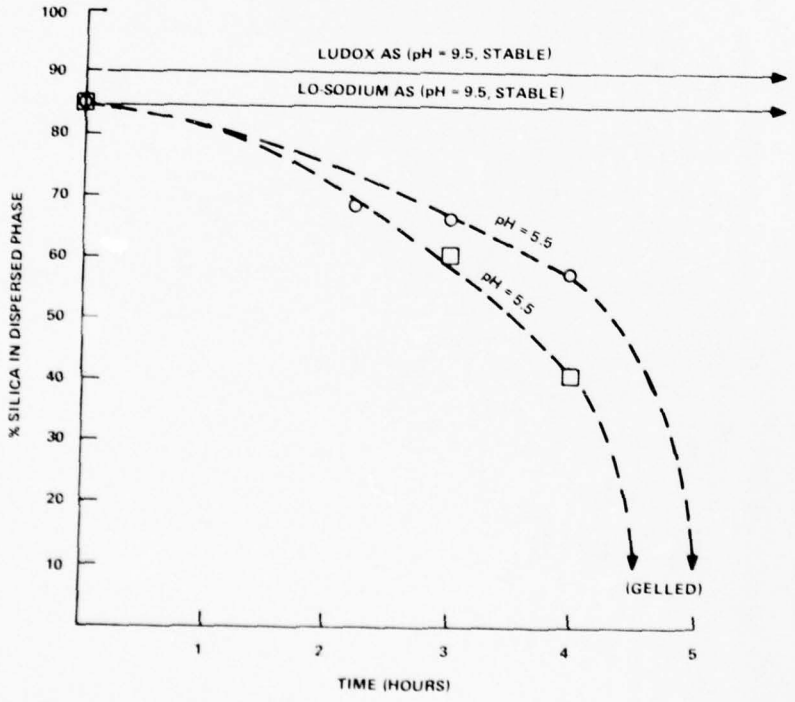

Figure 11. Percent Silica in Dispersed Phase Versus Time for Ludox Colloidal Silica Sols at Room Temperature

2.3.2.3 Heat Treatment Variations

The effect of varying the firing temperature during densification on the strength and modulus of ADL-4D6 composites was also evaluated.

2.3.2.3.1 Lower Firing Temperature - Preform number 423-5 was processed using the standard densification procedure except that a firing temperature of 550°C was used instead of the usual 650°C. It was anticipated that this lower firing temperature would yield a lower modulus and higher strain-to-failure composite by staying well below silica devitrification temperatures. The effect of less matrix sintering on the composite strength would be examined. Flexural test results for this process variation are shown in Table 16 in Section 3.

2.3.2.3.2 Higher Firing Temperature - Preform number 423-4 was processed using the standard densification procedure except that a firing temperature of 750°C was used instead of the usual 650°C. It was anticipated that this higher firing temperature would yield a higher composite modulus with lower strain-to-failure. Previous work had shown a loss of strength at these temperatures, but this effect was compounded by the added process parameter of differences in sodium ion content. The effect of higher repeated firing temperatures on porosity, colloidal silica pick-up during processing, and density was also to be observed. Flexural test results for this process variation are shown in Table 16 in Section 3.

2.3.2.4 Acid Stabilized Colloidal Silica

The colloidal silica particles in typical colloidal silica sols (Ludox and Nalco) are stabilized and prevented from growing or aggregating by the presence of hydroxyl groups on the particle surface. These hydroxyl groups impart a charge to the colloidal particle surface, causing mutual repulsion and thereby preventing the particle contact required for growth or aggregation. The pH of these colloidal silica sols is usually adjusted 9-10 with ammonium hydroxide to achieve this particle stabilization. By adjusting the pH of these colloidal silica sols to the acid range, the surface hydroxyl groups are neutralized resulting in no charge on the particle surface. But in the acid pH range, particle aggregation is still inhibited by the absence of hydroxyl groups required for siloxane linkage formation between particles. The absence of a surface charge on the colloidal particles may improve fiber wetting during impregnation with the colloidal silica. One Omniweave specimen was devoted to this evaluation. Sample FP-1 was densified with low-sodium Ludox with the pH adjusted to 1.0 with HCL.

The flexure bar-sized specimen had a final bulk density of 1.64 g/cm^3 (Table 9). If this increase over the nominal density of 1.60 g/cm^3 could be consistently achieved, other performance properties remaining equivalent, the process variation may well be of interest for this reason alone. Flexural test results for this process variation are shown in Table 17 in Section 3.

2.3.3 WATER DESENSITIZATION STUDIES

In the previous AMMRC program (Ref. 1), a water densensitization process was developed which inhibited water absorption by ADL-4D6 composites. The essence of this technique was to react a halogenated-organo-silane with the hydrated silica surfaces creating a hydrophobic coating on the silica surfaces. A complete description of the chemistry involved is given in Section 2.3 of Reference 1. The process selected at that time consisted of a one hour heat treatment at 900°F to remove the majority of the adsorbed water followed by exposure to methyltrichlorosilane vapors for 24 hours. The methyltrichlorosilane vapor reacts with the remaining adsorbed water to form the hydrophobic polysiloxane coating. The ADL-4D6 specimen treated by the above process exhibited a loss tangent of 0.0056 at 230 MHz after 24 hours storage at ambient conditions (Ref. 1, Table 11, Specimen # FA-1-1).

Since the pure silica-silica content of ADL-4D6 has an intrinsically low loss tangent (approximately 0.0005 at 250 MHz), it was decided to try to improve on the previously developed water desensitization process to achieve lower loss tangents in treated ADL-4D6 composites. The baseline process was modified by increasing the heat treatment time from one to four hours at 900°F prior to methyltrichlorosilane exposure. Following the extended heat treatment, the specimens, while still hot, were placed in a methyltrichlorosilane chamber and exposed to the vapors for 24 hours. The increased heat treatment time was intended to remove more of the surface adsorbed water from the silica surface, resulting in a thinner final polysiloxane coating from the silane-water reaction.

Standard and fine weave ADL-4D6 specimens designated for baseline property characterization were given this water desensitization treatment after densification processing. Generally, there is a is a weight increase of about 0.7 percent due to the polysiloxane formation from this process.

Dielectric constant and loss tangent measurements were made on specimens treated by this process, then stored at ambient conditions for up to 13 days. The dielectric properties were measured with a resonant cavity measurement system shown schematically in Figure 12. The resonant frequency and cavity Q were measured with and without the sample in the cavity. The dielectric constant and loss tangent were calculated from the decrease in resonant frequency and cavity Q, respectively. The sample size used for this investigation was a 5/8-inch diameter x 1/10 inch thick disc. The dielectric constant and loss tangent data are shown in Table 10 and Figure 13. From this data it can be seen that the loss tangent of treated ADL-4D6 stored at ambient for 24 hours is 0.0039 at 250 MHz which is improved over the previous process loss tangent of 0.0056 at 230 MHz in 24 hours.

The loss tangent still increases with time and appears to level off at about 0.0052 for the standard material and 0.0058 for the fine weave material in about 13 days.

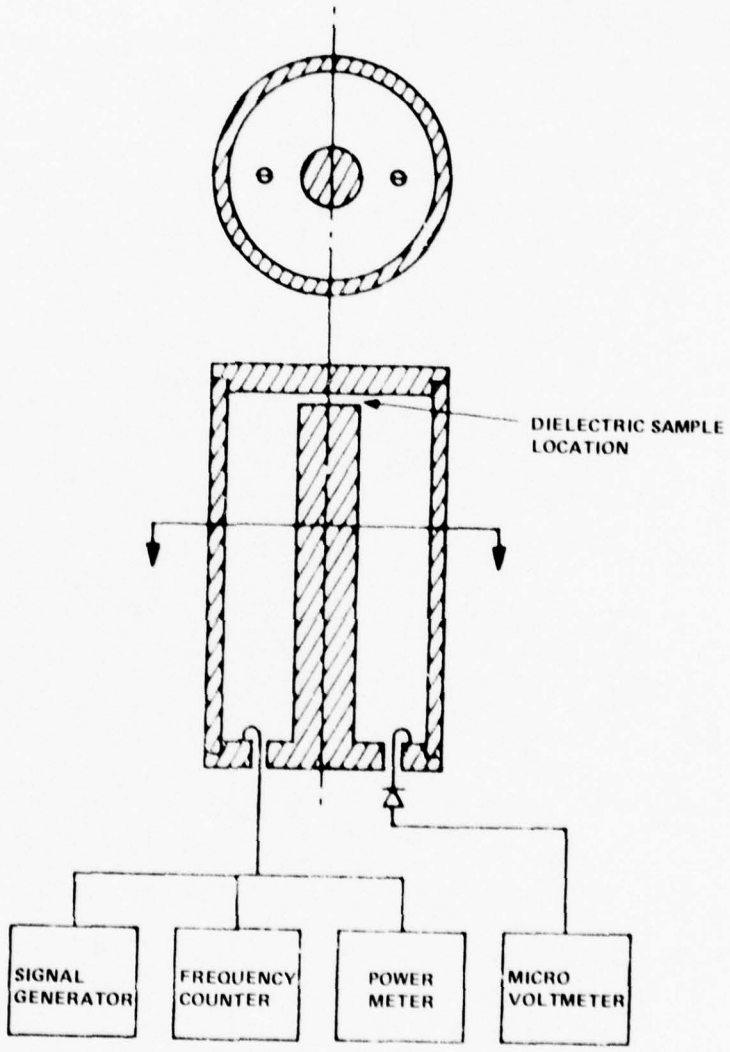

Figure 12. Resonant Cavity Measurement System

TABLE 10. DIELECTRIC PROPERTIES OF ADL-4D6 AT 250 MHz

Specimen ID	Material	Dielectric Property	**After Firing at 1000°C	After Water Densitization Treatment			
				*1/18/78 (after 1 day)	*1/19/78 (after 2 days)	*1/21/78 (after 4 days)	*1/23/78 (after 13 days)
418-2-A	Standard ADL-4D6	K	2.745	2.810	2.825	2.835	2.835
		tan delta	0.0005	0.0038	0.0040	0.0048	0.0052
424-1-B	Fine Weave ADL-4D6	K	2.792	2.863	2.877	2.894	2.895
		tan delta	0.0005	0.0039	0.0045	0.0052	0.0058

*Samples allowed to remain in lab air environment (70°F, 35% RH)

**Samples kept in dessicator after firing until measurement; measurement to establish baseline data on completely dry ADL-4D6.

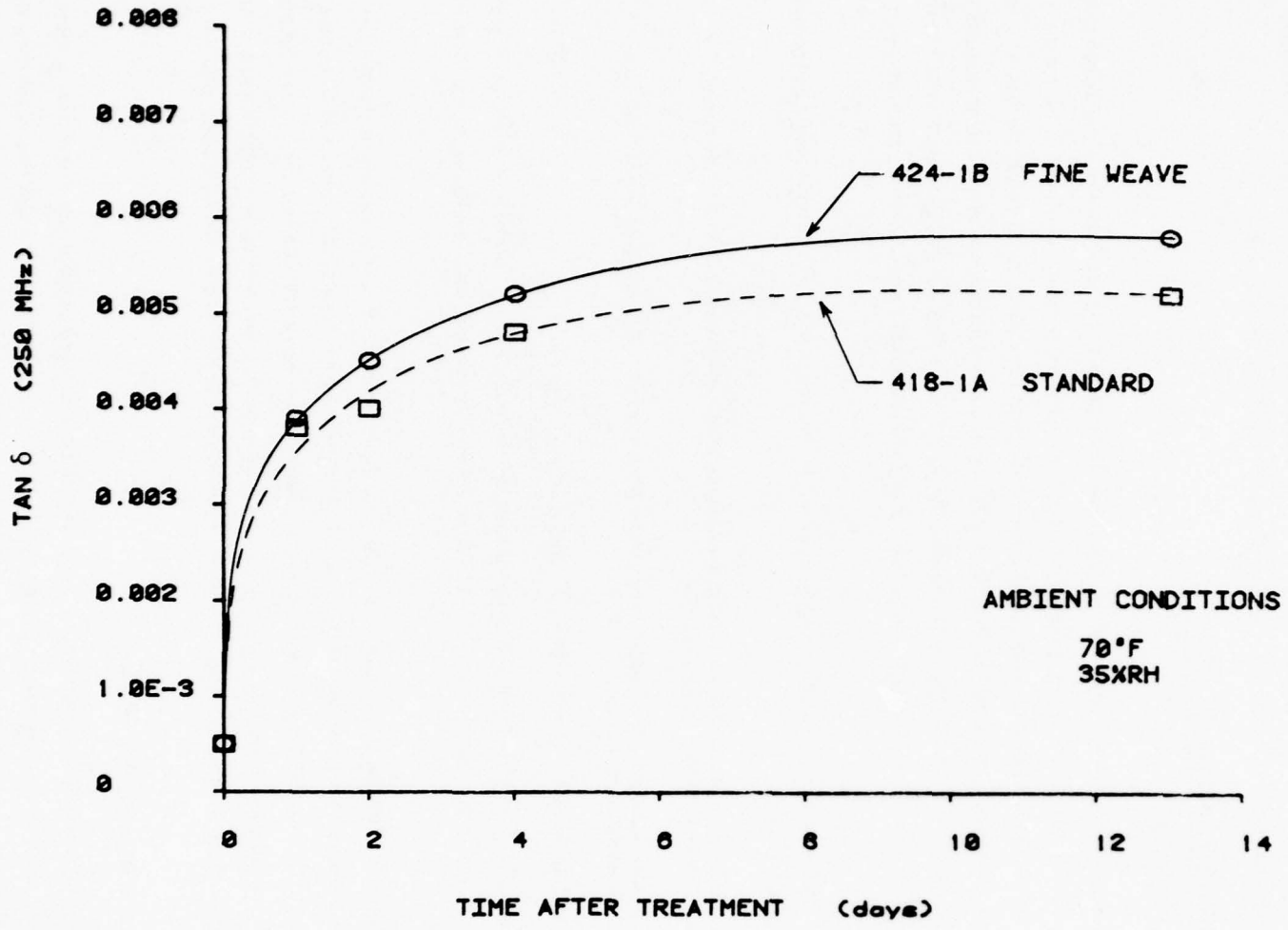

Figure 13. ADL-4D6: Tan Delta Versus Time at Ambient Conditions After Silane Water Desensitization Treatment

Figure 7. Sketch of #427 Finger Weave Preforms

Further refinements of this water desensitization process, such as more stringent heat treatments and a more thorough silane exposure through evacuation and backfilling of chamber with silane should result in even lower loss tangents for treated ADL-4D6 material.

2.4 BNQ COMPOSITE DENSIFICATION

2.4.1 BACKGROUND

The objective of the BNQ development task was to further the development of the boron nitride-silica hybrid composites investigated in the previous AMMRC program (Ref. 1). The desired characteristic of these hybrid composites is a very high strain to failure achieved by the use of a low strength (crushable) final rigidization matrix in combination with a boron nitride intermediate filler to "lubricate" the silica fibers as the composite deforms. A high BN solids content yarn prepreg process was developed in Reference 1, but a process suitable for manufacturing preforms was not achieved.

In that prior work, the following approaches to incorporating boron nitride into a silica-based composite were used:

1. Use of a boron nitride-filled non-charring resin-prepregged Astroquartz roving for Omniweave preform fabrication
2. Infiltration of Astroquartz Omniweave preforms with fine particle-sized boron nitride during weaving process, and
3. Combinations of both these techniques

Generally, the BNQ Composites fabricated via these approaches had either relatively low fiber content or low boron nitride content. The fiber volume decreased with increasing boron nitride content.

The goal in this program was to increase the fiber volume and boron nitride content of these composites such that relatively small amounts of rigidizing matrix would be required to reduce final porosity. This would allow the boron nitride "lubrication" characteristic to have greater influence on the toughness and elasticity aspect of the composite properties, while the strength and a reasonable value of initial modulus (100,000 psi or more) would be assured by the high fiber volume fraction.

2.4.2 COMPOSITE PROCESSING

Several approaches to fabricating the BNQ Composites were planned and are shown in Figure 14. One basic difference between approaches is the timing of the boron nitride addition in the composite fabrication sequence. The first method adds the boron nitride before or during the silica preform

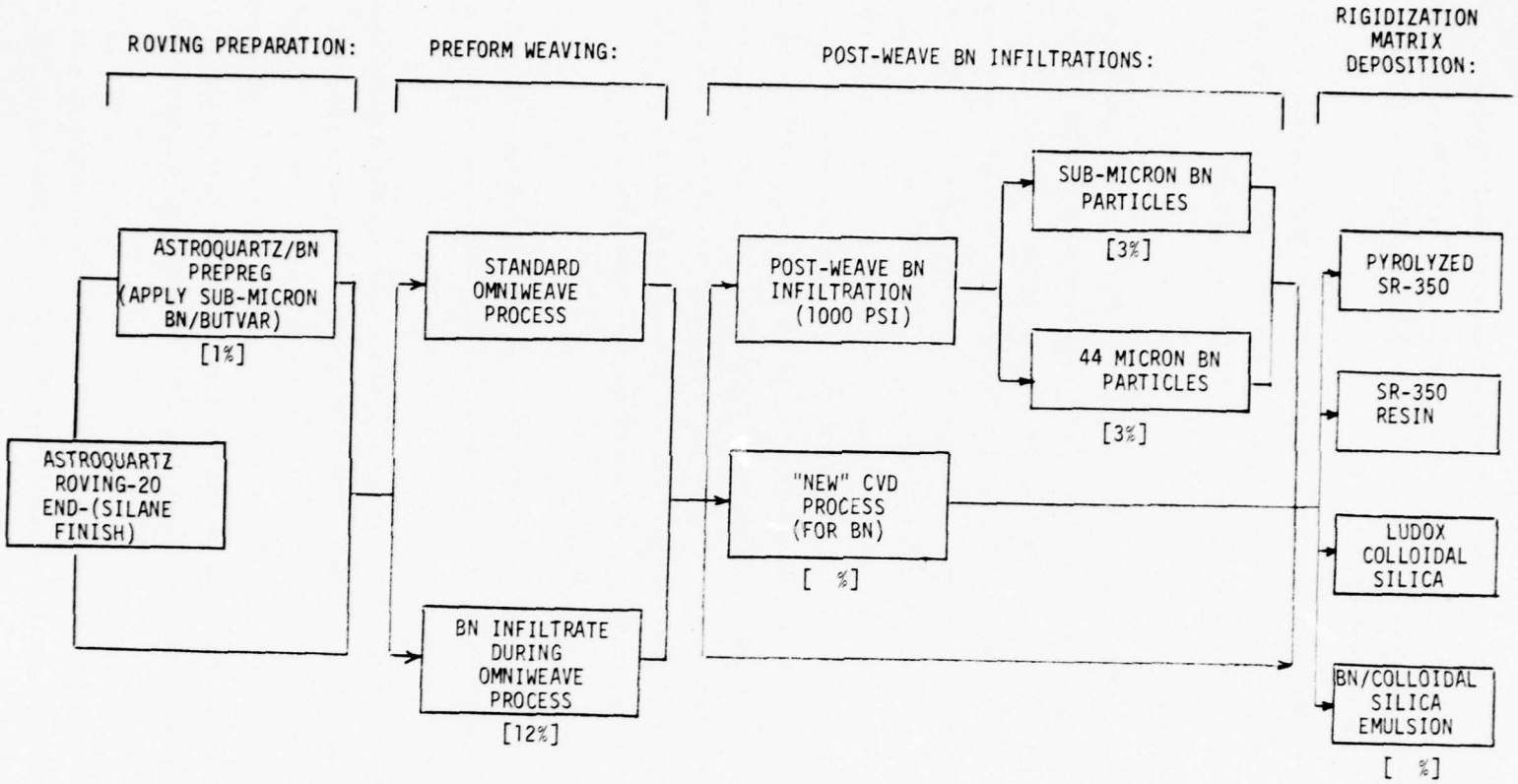

[%] INDICATES AVERAGE VOLUME PERCENT BN PICKUP AT EACH STAGE.

Figure 14. BNQ Composites: Fabrication Processes

fabrication step. The boron nitride addition techniques at this stage in the composite processing are the use of a boron nitride prepregged Astroquartz roving for weaving and/or packing the preform with a boron nitride emulsion during weaving. Both of these approaches are discussed under "BNQ Preform Fabrication" in Section 2.2.3.

The two techniques investigated for adding boron nitride to an already woven silica preform are infiltration with particulate boron nitride and chemical vapor deposition (CVD). The following procedure was used to infiltrate woven preforms with particulate boron nitride.

2.4.2.1 Autoclave Infiltration of Particulate BN

Two emulsions of 20 percent by weight boron nitride in distilled water were used for the infiltrations. One emulsion used 0.5 micron boron nitride powder and the other used a -325 mesh (44 microns) powder. This was done to check on any difference in degree of penetration between these particle sizes. Sections of the 427 fingerweave preforms, about 3 inches long, were immersed in the boron nitride emulsion and the container then placed in an autoclave. The autoclave chamber was evacuated to 28" Hg for 5 minutes, then backfilled with N_2 and 1000 psi applied for 30 minutes. The pressure was released and the parts were removed from the emulsion container and oven-dried at 200°F for 16 hours. No discernable difference in weight pickup or degree of penetration was evident between the 0.5 micron and -44 micron boron nitride particle emulsions. The amount of boron nitride added to the fingerweave preforms via this procedure ranged from 5 to 10 percent by weight and seems to be a function of the original preform density and boron nitride content. Those fingerweaves with a high fiber volume or a high boron nitride content (added during weaving) had the lower boron nitride weight pickups during post-weave infiltration.

2.4.2.2 Chemical Vapor Deposition of BN

Another method for introducing the boron nitride into a silica fiber preform is chemical vapor deposition. Unfortunately, delays in receiving the boron nitride precursor material required for the intended process prevented any experiments along this approach.

This approach takes advantage of a temperature gradient that exists through the thickness of a specimen placed against a heated surface. Precursor vapors containing the elemental components of the desired deposit are passed across the cooler, outer surface of the preform. The portion that diffuses into the weave decomposes at the inner, heated surface, gradually filling the voids against the heated surface and increasing the density. This improved thermal conductivity and the deposition region gradually pass through the thickness of the specimen, progressively increasing the density of the part.

An approach of this type was attempted with a silica woven structure, Reference 2, in which boron nitride was deposited in the interstices and among filaments in the fiber bundle (Ref. 8).

However, the relatively high temperature required to form boron nitride from B-trichloroborazole ($B_3N_3H_{30}C1_3$), i.e., 1100-1200°C had a deleterious effect on the fiber strength although the chemistry was advantageous in that solid by-products, which would have obstructed furnace lines and prohibited the long infiltration times required for high densification, were not formed.

Recently, however, a less stable compound, borazene ($B_3N_3H_6$), has become available (Ref. 9) from which boron nitride can be formed at quite low temperatures, e.g., 600-800°C. Thus, it should be possible to achieve high infiltration densities without divitrification damage to the silica fibers.

2.4.2.3 Densification Results

Table 11 lists the characteristics of the BNQ Composites processed up to the rigidization step.

It was originally planned to rigidize the BNQ preforms with the following matrices:

1. SR350 silicone resin,
2. Silica derived from the pyrolysis of SR350, and
3. Silica from Ludox colloidal silica

The BNQ preforms with low fiber volume fractions were to be debulked (compressed in the thickness direction) during rigidization to increase the fiber fraction in the rigidized composite. At this point, preliminarywork has been done with SR350 only. A series of BNQ specimens have been rigidized with SR350 resin under varied imprenation conditions in an attempt to arrive at satisfactory fiber, boron nitride and rigidizing matrix contents in the densified composite. The BNQ specimens were vacuum impregnated with a solution of SR350 resin in acetone, then oven-dried at 160°F for 16 hours followed by curing at 400°F for 2 hours. Specimens that were debulked were compressed to the desired final thickness with the sides constrained during the 400°F cure. Table 12 lists the characteristics of these SR350 rigidized BNQ specimens. Specimen 427-B-1, while having a slightly low fiber fraction, has a good ratio of fiber/BN/matrix contents.

TABLE 11. BNQ COMPOSITE CHARACTERISTICS (PRIOR TO RIGIDIZATION)

Composite I.D.	Boron Nitride Infiltration Process Used	Average Characteristics		
		Density (gm/cc)	Fiber Vol. (%)	BN Vol. (%)
427-A-1 to 6	prepreg post weave infiltrate	0.63	23	6
427-A-7 to 9	prepreg	0.59	22	1
427-B-1 to 6	prepreg in weave infiltrate post weave infiltrate	0.75	19	15
427-B-7 to 9	prepreg in weave infiltrate	0.77	21	15
427-C-1 to 6	post weave infiltrate	0.93	41	3
427-D-1 to 6	in weave infiltrate post infiltrate	0.89	25	12

TABLE 12. SR350 RIGIDIZED BNQ COMPOSITES

Specimen I.D.	Density (gm/cc)	Fiber Vol. %	BN Vol. %	SR350 Vol. %	Porosity %	Remarks
427-A-1	1.55	41	5	48	6	65% SR350 solution and faces constrained during cure.
427-A-3	1.67	44	2	55	0	low BN content high matrix content
427-A-5	1.45	35	2	52	11	40% SR350 solution and no debulking
427-A-6	1.38	38	2	46	14	high matrix and low BN content
427-A-2	1.28	35	2	41	22	35% SR350 solution and no debulking
427-A-4	1.23	35	2	37	26	high matrix and low BN content
427-B-1	1.55	31	28	19	22	25% SR350 solution and debulk 40% during cure
427-B-6	1.70	34	21	40	5	good component ratio

3. CHARACTERIZATION

3. CHARACTERIZATION

3.1 THE SAMPLING AND CHARACTERIZATION PLAN

This section contains the description of all performance property testing of multidirectional-reinforced composites developed on this program. Properties of constituents — fiber strength and chemical purity, thermal stability of fiber coatings, etc. — are contained in Section 2 along with descriptions of the composite formulation and fabrication.

The section begins with detailed ADL-4D6 plate layout plans, showing the selection of test samples from the densified plates, their configuration and dimensions, and recording the identification labelling. This very careful recording of specimen origin has proven its value in previous programs for such purposes as interpretation of test anomalies and verification of specimen orientation. It also serves as a convenient graphic material disposition accounting device.

Figures 15 through 24 contain the layout plans.

Figure 15 shows the layout plan for standard ADL-4D6 plate 418-2. Two 2.00 inch diameter discs were supplied from this plate (and fine weave standard process plate 424-2) to AMMRC for hot radar transmission tests in the CNRS 1000 kW Solar Furnace, Odeillo, France. These discs were of course completely processed through silane water desensitization. The drawing shows these two discs and two flexure bars in the standard configuration used in this series of programs to be cut with a 3/8 inch clearance from the top selvage stitches.

Below this are discs for various dielectric property measurements, coded as follows:

Code	Measurement
EMX-M	X-band, MIT
EMM-M (1.00" Dia.)	90 GHz, MIT
EMM-M (1/2" Dia.)	24 GHz, MIT
EMX-GE	X-band, GE-RESD
EML	L-band, GE-RESD

A large number of particle impact test (PI) specimens are indicated in two sizes, the 1.25" x 0.75" x 0.40" plates are for 1/2 and 1 mm (0.02 and 0.04 inches) diameter particle tests. The detailed layout for plate 423-3 (Figure 19) also shows 1.5" x 2.0" x 1.0" thick PI specimens designated for 5 MM (0.02 inches) diameter particle impact.

Figure 24 shows the master sampling plan for Omniweave preform 423. It is followed by the detailed densified plate layout plans for plates 423-1 through 423-6. With the exception of 423-3, all of these are process variation plates and show the flexure bar sampling used, with provision for later specification of other test specimen types, or material for further process variation studies.

The layouts for fineweave plates 424-1 and 424-2 are shown in Figures 23 and 24. Spall test specimens (US/FP) were taken from these plates for the flyer plate testing at ETI, intended to compare the shock resistance of this weave variation, processed by the standard process, to the standard weave and process ADL-4D6.

Uniaxial loading tension ("T-1") and compression ("C-1") specimens are also designated for plate 424-1.

The following sections describe the performance property measurements. "Mechanical Properties" are given first, in Section 3.2. These are followed by "Ultrasonic Measurements" (Section 3.3), "Shock Testing" (Section 3.4), including both plate and particle impact testing. The characterization section concludes with the results of "Electromagnetic Property Testing" (Section 3.5) done at the Laboratory for Insulation Research (LIR) of Massachussetts Institute of Technology.

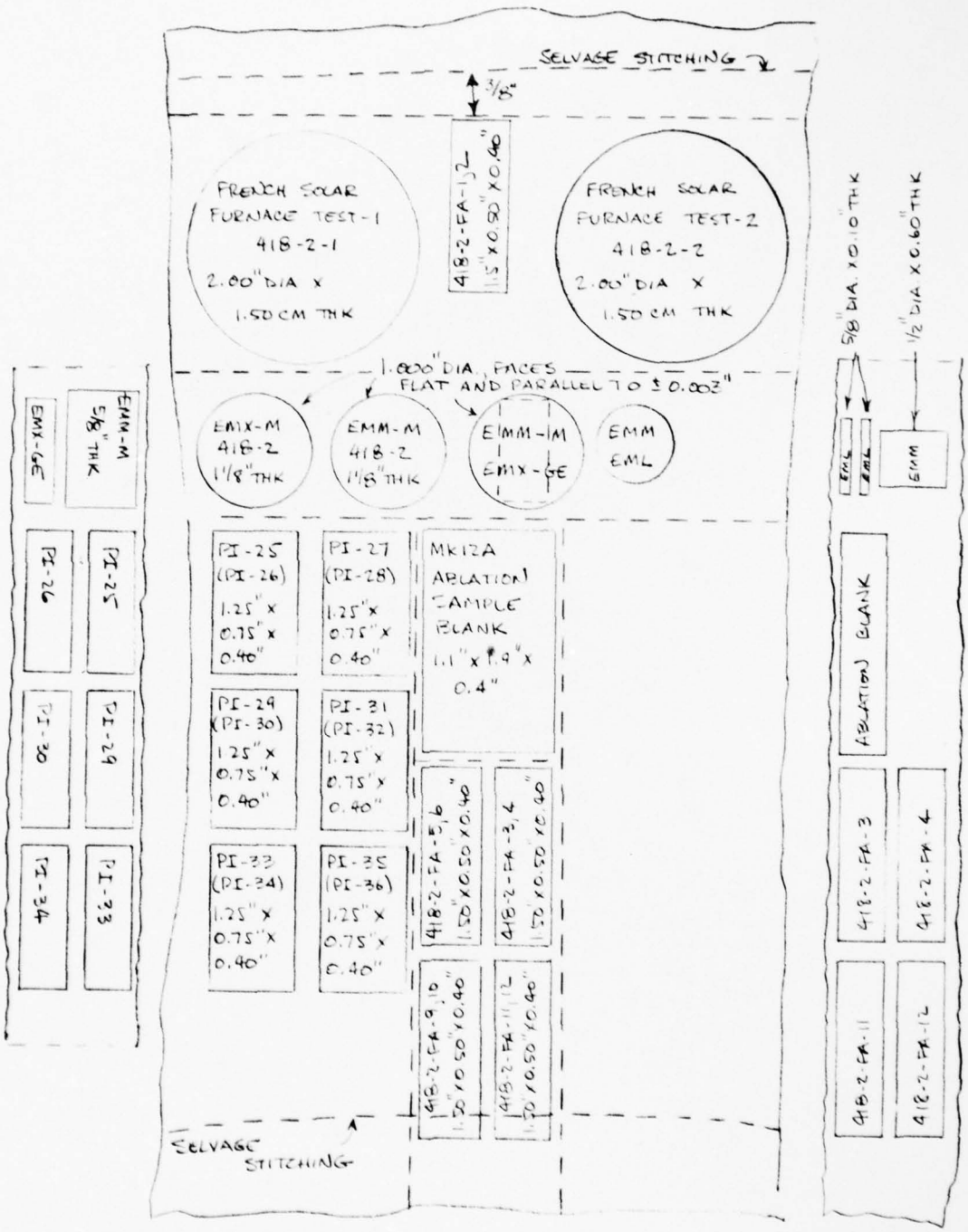

Figure 15. Sampling Plan: ADL-4D6 Plate 418-2

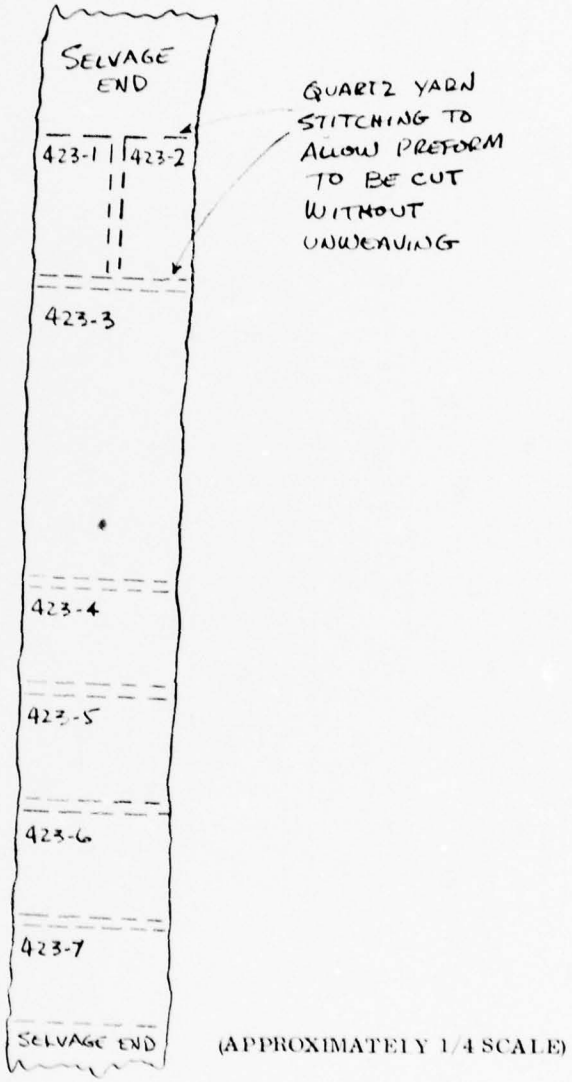

Figure 16. Astroquartz Omniweave Preform 423 Sectioning Plan

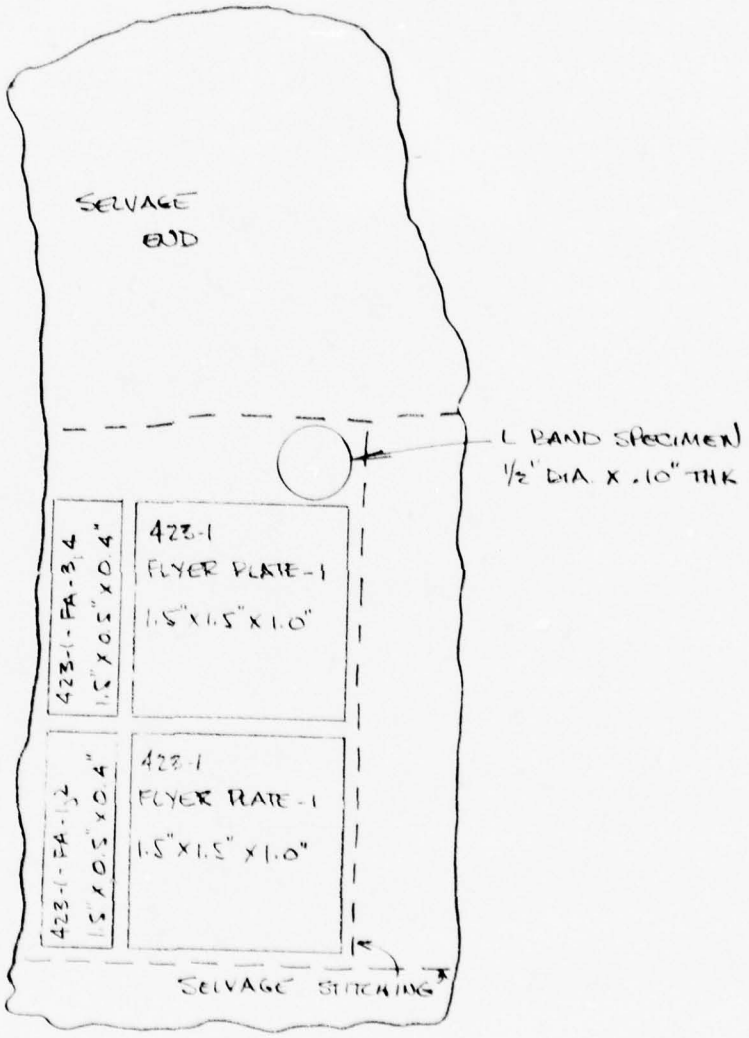

Figure 17. Sampling Plan: ADL-4D6 Plate 423-1

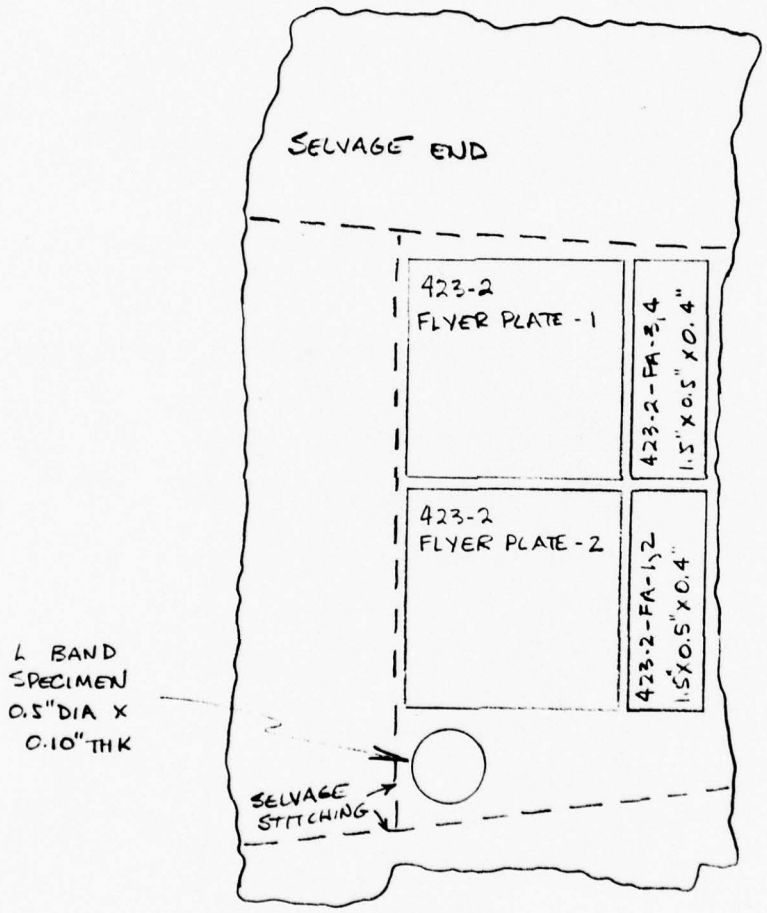

Figure 18. Sampling Plan: ADL-4D6 Plate 423-2

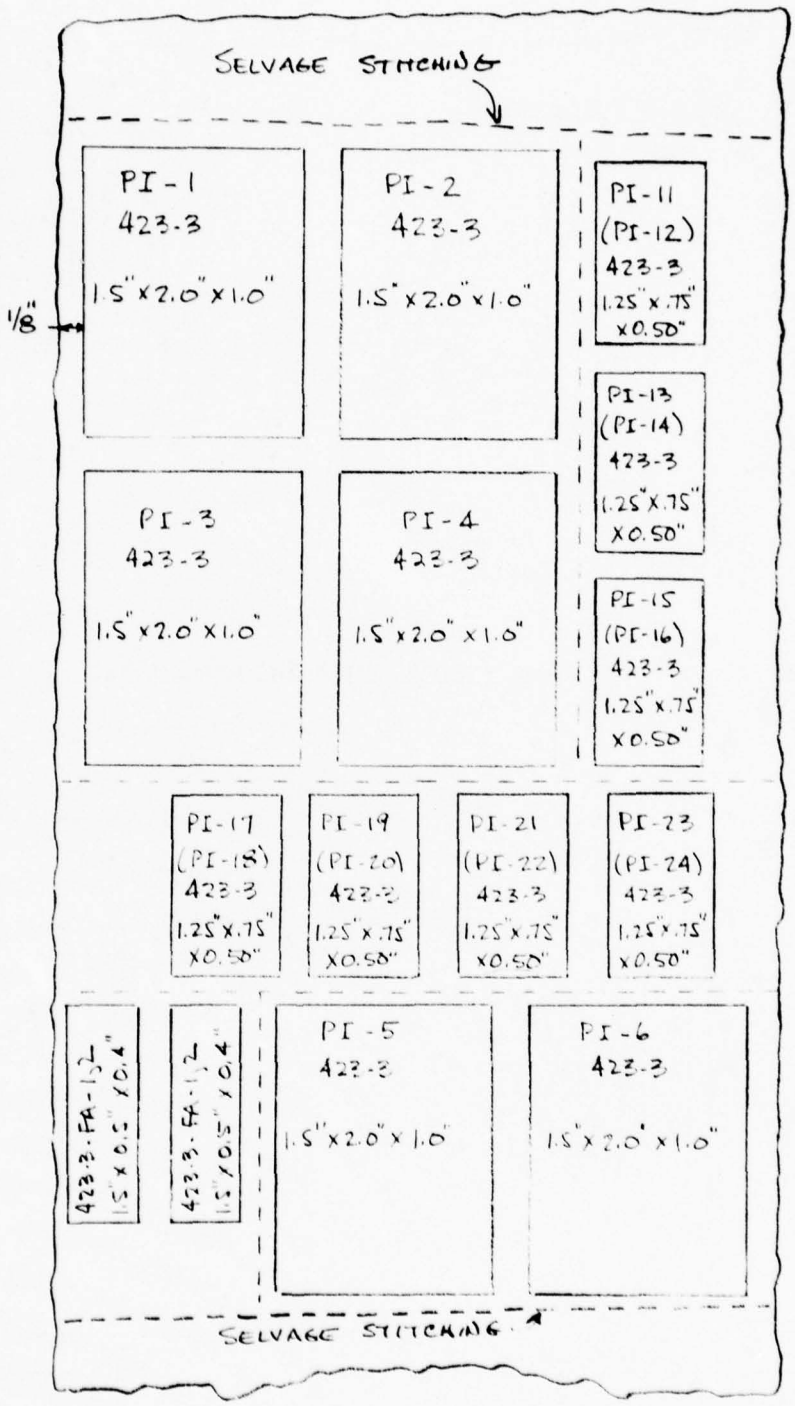

Figure 19. Sampling Plan: ADL-4D6 Plate 423-3

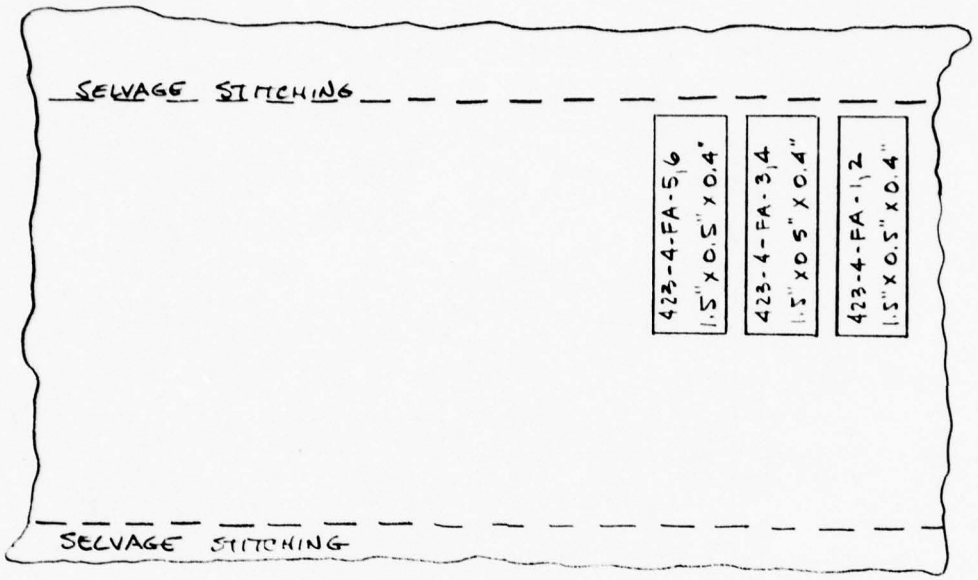

Figure 20. Sampling Plan: ADL-4D6 Plate 423-4

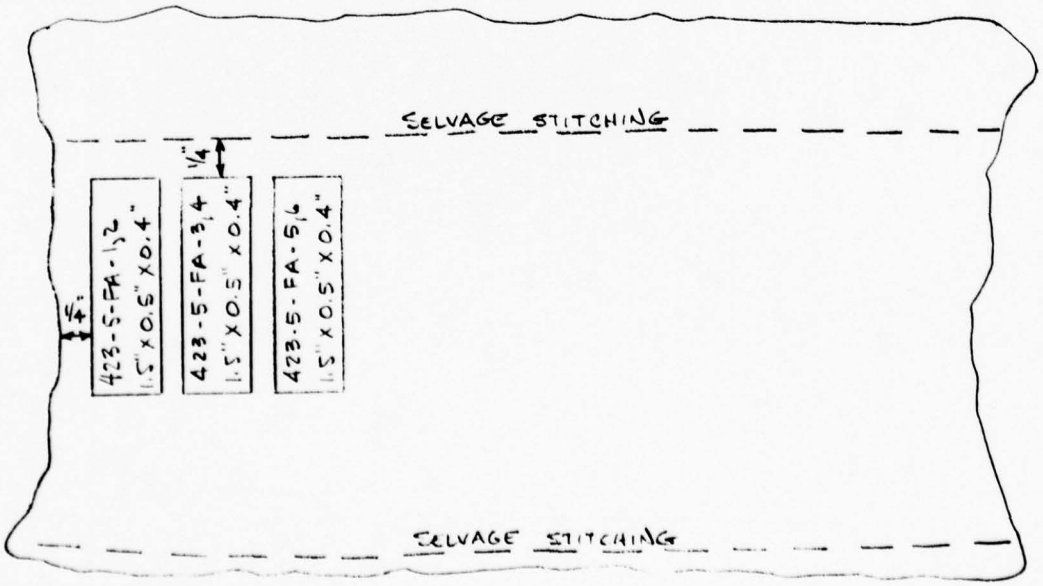

Figure 21. Sampling Plan: ADL-4D6 Plate 423-5

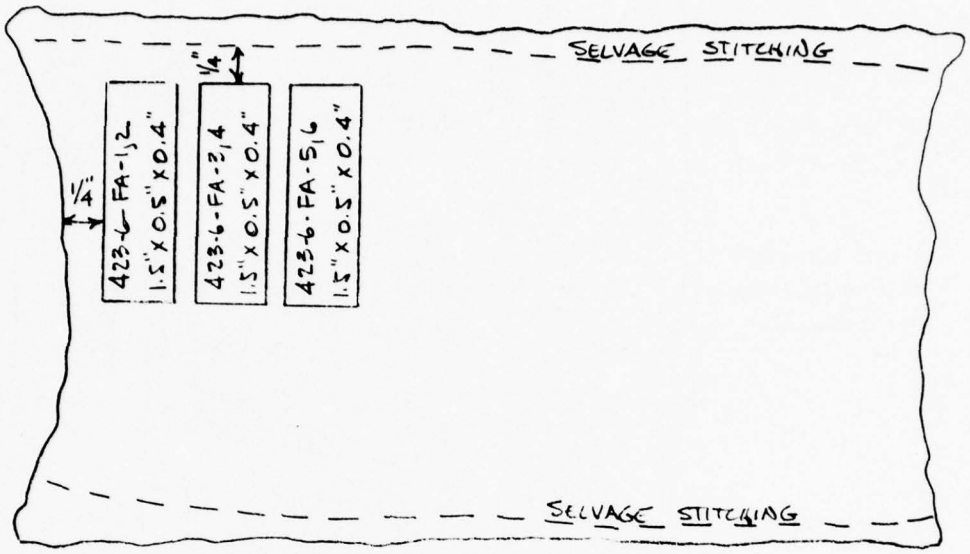

Figure 22. Sampling Plan: ADL-4D6 Plate 423-6

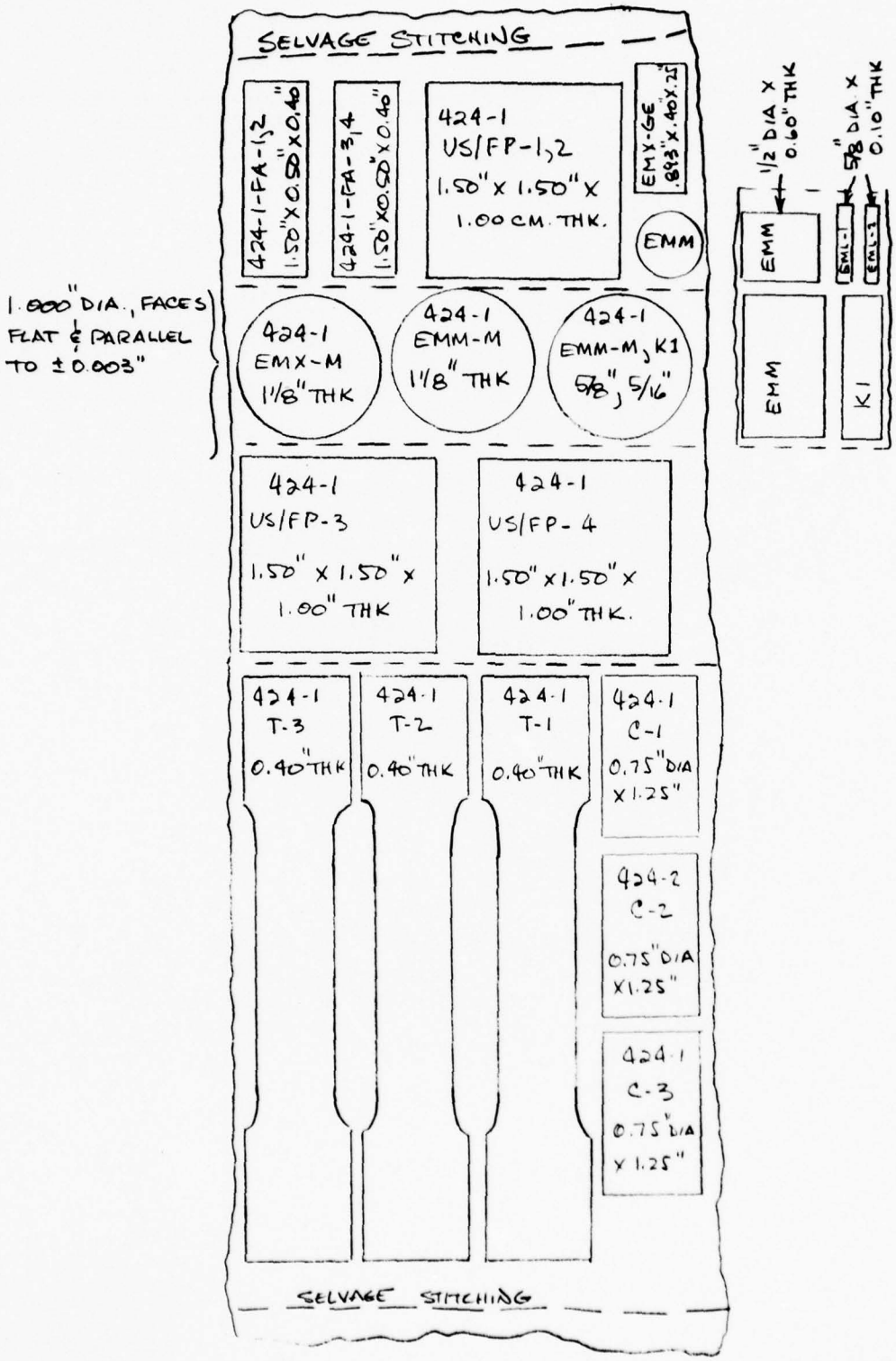

Figure 23. Sampling Plan: ADL-4D6 Plate 424-1

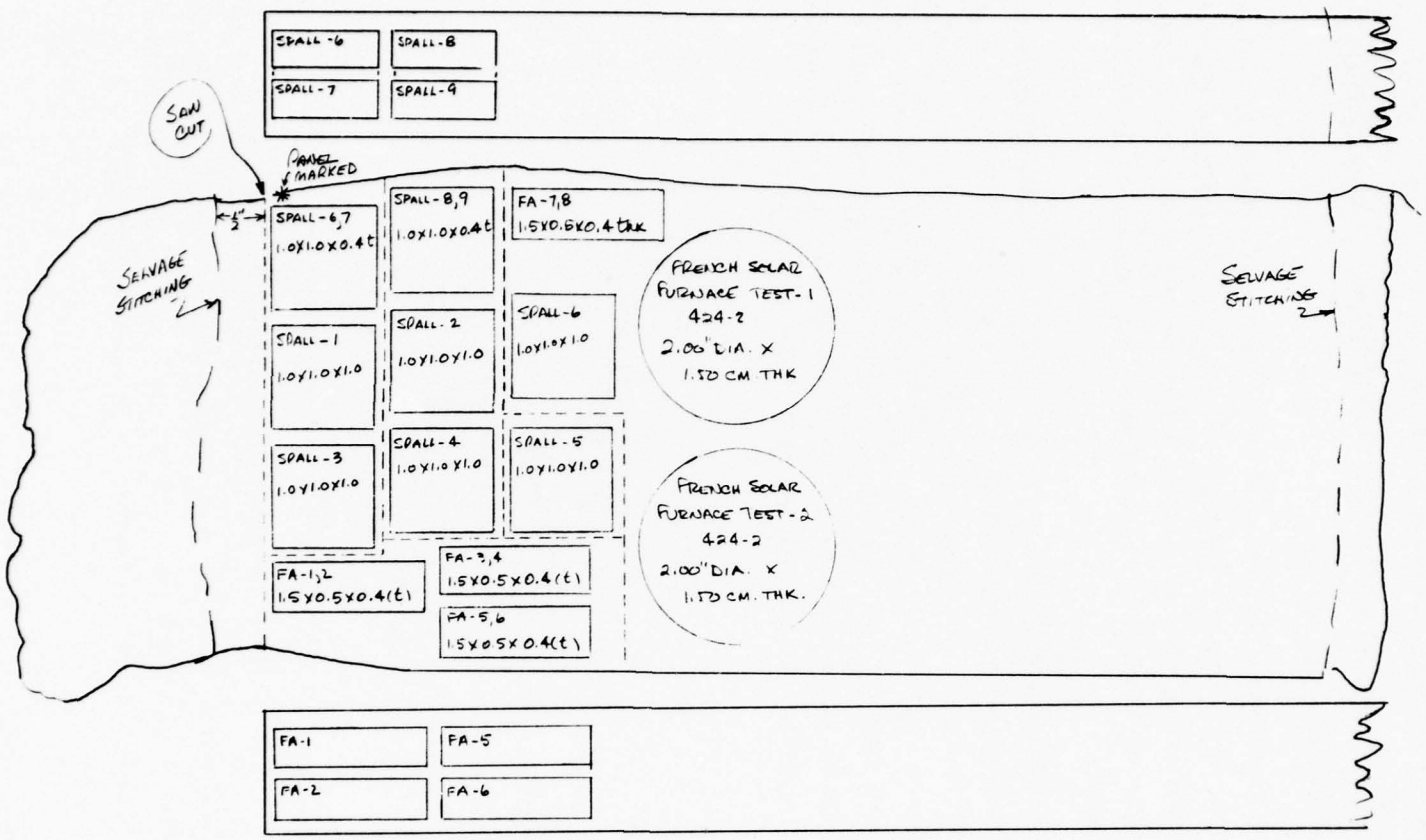

Figure 24. Sampling Plan: ADL-4D6 Plate 424-2

3.2 ADL-4D6 MECHANICAL CHARACTERIZATION

3.2.1 ADL-4D6 Ddensification process screening: flexural measurements

3.2.1.1 Review of Test Technique

For the purpose of providing a basis for evaluation of the effects of process variations on ADL-4D6, flexure tests were selected as the primary screening physical measurement. With this method of test, alignment, configuration and material quantity problems are eliminated and the data can be easily reduced and compared, providing all samples are tested under similar conditions.

A standard flexure specimen configuration (Ref. 10) was utilized in the tests on ADL-4D6. This same specimen was originally utilized in previous Advanced Hardened Antenna Window Materials Studies (Ref. 1). While being somewhat small (1.5" x 0.5" x 0.4"), this specimen configuration offers such advantages as: material conservation, reproducible test data and ease of handling. This specimen was tested in three-point flexure with a span length of 1.44". One strain gage was mounted on the tensile face of the specimen to measure strain at room temperature. Details of the application of the gage are shown in Figure 25.

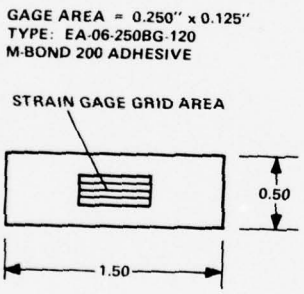

Figure 25. Details of Flexure Bar Strain Gage Application

For the purpose of screening, linear elastic calculations are utilized in the reduction of all the data. Although inadequate for design usage, due to the large degree of plasticity evident at failure levels, the results are sufficient for relative comparisons.*

*The correspondence of these flexural and uniaxial loading tensile test measurements is discussed in detail in Section 4.6.

The Modulus of Rupture (MOR) is calculated by the following formula:

$$M.O.R. = \frac{3PL}{2WT^2} \tag{1}$$

where:

P = Load (pounds)

L = Span Length (inches)

W = Width (inches)

T = Thickness (inches)

Some concern has been expressed over the possibility of a high transverse shear loading due to this geometry of test. The following formula may be utilized for a calculation of maximum transverse shear:

$$\text{Shear Stress} = \frac{3P}{4WT} \tag{2}$$

where:

P = Load (pounds)

W = Width (inches)

T = Thickness (inches)

Calculating the ratio of maximum transverse shear to modulus of rupture yields the following:

$$\text{Shear Stress}/M.O.R. = \frac{T}{2L} \tag{3}$$

where:

T = 0.40 inches

L = 1.44 inches

= 0.139

The amount of transverse shear which the specimen experiences is relatively minor and it is therefore felt that the specimen design is a valid one.

Elastic moduli are determined from the linear initial portion of the stress-strain curve. The modulus of rupture formula for the stress at the tension surface is utilized in unison with the strain gage data to calculate elastic modulus at room temperature.

The strain to failure measurement was unobtainable for the majority of specimens due to the large degree of plastic deformation that occurs. In order to obtain a meaningful initial modulus the strain scale had to be calibrated in a relatively high sensitivity range. It has been found that in this high range the transducer-amplifier becomes saturated during the large degree of plastic deformation and thus renders itself useless from that point on to failure.

This occurrence is denoted in the tables as a (>), "greater than" symbol, in the strain-to-failure column. On the stress-strain curves, the strain gage failure is denoted as a discontinuity in strain increase while the stress increases to failure level.

In addition to the mechanical property measurements of M.O.R., strain-to-failure and elastic modulus, some additional physical measurements were also made on each specimen. Individual specimen densities were measured to gain some insight on how the bulk density of the panel was distributed and to check for possible correlations with the mechanical properties.

As with all fibrous composites, the reinforcement angle is a major consideration. For each specimen the surface fiber pitch angle (SFPA) and the surface through the thickness angle (STTA) were measured in detail. The measurements obtained are the average of two independent measurements taken in the respective directions. Each of these independent measurements in themselves consisted of a series of measurements taken across the specimen.

One other measurement made on each of the post-tested specimens was the approximate fracture displacement from the point of applied load, nominally the geometric center of the bar. It was noted that on the majority of specimens, the fracture on the tensile surface was located at least 0.1 inch away from the applied load. The fact that this displacement corresponds to the 1/8 inch cell size of standard weave ADL-4D6 may provide some insight on the micro-mechanical shear transfer characteristics of the material.

Both pre-test and post-test visual examinations of the specimens were made and any anomalies noted. The nature of the fracture surfaces was also noted.

3.2.1.2 Experimental Results

3.2.1.2.1 ADL-4D6 Standard Weave/Standard Process

Three plates of ADL-4D6 standard weave and standard process were characterized during this program.

Plate 418-2, which was densified for the purpose of producing standard process ADL-4D6 material for solar furnace, particle impact, and mm wave dielectric tests, was sampled for six flexure bars as a check on plate quality. The results of the flexure tests are given in Table 13.

The flexure bar samples from plate 418-2 were somewhat below the nominal ADL-4D6 density of 1.6 g/cm^3. The mean M.O.R. of 6.15 ksi is within one estimated standard deviation of the 6.61 ksi mean M.O.R. reported in Reference 1 (p. 97). The strains-to-failure average above 1.0 percent; also typical of the standard material.

Plate 418-2 can accordingly be considered to have the nominal macroscopic mechanical strength of the ADL-4D6 material whose characterization was reported in Reference 1.

As with the M.O.R. data of Reference 1, there is no apparent correlation of strength with specimen density.

TABLE 13. STANDARD ADL-4D6 FLEXURE TESTS

	Thickness (Inches)	Density (g/cm^3)	M.O.R. (ksi)	Modulus (Msi)	Strain-To-Failure (%)	Approximate Failure Displacement (Inches)	Average SFPA (Degrees)	Average STTA (Degrees)
Plate 418-2								
FA-1	0.400	1.54	6.20	1.92	>1.03	0.10	40	23
FA-2	0.401	1.54	5.99	1.89	>0.5	0.40	41	30
FA-3	0.402	1.60	7.04	1.75	>1.03	0.00	43	36
FA-4*	0.401	1.58	5.72	1.83	>1.26	0.05	43	37
FA-5*	0.400	1.56	5.28	2.41	>1.07	0.10	40	40
FA-6	0.400	1.58	6.68	2.11	>1.40	0.05	42	38
Plate Mean:	0.401	1.57	6.15	1.98	>1.05	0.12	41	34
Plate S.D.:	0.001	0.02	0.64	0.24	--	0.14	1	6
Plate 423-3								
FA-1	0.400	1.56	7.48	2.02	>0.96	0.10	32	26
FA-2	0.402	1.58	8.86	3.12	0.57	0.10	30	30
FA-3**	0.403	1.54	6.76	1.92	>0.96	0.05	30	28
FA-4	0.400	1.54	8.31	1.96	>0.96	0.10	34	28
Plate Mean:	0.401	1.55	7.85	2.25	>0.86	0.09	31	28
Plate S.D.:		0.02	0.92	0.58			1.9	1.6
Plate FP-3	0.401	1.67	7.95	2.58	>1.19	0.10	38.8	42.7

*Some bundle pull-out

**Large void in compression surface approximately 0.2 inches from load line.

The mean elastic modulus as measured in this standard flexure test is 1.98 Msi as compared to 1.10 Msi for the material of Reference 1.

Plate 423-3, which was produced for the purpose of supplying particle impact erosion test specimens, were also sampled for four flexure bars to check on plate quality. The results of these flexure tests are given in Table 13.

Again, two out of four of these specimens have unusually low densities, 1.54 g/cm^3. The resulting mean M.O.R. of 7850 psi is, however, well above the 6,610 mean of the standard material in Reference 1. The elastic moduli are even higher than measured for standard plate 418-2, while the measured strains are equivalent to standard material values.

The measured values of surface fiber pitch and through thickness angles suggest that this change in strength and elastic values is attributable to somewhat shallower weave angles in this material. This effect must be taken into account in evaluating both these mechanical test results and the particle impact erosion tests on this plate.

Specimen FP-3, which is a single quality control type, densified for comparison to process variation specimens FP-1 and FP-2, had one of the highest densities, 1.67 g/cm^3. The resulting M.O.R. of 7950 psi, like that of plate 423-3, is also well above the 6610 psi mean of the standard material in Reference 1. The elastic modulus for this specimen was even higher than the mean value of plate 423-3, while the measured strains are about equivalent. The individual stress-strain curves for each specimen of each of the three plates are in Figures 26 through 28.

3.2.1.2.2 Flexural Screening Tests: ADL-4D6 Process Variation Studies

A. Background, Criteria for Screening

Seven densification process variations of standard weave ADL-4D6 were screened by three-point flexure testing at room temperature* to evaluate the effect of the process changes on the composite mechanical properties. The primary goal of this ADL-4D6 process variation study has been improvement of tensile strength to near theoretical levels. For some micromechanical models of ADL-4D6, based on a composite failure criterion involving silica filament tensile failure, this has been estimated to be as high as 30,000 to 40,000 psi and flexural tests on early ADL-4D6 material in fact showed M.O.R. values on this level (Ref. 2). Other models, based on more recently formulated failure mechanisms, have settled on a value near 10,000 psi (see Section 4, "Composite Micromechanical Analysis", of this report). It is obvious from previous work that the basic 4D silica-silica composite system can exhibit a wide range of mechanical behavior, depending on preform weave density and geometry, and the nature of the inorganic

*The mechanical properties discussion of this section, in all cases, refers to room temperature properties.

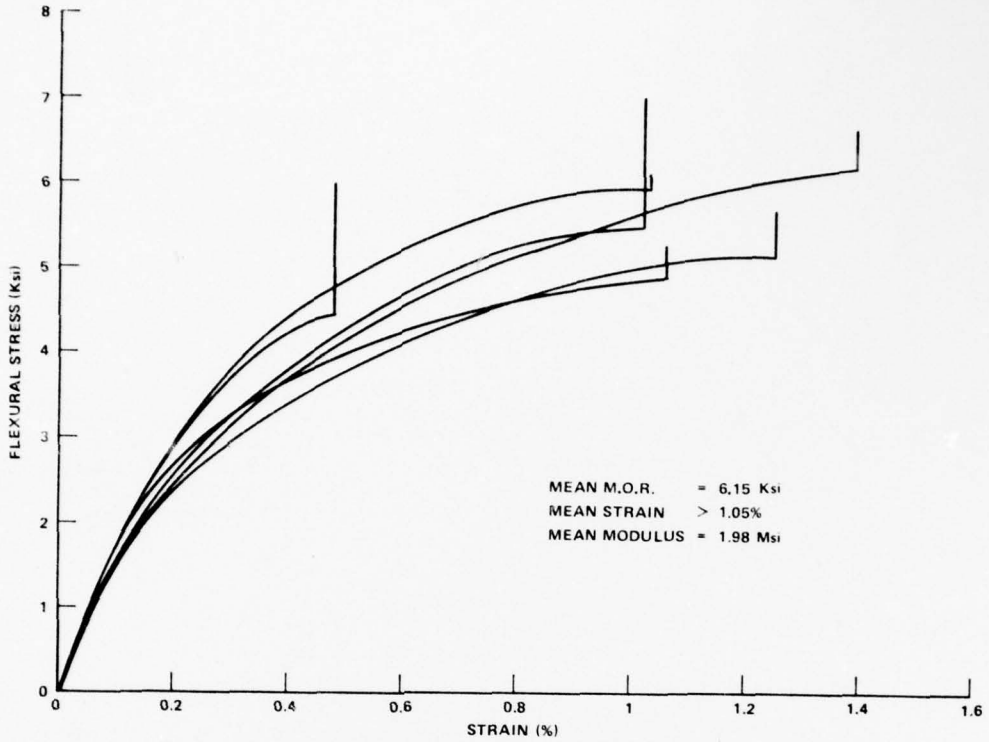

Figure 26. Flexural Stress-Strain, ADL-4D6 Panel 418-2, Standard Process

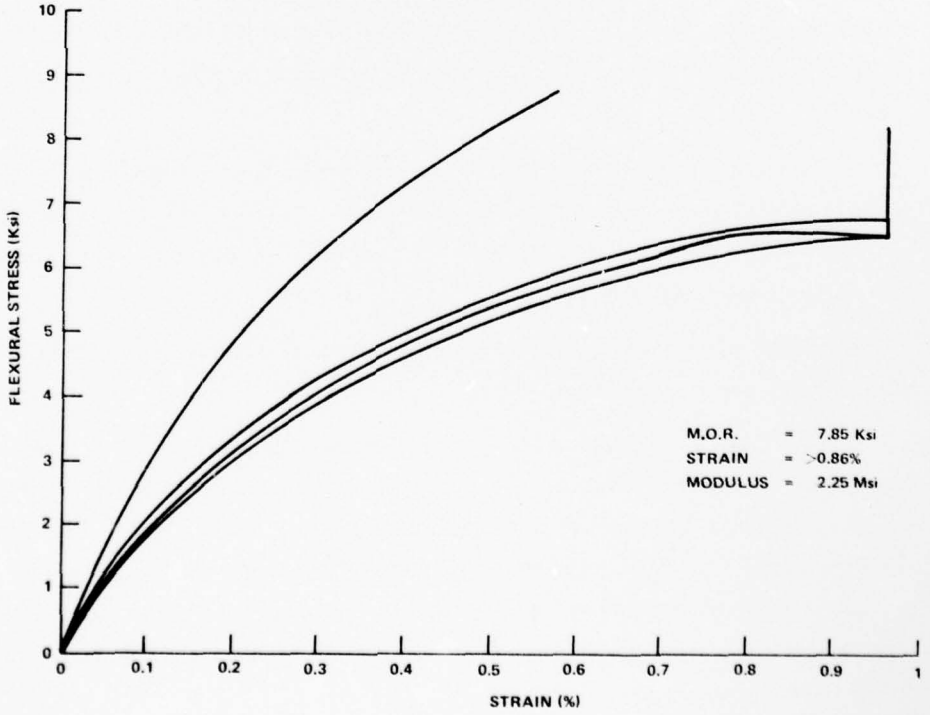

Figure 27. Flexural Stress-Strain, ADL-4D6 Panel 423-3, Standard Process

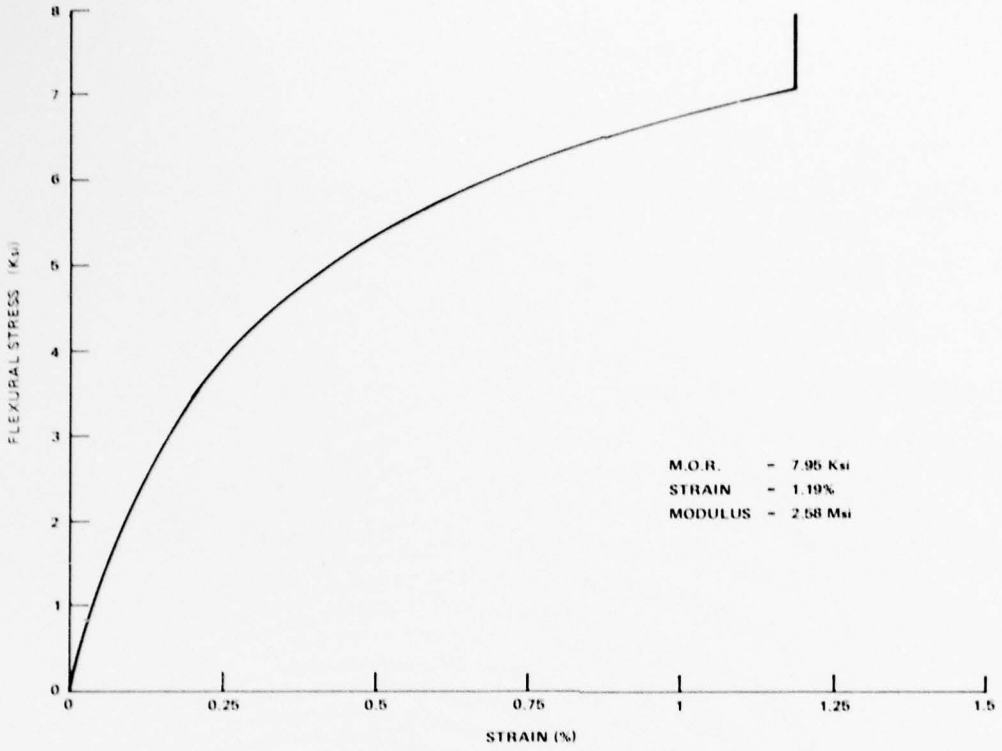

Figure 28. Flexural Stress-Strain, ADL-4D6 FP-3, Standard Process

silica matrix and its interaction with the fibrous preform array. *Most notably*, the mechanical screening work of Reference 1 (pages 66-79) showed the strong effect of the silane coupler step on flexure test results and Section 4.2 of this report shows the effect on uniaxial loading test results.

A new goal of 10,000 psi, verified by uniaxial loading tests, has been set for the tensile strength of an improved process version of ADL-4D6. This level is about twice that of conventional antenna window materials and is comparable to the effective tensile strengths of many current heatshield materials.

In addition to tensile strength as a primary structural property goal, strain-to-failure and elastic moduli must be considered.

The strain-to-failure of standard ADL-4D6 has been measured in flexural test to be in excess of 1.0 percent. Its measurement to failure in this test is limited by the strain measurement capability of the available bonded strain gages. * This extremely high ductility is an uncompromised, desirable property for the material in any forseeable application. Previous process studies had already demonstrated that it could be grossly altered; e.g., the two M.O.R. specimens given a final "Markite cycle" (Ref. 1, Table 19) had failure strains in the range of 0.48 to 0.57 percent.

*Uniaxial tensile strain measurements by clip-on extensometers on standard ADL-4D6 specimens showed 0.63 to 0.8% strain-to-failure, despite the test specimen problems in Reference 1 (Table 24, p. 89, "Plate 415B").

A further improvement in the strain capability of the material would then be welcome from a structural viewpoint, if the accompanying change in the strength and elastic modulus(i) did not significantly offset such strain capability improvement. For shock-hardened applications including particle impact, the micromechanical implications of such strain capability might be even more beneficial to overall window systems performance.

The standard, or "baseline" ADL-4D6 has a room temperature flexural modulus of 1.10 million psi, with a standard deviation in the experimental data of 0.17 Msi. For conventional size antenna windows in the usual stress-isolated installation, a much larger or a somewhat smaller modulus would be acceptable; but for use as a radome with load-bearing requirements, the various elastic moduli must fall into a narrower range.

This set of screening flexural measurements is intended then to examine the effects of the process variations on these three structural parameters, to infer the value of the material variations for other performance properties and to suggest further variations.

The results are grouped in the following text according to the format suggested by Figure 9 and Section 2.3.2 of this report. The individual process variations are compared to each other, most appropriately within the process variation groups, and to the standard ADL-4D6 material, for which the three pertinent flexural test properties are tabulated below for use as a baseline:

	Mean	Standard Deviation Of Data
M.O.R.	= 6610 psi	755 psi
strain-to-failure	1.0%	—
flexural modulus	= 1.10 Msi	0.17 Msi

Note that the tree diagram of Figure 9 serves as a convenient comparison device for process variation type and mechanical test results.

B. Experimental Results

Preform Heat Cleaning Variations: Two panels were processed under this variation. Panel 423-1 was processed without the initial teflon removal step and panel 423-6 with a higher (650°C) firing temperature. The purpose for 423-1 was to determine the effect of the teflon blockage on the colloidal silica infiltration during the first two infiltration/drying cycles before the sintering step. For 423-6 a more thorough fiber cleaning preceded the silane coupler and colloidal silica infiltration. The two processes are thus seen as opposed departures from the standard 950°F (510°C) cleaning process (Figure 8).

The flexural test results (Table 14) show a lowered modulus of rupture strength in both cases, 5640 psi for 423-1 and 4110 for 423-6, the lowest M.O.R. for any of the seven variations.

TABLE 14. ADL-4D6 FLEXURAL TESTS, PREFORM HEAT CLEANING VARIATION PROCESS STUDIES

	Thickness (Inches)	Density (g/cm^3)	M.O.R. (ksi)	Modulus (Msi)	Strain-To-Failure (%)	Approximate Failure Displacement (Inches)	Average SFPA (Degrees)	Average STTA (Degrees)
Plate 423-1 (Teflon removal deleted)								
FA-5*	0.401	1.60	6.09	1.26	>1.44	0.30	45	25
FA-6	0.401	1.58	5.75	1.11	>1.43	0.30	30	23
FA-7	0.401	1.57	4.67	1.31	>1.45	0.35	45	25
FA-8	0.401	1.60	6.07	1.26	>1.43	0.15	34	24
Plate Mean:	0.401	1.59	5.64	1.23	>1.44	0.27	38	24
Plate S.D.:	--	0.01	0.67	0.09				
Plate 423-6 (650°C Heat Clean)								
FA-1*	0.374	1.59	3.99	1.25	>1.42	0.30	41	30
FA-2	0.375	1.54	4.13	1.16	>1.43	0.30	42	28
FA-3	0.375	1.57	4.01	1.41	>1.39	0.40	41	34
FA-4	0.376	1.53	4.35	1.24	>1.40	0.20	41	28
FA-5	0.375	1.57	3.62	1.10	>1.38	0.50	42	30
FA-6	0.374	1.54	4.59	1.48	>1.40	0.25	42	30
Plate Mean:		1.56	4.11	1.27	>1.40	0.32	41.5	30
Plate S.D.:		0.02	0.33	0.14		0.11	0.5	2.2

* "Ideal" fracture surfaces, fiber bundles pulled out and very fluffy.

** Fiber bundles pulled out. Bundles are very fluffy.

The strains-to-failure, however, were quite high, in excess of 1.4 percent in all cases, as compared to the standard minimum value of 1.0 percent. The fracture surfaces of 423-1 in particular were of the "ideal" composite fracture type with extensive fiber bundle pull-out and very fluffy bundle texture, each filament visible.

This set of plates had the highest strain-to-failure of any investigated in the series.

The modulus results were in each case within one estimated standard deviation of the standard material.

Stress-strain curves for these two process variations are given in Figures 29 and 30.

Variation of Colloidal Silica Particle Size: Two panels were densified under this variation. Panel 423-2 was densified with the smaller particle Nalcoag 2326 colloidal silica process that was developed for reflective heat shield use in Reference 5. The single specimen FP-2 was processed using seven impregnations of "aggregated" low sodium Ludox as the densifier. Both of these variations had lower densities than standard, 1.51 mean for 423-2 and a very low 1.45 for FP-2, despite its seven impregnations.

Results from these tests (Table 15) show that both particle sizes yield the same M.O.R., 5220 psi and 5240 psi, respectively, which is two estimated standard deviations lower than the 6610 psi of standard material.

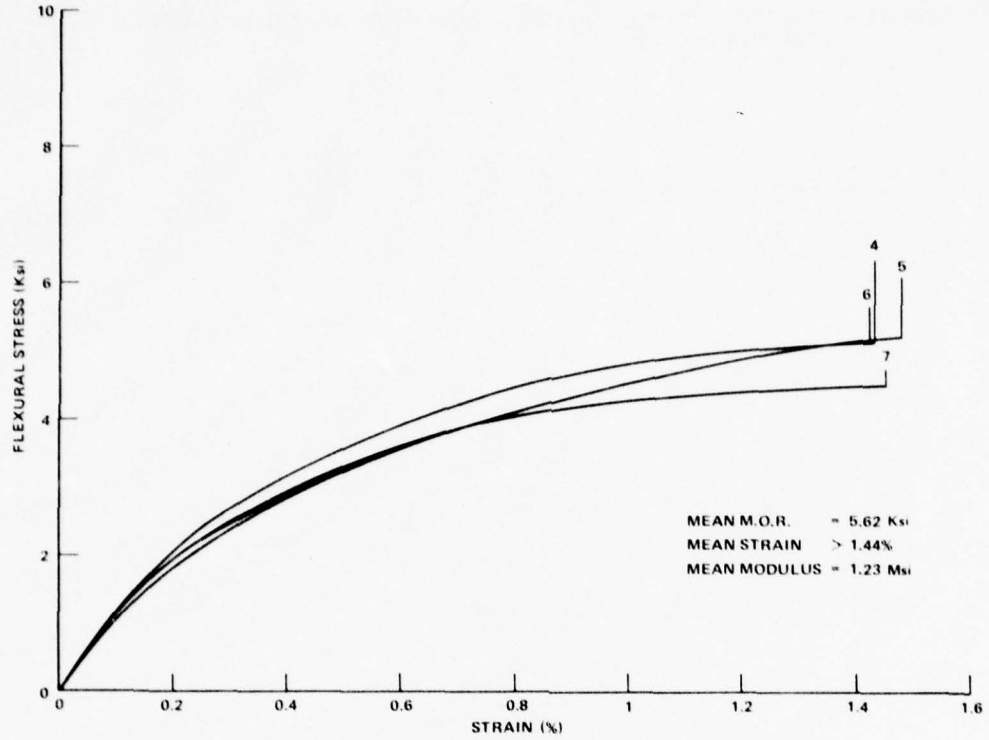

Figure 29. Flexural Stress-Strain, ADL-4D6 Panel 423-1, Delete Teflon Removal

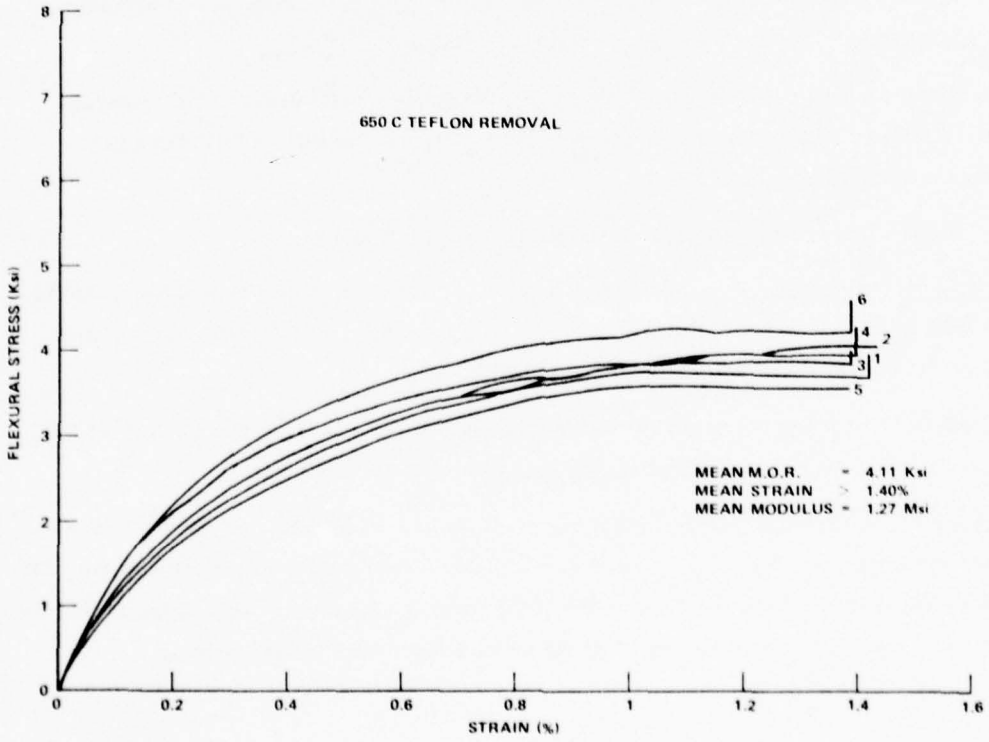

Figure 30. Flexural Stress-Strain, ADL-4D6 Panel 423-6, 650°C Teflon Removal

TABLE 15. ADL-4D6 FLEXURAL TESTS, VARIATION OF COLLOIDAL PARTICLE SIZE PROCESS STUDIES

	Thickness (Inches)	Density (g/cm^3)	M.O.R. (ksi)	Modulus (Msi)	Strain-To-Failure (%)	Approximate Failure Displacement (Inches)	Average SFPA (Degrees)	Average STTA (Degrees)
Plate 423-2 (Smaller colloidal silica)								
FA-5	0.402	1.51	5.00	1.90	0.95	0.05	35	23
FA-6	0.303	1.51	4.65	2.08	0.63	0.05	30	27
FA-7	0.402	1.50	5.51	1.85	1.13	0.05	36	23
FA-8	0.302	1.54	5.71	2.06	0.67	0.15	33	24
Plate Mean:	0.352	1.51	5.22	1.97	0.85	0.07	33	24
Plate S.D.:	--	0.02	0.48	0.11	0.24			
Plate FP-2 ("Aggregated" colloidal silica)								
FP-2	0.405	1.45	5.24	0.80	0.94	0.15	34.5	38.3

The significant difference between variations, however, is in the modulus. Panel 423-2 had a mean modulus of 1.97 Msi as compared to 0.80 Msi for FP-2.

The strain-to-failure also is significant in that the smaller particles in 423-2 markedly reduced the failure strain to a mean value of 0.85%. Note that the bonded foil strain gages did not fail in the 423-2 series.

The stress-strain curves for these tests are in Figures 31 and 32.

Heat Treatment Variations: Two panels were processed having variations in heat treatment to contrast with the standard 650°C firing temperature. Panel 423-4 was densified at a temperature of 750°C and panel 423-5 was densified at 550°C.

The 550°C (low) firing temperature variation of plate 423-5 shows a mean M.O.R. of 5020 psi (Table 16) as compared to 6610 psi for the standard ADL-4D6 material.

As anticipated, the mean strain-to-failure increased to 1.26 percent (minimum), compared to 1.0 percent (minimum) for standard process material. The stress-strain curves (Figure 33) show the widest range of yield-stresses of any of the process variations. This suggests that the composite was not uniformly consolidated by the lower temperature firing process.

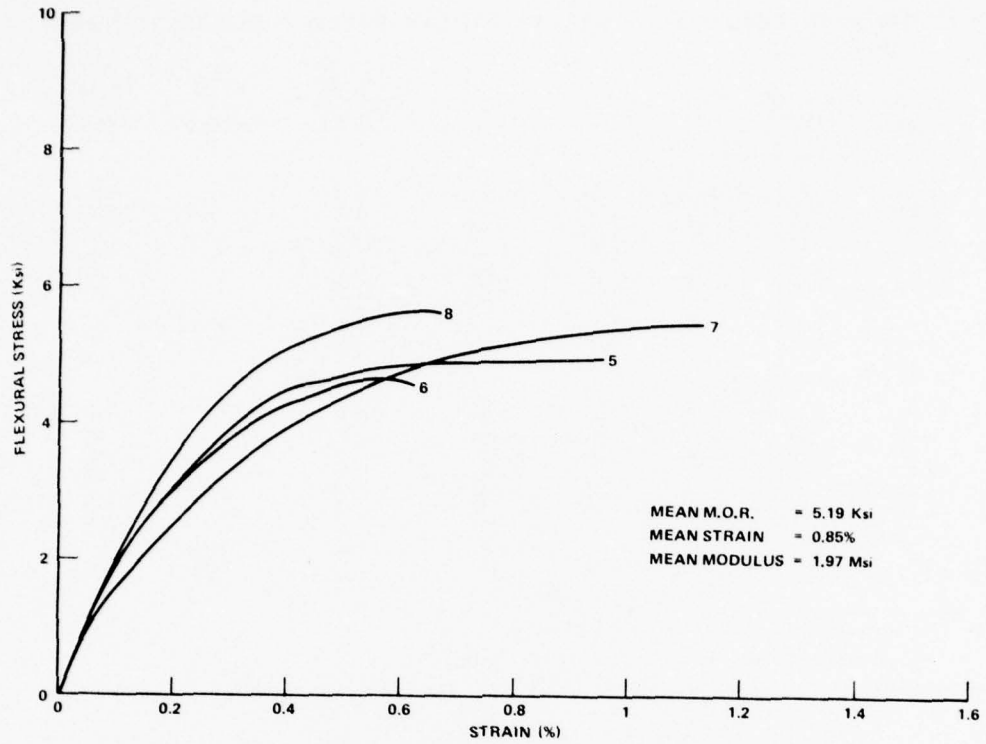

Figure 31. Flexural Stress-Strain, ADL-4D6 Panel 423-2, Smaller Colloidal Silica

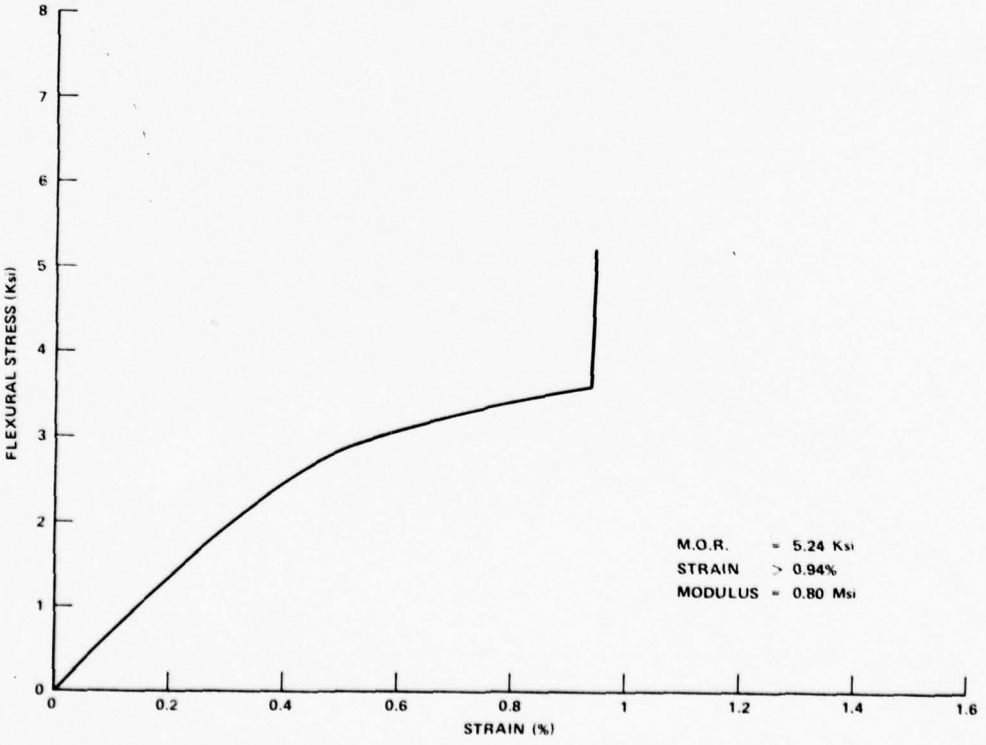

Figure 32. Flexural Stress-Strain, ADL-4D6, FP-2, Aggregated Colloidal Silica

TABLE 16. ADL-4D6 FLEXURAL TESTS, HEAT TREATMENT PROCESS VARIATION STUDIES

	Thickness (Inches)	Density (g/cm^3)	M.O.R. (ksi)	Modulus (Msi)	Strain-To-Failure (%)	Approximate Failure Displacement (Inches)	Average SFPA (Degrees)	Average STTA (Degrees)
Plate 423-4 (750°C firing temperature)								
FA-1*	0.402	1.56	4.76	1.58	>0.71	0.15	43	30
FA-2*	0.401	1.58	4.65	1.76	0.81	0.00	37	29
FA-3**	0.402	1.56	4.40	1.75	0.75	0.00	41	29
FA-4*	0.400	1.58	4.57	1.96	0.71	0.00	40	28
FA-5*	0.400	1.55	4.53	1.50	0.98	0.10	43	31
FA-6*	0.402	1.56	4.64	1.48	0.88	0.05	40	29
Plate Mean:		1.56	4.59	1.67	>0.81	0.05	40.7	29.3
Plate S.D.:		0.01	0.12	0.18		0.06	2.2	1.0
Plate 423-5 (550°C firing temperature)								
FA-1	0.404	1.56	5.40	1.71	>0.88	0.20	42	27
FA-2	0.397	1.59	4.48	1.34	>1.40	0.25	40	30
FA-3	0.402	1.55	4.86	1.39	>1.38	0.10	44	29
FA-4***	0.402	1.59	5.72	1.63	>1.41	0.05	46	30
FA-5	0.403	1.55	4.53	0.99	>1.40	0.30	43	32
FA-6***	0.396	1.58	5.15	1.09	>1.08	0.00	(32)?	32
Plate Mean:		1.57	5.02	1.36	>1.26	0.15	41.2	30
Plate S.D.:		0.02	0.49	0.29		0.12	4.9	1.9

*Minor fiber bundle pull-out. Bundles are not fluffy.

**Slightly more fiber bundle pull-out. Bundles are not fluffy.

***Fiber bundle pull-out. Bundles are extremely fluffy.

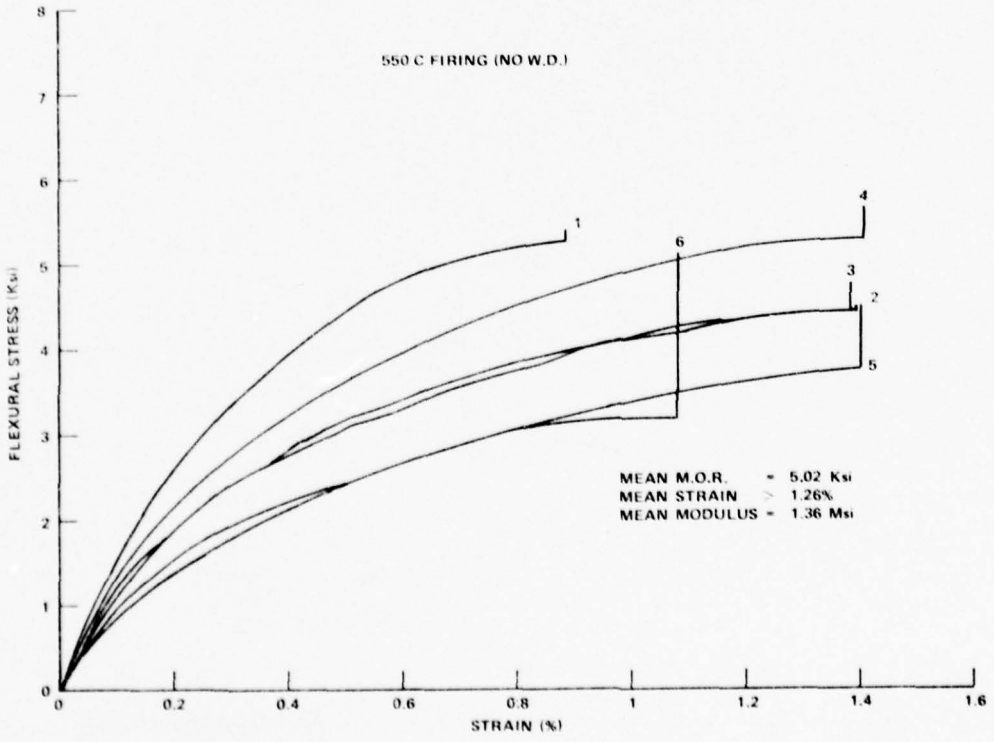

Figure 33. Flexural Stress-Strain, ADL-4D6 Panel 423-5, 550°C Firing

The modulus data show the unexpected result of a slightly higher mean value of 1.36 Msi, 1.5 estimated standard deviations above the standard mean of 1.10 Msi.

The 750°C high firing temperature variation of plate 423-4 confirmed the expected effect on modulus. It increased to a mean value of 1.67 Msi (Table 16) with a sharp drop in mean strain-to-failure to 0.81 percent — to the extent that the foil strain gages were able to follow the strain-to-ultimate-failure of the flexure bar tensile surfaces in all but one of the six tests. The fracture surfaces were very obviously more brittle-like than the standard material. Figure 34 shows the very close grouping of the stress-strain curves, in contrast to the case for the material fired at the lower temperature.

The mean M.O.R. was reduced to 4.59 ksi. A sintering temperature as high as 750°C is very definitely then not the way to proceed for improved strength and certainly not improved fracture resistance of this material.

Acid-Stabilized Colloidal Silica: A single flexure bar-sized specimen FP-1 was processed using six impregnations of "acidified" low sodium Ludox as the densifier to determine the effect of colloidal suspension pH on the composite flexural strength. Note that this specimen had the highest density of any tested in the series.

The test results (Table 17, Figure 35) show a strain-to-failure much greater than 1.23 percent. If the stress-strain curve is extrapolated, past gage failure to the yield stress level, a strain-to-failure well above 2.0 percent can be inferred.

It should be noted that for this individual flexure bar specimen, cut from a "finger-weave" Omniweave preform, the measured SFPA and STTA are within two degrees of 45. It is almost a perfectly cubic 4D composite, by that measure at least. The compounded effect of increased density and ideal weave configuration obviously recommend further investigation.

The modulus was found to be 0.80 Msi as compared to 1.10 Msi for the standard material.

The value for M.O.R. was also low, 4,790 psi as compared to 6,610 psi for the standard.

The combination of the exceptionally high flexure strain and the lower initial modulus (independent of the non-linear curvature of the stress-strain curve) suggests that uniaxial loading tensile tests on this material may be very worthwhile. The analysis of section 4.6, which compares flexure and uniaxial loading tests on these materials, implies that significantly higher tensile strengths may be indicated for such materials — if a suitable uniaxial test can be conducted.

3.2.1.3 Conclusions from Process Screening Tests

It can be concluded then that this series of ADL-4D6 process variations has not succeeded in finding a process for reaching the goal of near theoretical tensile strength materials, i.e.,

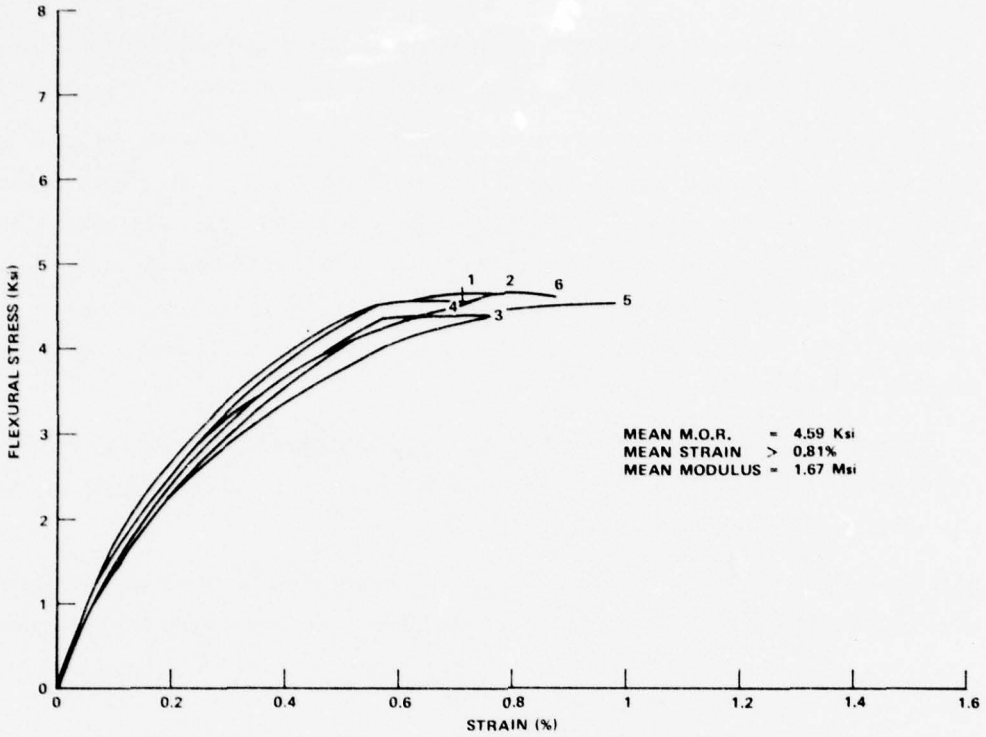

Figure 34. Flexural Stress-Strain, ADL-4D6 Panel 423-4, 750°C Firing

TABLE 17. ADL-4D6 FLEXURAL TESTS, ACID PROCESS VARIATION STUDIES

	Thickness (Inches)	Density (g/cm^3)	M.O.R. (ksi)	Modulus (Msi)	Strain-To-Failure (%)	Approximate Failure Displacement (Inches)	Average SFPA (Degrees)	Average STTA (Degrees)
FP-1	0.402	1.64	4.79	0.80	>1.23	0.00	44.5	46.7

10,000 psi. Certain process variations seem ruled out, such as the 750°C sintering temperature, for any purposes. However, means of significantly tailoring the strain-to-failure and modulus have been found, and these parameters may have their own pronounced effect on other ADL-4D6 composite performance properties such as particle erosion resistance and spall thresholds.

Since only a minor portion of most of these process plates has been consumed by the flexure tests, sufficient material remains to do additional superimposed process variations or testing.

Further analysis of this data, in particular the stress-strain curves, may also suggest uniaxial loading tensile tests on some of these material variations. Acquisition of this data is contingent on successful development of a tensile specimen design for a 4-D silica-silica composite. Section 3.2.2 shows progress in this direction for the fine weave ADL-4D6 material variation.

found that in this high range the transducer-amplifier becomes saturated during the large degree of plastic deformation and thus renders itself useless from that point on to failure.

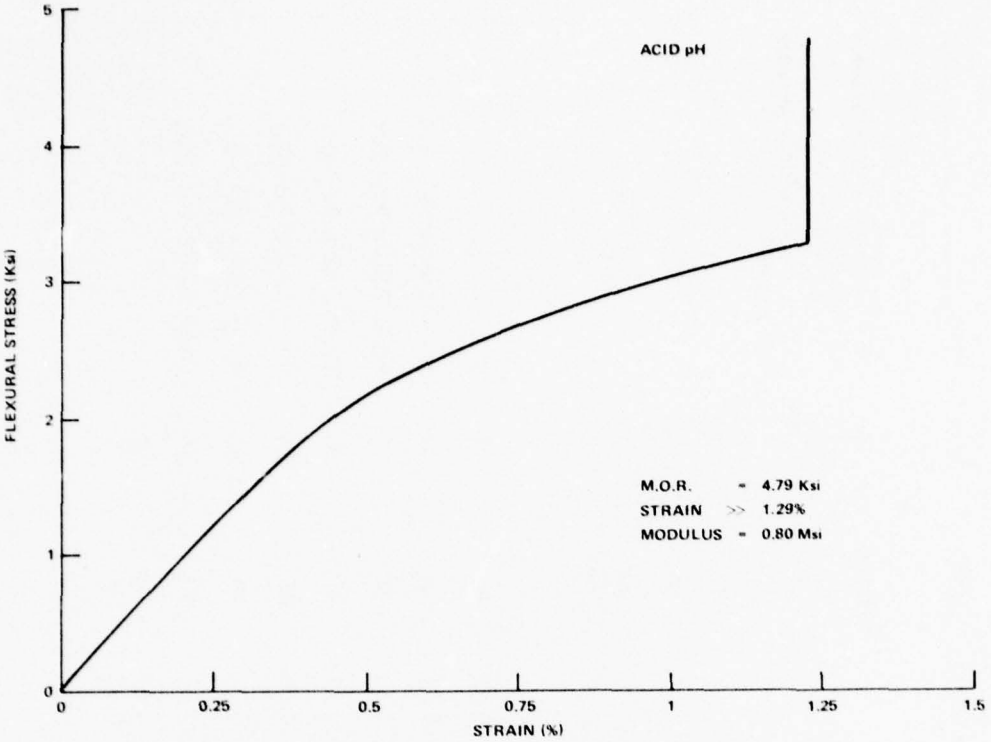

Figure 35. Flexural Stress-Strain, ADL-4D6 FP-1, Acid pH

3.2.2 FINE WEAVE ADL-4D6

3.2.2.1 Flexural Tests

The flexural tests of the two fine weave ADL-4D6 plates were conducted utilizing the same specimen geometry and data analysis techniques described in Section 3.2.1.1.

Both plates 424-1 and 424-2 were densified by the standard process. Plate 424-1 was sampled for four flexure specimens and plate 424-2 for seven. The data from these tests are given in Table 18. Plate 424-1 was found to have significantly higher mean M.O.R. than that recorded for the standard weave and process ADL-4D6 in the data of Reference 1, page 97; that being 7820 psi as compared to 6610 psi. The strains-to-failure are also exceptionally high, the minimum recorded value running well above 1.26 percent. The results for plate 424-2, however, were quite different. The mean M.O.R. value was 3740 psi, almost half that of plate 424-1. The strains-to-failure however were almost the same. The measured values of surface angles suggest that this change in strength is attributable to some extent to the higher weave angles in this plate, which were caused by compaction of the woven preform to get higher through thickness angles (Section 2.2.1). This should be considered in evaluating the test results.

The individual specimen stress-strain curves can be found in Figures 36 and 37.

TABLE 18. FINE WEAVE ADL-4D6 THREE-POINT FLEXURE TESTS

Specimen Number	Thickness (inches)	Density (g/cm^3)	M.O.R. (Ksi)	Modulus (Msi)	Failure Strain (%)	Fracture Displace. (inches)	Surface Fiber Angle SFPA°	STTA°	Notes
Panel 424-1									
FA-1	0.401	1.57	6.77	1.21	>1.33		41/35	37	SFPA's ranged widely between 41° and 35°
FA-2	0.401	1.57	7.04	1.30	>1.34		37	40/25	STTA's ranged widely between 25° and 40°
FA-3	0.402	1.56	8.27	1.03	>1.15		43	40	
FA-4	0.400	1.54	9.19	2.06	>1.20		39	23	
Plate Mean:	0.401	1.56	7.82	1.4	>1.26		39	33	
Plate S.D.		0.014	1.12	0.46	0.095		2.6	7.4	
Panel 424-2									
FA-2	0.402	1.58	4.27	1.42	>1.4	0.15	50	46	
FA-3	0.402	1.54	2.91	0.75	>1.3	0.0	52	50	Fiber Bundle Pull-Out
FA-4	0.405	1.56	4.03	1.13	>1.4	0.10	42	47	Fiber Bundle Pull-Out
FA-5	0.403	1.58	3.47	1.07	>1.0	0.10	47	55	Fiber Bundle Pull-Out
FA-6	0.401	1.58	2.75	1.01	>0.9	0.05	48	46	Minor Bundle Pull-Out
FA-7	0.404	1.58	4.69	1.53	>1.3	0.0	50	42	Minor Bundle Pull-Out
FA-8	0.404	1.55	4.05	1.16	>1.0	0.0	50	45	Fiber Bundle Pull-Out
Plate Mean:	0.403	1.57	3.74	1.15	>1.2	0.06	48	47	
Plate S.D.:	0.001	0.02	0.72	0.26	--	0.06	3	4	

As with the M.O.R. data of Reference 1, there is no apparent correlation of strength with specimen density.

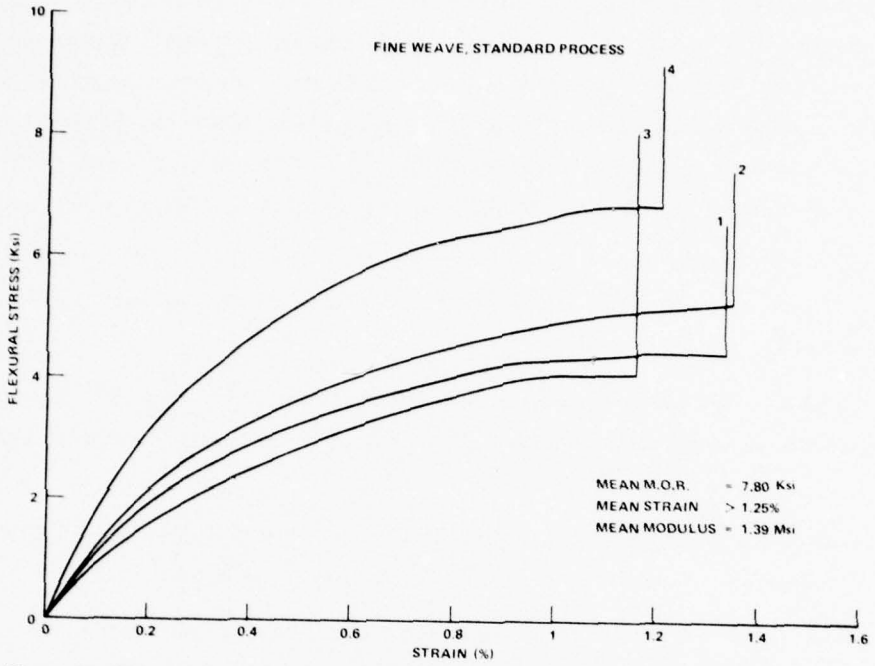

Figure 36. Flexural Stress-Strain, ADL-4D6 Panel 424-1 Fine Weave, Standard Process

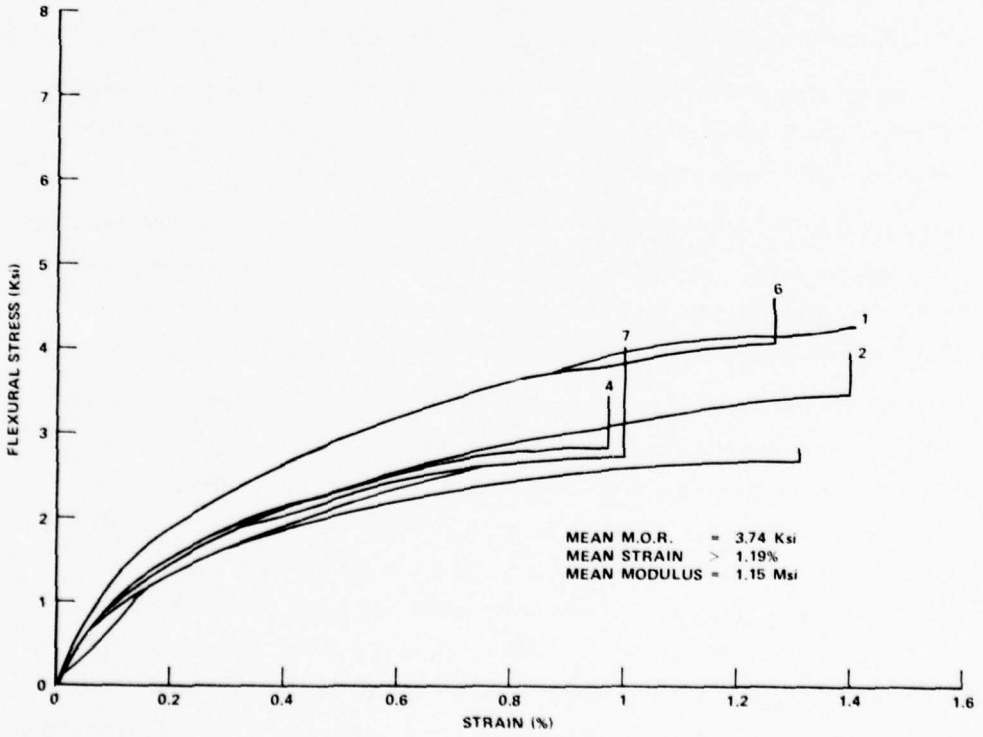

Figure 37. Flexural Stress-Strain, ADL-4D6 Panel 424-2 Fine Weave, Standard Process

*The mechanical properties discussion of this section, in all cases, refers to room temperature properties.

3.2.2.2 Uniaxial Loading Tests

The uniaxial tests had as their immediate purpose the resolution of the square versus round bar anomalies reported in Reference 1 (pp. 88-92, 177-180), and ultimately, the acquisition of uniaxial tensile data. The hypothesis here is that if "ineffective fiber bundle length" effects do dominate the observed positive correlation of ADL-4D6 square tensile bar strength with thickness, then similar tests on fine weave ADL-4D6 will show further increases in tensile strength due to the finer diameter fiber bundles and the greater number of fiber bundle cross-overs.

The specimen configurations machined from plate 424-1 are shown in Figure 38 and 39. The tensile bar employs a 0.40 inch thickness, in accordance with the thickest standard weave specimen of Reference 1.

The strains were measured with clip-on type extensometers which can follow the specimen elongation to failure, in contrast to the 1.0-1.5 percent upper limitation of bonded-on resistance foil types.

The compression specimen used is a solid cylinder as compared to the 0.4" x 0.4" x 0.45" specimens previously used. Bonded foil resistance strain gages were used.

The results obtained from the tensile test (Table 19) appear to support the "ineffective fiber bundle length" hypothesis. The mean tensile strength derived in the first set of measurements from plate 424-1 is 4680 psi as compared to the 3500 psi value from a standard weave ADL-4D6 standard process series of tests run on the same 0.40 inch thickness of specimen (Ref. 1, p. 89).

However, all three specimens failed in the fillet regions. This type of failure is usually the result of an inadequate specimen design for the material, causing stress concentrations. Thus the tensile strengths reported in this series are conservatively low.

The measured strains are for the central gage section of the specimens, which did not fail; therefore, they are not actually strains-to-failure. The mean value of 0.40 percent is about half what one would expect from the 0.40 inch thick tensile data of Reference 1 (p. 89, plate 415B) and less than one-third that suggested from the M.O.R. data of the previous section.

To further investigate the effect of specimen design on the measured tensile properties, the failed specimens were re-machined into rectangular bars 0.40 x 0.60 x 3.0 inches long; i.e., the one failed end of each bar was removed. These specimens were then butt-bonded on end with EA-934 epoxy adhesive to aluminum blocks. Doublers of 0.030 inch thick glass-epoxy were also bonded over all four faces to ensure failure in the ADL-4D6 gage section (Figure 38). Strains were again measured with a clip-on extensometer. The results from these re-machined specimens (Figure 40 and Table 19) show an increase in mean tensile strength from 4680 psi to 5143 psi. The strain-to-failure, however, decreased from a mean of 0.40 to 0.31 percent. It also should be noted that all three specimens failed at the end of the

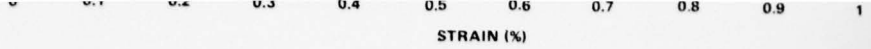

Figure 27. Flexural Stress-Strain, ADL-4D6 Panel 423-3, Standard Process

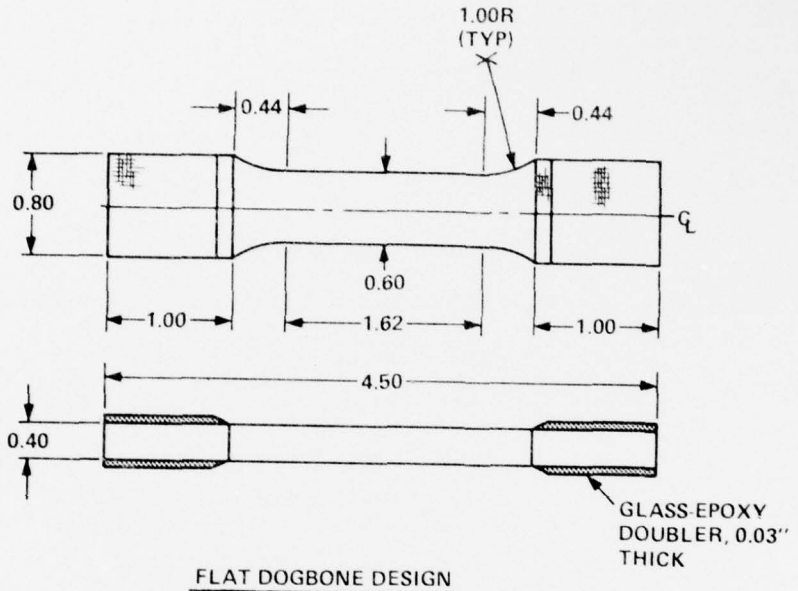

FLAT DOGBONE DESIGN

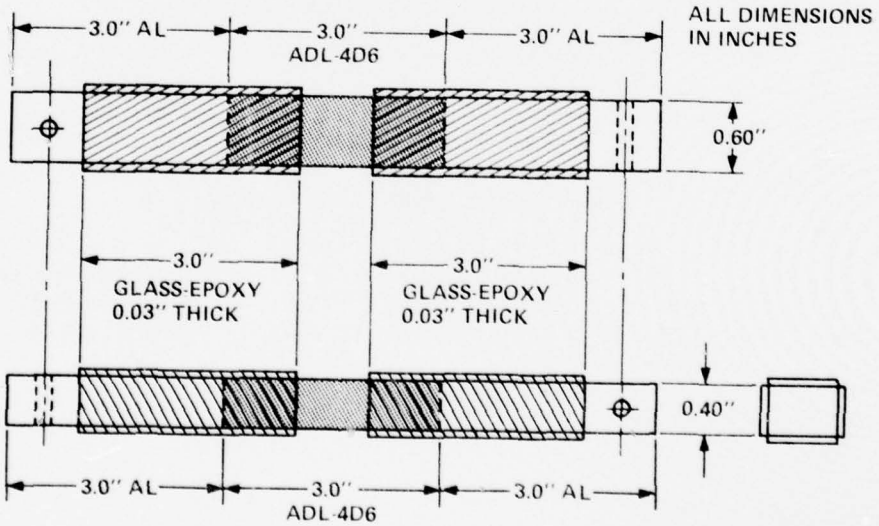

IMPROVED DOUBLER SURROUND/BUTT TENSION DESIGN

Figure 38. Evolution of ADL-4D6 Uniaxial Loading Tensile Specimen Design

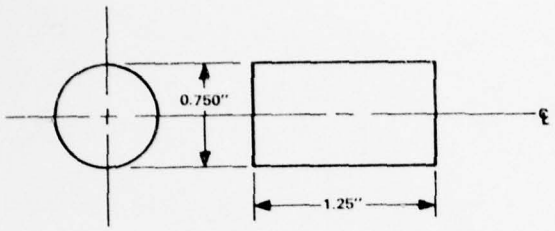

Figure 39. Circular Compression Specimen

TABLE 19. FINE WEAVE ADL-4D6 UNIAXIAL TENSION AND COMPRESSION

Panel 424-1	Density (gm/cc)	Strength (ksi)	Strain (%)	Modulus (Msi)	Notes
Tension					
TA-1	1.56	4.79	0.49	1.85	Failed in Fillet
TA-2	1.56	4.64	0.29	2.15	Failed in Fillet
TA-3	1.56	4.61	0.44	1.75	Failed in Fillet
Mean		4.68	0.40	1.92	
S.D.		0.09	0.10	0.21	
Re-Test					
TA-1		5.26	0.31	1.84	Failed at Doubler
TA-2		5.33	0.30	1.89	Failed at Doubler
TA-3		4.83	0.30	1.65	Failed at Doubler
Mean		5.14	0.31	1.80	
S.D.		0.27	0.01	0.13	
Compression					
CA-1	1.56	3.65	>0.83	0.58	Specimen Sheared
CA-2	1.55	2.81	0.80	1.96	Fibers Buckled
CA-3	1.60	2.85	0.44	3.66	Fibers Buckled
Mean		3.10	>0.69	2.07	
S.D.		0.47	—	1.54	

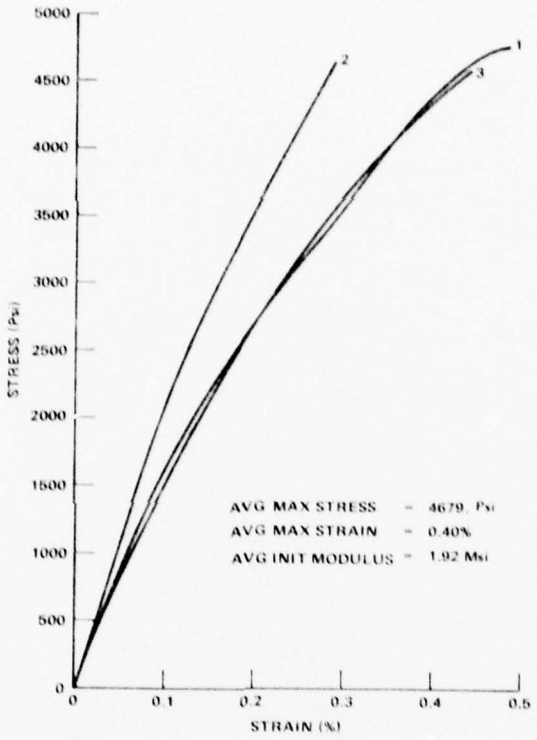

Figure 40. Panel 424-1 Axial Tension

doubler plates (i.e., again outside the extensometer gage section). From this it could be concluded that although higher strengths were obtained from this type of specimen design, some tensile test specimen modifications still have to be made, in order to obtain the true strength capability of the material.

The results from the compression tests show a failure strength of about half that of the standard weave ADL-4D6 tests run using the other specimen design from Reference 1 (p. 101) [3100 psi versus 6180 psi]. Some of this difference could be attributed to the specimen design; however, it should be noted that these compression specimens were machined from the end of the plate. (See plate layout diagram, Figure 23.) The angles at the end of the plate varied widely and hence, no firm grasp as to the actual angles in the specimens was obtained.

All of the uniaxial test results are in Table 19. The individual specimen stress-strain curves are in Figures 40 and 41.

3.2.2.3 Comparison of Uniaxial Loading and Flexural Tests

In comparing the results of the uniaxial tests with those of the flexure tests, it was found that in tension the measured strength was, on the average, 40 percent lower for the dogbone type and 34 percent lower for the re-tested specimens than the M.O.R. value, for the same plate of material (4.68 and 5.14 ksi as compared to 7.82 ksi). As previously stated, the lower tensile

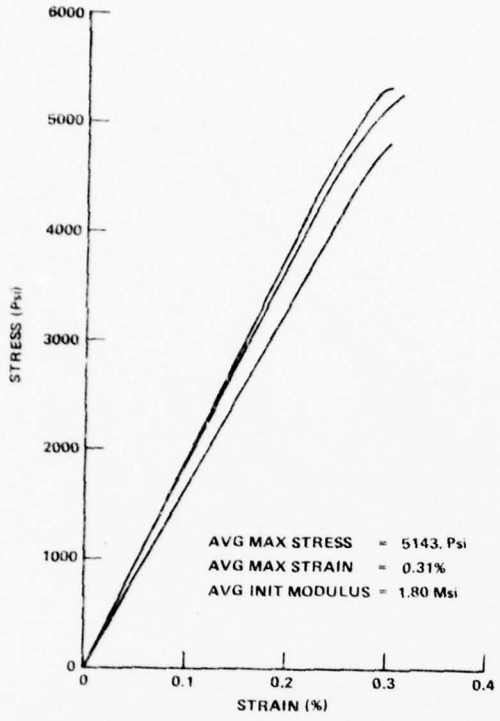

Figure 41. Re-Tested ADL-4D6, Axial Tension, Panel 424-1 Fine Weave

strength is probably the result of an inadequate specimen design for this material. The failure in the fillet region as well as at the end of the doublers not only affects the strengths, but the reported ultimate strains and modulus as well.

With the load concentrated in the fillet the maximum strain in the material also occurs in the same area, not in the center of the gage length, where the measurements were taken. Consequently the reported strains are lower and the modulus higher than what really exists. The degree to which this pertains can only be determined by additional specimen re-design and testing, so that failure will occur in the gage length.

Despite these measurement difficulties, it has been confirmed that the fineweave version of the standard process ADL-4D6 material has an axial tensile strength in excess of 5000 psi mean. It is also gratifying that the elastic properties deduced from three point flexure testing are not significantly far from the values measured in uniaxial loading; e.g., 1.8-1.9 Msi in Table 19 (uniaxial) versus 1.4 Msi in Table 18 (flexural) for panel 424-1.

This trend of measured property improvement is depicted in Figure 32. Measured ultimate tensile strength is plotted versus test specimen thickness, in all cases for rectangular cross section bars. The linear dependence of standard weave ADL-4D6 UTS on thickness is apparent, as discussed in Reference 1 (p. 88) and in Section 4.2 of this report. However, the fineweave material densified by the same "baseline" process has a measured strength level 40 to 60

percent higher, despite the measurement difficulties. Further improvement in test specimen design should yield higher measured strengths; while the improved confidence of uniaxial loading results should improve discrimination of the strength and elastic effects of the process variables investigated in this work.

These laboratory mechanical test and phenomenology studies have been complemented throughout this program by the findings of the "Composite Micromechanical Analysis" of Section 4. The combined result of the two efforts should be exploited in further work.

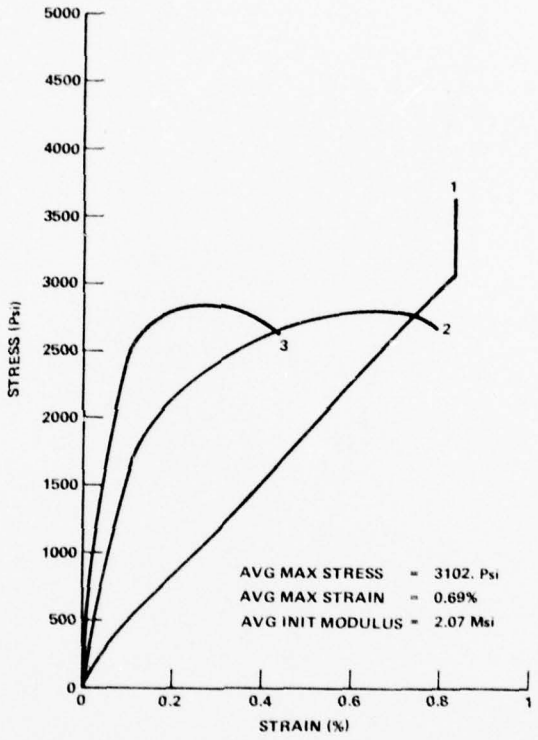

Figure 42. Panel 424-1 Axial Compression

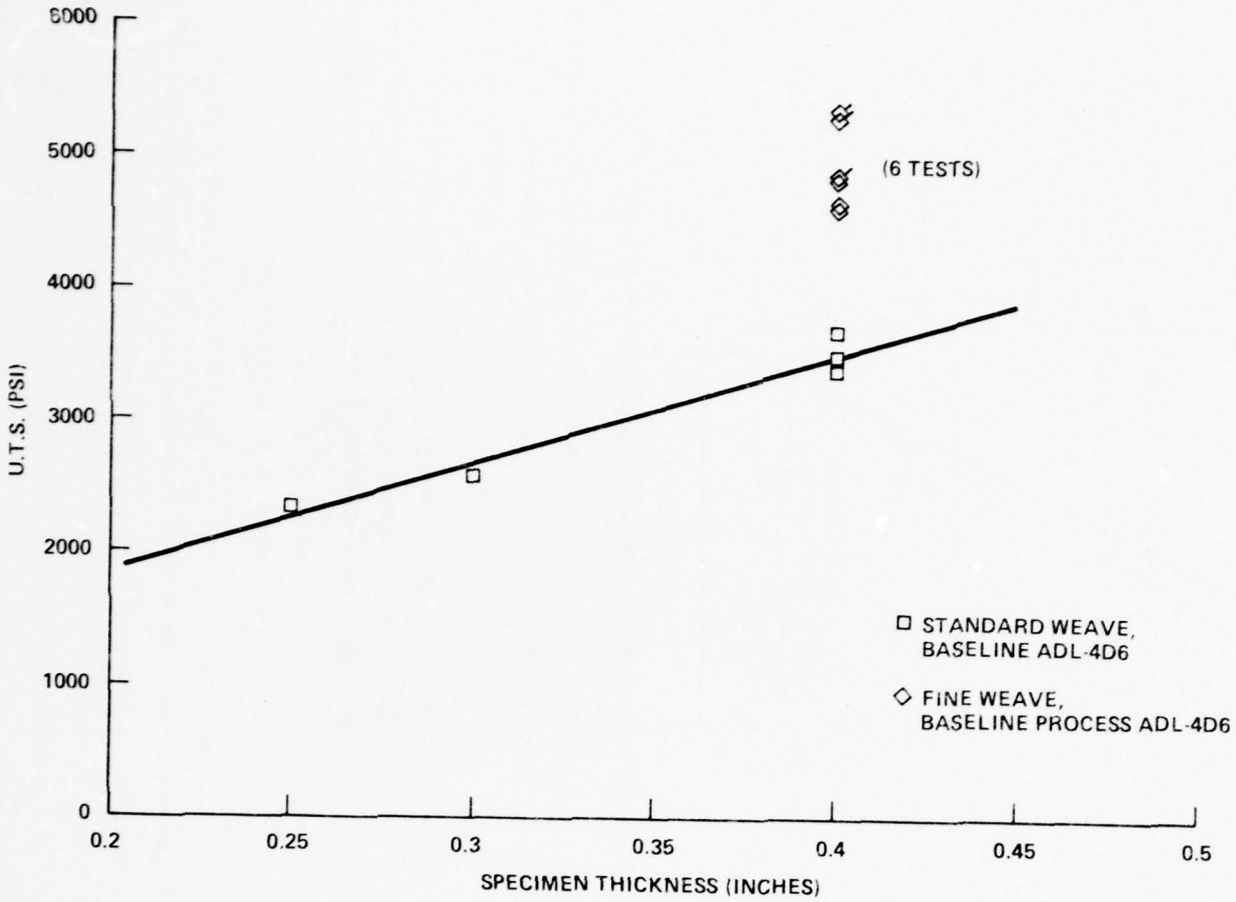

Figure 43. Effect of Rectangular Bar Uniaxial Loading Specimen Thickness on Measured ADL-4D6 Ultimate Tensile Stress, Standard and Fine Weave

3.3 ULTRASONIC MEASUREMENTS

3.3.1 INTRODUCTION

Ultrasonic wave velocity and attenuation of multidirectional composites are dependent upon many factors such as unit cell size, type of fiber and matrix, fiber angles and straightness, and adhesion of the matrix to the fibers. Because of this dependence, ultrasonic measurements are useful for checking the uniformity of the material, whether within a plate or from plate to plate.

Originally, in the ADL-4D6 development work, measurements were made at a frequency of 0.73 ± 0.03 MHz. At this frequency the total attenuation is high and we were frequently pushing the capability of the equipment to make measurements. Most of these earlier specimens were on the order of 1 cm in thickness or less. When much thicker specimens were made, for the higher impulse level testing of this program, the added attenuation made it impossible to transmit a meaningful signal through the specimens at 0.73 MHz and it became necessary to change the frequency employed for measurement. Lowering the frequency lowers the attenuation but, for these materials, would not be expected to significantly affect the velocity.

In order to compare attenuation data, it is necessary that the measurements be made at the same frequency since the attenuation is generally very frequency dependent. For the thickest specimen measured (PI-1 through 6 of Plate 423-3) it was necessary to drop the measurement frequency to 200 kilohertz in order to get a usable signal at the receiving transducer. However, the accuracy of both the velocity and attenuation measurements is generally better at higher frequencies. Thus the thinner specimens were measured at both 200 and 400 kilohertz (the former for comparison to the thick specimens). In a few cases, attenuation measurements were also made at 0.75 and 1.0 megahertz. At the higher frequencies the signal was too distorted to obtain accurate velocity data but demonstrates the rapid increase in attenuation with frequency increase.

A buffer-block technique was employed, as was the case for previous measurements (Ref. 1). With this technique, an initial transit time and attenuator reading are obtained for the signal transmitted through an aluminum buffer block. The test specimen is then inserted in series with this block, resulting in a change in transit time through the specimen. The change in attenuation is due both to specimen attenuation and to changes in interface reflection losses. The velocity and density data are used to calculate the interface reflection losses so that the attenuation in the specimen can be determined. Velocity is determined by measuring the transit time of the signal through the specimen using the sweep delay of a Tektronix oscilloscope.

The calibration of the sweep delay was checked against a crystal-controlled time mark generator to assure maximum accuracy. Attenuation measurements were made by means of a calibrated attenuator (1 decibel steps, 122 dB maximum attenuation).

3.3.2 EXPERIMENTAL RESULTS

3.3.2.1 Particle Impact Specimens

Ultrasonic velocity and attenuation measurements were made on particle impact specimens from plates 423-3 and 418-2. These were both standard process ADL-4D6 material. For 423-3 the surface through the thickness angle (STTA) was low but for 418-2 the STTA was nominal. The results of the measurements are given in Tables 20 and 21.

An initial attempt at measurement of 423-3 specimens was made at a frequency of 0.72 MHz on specimens PI-11 and PI-12 before the final impregnation step (i.e., the silane water desensitization treatment). The attenuation was so high (roughly 50 dB/cm) and the signal so badly distorted that meaningful measurements were not possible. It was, therefore, decided to defer additional measurements until processing was complete. This final processing increased density about 2 percent.

Measurements after final processing were again attempted at a frequency of 0.72 MHz. On the thicker specimens (PI-1 through -6) it was found that although the input signal frequency was 0.72 MHz, the signal which emerged through the specimen was only 0.21 MHz. This frequency shift phenomenon occurs in carbon-carbon composites also and since the shift results in data of dubious value, we have preferred to limit measurements in such cases to lower frequencies where such shifts do not occur. It was found that no shift occurred at 200 KHz in any of the ADL-4D6 specimens; and at 400 KHz no significant shift was apparent in the thinner specimens (i.e., PI-11 through -24). The measurements were therefore, limited to these frequencies.

The 423-3 specimens may be divided into three groups, according to thickness, and the measured velocities within any group are reasonably consistent but there is a significant variation in velocity from one group to another. The thickest specimens (approximately 25.4 mm) generally had rather low velocities (approximately 1.59 km/s average). Except for one specimen, all of the velocities for this group were lower than those reported in Reference 1. The thinnest specimens (approximately 11.4 mm thick) also exhibited low velocities (approximately 1.80 km/s average) but are generally within the lower quartile of the earlier data. The third group of specimens (approximately 12.7 mm thick) has an average velocity of 2.10 km/s, which is close to the average of the earlier data (2.19 km/s).

TABLE 20. ULTRASONIC VELOCITY AND ATTENUATION DATA STANDARD ADL-4D6, PLATE #423-3

Specimen Number	Density (g/cm^3)	Thickness (mm)	Measurement Frequency (MHz)	Wave Velocity (km/s)	Attenuation (db/cm)		Notes
PI-1	1.56	25.46	0.20	1.57	5.7		Measurements made at 200 kHz only due to frequency shift which occurs at higher frequencies (See Text).
PI-2	1.57	25.45	0.20	1.55	6.0		
PI-3	1.56	25.42	0.20	1.79	5.0		
PI-4	1.55	25.42	0.20	1.60	5.9		
PI-5	1.55	25.41	0.20	1.57	6.6		
PI-6	1.57	25.44	0.20	1.47	4.9		
PI-11	1.59	11.45	0.20	1.84	2.7		
PI-11	1.59	11.45	0.40	1.70		25.0	
PI-12	1.61	11.45	0.20	1.71	5.9		
PI-12	1.61	11.45	0.40	1.92		25.7	
PI-13	1.58	11.38	0.20	1.83	5.7		
PI-13	1.58	11.38	0.40	1.79		25.4	
PI-14	1.58	11.35	0.20	1.69	6.6		
PI-14	1.58	11.35	0.40	1.62		26.6	
PI-15	1.58	11.35	0.20	1.76	5.9		
PI-15	1.58	11.35	0.40	1.87		26.6	
PI-16	1.59	11.37	0.20	1.98	5.3		
PI-16	1.59	11.37	0.40	1.83		19.4	
PI-17	1.57	12.73	0.20	2.38	7.5		
PI-17	1.57	12.73	0.40	2.11		17.1	
PI-18	1.55	12.45	0.20	1.88	9.9		
PI-18	1.55	12.45	0.40	2.04		26.0	
PI-19	1.56	12.74	0.20	2.27	8.8		
PI-19	1.56	12.74	0.40	2.09		20.2	
PI-20	1.59	12.68	0.20	2.38	5.2		
PI-20	1.59	12.68	0.40	2.10		13.3	
PI-21	1.59	12.67	0.20	2.21	7.2		
PI-21	1.59	12.67	0.40	2.08		16.4	
PI-22	1.56	12.69	0.20	2.27	4.3		
PI-22	1.56	12.69	0.40	2.06		19.4	
PI-23	1.60	12.70	0.20	2.08	5.8		
PI-23	1.60	12.70	0.40	2.00		20.1	
PI-24	1.58	12.69	0.20	1.90	4.1		
PI-24	1.58	12.69	0.40	1.80		19.6	
PI-18	1.55	12.44	0.20	2.10	14.0		Remeasured at a later date. See Text.
PI-18	1.55	12.44	0.40	2.01		20.0	
PI-19	1.56	12.74	0.20	2.28	12.0		
PI-19	1.56	12.74	0.40	2.28		15.0	

TABLE 21. ULTRASONIC VELOCITY AND ATTENUATION DATA, ADL-4D6, PLATE 418-2

Specimen	Density (g/cm^3)	Thickness (cm.)	Measurement Frequency (MHz)	Velocity (km/s)	Attenuation (db/cm)				Fiber Angles (degrees)	
					0.20	0.40	0.75	1.00	SFPA	STTA
PI-25	1.59	1.017	0.20	2.11	12				40	40
"	"	"	0.40	2.05		10				
"	"	"	0.75	-			47			
"	"	"	1.00	-				58		
-26	1.58	1.018	0.20	2.09	13				42	38
"	"	"	0.40	2.04		11				
"	"	"	1.00	-				59		
-27	1.60	1.016	0.20	2.02	13				45	40
"	"	"	0.40	2.04		11				
-28	1.59	1.016	0.20	2.04	13				45	40
"	"	"	0.40	2.02		11				
-29	1.57	1.017	0.20	2.08	14				45	35
"	"	"	0.40	2.06		12				
-30	1.57	1.014	0.20	2.15	13				45	38
"	"	"	0.40	2.10		12				
-31	1.57	1.015	0.20	2.06	13				45	40
"	"	"	0.40	2.04		13				
-32	1.60	1.014	0.20	2.32	9				42	38
"	"	"	0.40	2.27		8				
"	"	"	0.75	-			28			
"	"	"	1.00	-				59		
-33	1.61	1.019	0.20	2.17	15				45	38
"	"	"	0.40	2.11		13				
-34	1.59	1.014	0.20	2.12	15				42	35
"	"	"	0.40	2.08		14				
-35	1.59	1.018	0.20	2.10	15				42	38
"	"	"	0.40	2.07		13				
-36	1.58	1.018	0.20	2.20	13				40	38
"	"	"	0.40	2.13		8				

The difference in wave velocities between groups is probably related to variations within the plate. That is, a given group may have been taken from one area of the plate and hence, would be more like one another than would specimens from an area remote from this group. The structural differences responsible for the wave velocity differences are not known at this time, but it appears that density variation is not responsible since plots of velocity as a function of density showed essentially no correlation of the two.

In the measurements on 423-3, we used a two-piece aluminum buffer block and the specimen was inserted between the two blocks. In the 418-2 measurements, made at a later data, we had considerable difficulty in using this method because of pick-up of the "main bang" signal. This pick-up interfered with the received signal, making it difficult to determine the state of the received signal (i.e., its location in time) and making attenuation measurement questionable. As we were unable to isolate the cause of the pick-up, we circumvented the problem by changing to rubber buffer blocks. The rubber provided a better impedance match to the ADL-4D6 (hence, lower reflection losses) and the wave velocity in the rubber was sufficiently low that the received signal was delayed enough to separate it from the pick-up noise.

The attenuation behavior of the specimens from plate 418-2 is unusual in that all specimens except PI-31 show a somewhat lower attenuation at 400 kHz than at 200 kHz. Because of this we checked three specimens at higher frequencies and found the attenuation increased as expected. In addition, two specimens from plate 423-3, measured previously, were re-measured. The attenuation measurements on these gave three to four decibel higher values at 200 kHz and five to six decibel lower values at 400 kHz. The reason for the change is not known.

3.3.2.2 Flyer Plate Specimens

Ultrasonic measurements were made on flyer plate specimens machined from plates 424-1 and -2. This material was a fine weave ADL-4D6 and was densified by the standard process. Results of the measurements are given in Table 22.

An interesting feature of the data from plate 424-1 is the difference between the thick and thin specimens. The thick specimens showed higher wave velocities and lower attenuation. Fiber angles were checked both by surface measurement and by making use of the "light pipe" effect to trace individual fiber bundles. The difference in surface reinforcement angles which was observed for the flexural test specimens from these two fine weave plates was not detectable. Since the flexural test results (Section 3.2.2, p. 3-41) did show drastically different results, attributed to the compaction of the preform after weaving, it must be inferred that this is also the cause of the differences in ultrasonic properties between the two densified panels.

TABLE 22. ULTRASONIC MEASUREMENTS ON FLYER PLATE SPECIMENS

Specimen Number	Density (g/cm^3)	Thickness (mm)	Measurement Frequency (MHz)	Wave Velocity (km/s)	Attenuation (db/cm)
ADL-4D6, Plate #424-1, Fine Weave					
US/FP-1	1.61	10.15	0.20	1.66	8.8
			0.40	1.65	18.4
US/FP-2	1.60	10.15	0.20	1.59	10.9
			0.40	1.61	20.7
US/FP-3	1.62	25.42	0.20	2.16	3.8
			0.40	2.08	7.3
US/FP-4	1.62	25.41	0.20	2.17	4.4
			0.40	2.11	6.8
ADL-4D6, Plate #424-2, Fine Weave					
S-6	1.57	10.18	0.20	2.25	8.0
			0.40	2.16	15.0
S-7	1.57	10.18	0.20	2.26	12.0
			0.40	2.15	18.0
S-8	1.54	10.18	0.20	2.21	14.0
			0.40	2.13	20.0
S-9	1.57	10.18	0.20	2.43	9.0
			0.40	2.24	13.0

3.4 SHOCK TESTING

3.4.1 INTRODUCTION

This section contains a description of the plate impact and particle impact testing performed at Effects Technology, Inc. for evaluation of ADL-4D6. The plate impact tests were performed on specimens from the fine-weave plates 424-1 and 424-2 for comparison with the standard-weave material. Exploding foil plate impact test techniques have been discussed in detail in a previous report (Ref. 2). The particle impact tests were performed on standard-weave specimens. Small glass spheres were fired along a trajectory 10^{o} to the surface of the specimen. The methods used for launching the particles are given in a separate paper (Ref. 11).

Eight of the plate impact tests were performed using carbon piezoresistive stress gages on the impact surface to measure the magnitude of the impact stress. This information was used in conjunction with the impact velocity and equation-of-state of the impacting material to obtain equation-of-state data which were compared with the equation-of-state data on the standard-weave ADL-4D6 tested previously. Gages were also used on the rear surface in order to measure the transmitted stress and thus determine the attenuative properties of the material in the stress regime of interest for vulnerability analysis. The results of the equation-of-state and attenuation tests yield valuable insight to the interpretation of the resistance of this class of material to damage by impulsive loading. The data indicate that the stress-wave response curve for the fine-weave material follows the acoustic response line up to 30 kbar and then rises above the standard-weave ADL-4D6 curve.

A series of six tests were performed using 14 mil Mylar flyer plates to determine the extent of damage versus impact velocity for three different thicknesses of the material. The equation-of-state data were used to calculate the delivered impulse for each flyer plate impact velocity. The impulse calculated in this way may be considerably different from either the initial flyer plate momentum or the impulse calculated by means of the acoustic approximation. The damage results are compared with results obtained previously on the standard-weave material.

3.4.2 EQUATION-OF-STATE AND ATTENUATION

Determination of the equation-of-state for the fine-weave ADL-4D6 was based on measurements of impact stress and velocity as discussed in Reference 2. Using the equation-of-state of the impacting material and these measured parameters, points on the stress versus particle velocity curve are determined. Additional data useful in evaluating the stress wave response of the material are given in Table 23. Acoustic impedence (obtained as the product of density and ultrasonic wave velocity) gives an initial estimate of the response of the material in the

TABLE 23. MATERIAL PROPERTIES FOR FINE-WEAVE ADL-4D6 SPECIMENS USED ON EQUATION OF STATE TESTS

PLATE	SPECIMEN	DENSITY (gm/cm^3)	THICKNESS (cm)	MEASUREMENT FREQUENCY (MHz)	ULTRASONIC VELOCITY (cm/μsec)	ACOUSTIC IMPEDANCE (gm/cm^2 μsec)	ATTENUATION (dB/cm)
424-1	US/FP-1	1.61	1.015	0.20	0.166	0.267	8.8
424-1	US/FP-2	1.60	1.015	0.20	0.159	0.254	10.9
424-1	US/FP-3	1.62	2.542	0.20	0.216	0.350	3.8
424-2	S-9	1.57	1.018	0.20	0.243	0.382	9

low stress regime. Ultrasonic attenuation, while not directly comparable to shock wave attenuation, provides a check on the variability of the material as well as a potential correlating parameter for plate impact and particle impact damage.* Test conditions and results from the equation-of-state shots are summarized in Table 24. Measured stresses are plotted versus velocity and compared with the previously-obtained data on standard-weave material in Figure 44.

A more useful representation of the data is the stress versus particle velocity curve. The stress versus impact velocity data may be converted to stress versus particle velocity by means of the Rankine-Hugoniot expressions for conservation of momentum, mass and energy as discussed in Reference 2. Values of the shock wave parameters derived from the measurements on the fine-weave material are given in Table 25. Data in the last entry show anomalously low stress, possibly due to the presence of a void near the surface of the material. The results for the two fine-weave plates are compared with the results from the standard-weave material in Figure 45. The stress versus particle velocity curves for the Plexiglas and Mylar flyer plate materials are shown in Figure 46. The curves in these two figures were used to compute the stresses and delivered impulses on the damage tests discussed in the following section.

*Ultrasonic data were not available for the thicker specimens due to measurement problems discussed in Section 3.3. As a result, correlation with plate impact data was not possible and only limited correlation could be performed with particle impact data.

TABLE 24. SUMMARY OF EQUATION OF STATE AND ATTENUATION PLATE IMPACT TEST CONDITIONS AND RESULTS FOR FINE-WEAVE ADL-4D6

TEST NUMBER	SPECIMEN			FLYER			IMPACT STRESS		TRANSMITTED STRESS WAVE		ATTENUATION
	MATERIAL	I.D.	THICKNESS (cm)	MATERIAL	THICKNESS (cm)	VELOCITY (cm/usec)	MEASURED (Kbar)	AVERAGE (Kbar)	AMPLITUDE (Kbar)	VELOCITY (cm/usec)	(dB/cm)
4534	424-1	US/FP-1	0 0 1.015	Plexiglas	0.152	0.272	13.0 11.3	12.2	2.35	0.274	7.65
4535	424-1	US/FP-2	1.015	Plexiglas	0.140	0.137	---	---	---	0.266	---
4536	424-2	S-9	0 0 1.018	Plexiglas	0.152	0.272	12.7 12.0	12.4	4.90	0.274	3.96
4537	424-2	S-10	0 0 1.016 1.537	Plexiglas	0.074	0.100	19.5 17.3	18.4	2.6 2.6	0.333 0.336	8.36 5.53
4538	424-2	S-5	0 1.384	Plexiglas	0.071	0.216	55.3	55.3	5.0	0.386	7.54
4542	424-2	S-12	0 0 0.477 1.472	Plexiglas	0.076	0.247	71.1 74.3	72.7	46.0 7.5	0.342 0.335	4.17 6.70
4544	424-2	S-13	0 0 1.472	Plexiglas	0.076	0.254	28.2 33.3	30.8	5.0	0.320	5.36
4545	424-2	S-14	0 0 1.472	Plexiglas	0.076	0.150	27.4 27.9	27.6	2.8	0.383	6.75

AD-A076 769 GENERAL ELECTRIC CO PHILADELPHIA PA RE-ENTRY AND ENV--ETC F/G 17/5
MILLIMETER WAVE HARDENED ANTENNA WINDOW MATERIALS DEVELOPMENT.(U)
AUG 79 J P BRAZEL , R FENTON , J A ROETLING DAAG46-79-C-0047
UNCLASSIFIED AMMRC-TR-79-45 NL

2 OF 3
AD A076769

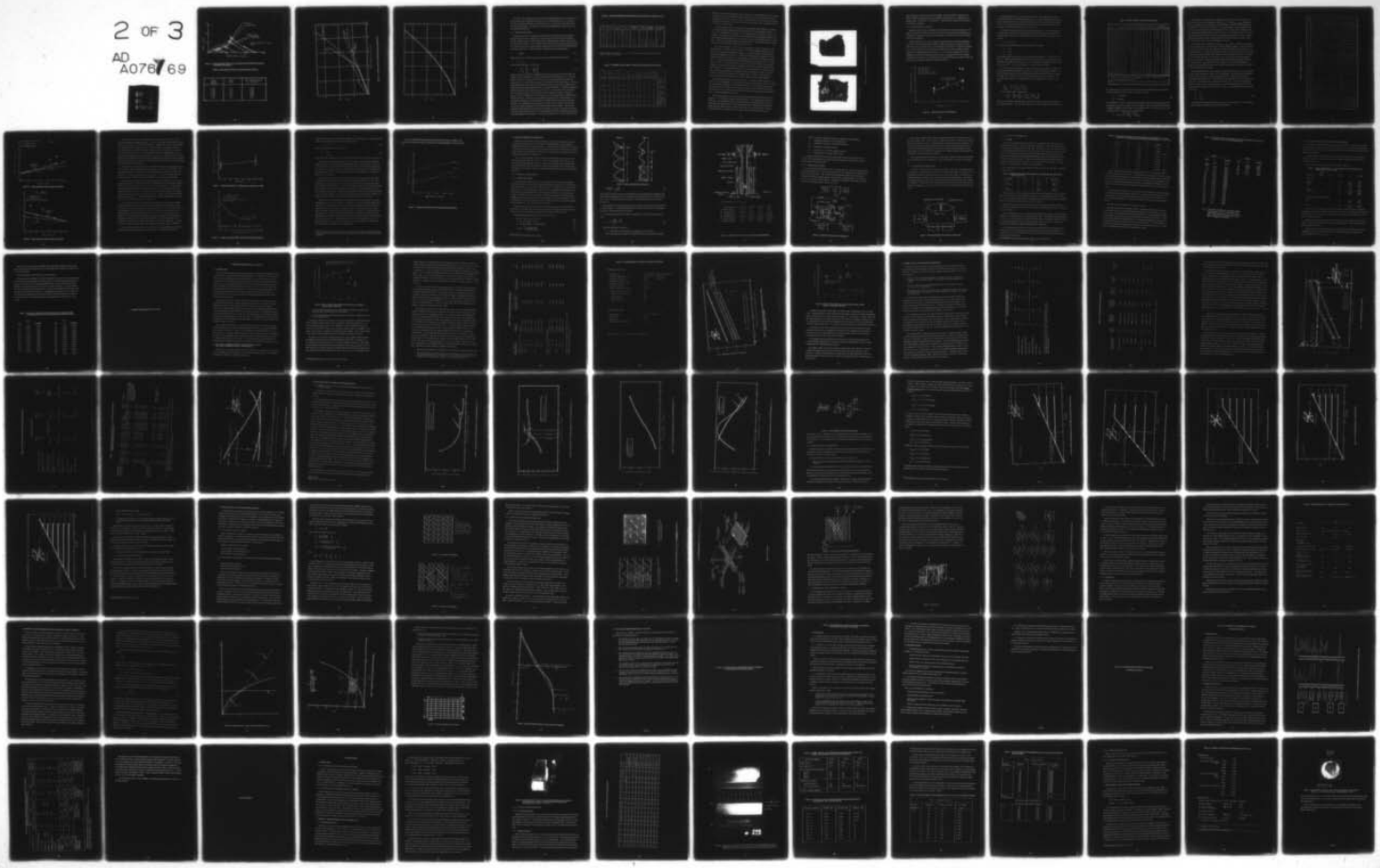

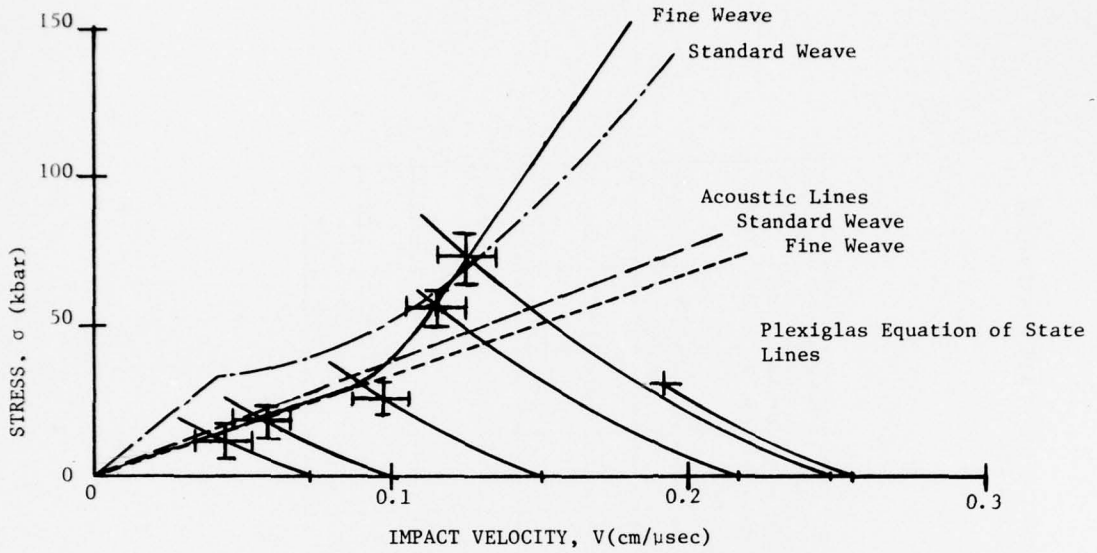

Figure 44. Results of Equation of State Tests on ADL-4D6 Fine Weave Material and Comparison with Standard Weave Response

TABLE 25. EQUATION-OF-STATE DATA FOR FINE WEAVE ADL-4D6

IMPACT VELOCITY V(cm/μsec)	STRESS σ (Kbar)	SHOCK PARTICLE VELOCITY U_p (cm/μsec)
0.247	72.7	0.124
0.216	55.3	0.115
0.150	27.6	0.096
0.100	18.4	0.058
0.072	12.4	0.044
0.072	12.2	0.044
0.254	30.8	0.191

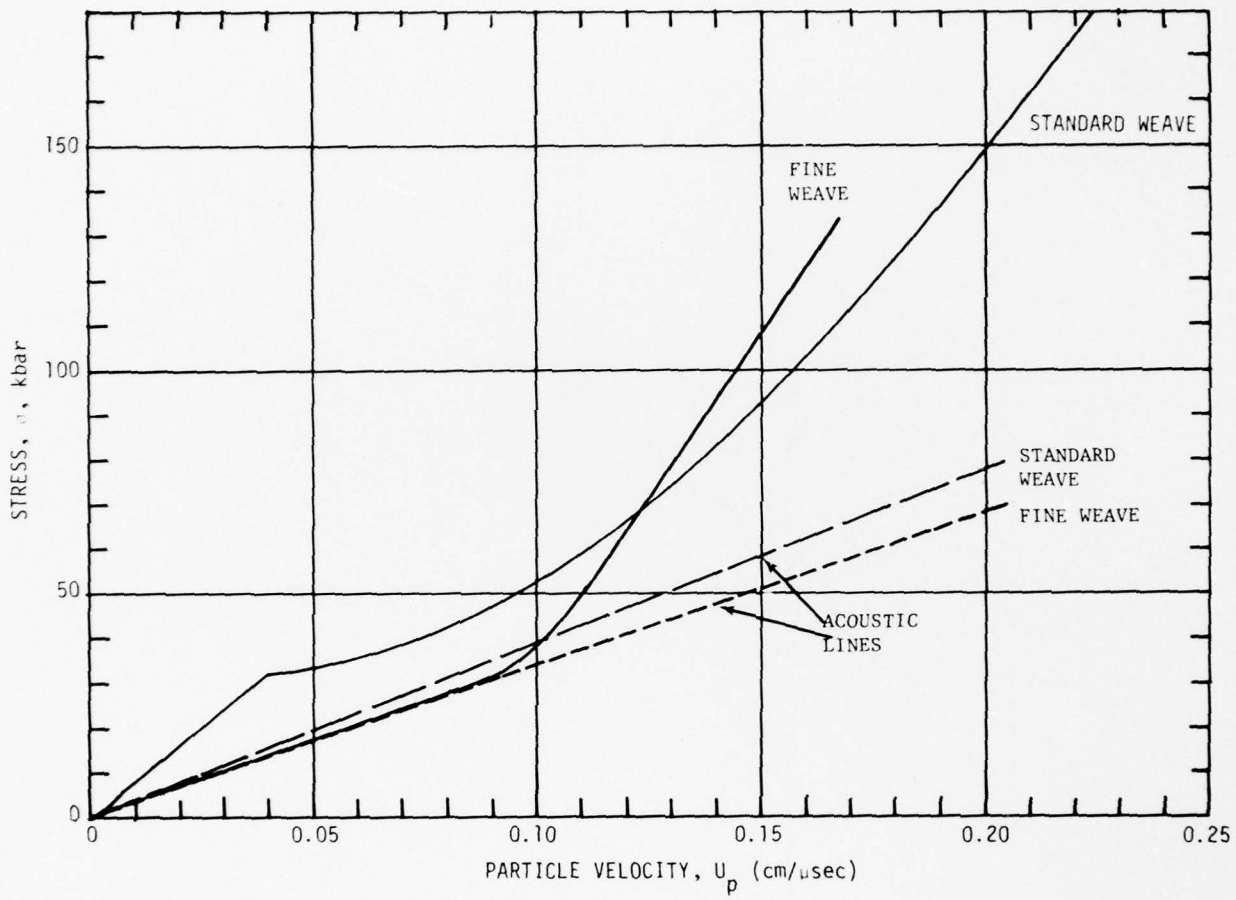

Figure 45. Equation of State of ADL-4D6, Stress Versus Particle Velocity

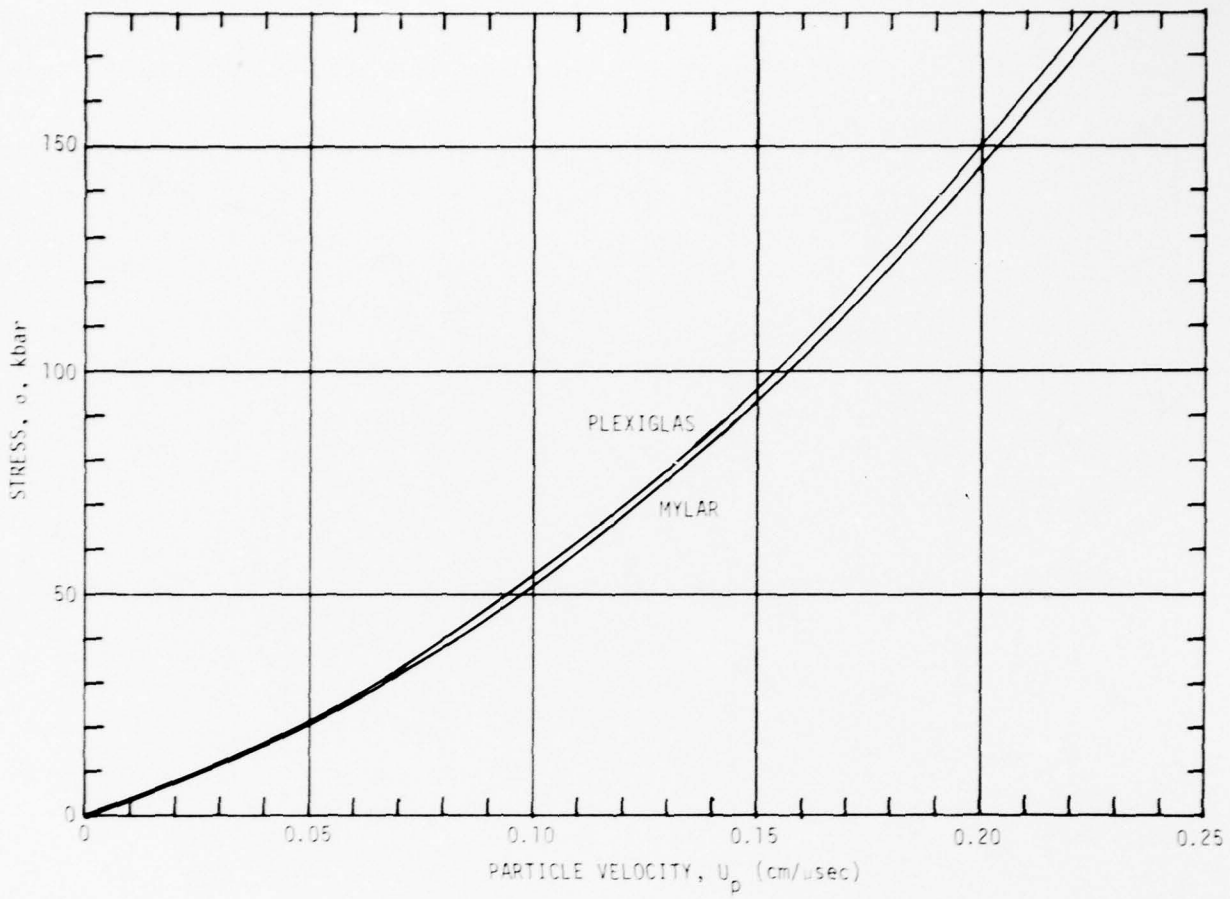

Figure 46. Equation of State of Plexiglas and Mylar, Stress Versus Particle Velocity

The values of rear surface stress were compared with the initial stresses to determine the extent of stress wave attenuation in the material. For nominal impact stresses of 12 kbar to 73 kbar, the nominal attenuation rate was found to be 6.2 ± 0.15 dB/cm for fine-weave ADL-4D6 under shock loading. This quantity will be useful in estimating rear surface stresses for the damage threshold tests.

3.4.3 DAMAGE RESISTANCE

Plate impact tests were performed on two thicknesses of plate 424-2 and one specimen from plate 424-1 in order to evaluate the resistance of the material to damage by impulsive loading. The thicknesses, densities and ultrasonic properties of the specimens used on these tests are listed in Table 26. Test conditions and results for the damage tests are given in Table 27. Impact stresses were obtained using the equation-of-state curves for ADL-4D6 and Mylar, as discussed previously. Delivered impulse is defined by the stress-time integral

$$I = \int \sigma \, dt \tag{4}$$

which, for the case of thin flyer plate impact may be calculated from the expression

$$I = \sigma_i \tau_o \tag{5}$$

where the pulse duration, τ_o, is given by

$$\tau_o = \frac{X_f}{U_{sf}} \left[2 - \frac{U_{pf}}{R_{sf}} \right] \tag{6}$$

In this expression, X_f is the flyer plate thickness and U_{sf} and U_{pf} are the shock velocity and particle velocity, respectively, in the flyer plate material at the initial stress σ_i. The pulse duration is just the time required for the shock wave to traverse the thickness of the flyer plate, reflect as a rarefaction wave and return to the specimen/flyer plate interface. The form of Equation (6) takes into consideration the fact that the release wave travels through the compressed flyer plate material which is therefore, reduced in thickness. It should be emphasized that this expression assumes that the stress relieves to zero upon arrival of the rarefaction wave at the impact surface. In cases where the shock impedance of the flyer material is greater than the shock impedance of the specimen, the stress will not relieve completely after the first reflection. In those cases, the calculation simply gives the "prompt impulse," i.e., the portion of the impulse associated with the first double-transit of the shock wave through the flyer. The remaining portion of the impulse is delivered over a period of time which depends on the relative impedances of the specimen and flyer plate materials. The total integrated momentum delivered to the specimen (after many stress wave reflections) will be equal to the flyer plate momentum whenever the shock impedance of the flyer material is greater than the shock impedance of the specimen. As discussed in Reference 2, only the prompt portion of

TABLE 26. MATERIAL PROPERTIES FOR SPECIMENS USED ON DAMAGE THRESHOLD TESTS

PLATE	SPECIMEN	DENSITY (gm/cm^3)	THICKNESS (cm)	MEASUREMENT FREQUENCY (MHz)	ULTRASONIC VELOCITY (cm/μsec)	ACOUSTIC IMPEDANCE (gm/cm^2 μsec)	ATTENUATION (db/cm)
424-2	S-3	1.55	2.558	*	*	*	*
424-2	S-2	1.56	2.555	*	*	*	*
424-2	S-1	1.55	2.558	*	*	*	*
424-2	S-8	1.54	1.018	0.20	0.221	0.340	14
				0.40	0.213	0.328	20
424-2	S-6	1.57	1.018	0.20	0.225	0.353	8
				0.40	0.216	0.339	15
424-2	US/FP-4	1.62	2.541	0.20	0.217	0.352	4.4
				0.40	0.211	0.342	6.8

*Ultrasonic properties of specimens S-1, S-2, S-3 could not be measured due to large attenuation and scattering in the 1-inch thickness.

TABLE 27. SUMMARY OF PLATE IMPACT DAMAGE TESTS ON FINE-WEAVE ADL-4D6

	SPECIMEN			FLYER				CALCULATED IMPACT CONDITIONS			CALCULATED REAR SURFACE CONDITIONS		
TEST NUMBER	MATERIAL	ID 200-400	THICKNESS (cm)	MATERIAL	THICKNESS (cm)	VELOCITY (cm/μsec)	MOMENTUM (kbar)	IMPACT STRESS (kbar)	DURATION (μsec)	DELIVERED IMPULSE* (kbar)	STRESS (kbar)	PULSE DURATION (μsec)	COMMENTS
4527	424-2	S-3	2.558	Mylar	0.0356	0.310	15.2	109.2	0.130	14.2	2.8	5.0	Front surface structurally fragmented. Partial rear surface spall 0.70 cm thick recovered.
4528	424-2	S-2	2.555	Mylar	0.0356	0.150	7.4	29.0	0.198	5.7	0.76	7.6	Front surface crushing. Specimen thickness decreased 0.018 cm.
4529	424-2	S-1	2.558	Mylar	0.0356	0.220	10.8	55.8	0.163	9.1	1.4	8.3	Front surface structurally fragmented. Incipient spall cracks along rear surface edges.
4530	424-2	S-8	1.020	Mylar	0.0356	0.150	7.4	29.0	0.198	5.7	0.8	0.9	Specimen structurally fragmented. Spall fragments (0.6 cm thick) recovered.
4531	424-1	US/FP-4	2.555	Mylar	0.0356	0.220	10.8	55.8	0.159	9.1	1.5	8.3	Specimen structurally fragmented. Partial spall.
4532	424-2	S-6	1.020	Mylar	0.0356	0.086	4.2	15.8	0.231	3.7	3.7	1.0	No damage.

the pulse is considered in the damage analysis, because it is assumed that most of the damage to the material is associated with the highest stress level, which is maintained only during that portion of the pulse. The effect of this assumption in the case of the fine-weave material is that the ratio of delivered momentum to flyer plate mementum reaches a minimum of about 0.77 in the 5-7 kilotap range.

As with the standard-weave material, the primary damage mode indicated by the damage tests was front surface crushing, and damage of this form was seen at delivered impulse levels above approximately 5.7 kilotaps. No crushing damage was observed at a level of 3.7 kilotaps. This result may be compared to the standard-weave material which exhibited some front surface crushing and slight increase in thickness (likely due to internal spall) at 4.8 kilotaps. The degree of crushing damage was moderate at the 5.7 kilotap level, and was confined to the region near the surface, approximately 1 mm deep.

At a delivered impulse of 9.1 kilotaps, the crushing was severe but confined to a region approximately 0.5 cm thick at the front surface. The extent of damage to the specimen in this test is visible in the photographs of Figure 47. A similar result was obtained with the same impact conditions on plate 424-1. Crushing of the impact surface extended to a depth of approximately 0.5 cm, and no rear surface damage was observed. Both specimens were over 2.5 cm thick, and exhibited spall cracking at a depth of approximately 0.5 to 1 cm from the rear surface. The material in front of the spalled section fractured laterally and fragmented to an extent which precluded determination of the depth of crushing. On the basis of these results, it is concluded that the threshold level for degradation of the material by front face crushing is approximately 5.7 kilotaps, which is approximately the same as the value found for the threshold for crushing of the standard-weave material. The performance of fine-weave plates 424-1 and 424-2 was essentially identical at the threshold condition.

The threshold for spall failure appears to be near 9.1 kilotaps for both of the fine-weave plates in the 2.5 inch thickness. As mentioned, both showed spall cracking at this level. Plate 424-2 was tested at both higher and lower impulse levels. At 14.2 kilotaps, complete spall was observed; at 5.7 kilotaps no spall cracks were evident. These results place the spall performance of the 2.5 cm-thick fine-weave material within the uncertainty limits obtained for the 2.5 cm-thick standard-weave material.

The two tests performed on 1 cm-thick specimens bracketed the spall threshold for that thickness. At 5.7 kilotaps, complete spall was observed. At 3.7 kilotaps the specimen was undamaged. The performance of the 1 cm-thick fine-weave materials cannot be compared directly with the standard weave, since previous testing of the standard-weave material did not include shots which produced a definite spall. However, it appears that the 1-cm-thick fine-weave material is somewhat weaker than the standard-weave material in terms of

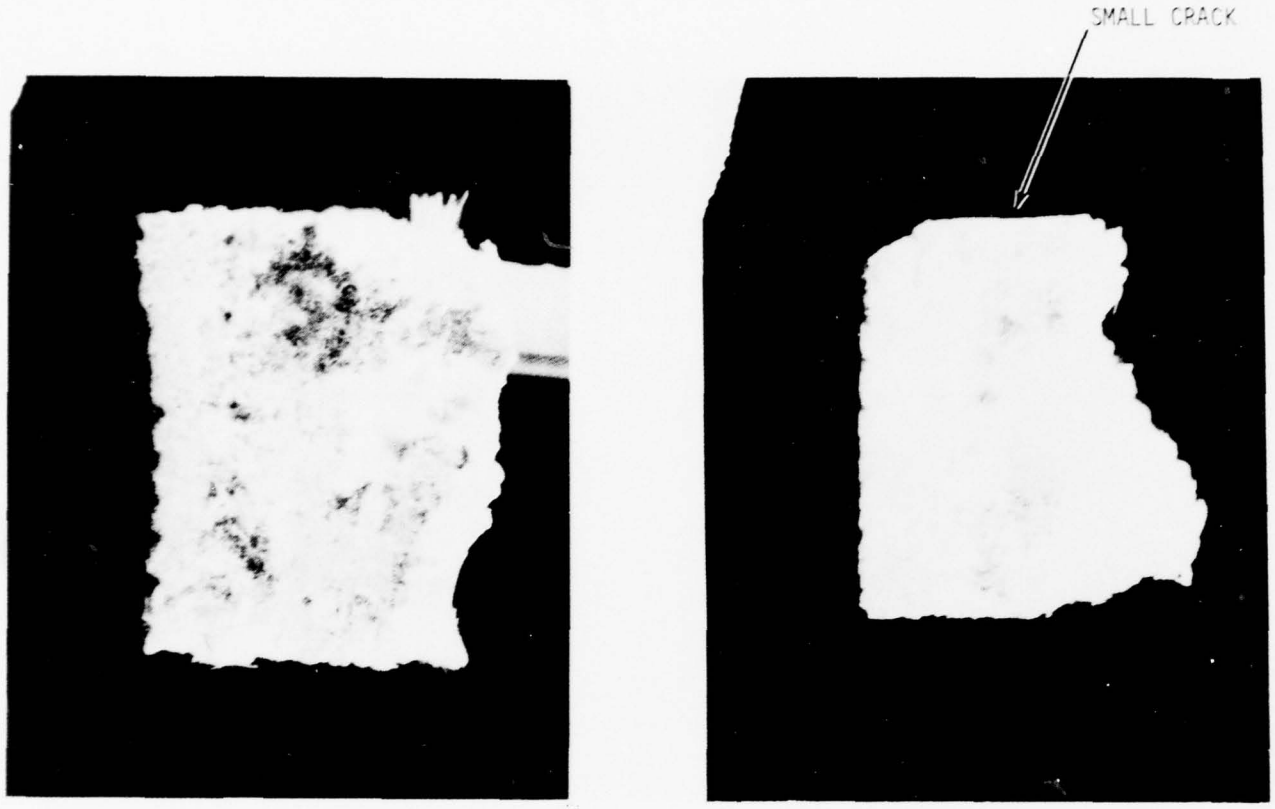

Figure 47. Test Number 4529, ADL-4D6 Specimen #424-2-S-1

delivered impulse required to produce spall damage. The best estimate of performance is shown in Figure 48, which indicates most probable spall thresholds of 4.7 kilotaps for 1-cm thickness and 9.1 kilotaps for 2.5 cm thickness. Test data for the standard-weave material are shown for comparison.

3.4.4 PARTICLE IMPACT TESTING

Specimens from two plates of standard-weave ADL-4D6 were subjected to impacts at 10°, using 1/2 mm and 1 mm glass particles in order to characterize the erosion performance of this material. Variations in mass loss due to particle size, impact velocity and test temperature were investigated.

Midway through the test series, variations in specimen density and acoustic attenuation were noted. These variations appeared to have significant influence on the mass loss data, which showed wide scatter under some test conditions (1 mm particles at 12 kft/sec in particular). It became evident that a larger number of replicate tests at these conditions would be required for an acceptable degree of precision. As a result of this finding, and in view of difficulties encountered with launching large particles, the original test plan was modified; testing with 5 mm particles was dropped from the matrix and additional tests with 1/2 and 1 mm particles were scheduled to further investigate these effects.

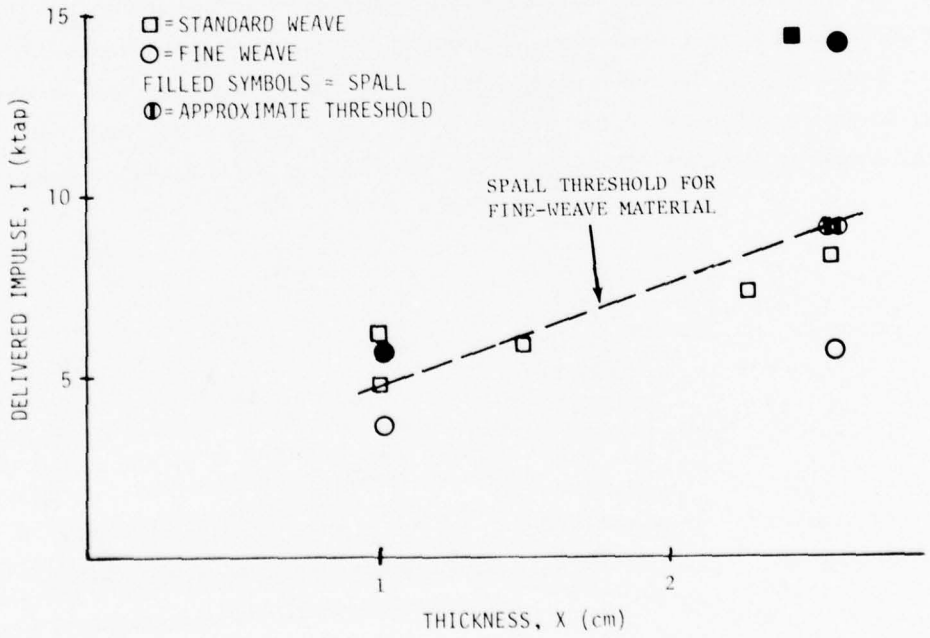

Figure 48. Spall Test Results for ADL-4D6 Materials

The particle impact tests are summarized in Table 28. Also included in the table are the 200 KHz ultrasonic attenuation data obtained by GE. Because of the difficulties in measurement discussed in Section 3.3, specimens from plate 418-2 were tested with different buffer blocks. As a result, the ultrasonic data from the two plates cannot be compared directly for the purpose of isolating attenuation effects on mass loss.

The influence of specimen density was investigated analytically. A trivariate regression was performed on all of the room temperature data to separate the effects of velocity and material density on mass loss. The model which was used for the regression analysis was of the form:

$$G = G_o + A\rho + BV \tag{7}$$

The analysis yielded the following relative values for the constants:

$$\begin{aligned} G_o &= 13.17 \\ A &= -8.53 \\ B &= 0.109 \end{aligned} \tag{8}$$

when normalized by the value of mass loss at the nominal conditions (ρ = 1.58 gm/cm^3, V=12 Kft/sec). (In this representation, the mass loss for a density of 1.58 gm/cm^3 and a velocity of 12 Kft/sec is arbitrarily set equal to 1.00.) The coefficient of determination found for this regression was $R^2 = 0.557$, which indicates a reasonably strong correlation.

In order to display the dependence of mass loss on the various parameters, a normalization procedure must be established to account for the changes in independent variables. To this end, Equation (7) may be used to estimate the mass loss which would have been obtained at reference test conditions, given the measured results and actual test conditions. The following expression gives the relationship between the equivalent and measured mass loss ratios:

$$\frac{G_{eq}}{G_{meas}} = \frac{G + A\rho_{ref} + BV_{ref}}{G_o + A\rho_{meas} + BV_{meas}} \tag{9}$$

One may define a further normalization:

$$\hat{G} = \frac{G_{eq}}{G_N} = \frac{G_{meas}}{G_N}\left[\frac{G_o + A\rho_{ref} + BV_{ref}}{G_o + A\rho_{meas} + BV_{meas}}\right]$$

where G_N is an arbitrary constant which is introduced in order to avoid direct reference to actual mass loss ratios. Since the average density of all of the specimens tested in this study

TABLE 28. PARTICLE IMPACT TEST DATA FOR ADL-4D6

TEST NUMBER	SPECIMEN ID	SPECIMEN DENSITY (gm/cm^3)	ULTRASONIC*** ATTENUATION (db/cm)	PARTICLE DIAMETER (mm)	PARTICLE VELOCITY (Kft/sec)	TEST TEMPERATURE (°F)	RELATIVE* MASS LOSS RATIO	
							GRAVIMETRIC	VOLUMETRIC
2978	423-3-23	1.60	5.8	1.0	12.5	70	0.845	0.936+
2979	423-3-22	1.56	4.3	1.0	12.6	70	1.804	1.778+
2980	423-3-20	1.59	5.2	1.0	8.2	70	0.436	0.487
2981	423-3-21	1.59	7.2	1.0	7.0	70	0.413	0.360
2982	423-3-14	1.58	6.6	0.5	7.5	70	0.686	0.480
2983	423-3-13	1.58	5.7	0.5	7.5	70	1.755	0.695
2985	423-3-11	1.59	2.7	0.5	12.0	70	--	0.580
2986	423-3-12	1.61	5.9	0.5	12.2	70	--	0.767
2987	423-3-15	1.58	5.9	0.5	7.5	1200	--	--
2994	423-3-24	1.58	4.1	1.0	11.8	1200	--	1.092
2995	423-3-16	1.59	5.3	1.0	11.2	1200	--	1.074
3205	423-3-19	1.55	8.8(12)	1.0	11.7	70	1.088	0.871
3206	423-3-18	1.56	9.9(14)	1.0	12.0	70	1.383	0.979
3207	418-2-33	1.61	(15)	1.0	11.5	70	0.912	0.752
3208	418-2-26	1.58	(13)	1.0	11.5	70	3.169	1.374+
3209	418-2-29	1.57	(14)	1.0	10.6	70	1.014	0.855
3210	418-2-30	1.57	(13)	1.0	7.8	70	0.594	0.637
3211	418-2-31	1.57	(13)	1.0	8.1	70	2.395	0.609
3216	418-2-34	1.59	(15)	1.0	8.4	1200	--	0.603
3217	418-2-35	1.59	(15)	1.0	8.3	1200	--	0.450
3218	418-2-27	1.60	(13)	0.5	11.7	70	--	0.589
3219	418-2-28	1.59	(13)	0.5	11.8	1200	--	0.921
3220	418-2-27**	1.60	(13)	0.5	10.9	1200	--	2.748+
3221	418-2-25	1.59	(13)	0.5	7.4	1200	--	0.822+
3222	418-2-32	1.60	(9)	0.5	--	1200	--	0.409
3223	418-2-32**	1.60	(9)	0.5	7.5	1200	--	0.529

*Referenced to the average RT, 1.58 gm/cm^3, 12 Kft/sec volumetric value; i.e., $G_V(1.58,12)$ was set equal to 1.0.
**Test performed on reverse side.
***Values in parentheses were obtained with rubber buffer blocks (Section 3.3)
+See Text.

was approximately 1.58 gm/cm^3, this value was selected as the density for normalization. The normalization velocity was taken to be 12 Kft/sec. Thus

$$\rho_N = 1.58 \text{ gm/cm}^3$$
$$V_N = 12 \text{ Kft/sec} \qquad (10)$$

All of the mass loss values reported have been reduced by the value of volumetric mass loss indicated by the regression analysis for these conditions, and it is in this procedure that the constants of Equation (8) were defined. The procedure sets $\hat{G} = 1.00$ at $\rho = \rho_N$, $V = V_N$. The normalized mass loss ratio may then be expressed as:

$$\hat{G} = G_{meas} \frac{G_o + A\rho_{ref} + BV_{ref}}{G_o + A\rho_{meas} + BV_{meas}} \qquad (11)$$

For the purpose of examining velocity dependence of the mass loss ratio, equivalent (normalized) mass loss ratios are obtained by setting $\rho_{ref} = 1.58$ and $V_{ref} = V_{meas}$ in Equation (11). Values obtained by this procedure are listed in Table 29 and the room temperature data is plotted at $\widehat{G}(1.58, V)$ versus V in Figure 49. It is noted that three of the gravimetric mass loss values fall considerably higher than the bulk of the data. This scatter is attributed to the loss of material at locations remote from the crater site. This behavior is typical of the more brittle woven materials, and may have little relationship to performance in service. With the exception of those three points, both the gravimetric and the volumetric data cluster around the regression line with a scatter of approximately 30 percent.

Density dependence is examined by setting $\rho_{ref} = \rho_{meas}$ and $V_{ref} = 12$ Kft/sec in Equation (11). Normalized values are listed in Table 29 and are plotted in Figure 50 as $\widehat{G}(\rho, 12)$ versus ρ. The normalized values of mass loss which were obtained at a nominal velocity of 8 Kft/sec are listed in parentheses. In addition, normalization of the 8 Kft/sec data to the 8 Kft/sec reference condition was performed and the values obtained are listed in Table 29 as $\widehat{G}(\rho, 8)$. These quantities were plotted separately on the $\widehat{G}$ versus ρ curve and were found to group around the 8 Kft/sec regression line. Since no additional insight was obtained by examination of that plot, the $\widehat{G}(\rho, 12)$ versus ρ representation was used to display all of the room temperature data. Again, the data falls within approximately 30 percent of the regression line with the exception of the three gravimetric data points.

Subsequent detailed microscopic examination of impacted specimens revealed the existence of large cavities adjoining the craters in 5 of the specimens. The tests on which this phenomenon was observed were the room temperature shots 2978, 2979 and 3208, and the high-temperature shots 3220 and 3221. Examination of the data in Table 29 shows that each of these shots also yielded relatively large volumetric mass loss ratios. In view of the potential importance of this result, the statistical analysis was repeated, using the data from Table 28, but omitting these apparently anomalous data. The new constants which were generated in this analysis are:

$$\begin{aligned} G_o &= 7.56 \\ A &= -4.74 \\ B &= 0.060 \end{aligned} \qquad (12)$$

The coefficient of determination of this regression was found to be $R^2 = 0.668$, indicating a notably stronger correlation than was previously obtained.

TABLE 29. NORMALIZATION OF MASS LOSS DATA

TEST NUMBER	SPECIMEN ID	GRAVIMETRIC					VOLUMETRIC					MEASURED VELOCITY (kft/sec)	SPECIMEN DENSITY (gm/cm^3)	TEST TEMP (°F)	PARTICLE DIAMETER (mm)
		$\hat{G}(1.58,V)$	$\hat{G}(n,12)$	$\hat{G}(n,8)$	$\hat{G}(1.58,12)$	$\hat{G}(1.58,8)$	$\hat{G}(1.58,V)$	$\hat{G}(n,12)$	$\hat{G}(n,8)$	$\hat{G}(1.58,12)$	$\hat{G}(1.58,8)$				
2978	423-3-23	1.007	0.792	--	0.955	--	1.117	0.879	--	1.059	--	12.5	1.60	70	1.0
2979	423-3-22	1.553	1.706	--	1.456	--	1.531	1.682	--	1.437	--	12.6	1.56	70	1.0
2980	423-3-20	0.510	(0.793)	0.417	(0.867)	0.491	0.569	(0.885)	0.466	(0.967)	0.548	8.2	1.59	70	1.0
2981	423-3-21	0.507	(1.013)	0.533	(1.107)	0.627	0.442	(0.883)	0.464	(0.965)	0.546	7.0	1.59	70	1.0
2982	423-3-14	0.685	(1.337)	0.757	(1.337)	0.757	0.480	(0.936)	0.530	(0.936)	0.530	7.5	1.58	70	0.5
2983	423-3-13	1.753	(3.421)	1.938	(3.421)	1.938	0.694	(1.355)	0.768	(1.355)	0.768	8.5	1.58	70	0.5
2985	423-3-11	--	--	--	--	--	0.632	0.579	--	0.633	--	12.0	1.59	70	0.5
2986	423-3-12	--	--	--	--	--	1.021	0.744	--	0.999	--	12.2	1.61	70	0.5
2987	423-3-15	--	--	--	--	--	--	--	--	--	--	7.5	1.58	1200	0.5
2994	423-3-24	--	--	--	--	--	1.091	1.115	--	1.115	--	11.8	1.58	1200	1.0
2995	423-3-16	--	--	--	--	--	1.183	1.185	--	1.295	--	11.2	1.59	1200	1.0
3205	423-3-19	0.839	1.115	--	0.888	--	0.688	0.893	--	0.711	--	11.7	1.55	70	1.0
3206	423-3-18	1.180	1.381	--	1.180	--	0.835	0.978	--	0.835	--	12.0	1.56	70	1.0
3207	418-2-33	1.248	0.982	--	1.320	--	1.030	0.811	--	1.089	--	11.5	1.61	70	1.0
3208	418-2-26	3.164	3.345	--	3.345	--	1.372	1.451	--	1.451	--	11.5	1.58	70	1.0
3209	418-2-29	0.920	1.177	0.707	1.085	0.614	0.775	0.992	0.596	0.914	0.518	10.6	1.57	70	1.0
3210	418-2-30	0.513	(1.021)	0.613	(0.941)	0.533	0.550	(1.096)	0.658	(1.010)	0.572	7.8	1.57	70	1.0
3211	418-2-31	2.084	(3.917)	2.352	(3.610)	2.045	0.531	(0.997)	0.599	(0.919)	0.421	8.1	1.57	70	1.0
3216	418-2-34	--	--	--	--	--	0.700	(1.050)	0.552	(1.147)	0.650	8.4	1.59	1200	1.0
3217	418-2-35	--	--	--	--	--	0.524	(0.801)	0.421	(0.875)	0.496	8.3	1.59	1200	1.0
3218	418-2-27	--	--	--	--	--	0.714	0.612	--	0.738	--	11.7	1.60	70	0.5
3219	418-2-28	--	--	--	--	--	1.008	0.942	--	1.030	--	11.8	1.59	1200	0.5
3220	418-2-27*	--	--	--	--	--	3.402	3.205	1.530	3.863	2.188	10.9	1.60	1200	0.5
3221	418-2-25	--	--	--	--	--	0.989	(1.804)	0.949	(1.972)	1.117	7.4	1.59	1200	0.5
3222	418-2-32	--	--	--	--	--	--	--	--	--	--	--	1.60	1200	0.5
3223	418-2-32	--	--	--	--	--	0.791	1.281	0.612	1.544	0.875	7.5	1.60	1200	0.5

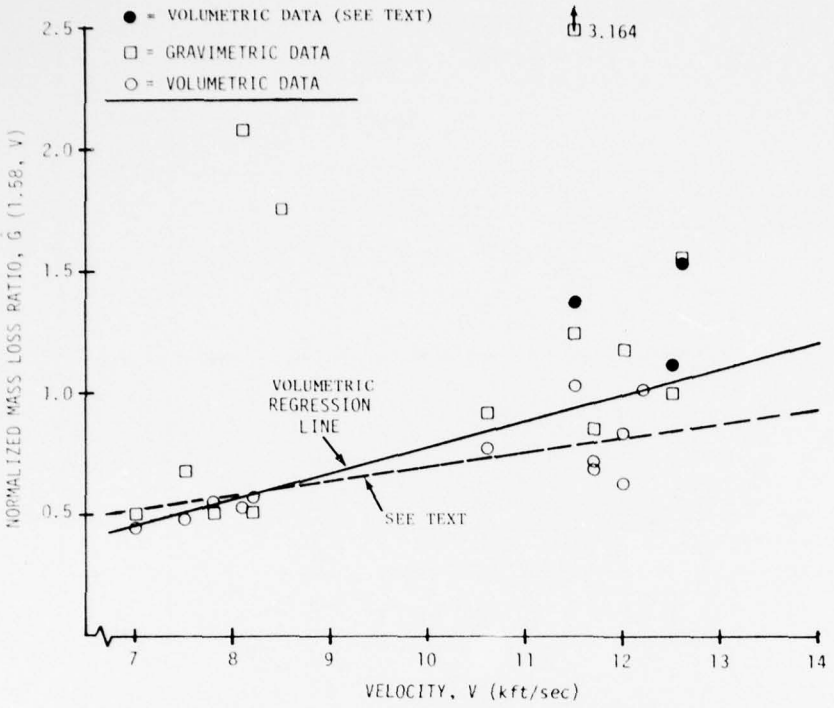

Figure 49. Velocity Dependence of Mass Loss Ratio for ADL-4D6

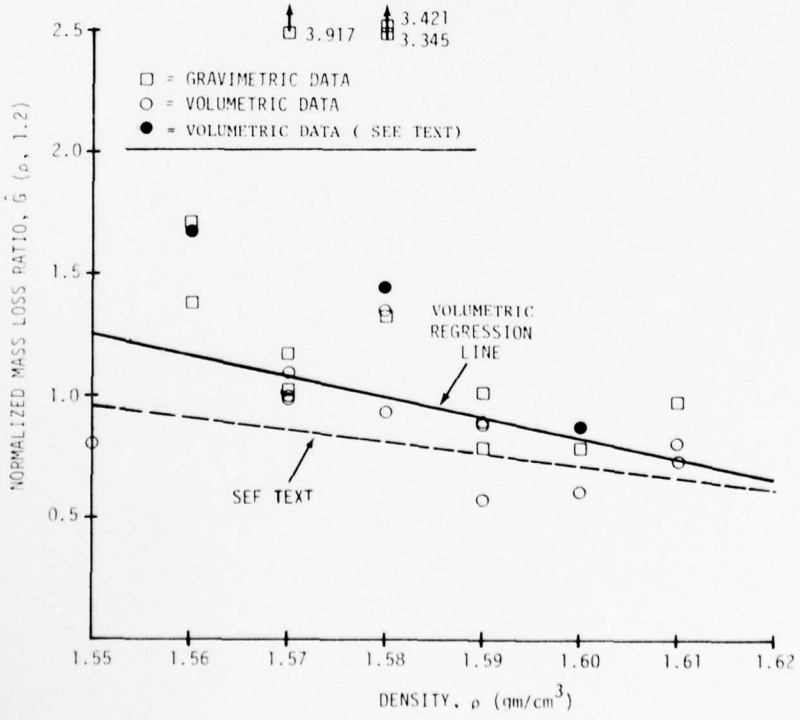

Figure 50. Density Dependence of Mass Loss Ratio for ADL-4D6

The new constants (12) were used with Equation (7) to generate new values for the he velocity dependence and angular dependence. These are represented as dashed lines in Figures 49 and 50, respectively. The plots clearly indicate a significant effect on the regression lines. The average mass loss ratio in the 12 Kft/sec velocity regime is approximately 20 percent lower and the scatter is greatly reduced for the new regression. Similarly, the average mass loss ratio in the low density (1.55 gm/cm^3) regime is reduced by approximately 30 percent with an attendant reduction in data scatter for the new regression. Thus, analysis of the room temperature data without the three points which exhibited cavities adjoining the craters indicates much weaker dependences on both velocity and density than was obtained from analysis including the entire room temperature data base.

To investigate the possibility of particle size dependence, the room temperature values of $\hat{G}(1.58, 12)$ from Table 29 (omitting the suspect data) for 0.5 mm and 1.0 mm particles were examined independently. Mean values and standard deviations were found to be 0.932 ± 0.279 and 0.936 ± 0.114 for the two particle sizes, respectively. Since the mean values differ by much less than the standard deviations, the differences are not considered significant.

The high temperature behavior of the material was also investigated in a series of tests performed at 1200°F. The data from these tests (omitting the two suspect data) are compared with room temperature data in the plot of $\hat{G}(1.58, 12)$ versus T in Figure 51. The mean and standard deviation of the high temperature data is 1.168 ± 0.230 as compared to the room temperature values of 0.923 ± 0.183. In this case the mean value of the mass loss at 1200°F exceeds the mean value of the room temperature by 26.5%, which is larger than the standard deviation of either data set. The difference between the elevated temperature and room temperature response in therefore taken to be significant.

As mentioned previously, the data taken early in the program on plate 423-3 exhibited a strong correlation to the 200 KHz attenuation data. Although a strong dependence of mass loss ratio on stress wave attenuation is to be expected based on the ETI erosion model (Ref. 12), the relationship to ultrasonic attenuation is unknown. Nevertheless, the correlation is sufficiently strong to warrant further investigation. In Figure 52, normalized mass loss is plotted as a function of ultrasonic attenuation, with separate symbols associated with the data obtained by the two different techniques (aluminum buffer blocks and rubber buffer blocks). Two points for which data was taken by both techniques are joined by dashed lines. Note that for these two points, the rubber buffer block technique yielded larger values of attenuation.

The very strong trend for decreased mass loss with increasing attenuation is apparent for the data taken with aluminum buffer blocks (plate 423-3). One notable exception is the

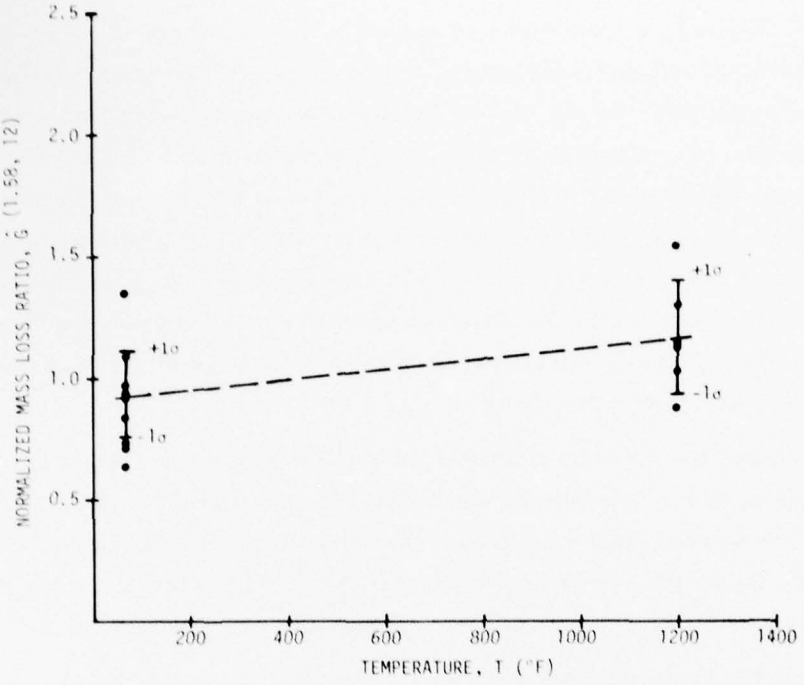

Figure 51. Temperature Dependence of Volumetric Mass Loss Ratio for ADL-4D6

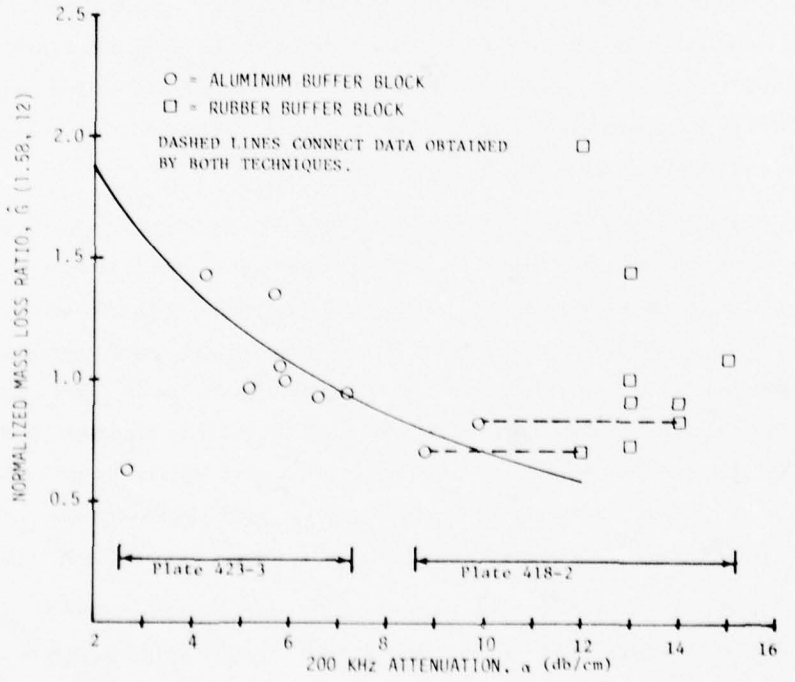

Figure 52. Correlation of Volumetric Mass Loss Ratio with Ultrasonic Attenuation

anomalously low mass loss ratio associated with the 2.7 dB/cm attenuation. With the exception of this one point, this data may be represented by the form

$$\hat{G} = \hat{G}_o e^{-n\alpha} \tag{13}$$

where regression analysis yields the values

$$\begin{aligned} \hat{G}_o &= 2.355 \\ n &= -0.714 \end{aligned} \tag{14}$$

with a correlation coefficient of -0.799. Equation (13) is plotted as a solid curve on Figure 52.

No correlation is evident between mass loss ratio and the attenuation obtained using the rubber buffer block technique (this was performed primarily on specimens from plate 418-2). It is clear that the scatter in the room temperature mass loss ratio for plate 423-3 is strongly related to the variation in attenuation. However, the lack of consistency of techniques used and data obtained on plate 418-2 precludes incorporation of the attenuation as a parameter in the mass loss relationship.

The performance of ADL-4D6 under particle impact may be compared with that of other current antenna window materials by reference to recent SAMSO data (Ref. 13). This data constitutes a fairly comprehensive characterization of velocity and angle dependence of mass loss for AS3DX and HPBN (TS1251)*. The velocity dependence data for these materials, which were obtained at an impact angle of 9 degrees, is adjusted to give the equivalent 10 degrees response for the comparison. Normalized mass loss ratios for the three materials are plotted versus velocity in Figure 53. The curve for ADL-4D6 was generated by means of Equation (7) with the constants of Equation (12) assuming the nominal density of 1.60 gm/cm^3.

Comparison of the curves indicates a somewhat weaker velocity dependence for AS3DX and HPBN than was observed for ADL-4D6. The mass loss ratios for AS3DX and ADL-4D6 are comparable at a velocity of 10.5 Kft/sec. At lower velocities, ADL-4D6 shows the best performance (lowest mass loss ratio). At higher velocities, the ADL-4D6 curve lies slightly above the AS3DX curve but well below the HPBN curve. This behavior is attributed to an observed tendency for removal of fiber bundles adjacent to the crater at the higher velocities. Fiber pullout was observed both in depth at the crater wall, and at the surface of the material, adjacent to the main crater. A significant improvement in particle impact mass loss is expected for the fine-weave version of ADL-4D6 as a result of the reduced size of the matrix pockets and increased confinement of the fiber bundles.

*TS1251 hot pressed boron nitride is an improved chemical purity grade of HPBN developed by Union Carbide for aerospace antenna window applications. It is similar to grade HBC in other properties.

For a more detailed discussion of the particle impact test results, including crater "maps" and raw data, the reader is referred to the classified addendum to this report (Ref. 14).

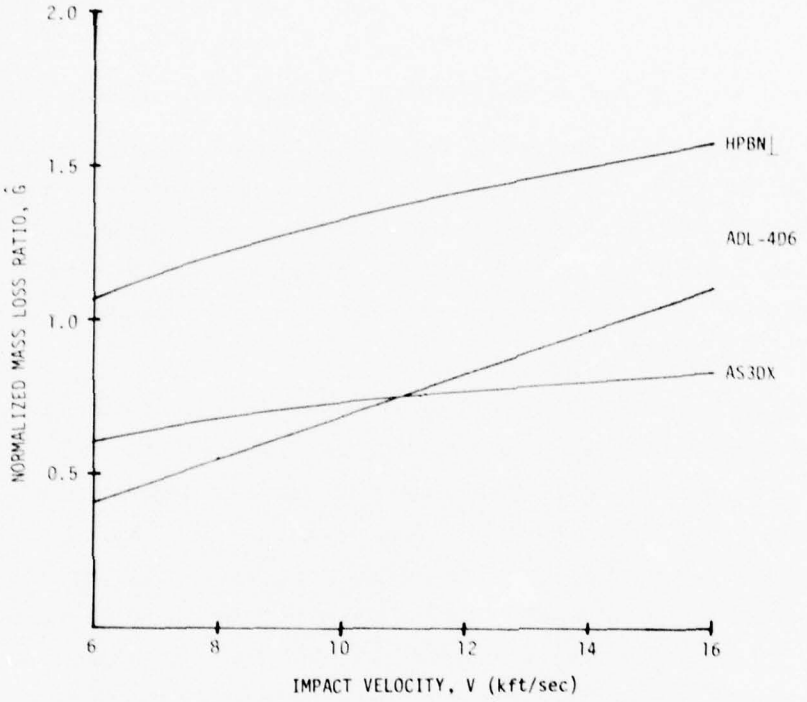

Figure 53. Relative Erosion Performance of Virgin Antenna Window Materials

3.5 DIELECTRIC PROPERTY MEASUREMENTS

Dielectric constant and loss tangent properties of most of the materials developed and fabricated in this program* were measured by W. Westphal at Massachusetts Institute of Technology Laboratory for Insulation Research. L-Band (250 MHz) measurements of dielectric constant and loss tangent had been previously made on AD1-4D6 at GE-RESD; as were X-band (10GHz) transmission and reflection measurements to surface melting conditions under a laser heating environment (Ref. 1, Section 3.5).

To assess the performance of these materials in the millimeter wave region, measurements were planned in the LIR's 24 GHz (12.5 mm, free space) and 90 GHz (3.3 mm, free space) klystron-fixed frequency facilities. Together with additional X-band measurements to verify the RESD data, this data base would span the mm wavelength region, characterizing the materials' performance in the region of the two atmospheric high transmission frequencies of interest.

3.5.1 METHODS OF MEASUREMENT

3.5.1.1 Standing Wave Method

The standing wave method was used at 8.5 GHz and 24 GHz for the room temperature measurements and for some elevated temperature measurements up to 800°C. The measurement is performed in a (TM11 mode) circular wave guide, 1 inch ID for 8.5 GHz and 3/8 inch ID for 24 GHz. The metal sample holder at the end of the waveguide provides an electrical short and causes a high standing wave in the waveguide. With the use of a traveling probe located in a slotted section of the waveguide, measurements of the position and width of the standing wave node are made before and after the sample is inserted into the holder. Most of the samples were of sufficient thickness to be measured in the short circuit position (against the wave guide short). This data was reduced as follows:

Probe position readings are taken at twice minimum power points on either side of the lowest node. The width of the node DS is the difference in the readings, the node position SN is the average. Similar readings are taken with empty holder to obtain DA, AN.

The general mathematical relations in terms of Figure 54 are

$$DX = DS - DA(Y + ns\lambda/2)/(na\lambda/2) \tag{15}$$

$$Y = SN - AN + na\lambda/2 - ns\lambda/2 - D \tag{16}$$

$$X = \sin(\pi DX/LW)/\left[2 - \cos^2(\pi DX/LW)\right] \tag{17}$$

$$ZB/ZB1 = \frac{X - j\tan(2\pi Y/LW)}{1 - j\,X\tan(2\pi Y/LW)} \tag{18}$$

*this includes the monolithic nitride ceramics

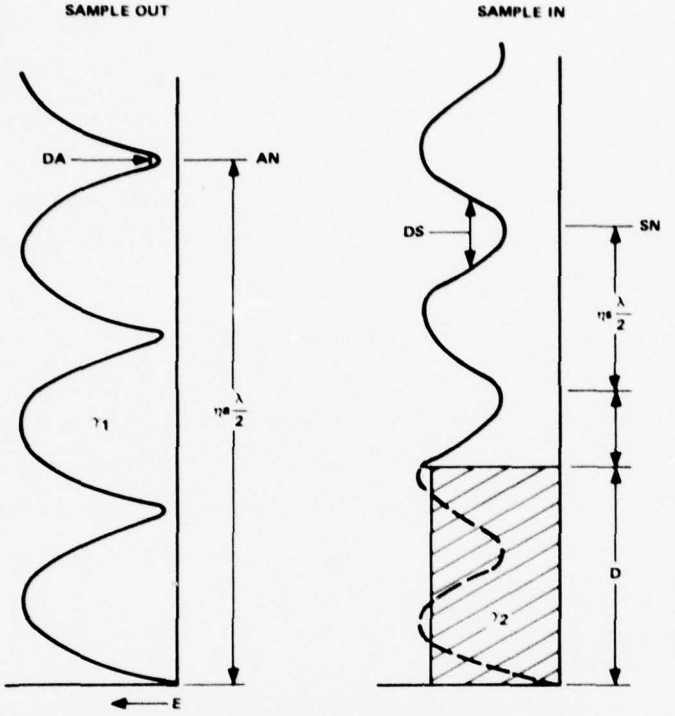

Figure 54. Notation in Standing Wave Measurements

$$\frac{\tanh \gamma_2 d}{\gamma_2 d} = \frac{1}{\gamma_1 d}\frac{ZB}{Z1} \tag{19}$$

Thin samples are placed at the open circuit position in the waveguide to take advantage of the high electric field at this position. The samples are held at this position with a low loss dielectric spacer. The data reduction in this case is somewhat different and is described in Reference 15.

Measurements at elevated temperatures were performed in a heated silver sample holder as shown in Figure 55. The heated sample holder is attached to the bottom of the waveguide used for the room temperature measurements.

$\gamma_2 d$ is determined from charts or tables of tanhX/X or a numerical computer solution. Then

$$K^* = \frac{u - (\frac{LW}{2\pi d} \cdot \gamma_2 d)^2}{1 + u} \tag{20}$$

In the above equations and Figure 54:

Y is the distance of first minimum in standing-wave above sample

DX is the width of the minimum corrected for wall loss between probe and sample

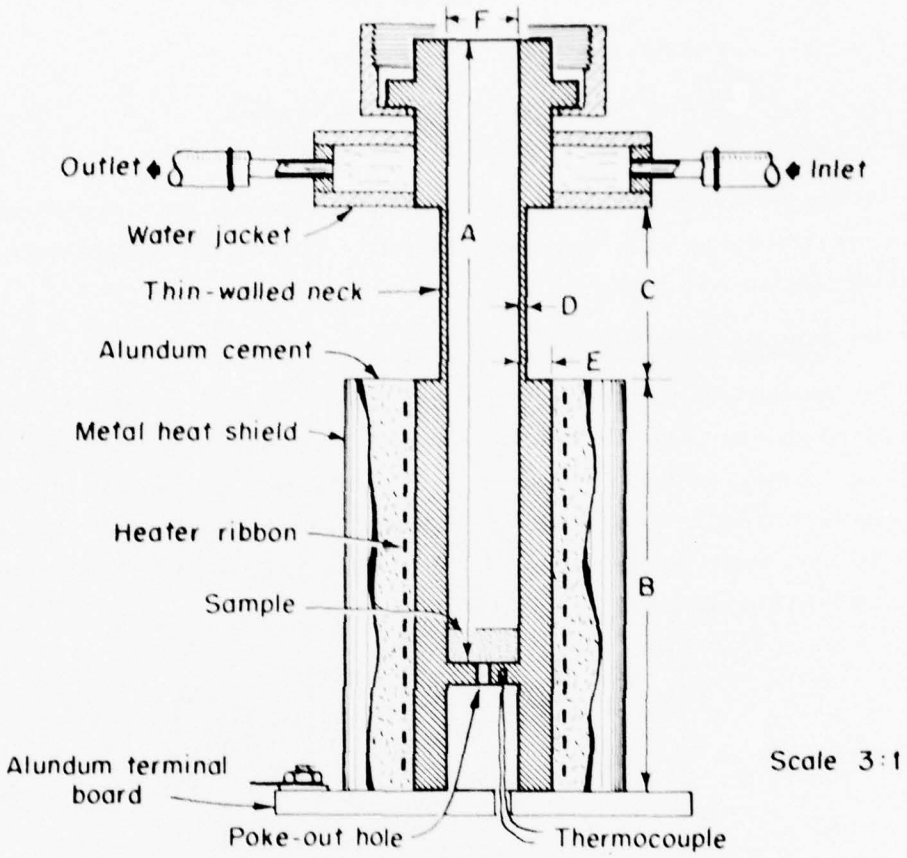

TYPICAL DIMENSIONS ARE AS FOLLOWS:

	Nominal frequency	8.6×10^{9}	1.4×10^{10}	2.4×10^{10}	5×10^{10}
A.	Inside length	15.0 cm	7 cm	5.5 cm	3.1 cm
B.	Length heated	10.0 cm	4.2 cm	3.0 cm	2.4 cm
C.	Length of neck	3.6 cm	2.1 cm	1.0 cm	0.8 cm
D.	Neck thickness	0.030 in.	0.012 in.	0.010 in.	0.008 in.
E.	Wall thickness	1/8 in.	1/8 in.	1/16 in.	1/16 in.
F.	Inside diameter	1.0 in.	5/8 in.	3/8 in.	11/64 in.

Figure 55. Longitudinal Section of Circular, High-Temperature Sample Holders

ZB/Z1 is boundary impedance relative to air-filled waveguide impedance

γ_1 - propagation function for air-filled waveguide

γ_2 - propagation function for sample-filled waveguide

LW - wavelength in air-filled waveguide

u - $(LW/\lambda c)^2$; $\lambda c = 1.706293 \times$ waveguide diameter

K* - complex dielectric constant relative to air

A computer program has been developed which finds the value of K*, then corrects for wall loss in the sample-filled section and corrects the dielectric constant for the air space between sample and waveguide wall.

3.5.1.2 Resonant-Cavity Method

For measurements higher than 800°C at 8.5 GHz and at 24 GHz, a dielectric filled resonant cavity technique was used. The same sample that was used for standing wave measurement was used for this measurement. The resonant cavity measurement setup is shown in Figure 56. The cavity is formed by wrapping platinum foil around the cylindrical sample. Heat and pressure are used to weld the edges of the foil. Small holes in the platinum foil at the center of the axis are used to couple energy in and out of the cavity.

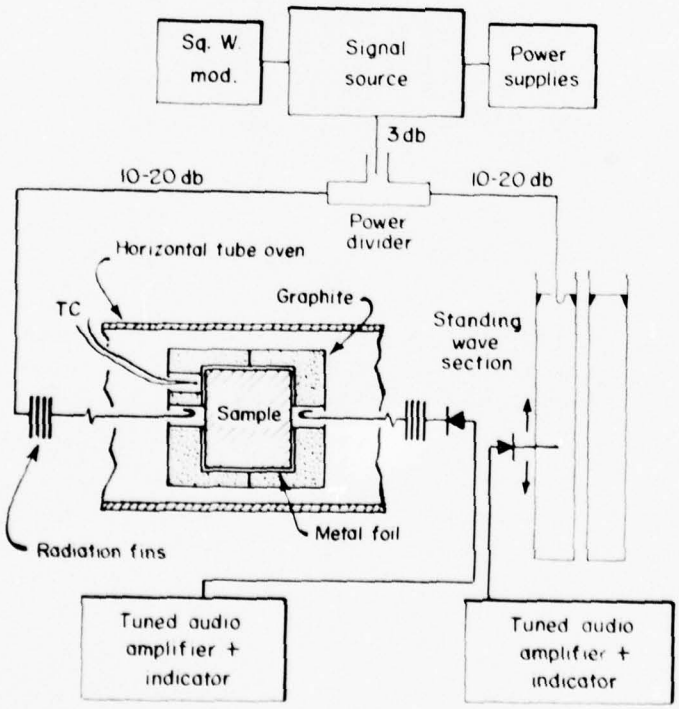

Figure 56. Equipment for Resonant-Cavity Measurements

The dielectric constant and loss tangent are determined from the resonant frequency and Q of the assembled cavity. Since the cavity resonates in many modes, a mode must be selected that is in the range of the source. The frequencies of the various modes are determined from the previously measured room temperature dielectric constant and the sample dimensions. In some cases, the sample length must be shortened to change the resonant frequency into the range of the source. The frequency measurements are obtained with the slotted standing wave line which is used in the standing wave method.

The relationship between the dielectric constant and loss tangent, and the measured parameters are different for each resonant mode. These relationships are adapted from Reference 16.

3.5.1.3 Transmission Bridge (90 GHz)

At 90 GHz, the wavelength is too small for waveguide or cylindrical cavity measurements to be practical. A transmission bridge was used for these measurements (see Figure 57). The sample was positioned in a light pipe waveguide in one arm of the bridge. In the other arm, a calibrated attenuator and phase shifter was used to bring the bridge to balance. The amount of attenuation and phase shift are the measured parameters from which the dielectric constant was calculated. Measurements were repeated with the sample position moved a quarter wavelength in the light pipe in order to average out the effect of the small standing wave in the waveguide.

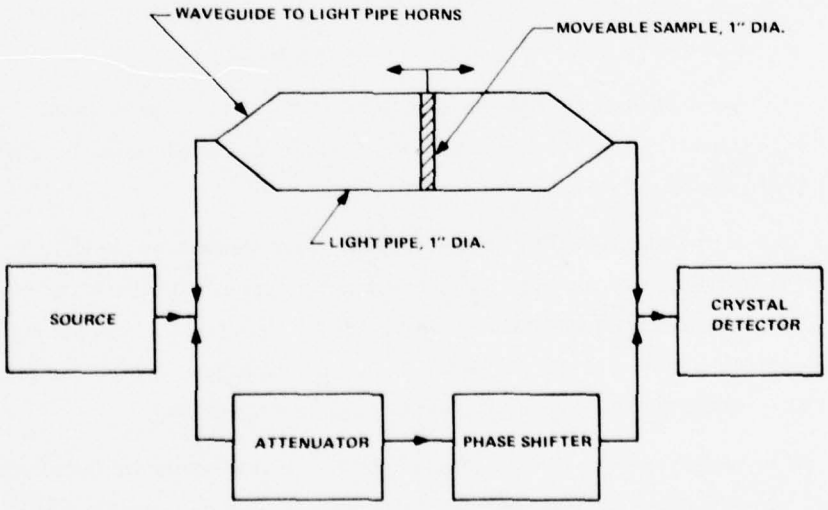

Figure 57. Transmission Bridge for 90 GHz Dielectric Measurement

3.5.2 RESULTS OF MEASUREMENTS

3.5.2.1 X-Band

RF dielectric properties have been measured by W. Westphal of the MIT Laboratory for Insulation Research on two variations of ADL-4D6 at X-band (8.5 GHz). The two variations of the material are the standard 3mm cell ADL-4D6, represented by a specimen taken from plate 418-2 and designated by that number, and a specimen taken from fine weave (2 mm cell), plate 424-1. Both of these plates were densified by the standard ADL-4D6 process developed in Reference 1, but given a new and prospectively improved version of the silane water desensitization treatment described there.* The two specimens had in both cases been exposed to laboratory air and humidity environment for times on the order of several days - more than adequate to insure stabilization of the water absorption effect.

Room temperature (22°C) measurements were made on each of the specimens, yielding the results of Table 30.

TABLE 30. ROOM TEMPERATURE DIELECTRIC DATA ON STANDARD AND FINE WEAVE ADL-4D6 AT 8.5 GHz

Sample No.	Face	K	tan delta
418-2 1.59 gm/cc	1 2	2.832 2.850	.00412 .00408
424-1 1.62 gm/cc	1 2	2.929 2.909	.00572 .00554

The specimens were each measured first with one face at the shorted end of the waveguide (where the electric field is zero) and then switched end for end and rotated 90 degrees. This is the "Face" designation in Table 30 and is a standard test for homogeneity and anisotropy effects, which are of course to be expected in this composite material.

Standard weave specimen 418-2 was then fitted with a silver high temperature holder and its dielectric constant and loss tangent were measured by the standing-wave method. The results are given in Table 31.

This high temperature series of measurements began with the specimen in the as-fabricated condition; i.e., with the silane water "densensitization" intact. The dielectric constant measurements at 22°C in the silver holder are within 0.02 of the values in the unbound condition; while the loss tangent indicated by this second, high temperature method is 0.00492, as compared to 0.00412 and 0.00408 for the unbounded specimen at this temperature.

As the temperature rises above the 106°C point, absorbed water and the silane treatment itself are driven off, and the loss tangent falls below a three zeros value to a minimum of 0.00036 at 387°C, rising to 0.00082 at the 640°C point, near the standard densification process sintering temperature of 650°C.

*cf. Section 2.3.3 of this report for improved silane process description.

TABLE 31. DIELECTRIC CONSTANT AND LOSS TANGENT OF STANDARD WEAVE ADL-4D6 SPECIMEN 418-2 MEASURED BY THE STANDING WAVE METHOD, 22°C, AT 8.5 GHz

T (°C)	K	tan delta
22	2.833	0.00492
74.5	2.843	0.00326
106	2.840	0.00207 ± 0.0002
231	2.826	0.00055
304	2.756	0.00049
387	2.800	0.00036
541	2.798	0.00047
640	2.774	0.00082
67.5	2.785	0.00082

Upon cooling in the high temperature sample holder to 67.5°, this same low value of 0.00082 was measured for the loss tan. This data point can obviously not be taken as representative of the ADL-4D6 material at room temperature, since absorbed atmospheric water vapor would raise tan delta well above 0.01 in a few hours standing open to even the laboratory environment. It does however show the intrinsically low loss properties of the high purity Astroquartz fiber and the purified Ludox colloidal silica matrix material of which the composite is made.

The same ADL-AD6 sample of 418-2 used for the 640°C temperature run with the standing-wave method was reduced in length (2.389 from 2.54 cm) for dielectric filled cavity measurements to 1400°C. No standing-wave measurements were made on the new length; but as a cavity the material appeared to be much more anisotropic for electric fields perpendicular to the axis.

The results of these measurements are given in Table 32.

During the temperature run the lower dielectric constant was followed with occasional measurements in the second mode showing higher dielectric constant. Initial loss decrease was due to loss of inadvertent moisture pickup during the setup. The loss tangents tabulated include coupling loss and other extraneous imperfections from the ideal cavity walls. These are normally evaluated by comparison with room temperature standing-wave measurements. This procedure was not possible here because of moisture sensitivity. The best estimate is obtained by comparing the minimum losses in the present run with the previous run. On this basis .0003 should be subtracted from all tabulated loss values.

TABLE 32. DIELECTRIC CONSTANT AND LOSS TANGENT OF STANDARD WEAVE ADL-4D6 SPECIMEN 418-2 BY CAVITY METHOD TO 1400°C

Mode 1			Mode 2		
T (°C)	K	tan delta	T (°C)	K	tan delta
22	2.656	.00153	22	2.8295	.00196
1 hour			130	2.8284	.00122
22	2.660	.00218	189	2.826	.00086
67.5	2.658	.00202	623	2.832	.00079
83.5	2.657	.00185	731	2.835	.00126
116.6	2.655	.00093	1016	2.860	.00302
123	2.654	.00083			
190	2.650	.00079			
252	2.649	.00061			
300	2.652	.00066			
411	2.663	.00120			
429	2.665	.00086			
503	2.673	.00062			
587	2.684	.00092			
735	2.703	.00120			
790	2.709	.00132			
835	2.714	.0016			
973	2.726	.0028			
1100	2.736	.0032			
1178	2.741	.0036			
1234	2.746	.0040			
1290	2.77	.0045			
1321	2.79	.0048			
1400	2.82	.0057			

NOTE: Measured by the dielectric cavity filled method: specimen heated to 150°C in air furnace, then encapsulated in platinum foil holder for measurement. (Measurement made after previous run to 640°C by standing wave method.)

3.5.2.2 Millimeter Wave 24GHz Dielectric Measurement Results

Two samples of ADL-4D6 material were measured at 24GHz by the standing wave method. It was originally planned to perform these measurements by the resonant cavity method; but the range of variation of the dielectric constant was found to be too large to allow accurate measurements by this technique.

Room temperature measurements were made on the specimens as received, with the improved silane water desensitization process, after standing in laboratory ambient air for a minimum of two days.

The results of these measurements are given below in Table 33.

TABLE 33. ROOM TEMPERATURE (23°C) DIELECTRIC DATA ON STANDARD AND FINEWEAVE ADL-4D6 AT 24 GHz

Sample No.	Bulk Density (gm/cc)	Face	Rotation	K	tan delta
As-Received					
418-2		1	H	2.901	0.0078
(Standard	1.54		L	2.840	0.0088
Weave)		2	H	2.915	0.0078
			L	2.844	0.0105
424-1		1	H	2.932	0.0092
(Fineweave)	1.56		L	2.902	0.0097
		2	H	2.936	0.0092
			L	2.892	0.0103
After Oven Drying to 135°C Overnight					
418-2		1	H	2.867	0.0055
			L	2.838	0.0070
424-1		1	H	2.848	0.0058
			L	2.811	0.0057

The "H" and "L" designations stand for "high" and "low" measured values, as generated by rotation of the composite sample in the waveguide. The "Face" designation refers to measurements with each of the cylinder faces placed against the shorted end of the waveguide, a measure of material uniformity.

After this measurement, the specimens were heated to 135°C overnight to remove water vapor. The dielectric measurements were then promptly repeated. The results are given in the second part of Table 33.

These data show the increased significance of absorbed water at the 24GHz frequency, as compared to the 8.5GHz and 250MHz measurement frequencies where loss tangents of as-received ADL-4D6 did not exceed 0.006.

The dry specimens were then encapsulated in the silver high temperature sample holder and measurements were performed to 800°C. Both samples were oriented in the higher dielectric constant direction.

The results of these measurements are given in Table 34.

The specimens were allowed to cool in the instrument and in each case check measurements were made near room temperature, showing much lower loss tangents after high temperature exposure. Since 800°C is not a high enough temperature to fuse the colloidal silica matrix, although it is known from process studies to cause increased sintering, it is obvious that the effect of a given quantity of absorbed moisture is much more significant in the millimeter wave band than at conventional radar frequencies. Although the loss tangent returns to a relatively low value at room temperature (0.002-0.003) after 800°C tests, the intrinsic loss tangent of the dried composite is still significantly above the comparable value measured at 8.5 GHz, 0.00082.

TABLE 34. *DIELECTRIC CONSTANT AND LOSS TANGENT AT 24 GHz OF ADL-4D6 STANDARD AND FINE WEAVE, BY STANDING WAVE METHOD TO 800°C*

	418-2			424-1	
T°C	K	tan delta	T°C	K	tan delta
24	2.878	.0072	25	2.866	.00816
117	2.878	.0055	149	2.866	.00357
217	2.856	.0039	195	2.862	.00244
271	2.841	.0023	282	2.850	.00110
320	2.833	.0016	358	2.845	.00085
404	2.823	.0018	412	2.840	.00098
496	2.813	.0020	464	2.837	.00152
546	2.809	.0021	532	2.836	.00233
698	2.797	.0022	665	2.846	.0023
750	2.793	.0023	702	2.851	.0021
800	2.790	.0023	733	2.854	.0020
95	2.822	.0020	800	2.86	.0022
			136	2.811	.00259

4. COMPOSITE MICROMECHANICAL ANALYSIS

4. COMPOSITE MICROMECHANICAL ANALYSIS

4.1 INTRODUCTION

The development of improved antenna window materials with sufficient strength and strain to failure for use in advanced antenna window applications is a complex task. These materials utilize complex constituents and processing techniques in order to achieve the desired RF properties as well as sufficient structural properties to provide the structural integrity necessary for the successful application of these materials. During the development of advanced materials of this type, questions generally arise which can be categorized as: What are the potential properties of the given material system, and are the properties being measured for the experimental materials truly representative of the materials' inherent properties? Questions of the above type can be most easily addressed through analytical studies of these and similar material systems.

The engineering services being provided in the current study are directed towards providing an interpretation of the properties being achieved with the current materials and hopefully guidance relative to which constituent failure mechanisms are the most important relative to controlling the final composite properties. Data correlations with properties measured on previously constructed Omniweave materials were utilized to establish an improved set of in situ constituent properties. Since the material properties on current antenna window materials show both differences in tensile and compressive moduli and large strains to failure, an evaluation of the currently utilized testing techniques was made to assess the validity of the measured composite properties.

Increased utilization of three-directionally reinforced materials for thermal protection system applications has resulted in standard specifications for weave type, fiber distribution, and coarseness of the weaves. In the case of an Omniweave material and other 4-D and 5-D weave geometries, a standard method of characterizing these weaves has not been established. The basic material configurations and controlling geometric parameters have been reviewed as relating to the Omniweave material and a recommended approach to specifying the weave orientation, fiber distribution, and coarseness of the woven material has been proposed herein.

4.2 ANALYSIS OF SPECIMEN GEOMETRY AND THICKNESS EFFECTS IN SILICA/SILICA COMPOSITE UNIAXIAL TENSION TESTS

This section is an evaluation of the results shown in Figure 58. (Figure 45, Ref. 1) on the effect of specimen geometry and thickness on the tensile strength of AD1-4D6. The following was summarized about the results shown in Figure 58.

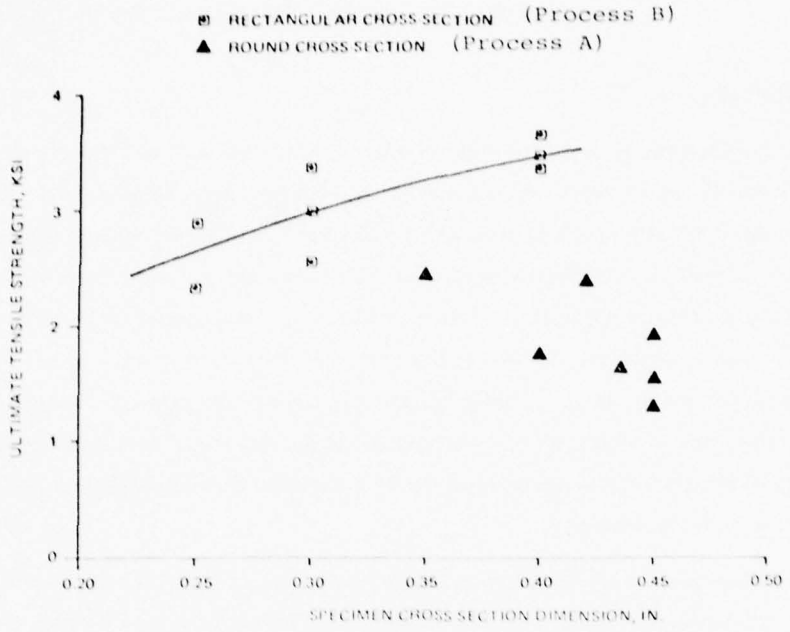

Figure 58. Effect of Uniaxial Tension Specimen Thickness and Type on Measured Ultimate Strength of ADL-4D6

1. The rectangular specimens generally show a higher strength level than the round specimens and the strength increases with thickness.

2. For the round specimens, the opposite behavior is displayed; strength decreases as cross-section increased.

The general conclusions regarding the effects of specimen geometry and thickness upon tensile strength as shown in Figure 58 were attributed to machining techniques; e.g., effects of machining the specimens on fiber continuity. In order to machine a round cross section, a greater number of fibers are cut to shorter lengths, while in a rectangular cross section a larger degree of continuity exists (ineffective fiber length). Thus a reduction in the effective load carrying capability of the specimen could be attributed to cut fibers.

The effect of fiber ineffective lengths on the load carrying capability of both round and rectangular tensile specimens was originally investigated in Section 4.4.3 of Reference 1. The evaluation procedure in Reference 1 consisted of assuming an ineffective region around the specimen edge for both geometries and calculating a ratio of A_{eff}/A_{actual} for each. Results of Reference 1 indicated that the edge effect would be greater for the rectangular specimen*, just the opposite of the reported test results. However, a closer investigation of the

*0.782 effective area versus 0.8711 for the circular section

4.4 MULTI-DIRECTIONAL MATERIAL STRENGTH PREDICTIONS

4.4.1 INTRODUCTION

results of Reference 1 indicated that the (A_{eff}/A_{actual}) ratio for the circular specimen was computed using the diameter of the specimen and not the radius. Therefore, the correct value for A_{eff}/A_{actual} for the circular specimens with an ineffective length of 0.03 inch is $A_{eff}/A_{actual\ (Circ.)} = 0.7511$, as compared to an equivalent rectangular specimen with $A_{eff}/A_{actual\ (Rect.)} = 0.782$. This therefore suggests that the ineffective length has only a slightly larger effect on the circular cross section specimens. However, the differences between the two specimen geometries is very small, thus the test results shown in Figure 58 should be nearly equivalent. A tabulated summary of the data plotted in Figure 58 is shown in Table 35. (Table 24, Ref. 1).

It can be seen in Table 35 that a (A_{eff}/A_{actual}) ratio for each of the test specimens has been calculated assuming an ineffective length of 0.03 inch. Note that the ultimate tensile strengths summarized in Table 36 are based on the actual cross sectional area of the test specimen. Therefore, the ultimate stresses plotted in Figure 58 (and tabulated in Table 35) must be ratioed by the factor $\frac{1}{A_{eff}/A_{actual}}$ in order to compare results on a one-to-one area basis. The results are shown in Figure 59 as a plot of $\bar{\sigma}$ (equivalent strength) versus specimen cross section dimension. As can be seen from Figure 59, the effect of geometry on ultimate strength is apparently still clearly visible.

After further investigation of the results shown in Figure 58, it was determined that two different densification processes were employed, one for the circular specimens and a different process for the rectangular specimens. The circular specimens were densified via process "A" which involved infiltration of the silica Omniweave fabric with colloidal silica after the teflon removal process; while the rectangular specimens were densified via process "B", in which a silane coupling agent was applied to the quartz Omniweave fabric after teflon removal and prior to the first densification cycle. A comparison of the modulus of rupture for each of the above mentioned processes is shown in Figure 60 (Figure 34, Ref. 1). It can be seen from Figure 60 that the moduli of rupture for the process "B" specimens are approximately 1.5 times higher than that obtained for the process "A" specimens. Therefore, it is reasonable to assume that the tensile strength for the process "B" specimens will be of the same order of magnitude greater than the tensile strength of the process "A" specimens. If one reduces the curve through the process "B" data in Figure 59 by a factor of 2/3, it is seen that there are not significant differences between the square and round cross section data. The differences shown in Figure 59 might be contributed to:

1. Differences in the ineffective length (δ) for each of the specimen geometries ($\delta_f \neq \delta_m$).
2. Differences in the percent fiber content in each of the panels. The average fiber volume fraction for the process "A" panels was ~45 percent, while for the process "B" panels an average fiber volume fraction of 45–50 percent was observed.

TABLE 35. TENSILE TEST SPECIMEN COMPARISON

Test Specimen Designation	Type of Specimen	Ultimate Tensile Strength (psi)	A_{eff}/A_{actual} +	$\bar{\sigma}$ ++
Process "A" (No Silane Coupler)				
414A - TA - 1	Round - 0.449	1930	.7505	2571
414B - TA - 1	Round - 0.426	2400	.7381	3251
- TA - 2	Round - 0.349	2460	.6857	3587
- TA - 3	Round - 0.399	1760	.7218	2438
413-1 - TA - 1	Round - 0.45	1570	.7511	2090
- TA - 2	Round - 0.436	1620	.7437	2178
- TA - 3	Round - 0.451	1300	.75162	1730
Process "B" (Silane Coupler)				
413-2 - TA - 1T	Dogbone - 0.30	2570	.720	3569
- TA - 1B	Dogbone - 0.25	2330	.684	3406
415B - TA - 2	Dogbone - 0.40	3660	.782	4680
- TA - 3	Dogbone - 0.40	3370	.782	4310
- TA - 4	Dogbone - 0.40	3480	.782	4092

+Based on an ineffective length of 0.03 inch

++Based on an (A_{eff}/A_{actual}) = .72

TABLE 36. CHARACTERISTICS OF QUARTZ FILAMENTS AND ROVING

Filament Properties

Designation	Astroquartz*	(Brazilian Quartz)
Filament Diameter, in.	3.55×10^{-4}	(Nominal)
Filaments/20-end	4800	(Nominal)
Filament Density, g/cc	2.2	
Young's Modulus, psi	1×10^{7}	
Poisson's Ratio	0.17	
Chemical Analysis SiO_2, %	99.95	
Alkali metals, ppm	15	
Alkaline metals, ppm	26	
Boron, ppm	10	
Aluminum, ppm	100	
Others, ppm	21	

Roving Properties

Designation	552 Astroquartz*
End Count	20
Yards/lb	750
Breaking Strength, lb	25

*Designation of J. P. Stevens & Company, Inc.

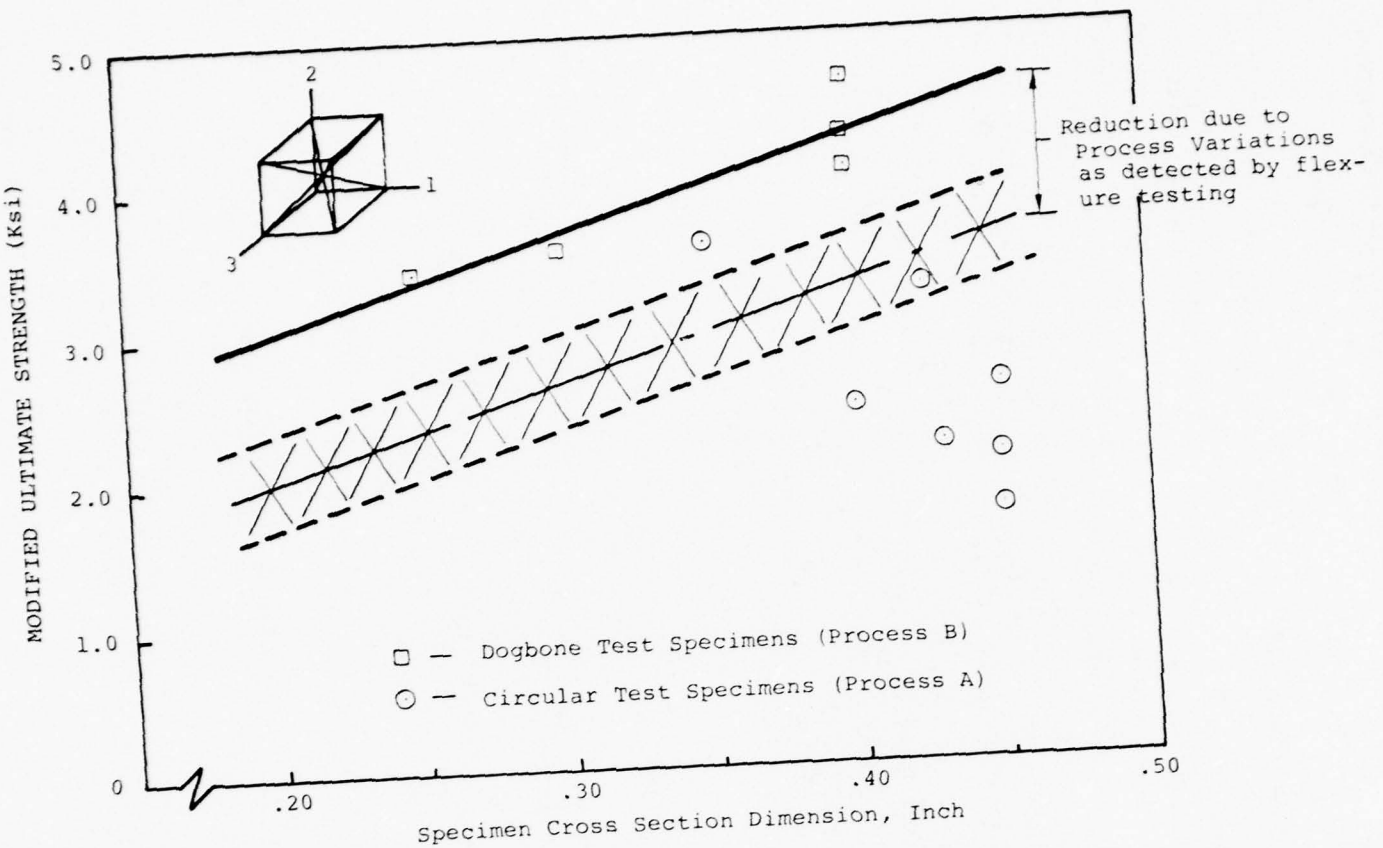

Figure 59. Effect of Uniaxial Tension Specimen Thickness and Type on Ultimate Strength (Modified) of ADL-4D6

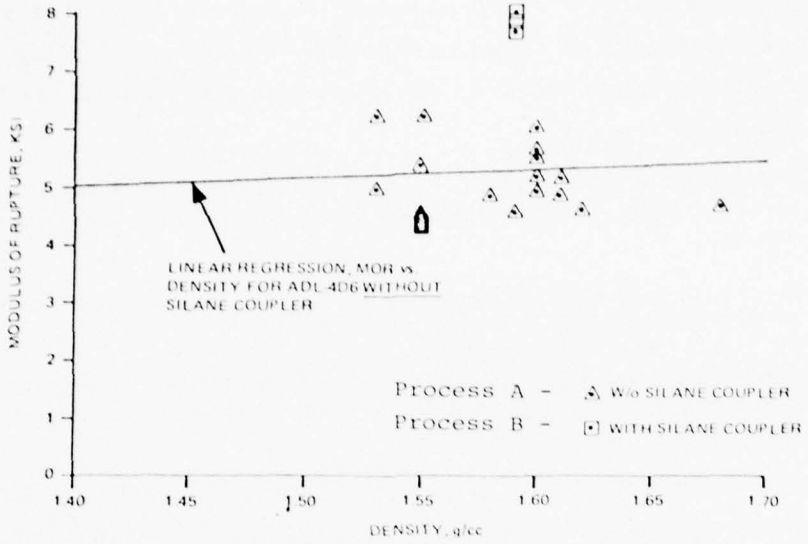

Figure 60. Results of Flexural Screening Tests to Determine the Effect of Silane Coupler on the Strength of ADL-4D6

It should also be pointed out that Figure 58 contains tensile strength data for bias test specimens. Typical differences in axial and bias direction modulus measurements should show approximately a 10 percent increase in bias direction modulus over axial modulus. A similar comparison of measured differences in strengths for these two directions is more difficult to compute, but it is estimated that the bias direction strength should be on the order of 15-20 percent higher than the axial strength, Reference 17. These points were not included in the results shown in Figure 59.

In conclusion, it may be stated that the previously unresolved effect of tensile specimen geometry (circular versus rectangular) on the measured tensile strength of this material has been shown to be of secondary importance in comparison to the primary effect of materials processing parameters and scatter in the data for these.

The rectangular tensile specimen does show an increase in indicated strength up to the 0.40 inch thickness dimension used, so this is certainly a minimum thickness to plan on using for additional ADL-4D6 uniaxial tensile testing.

The thickness effect on the measured tensile strength of the round specimens remains unresolved and complicated by the process difference between the sets of specimens used in Reference 1. Should use of this geometry be again desired (for high temperature tensile testing), this geometry effect will have to be resolved by comparison testing of a standard process lot of material.

4.3 CORRELATION OF ADL-4D6 MATERIAL PROPERTIES

Analytical correlation of predicted composite properties for ADL-4D6 using the MSC-XCAP computer program with that of actual test data obtained from References 1 and 17 has been made. Analytical correlation of predicted composite properties with test data can serve several purposes:

1. Provide a check on constituent properties or alternately, provide a mechanism for defining a set of constituent properties from composite test data through data correlation.

2. Serve as a check case for determining the accuracy of the analytical predictions for various weave configurations.

3. Data enhancement. After correlation is achieved with a limited number of test points, the analytical model can be utilized to predict a complete set of composite properties in all directions.

The silica matrix employed in the ADL-4D6 material cannot be produced in bulk form using the same process used in the densification of the weaves. Even if it could be made in bulk form, one could not be assured that the bulk matrix would be representative of the matrix which is present in the densified weaves. Therefore, the intent of this analysis was to define a reasonable set of constituent properties for the matrix material. Fiber properties for the quartz fibers used in ADL-4D6 are summarized in Table 36.

Weave characteristics for the ADL-4D6 material tested in Reference 1 are shown in Table Table 37. Data correlations presented in this section were limited to test results obtained from test specimens cut from panels 413-2 and 515B (R.T. only). Results of these tests have been included for reference purposes, and are summarized in Table 38. Because of the discrepancy between the flexure and extensional moduli, analytical correlation is limited to the tensile test results shown in Table 38. A complete explanation of these differences is provided in a subsequent section.

Referring to Table 37 on ADL-4D6 panel characterization, it should be pointed out that the surface through the thickness projected fiber angles (STTA) required in modeling the material were not available. Location of the failed specimens for the purpose of measuring the through the thickness angle (STTA) turned out fruitless. Surface through the thickness angles for a limited number of specimens tested under the current contract were available and are shown summarized in Tables 7 and 9. Typical surface through the thickness angles of 24-30 degrees were seen. A lower limit of 25 degrees for the through-the-thickness angle (STTA) was assumed in the subsequent material property parametrics. It should be pointed out that the surface through the thickness angles summarized in Tables 7 and 9 were used solely to provide a realistic bound for the subsequent parametric studies.

Results of the parametric studies for the ADL-4D6 material configuration are shown in Figures 68 thru 72. When available, composite test data for ADL-4D6

TABLE 37. ADL-4D6 PANEL CHARACTERIZATION
(PANELS DENSIFIED VIA PROCESS "B")

	Panel Number				
	413-2	415-A	415-B	416	418
Omniweave Fabric Number	413	415	415	416	418
Fabric Density (gm/cc)	1.23	1.12	1.07	1.03	1.07
Fiber Pitch Angle (SFPA)	47°	50°	50°	50°	50°
LUDOX AS Type	"low sodium"				
Panel Bulk Density (gm/cc)	1.60	1.56	1.54	1.46*	1.54
Fiber Volume %	56	51	49	47	49
Porosity %	27	29	30	34	30

*This smaller fabric was processed with the selvage edge intact to avoid unstitching of the weave when cut. This is reflected in a lower measured fabric and panel density.

TABLE 38. UNIAXIAL TENSILE TEST RESULTS*

Test Specimen Designation	Test Temp. (F°)	Type of Specimen Dimension (in.)	Ultimate Tensile Strength (psi)	Elastic Modulus (10^6 psi)	Failure Strain (%)	Poisson"s Ratio
413-2 -TA-1T	R.T.	Dogbone-0.30	2570	1.46	0.84	-
-TA-1B	R.T.	Dogbone-0.25	2330	1.51	0.58	-
-TB-1T	R.T.	Dogbone-0.30	3000	1.84	0.29	-
-TB-2B	R.T.	Dogbone-0.25	2900	1.56	0.22	-
-TB-4T	R.T.	Dogbone-0.30	3380	2.11	0.31	-
415B -TA-2	R.T.	Dogbone-0.40	3660	1.45	<0.81	0.43
-TA-3	R.T.	Dogbone-0.40	3370	1.25	0.76	0.33
-TA-4	R.T.	Dogbone-0.40	3480	1.39	0.63	0.36

*Specimens fabricated by process B (Silane Coupler)

Correlation of predicted composite properties with available test data (Ref. 1) includes the effect of variation of the matrix modulus as well as the surface through the thickness fiber angle on resulting composite properties.

It should be noted that the matrix was assumed to be isotropic and have a Poisson's ratio of 0.30. The results are shown in Figure 61 (Ref. 1). It can be seen in Figure 61 that the effect of varying the surface through the thickness fiber angle has only a minor effect on the composite property in the axial direction (1-direction). Whereas, a much larger effect is seen in the transverse direction (3-direction). Furthermore, it can be seen that a matrix modulus in the range of 1.85 to 2.0 msi is required in order to obtain a composite modulus of 1.41 msi in the 1-direction as obtained by test. The corresponding range of predicted composite transverse properties (E3) is shown to be between 1.44 and 1.85 msi. However, no transverse tests were available for comparison. Bias direction tests were performed, however, with test results shown in Table 38. In order to compare predicted composite properties in the bias direction with test data, a rotation of the 1-axis into the bias direction (about the 2-axis) is required. Results of this rotation on composite properties are shown in Figure 61 for the case in which SPPA=STTA = 50 degrees. It can be seen that the predicted bias modulus compares reasonably well with test data. Thus, the following set of constituent properties for the silica matrix as obtained from the above correlation will be used in subsequent analyses: $E_m \cong 1.85 - 2.0$ msi; $\nu_m = 0.3$.

An attempt to compare predicted composite properties with that of flexural data for the weave configuration characterized in Table 39 (Ref. 17) was made. Once again it can be seen from Table 39 that the surface through the thickness fiber angles for each specimen were not available. Therefore, the same approach was taken as for the previous weave (Figure 61) in which the STTA was allowed to vary over a specific range. Constituent properties used in the analyses consist of the fiber properties summarized in Table 35 along with the matrix properties summarized above.

For reference purposes the results of the flexural tests have been included, see Table 40. Analytical prediction of the composite properties as a function of surface through the thickness fiber angle are shown in Figure 62. Observe that a surface through the thickness fiber angle of ~25 degrees is required to compare the predicted extensional modulus with that of the flex modulus shown in Table 40 (Ref. 17). It can be seen from Figure 62 that correlation of the flexure data with the transverse extensional modulus is very poor. This lack of correlation in the transverse direction can be attributed to the fact that flexure data for this material is not representative of the extensional moduli. A detailed discussion of the differences between flex and tensile tests can be found in Section 4.6.

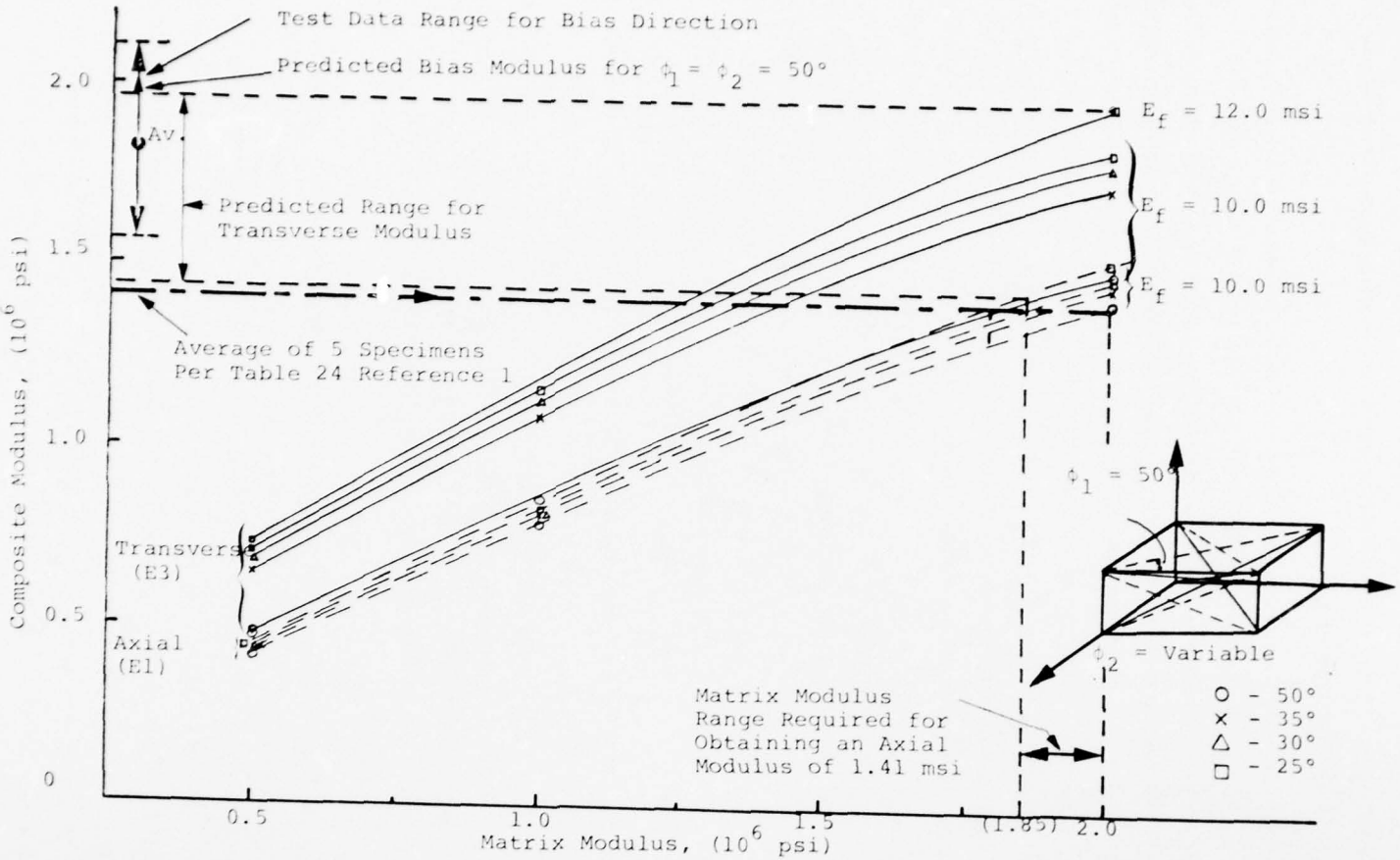

Figure 61 ADL-4D6 Material Property Comparison

TABLE 39. REFLECTIVE HEAT SHIELD PANEL CHARACTERIZATION

	Panel Identification: 421-1	422-1	422-2
Omniweave Fabric Number	421	422	422
Fabric Section Density (gm/cc)	0.94	1.00	1.00
Purified Colloidal Silica Type & Batch	Ultra Low Sodium LUDOX AS (Batch 1,2)	(Batch 1,2)	Nalcoag 2326 (Batch 1)
Number of Infiltration Cycles	22	18	25
Panel Dimensions (ins)	(4.5 x 6.9 x 1.2)	(4.5 x 6.1 x 0.8)	(5.3 x 6.8 x 0.9)
Panel Bulk Density (gm/cc)	1.60	1.64	1.51
Fiber Volume %	43	45	45
Porosity	27	25	31
Fiber Axial Angle	32 1/2°	37 1/2°	42 1/2°

TABLE 40. IMPROVED PURITY STANDARD WEAVE ADL-4D6 MOR MEASUREMENTS AT ROOM TEMPERATURE, PLATE 421-1

	Specimen Designation	SFPA (degrees)	Specimen Density (g/cc)	Thickness[1] (mc, inches)	Modulus of Rupture MN/M^2 (psi)	Elastic Modulus GN/M^2 (10^6 psi)	Failure[2] Strain (%)	Remarks
Axial Direction (panel nominal SFPA = 32.5°)	FA-1	30	1.397	1.021 (.402)	31.17 (4520)	13.35 (1.94)	0.55	
	FA-2	34	1.361	1.019 (.401)	26.13 (3790)	13.45 (1.95)	0.41	Obvious defects in samples (open voids), see density; this data not included in computed mean
	FA-3	34	1.576	1.016 (.400)	31.65 (4590)	17.79 (2.58)	0.45	
	FA-4	34	1.580	1.019 (.401)	34.13 (4950)	15.79 (2.29)	0.41	
	FA-5	34	1.570	1.016 (.400)	32.41 (4700)	18.00 (2.61)	0.61	
	FA-6	34	1.529	1.016 (.400)	36.72 (5180)	14.83 (2.16)	0.70	
	FA-7	32	1.583	1.016 (.400)	36.96 (5360)	16.69 (2.42)	0.64	
	FA-8	31	1.580	1.016 (.400)	37.23 (5400)	16.48 (2.39)	0.60	
	Mean (3-8)	33	1.561		34.68 (5030)	16.62 (2.41)	0.57	
	S.D.	--	0.025		2.34 (340)	1.17 (0.17)	0.11	
Transverse Direction (panel nominal SFPA = 57.5°)	FT-1	58	1.573	1.021 (.402)	15.11 (2192)	6.62 (0.96)	1.40	
	FT-2	57	1.487	1.019 (.401)	17.22 (2498)	5.72 (0.83)	1.40	
	FT-3		1.573	1.019 (.401)	16.75 (2430)	7.03 (1.02)	1.50	Open voids in one end 40% of length
	FT-4		1.553	1.026 (.404)	21.06 (3058)	9.58 (1.39)	1.50	
	FT-5	58	1.553	1.024 (.403)	17.02 (2469)	6.55 (0.95)	1.50	
	FT-6	57	1.553	1.024 (.403)	15.74 (2283)	7.17 (1.04)	1.50	
	Mean	57.5	1.549	-	17.17 (2490)	7.10 (1.03)	1.50	
	S.D.	-	0.032	-	2.36 (342)	1.52 (0.22)	-	

Notes: 1. All specimens 3.81 cm (1.50 inches) long, 1.27 cm (0.50 inches) wide and 1.016 cm (0.40 inches) thick unless noted. Tested in 3-point flexure.

2. Strain measured by means of strain gages applied on the tensile surface. In those samples with the strain labeled, the strain to failure was beyond the gage range.

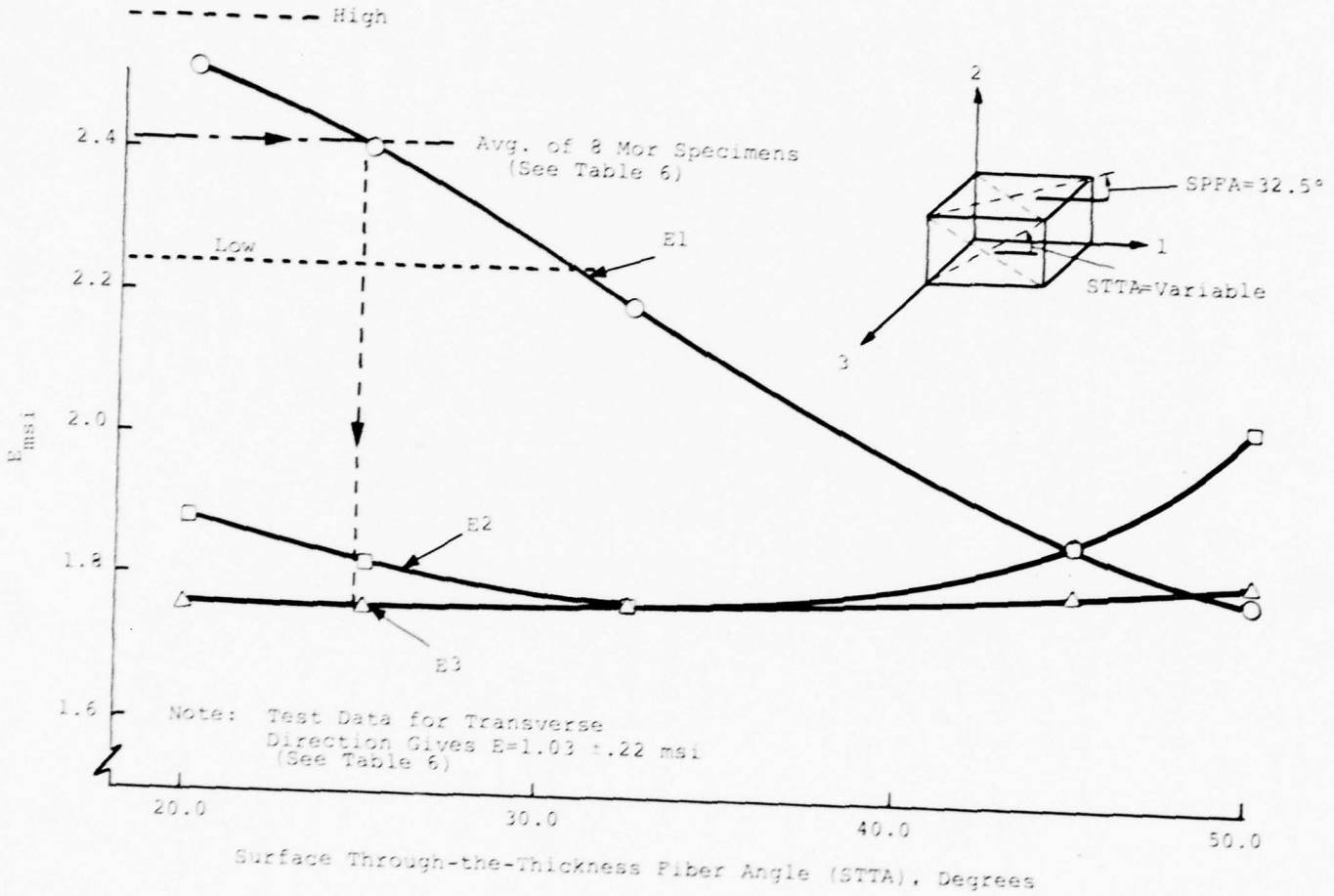

Figure 62. Modulus Versus Surface Through the Thickness Fiber Angle (STTA) for a 4-D ADL-4D6 Omniweave

*0.782 effective area versus 0.8711 for the circular section

4.4 MULTI-DIRECTIONAL MATERIAL STRENGTH PREDICTIONS

4.4.1 INTRODUCTION: 4-D FAILURE MECHANISMS; FINDINGS OF A STUDY ON 4-D GRAPHITE/EPOXY

The following section discusses the governing failure mechanisms for a 4-D Omniweave material and how the composite strength can be increased by improving specific material properties.

A recent study (Reference 18) showed that the governing initial failure modes for a 4-D Omniweave material consist of either transverse tensile failure of the fiber bundles or shear failure of the fiber bundles, depending on the direction of the applied load as well as the projected fiber angle of the body diagonals.

Typical plots of strength versus projected angle for a 4-D T-300/5208* Omniweave material as obtained in Reference 18 are shown in Figures 63 thru 66. Projected fiber angles of 20, 45 and 75 degrees are shown in Figure 67. It should be noted that the projected fiber angle for the 2-3 face is held at 45 degrees so that the surface fiber projected angle (SFPA) on the 1-3 face is equal to the fiber projected angle on the 1-2 face (see Figure 67). The point at which the failure mode changes is very important from the standpoint of understanding the effects improved strengths might have on the resulting composite strengths in the various directions. Take for example the three cases illustrated in Figure 64. It can be seen that the only way of increasing the composite strength for case "A" (1)† would be by increasing the transverse tensile fiber bundle strength up to the point at which the shear strength governs failure (2). Any additional increase in transverse tensile fiber bundle strength without a corresponding increase of shear strength would be worthless from the standpoint of increasing the composite strength in this particular direction. However, strength improvements in other directions may be seen depending on the governing failure mode for that direction. For case "B" (Figure 64), the only way of increasing the composite strength would be by improving both the transverse tensile strength as well as the shear strength of the fiber bundle. For case "C" (4), increasing the shear strength of the fiber bundle will result in a corresponding increase in composite strength up to the point at which the transverse tensile strength of the fiber bundle governs failure (5). Thus, knowing just the failure mode and strength of a weave in a particular direction are not enough when one is investigating which constituent property improvements are required in order to increase the strength of the composite material in a particular direction.

Strength parametrics of the type shown in Figures 63 thru 66 for a 4-D T-300/5208 Omniweave material can be employed for describing the failure modes (initial damage) of X-D

*Epoxy matrix
†Numbers in circles refer to Figure 63.

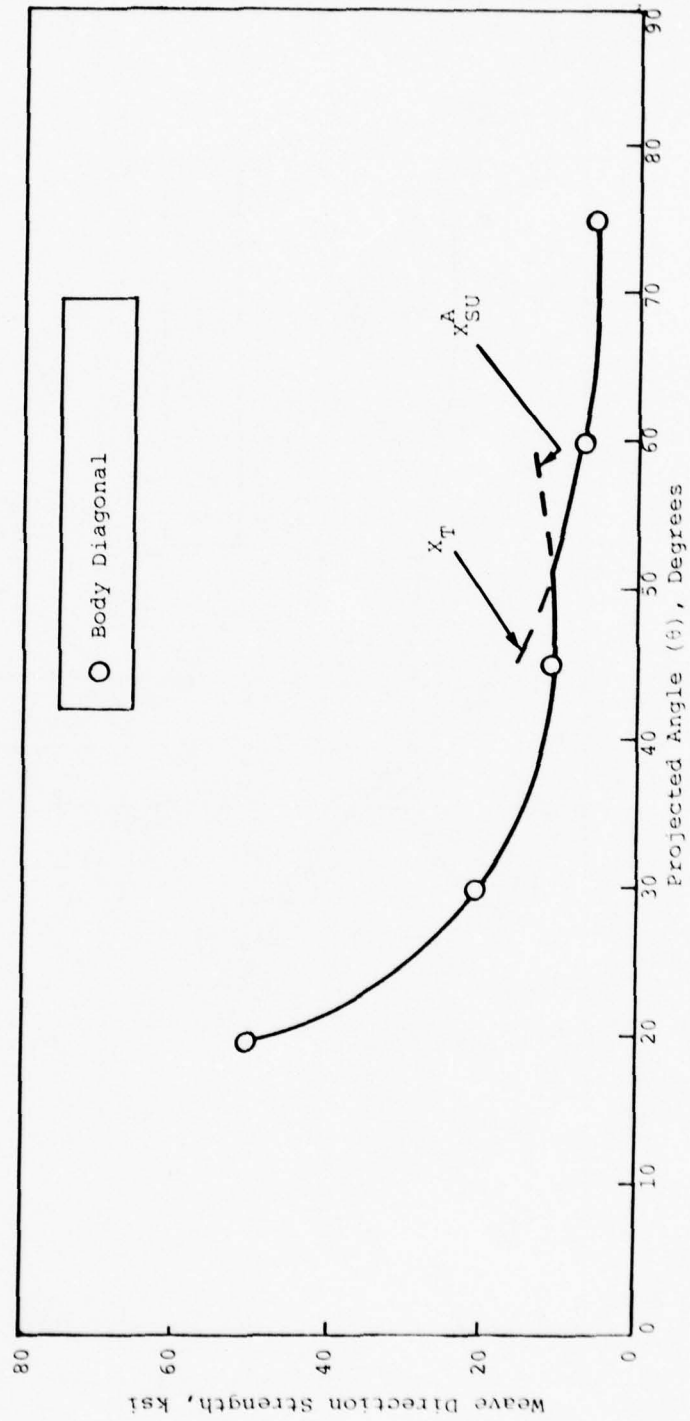

Figure 63. Tensile Strength Versus Projected Angle for a 4-D T-300/5208 Material; FVF = 0.4

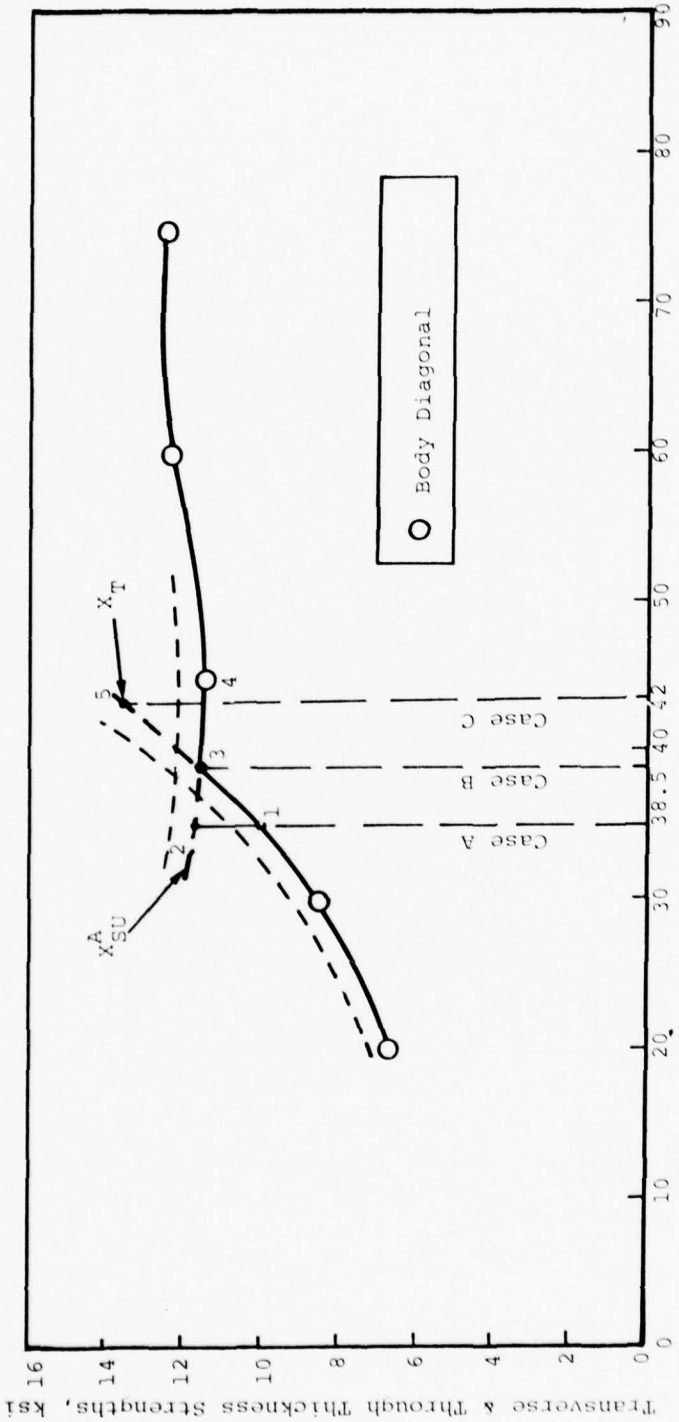

Figure 64. Tensile Strength Versus Projected Angle for a 4-D T-300/5208 Material: FVF = 0.4

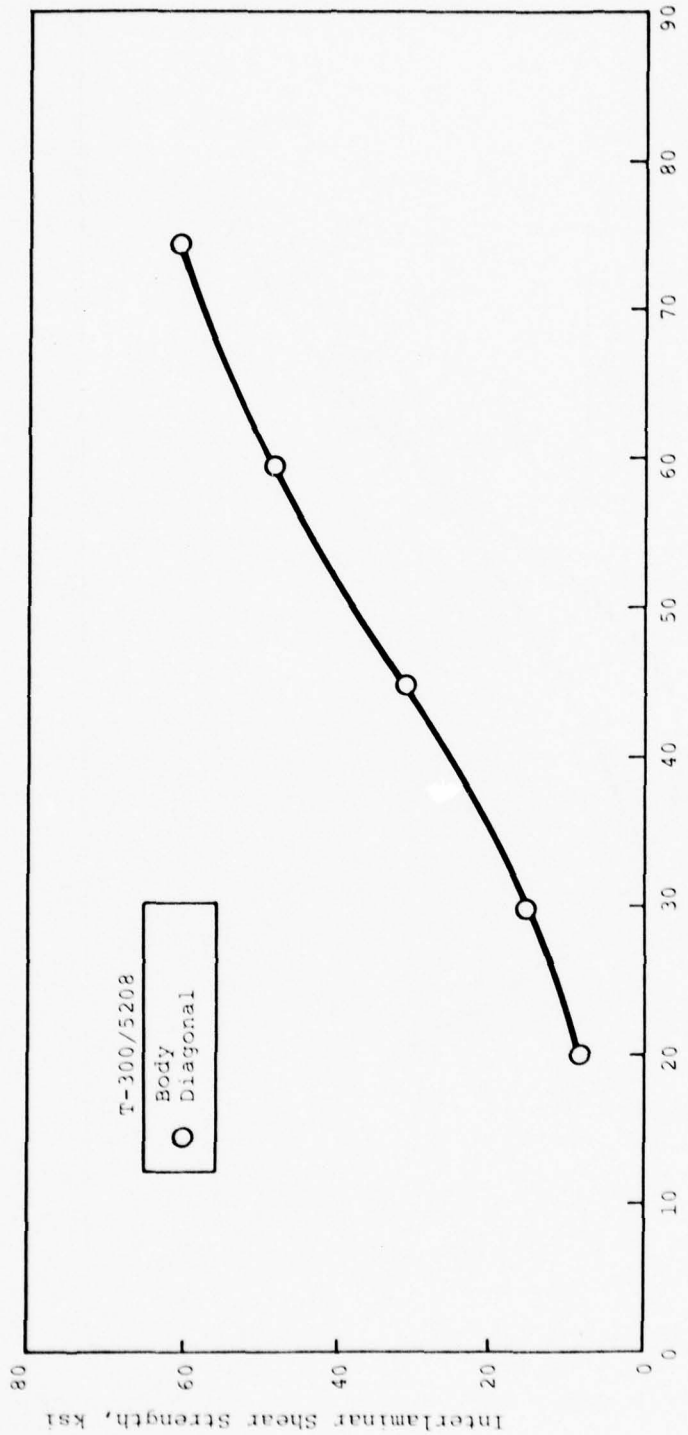

Figure 65. Shear Strength Versus Projected Angle for a 4-D T-300/5208 Material; FVF = 0.4

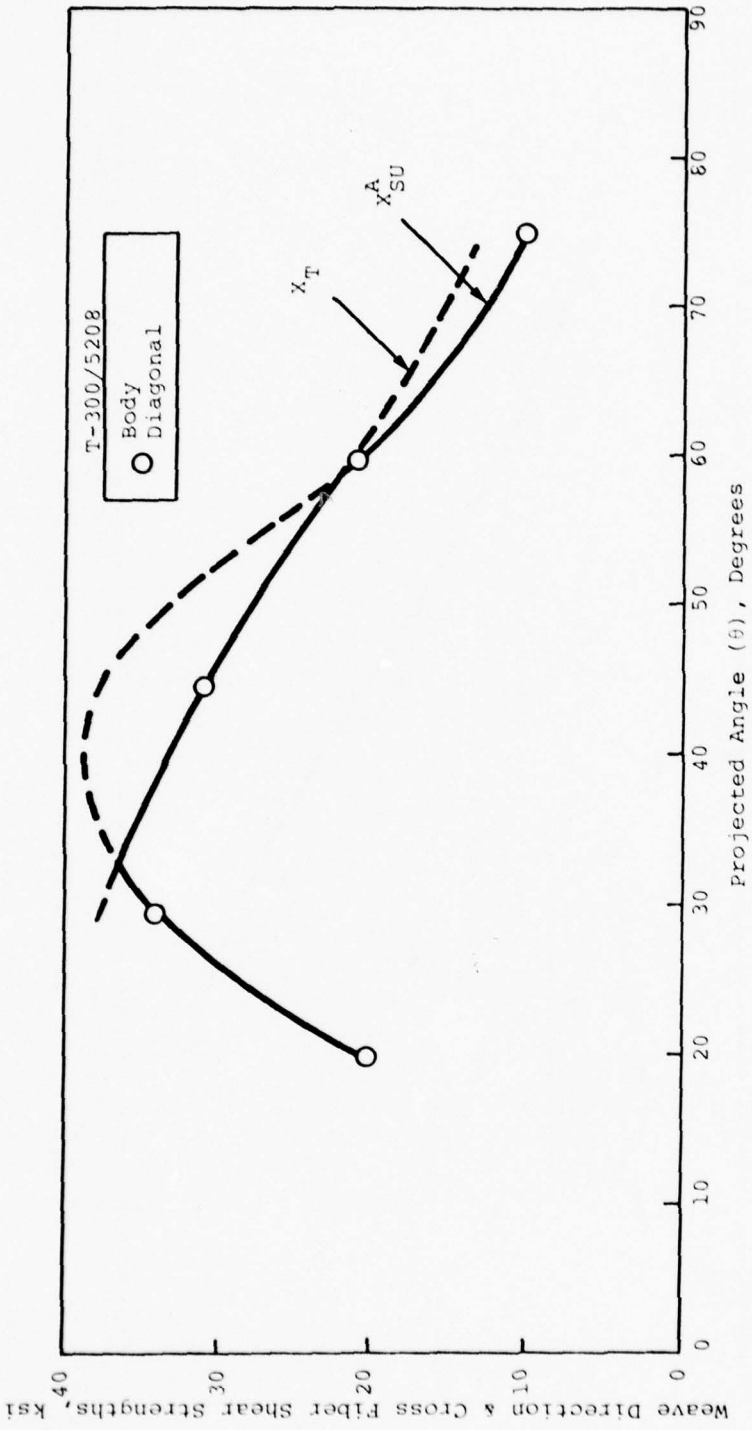

Figure 66. Shear Strength Versus Projected Angle for a 4-D T-300/5208 Material; FVF = 0.4

lot of material.

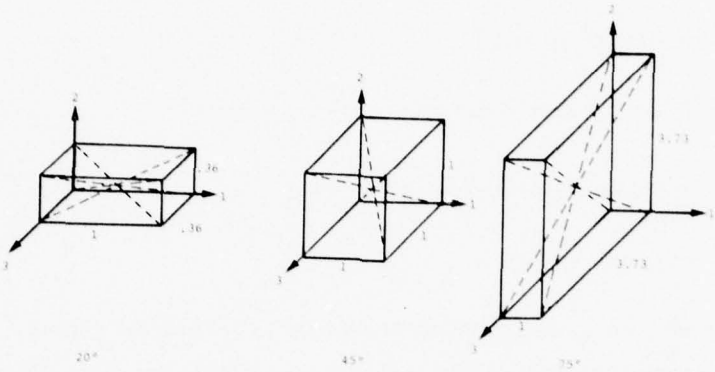

Figure 67. Unit Cell Bundles for Different Projected Angles

materials in general. Additionally, the strength parametrics can be used to bound the constituent properties when sufficient test data is available on the particular weave configuration in various directions. The following section on "ADL-4D6 Strength Parametrics" describes this procedure.

4.4.2 ADL-4D6 STRENGTH PARAMETRICS

Strength predictions for the ADL-4D6 material system analyzed in this study takes the form of parametric studies in which both the transverse tensile and shear strengths of the fiber bundle were varied over a specific range.

Parametric studies of the type presented herein can be employed to:

1. Identify critical constituent properties which affect composite properties in various directions.

2. Bound constituent strength properties given composite test data in various directions.

Note that the procedures discussed in this section can be employed for any X-D material in general. Discussion of strength predictions for the ADL-4D6 material will be limited to that of bounding the constituent properties given composite test data.

Two versions of ADL-4D6 were examined. The first weave analyzed was that of the 4-D silica-silica Omniweave used for data correlation in the previous section (see Table 38).

Results of the parametric studies for the ADL-4D6 material configuration are shown in Figures 68 thru 72. When available, composite test data for ADL-4D6 has been included in their respective figures (e.g., Figures 69, 70, and 72). It can be seen in Figure 69 that the minimum constituent properties necessary for predicting the composite strength obtained from tests are as follows:

$\sigma_{22} \approx 3.1$ ksi (Test Data)†

$\sigma^{su}_{F.B.} \cong 1.7\text{-}1.75$ ksi (Predicted)

$\sigma^{t}_{F.B.} \cong 2.75\text{-}2.8$ ksi (Predicted)

$\sigma_{m} \approx 0.7$ ksi (Predicted)

Note that, for now, the above strengths are referred to as being the minimum constituent strengths, because the mode of failure of the test specimen is unknown. Therefore, additional test data in the other directions must be employed to bound the constituent properties and thus identify the governing failure mode for each loading condition. Minimum constituent properties required to obtain the shear strength observed from tests (see Figure 70) are summarized below:

$\sigma_{13} \approx 3.65$ ksi (Test Data)

$\sigma^{su}_{F.B.} \cong 1.45$ ksi (Predicted)

$\sigma^{t}_{F.B.} \cong 2.2\text{-}2.4$ ksi (Predicted)

$\sigma_{m} \cong 0.45$ ksi (Predicted)

Mimimum constituent strengths required in the bias direction (see Figure 72) are as follows:

$\sigma_{bias} \cong 3.2$ ksi (Test Data)

$\sigma^{su}_{F.B.} \simeq 1.5$ ksi (Predicted)

$\sigma^{t}_{F.B.} \simeq 2.75$ ksi (Predicted)

$\sigma_{m} \simeq 0.45$ ksi (Predicted)

Examination of the minimum constituent strengths required for the three directions show the following relative to the failure mode and constituent properties:

†Note that the weave direction corresponds to the 2-2 direction

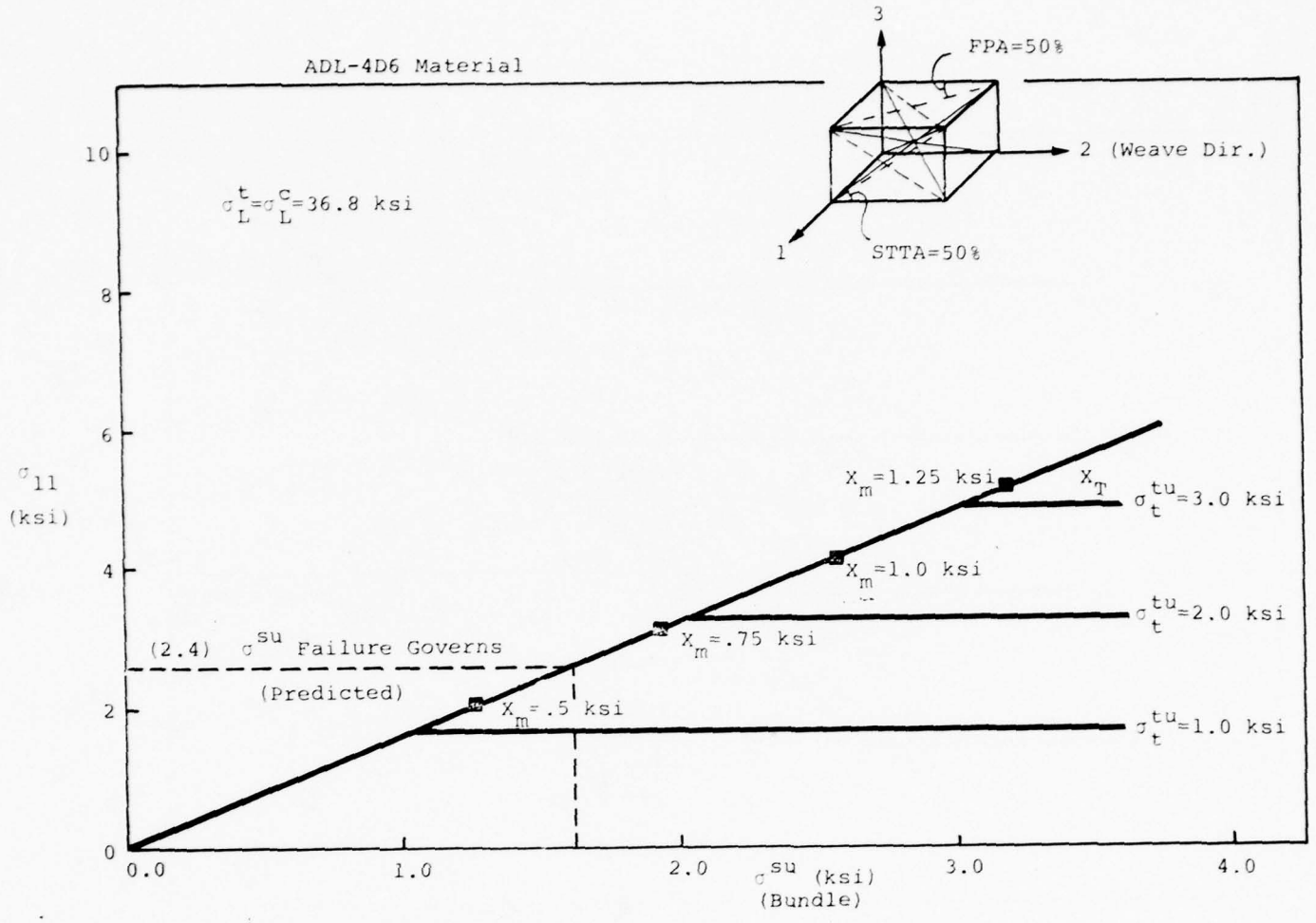

Figure 68. Predicted Strength Parametrics for ADL-4D6 in the 1-Direction (Transverse Direction)

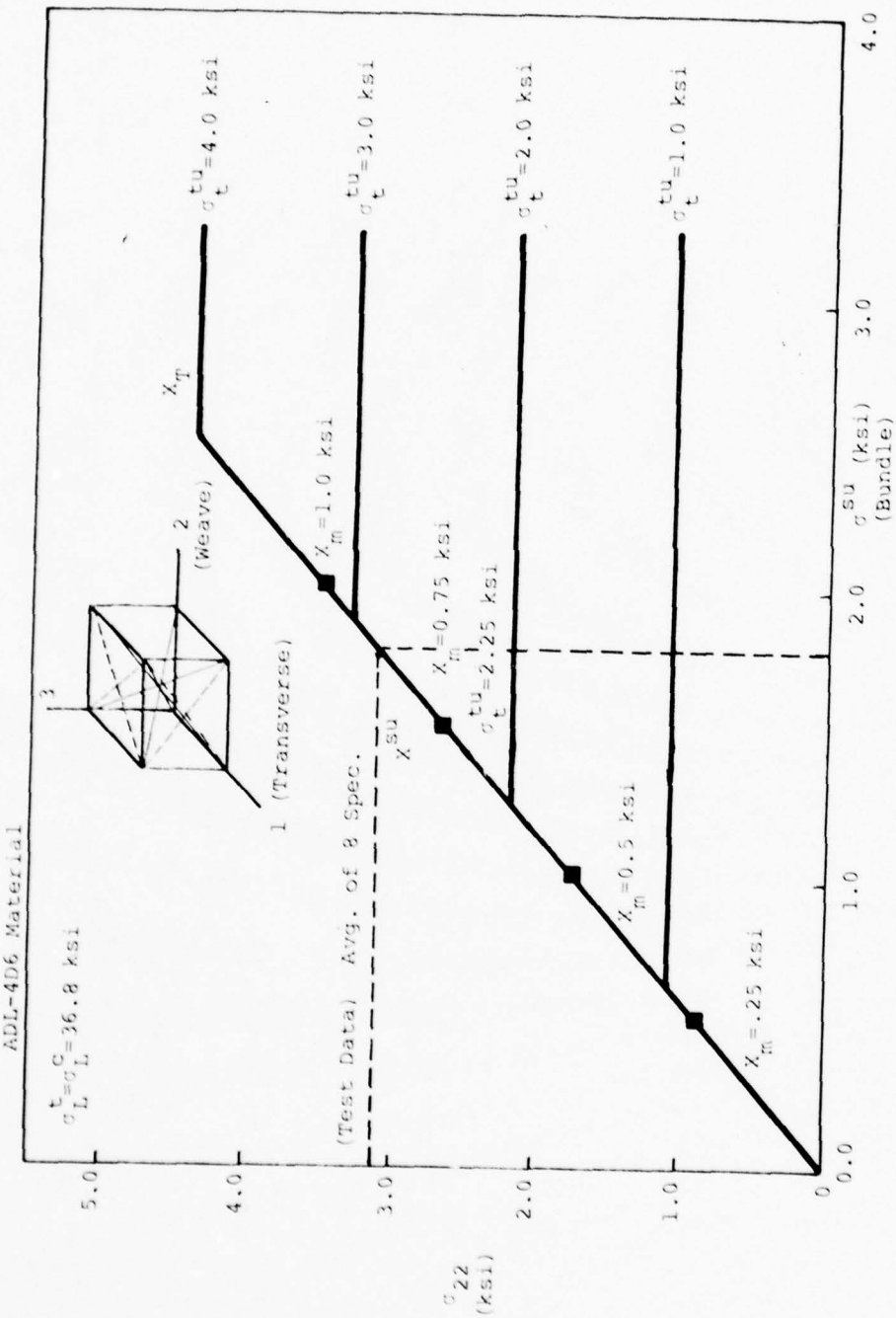

Figure 69. Predicted Strength Parametrics for ADL-4D6 in the 2-Direction (Weave Direction)

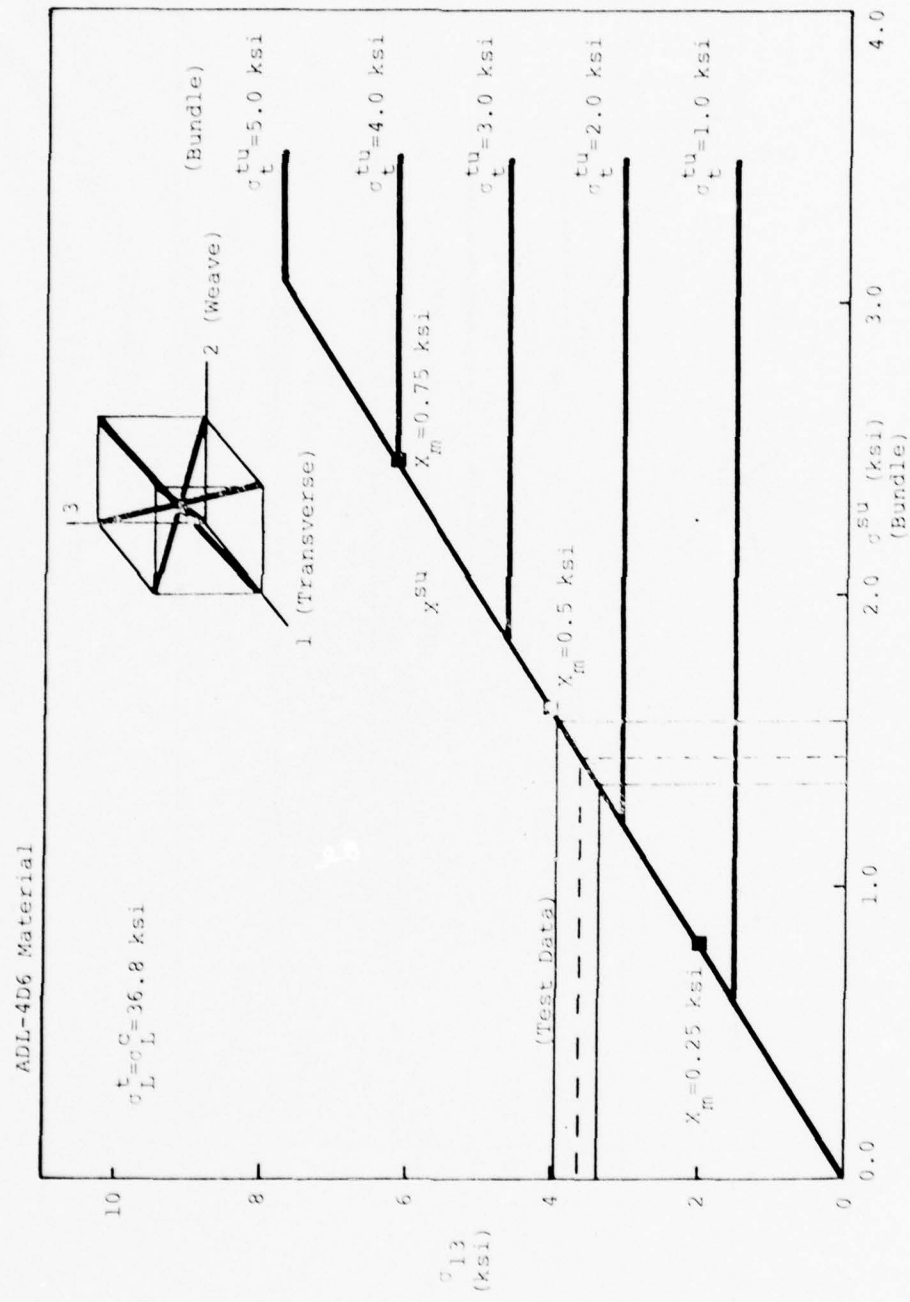

Figure 70. Predicted Strength Parametrics for ADL-4D6 in Shear

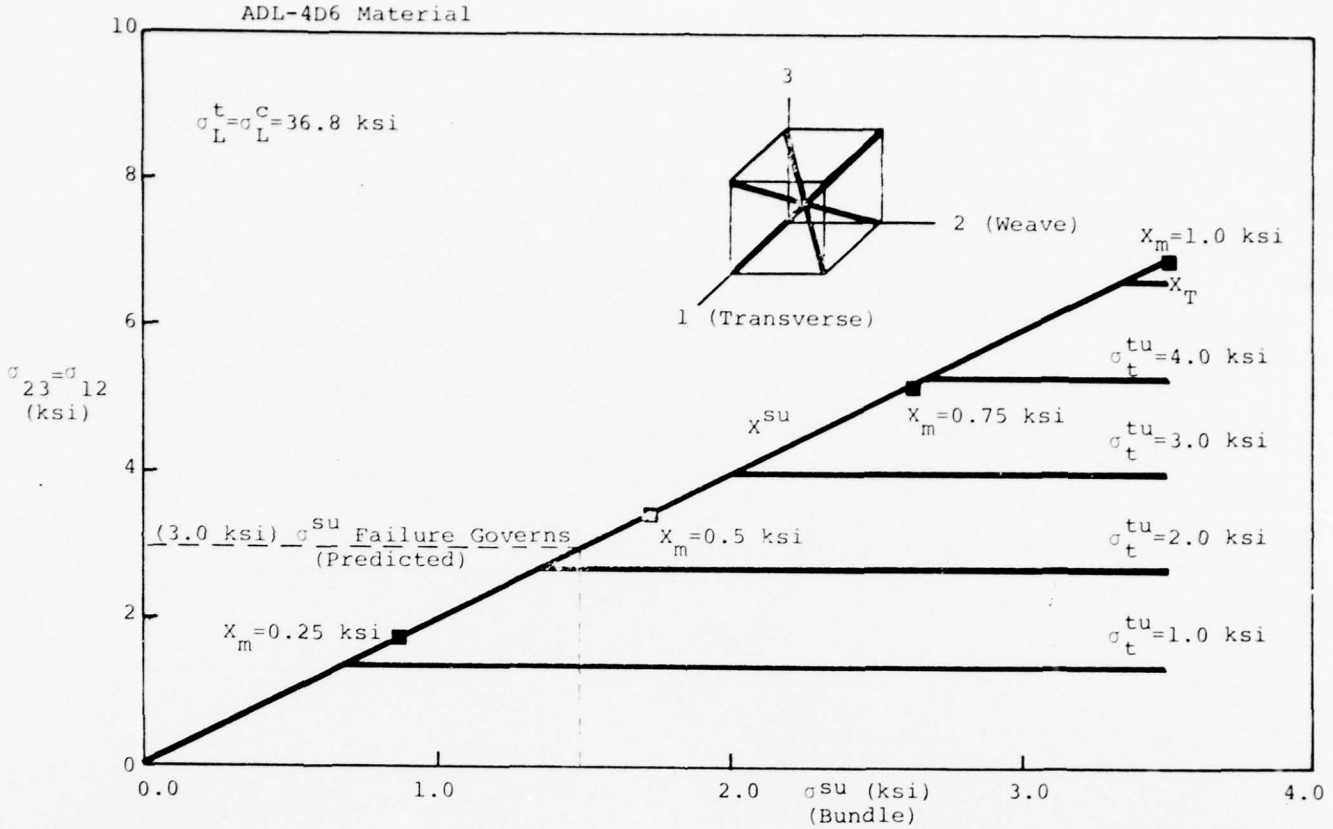

Figure 71. Predicted Strength Parametrics for ADL-4D6 in Shear

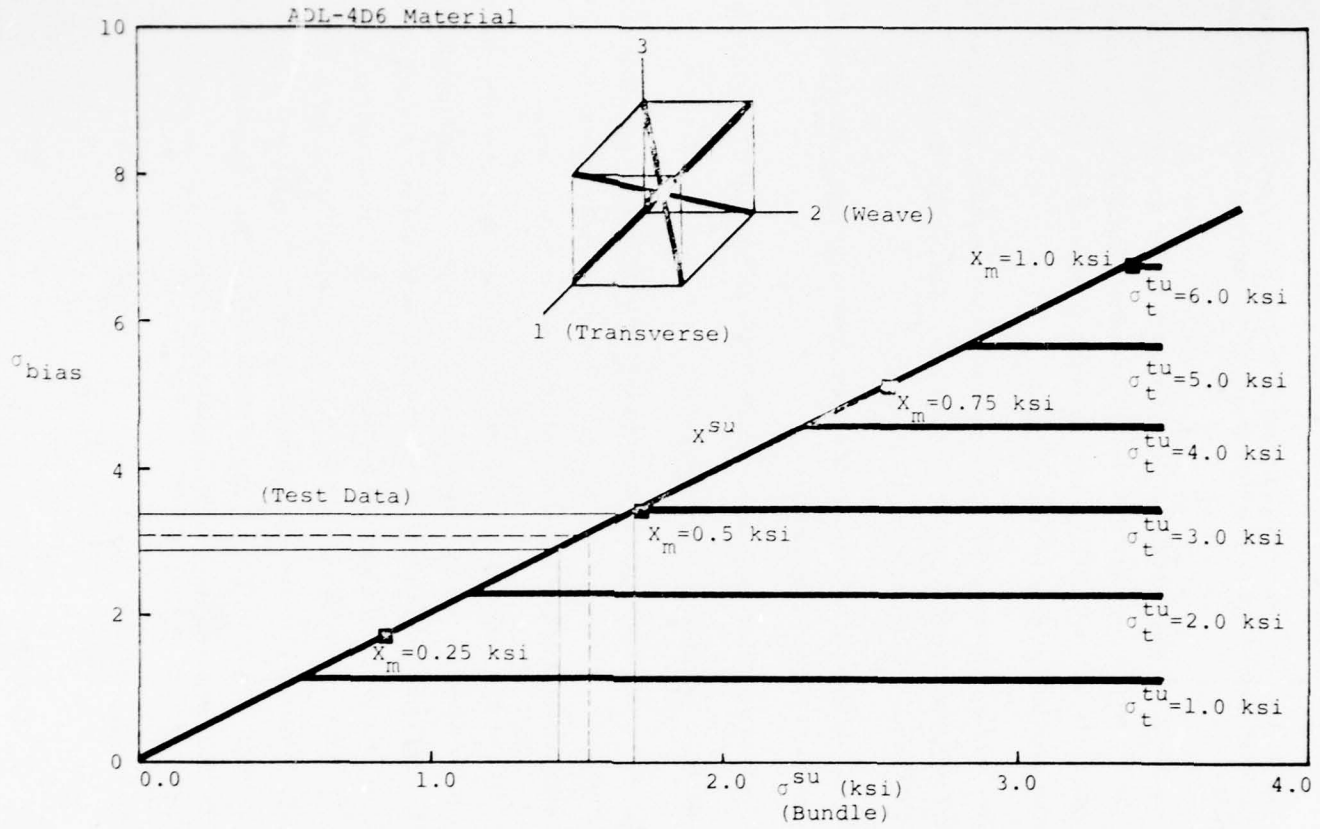

Figure 72. Predicted Strength Parametrics for ADL-4D6 in the Bias Direction

1. Fiber bundle and matrix strengths:

$\sigma^{su}_{F.B.} \cong 1.75$ ksi; $\sigma^{t}_{F.B.} \cong 2.75$ ksi; $\sigma_{m} \cong 1.0$ ksi

2. It can be seen from Figures 69, 70, and 72 that composite failure in each case is due to a combination of transverse fiber bundle failure and axial shear fiber bundle failure.

Assuming the constituent strengths (1) to be accurate, we can now predict the composite strength in the 1-direction (see Figure 68) as well as in shear (see Figure 71). Note that the composite tensile strength in the 1-direction is governed by shear of the fiber bundles. Shear failure also governs failure in the 2-3 and 1-2 planes.

It can be seen from the above example that bounds on the constituent properties can be made knowing composite strengths in various directions. Additionally, the mode of failure can be identified for composite failure in various directions.

It should be noted that in order to increase the composite strength in the weave direction (2-2 direction) one of the following must occur:

1. Increase in the transverse tensile and axial shear strengths of the fiber bundle

2. Variation of the projected fiber angles.

Current analysis techniques do not, however, allow for the strength prediction of multi-directional materials*. Therefore, predicting the effect of projected fiber angles on the resulting composite strength without sufficient test data would be very difficult.

Tensile test data generated under the current program for a fine weave ADL-4D6 panel are summarized in Table 19. It can be seen from Table 19 that the tensile strength for the fine weave material (4.68 ksi) is 50 percent greater than the tensile data reported in Reference 1. Referring to Table 8 it can be seen that the fiber projected angles for the fine weave material (i.e., SFPA-39°, STTA-33°) are much less than for the material tested in 1976 (see Table 38). The difference in tensile strength can therefore be attributed in part to the differences in projected fiber angles. Thus, it can be stated that the material tested under the current contract (Table 19) is comparable to the material tested in 1976 (Ref. 1).

*Unless constituent strengths are known.

4.5 SPECIFICATION OF 4-D AND 5-D PREFORM GEOMETRIES

A complete physical description of an Omniweave panel requires definition of a) the volume fraction of fibers in the panel, b) orientation of the fibers, and c) coarseness of the weave. In addition, some information relative to the variability of these parameters in the panel should be specified. Although these descriptions are relatively straightforward in a 3-D orthogonal weave, the 4-D and 5-D class of Omniweave materials present several difficulties which must be addressed. Materials Sciences Corporation proposes that the following approach be adopted to provide a complete description of Omniweave materials.

4.5.1 VOLUME FRACTION OF FIBERS

With 3-D orthogonal materials it is customary to specify the volume fraction of fibers in either one of two ways. The volume fractions of fibers in each of the three principal directions can be specified directly or, equivalently, the total fiber volume fraction in the composite can be specified along with the distribution of fibers in each direction.

Example: Stating that a weave contains:

10 percent fibers in the X1 direction,
15 percent fibers in the X2 direction, and
25 percent fibers in the X3 direction

is exactly equivalent to stating that the material contains 50 percent fibers with a distribution of:

20 percent in the X1 direction,
30 percent in the X2 direction, and
50 percent in the X3 direction.

In the case of Omniweave materials, it is suggested that a minimum of confusion will result if the fiber content is specified as the total volume fraction of fibers in the panel, followed by the percentage distribution in each direction if required. A standard 4-D Omniweave panel has a balanced weave such that 25 percent of the fibers are oriented in each of the diagonal directions. Therefore, one needs only to define the total fiber content on a volume basis to know how the fibers are distributed in the panel.

In the case of an Omniweave panel with additional reinforcement directions, resulting in a 5-D or 6-D material, it is necessary to define both the total fiber volume fraction and the distribution of fibers. The best approach in this case would be to examine a cross section of material which is perpendicular to the additional reinforcement directions. The ends of the additional reinforcement yarns will form a repeating pattern. The area fraction of the extra reinforcement fibers defines the volume fraction of the fifth and sixth direction reinforcement.

The total fiber volume fraction minus the volume fraction of the additional directions thus defines the volume fraction of fibers in the four diagonal directions. Note, however, that the area fraction of fibers in the additional direction must be utilized and not the area fraction of the bundle of fibers. This latter number defines the prism volume fraction of the additional reinforcements and not the fiber volume fraction.

The prism volume fraction, V_i^P, and fiber volume fraction, V_i^f, in a given direction are related through the volume fraction (or equivalently area fraction) of fibers within the prism, known as the fiber bundle volume fraction F_i^{FB} through

$$V_i^f = V_i^P \times V_i^{FB}$$

This can be shown rather easily since:

$$V_i^f = \frac{\text{Area of fiber}}{\text{Area of cell}} = \frac{A^f}{A_c}$$

$$V_i^P = \frac{\text{Area of bundle prism}}{\text{Area of cell}} = \frac{A^P}{A_c}$$

$$V_i^{FB} = \frac{\text{Area of fibers in bundle prism}}{\text{Area of prism}} = \frac{A^f}{A^P}$$

Thus:

$$V_i^P \times V_i^{FB} = \frac{A^P}{A_c} \times \frac{A^f}{A^P} = \frac{A^f}{A_c} = V_i^f$$

Several examples of 4-D and 5-D weaves are shown in Figures 73 and 74. Figure 73 gives a theoretical slice of a 4-D Omniweave material assuming that the fibers are parallel to a unit cube. (Orientations of the diagonals will be discussed subsequently.) It can be shown that the prisms of this 4-D material will occupy 75 percent of the weave volume. Assuming a maximum theoretical packing of fibers within each prism (about 91 percent) the maximum theoretical fiber volume fraction becomes 68 percent. Practical current weaving techniques result in roughly 60% packing of the fibers within the fiber bundle. Thus, the practical fiber content for this material is about 45 percent.

Figure 74 shows a 5-D material which was derived from Figure 73 by removing pairs of diagonal fibers, which results in an area for four Z bundles of the same cross sectional area as the diagonal fibers. A repeating element is identified in Figure 74. It can be seen that the Z bundles occupy 25 percent of the area of the repeating pattern. The volume fraction of Z direction fibers can be defined by knowing the area of the repeating pattern plus the number of Z fibers within each Z bundle and the cross sectional area of each fiber. The as woven panel density defines the total fiber volume fraction and the above procedure defines the Z direction

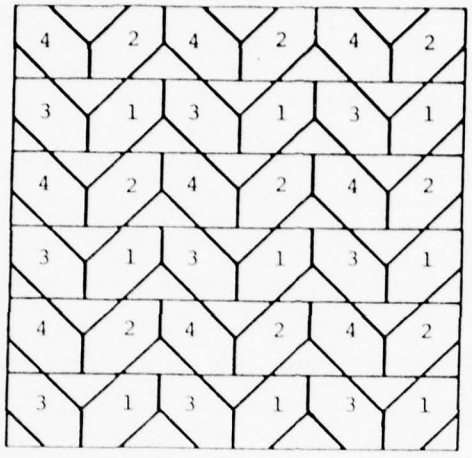

Figure 73. Cross Section of 4-D Material

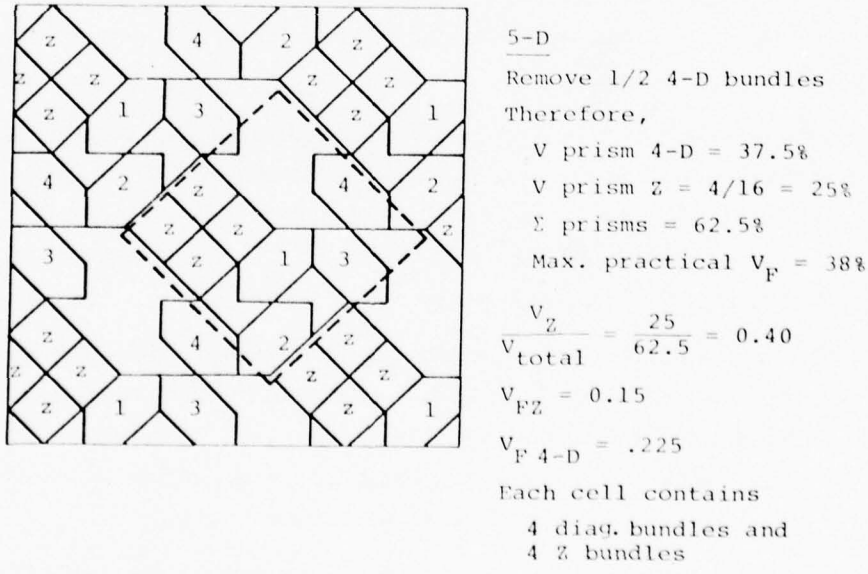

Figure 74. Cross Section of 5-D Material

The current flexure specimen geometry has been analyzed to assess its validity for the following two cases:

fiber volume fraction. Thus, the total fiber volume fraction of diagonal fibers is the difference between the above two quantities.

Figure 75 shows the excellent correlation between the theoretical fiber bundle configuration in a 4-D material and an actual configuration of material.

4.5.2 ORIENTATION OF FIBERS WITHIN PANEL

An accurate description of the orientation of the fibers within an Omniweave panel is important. It has been shown in previous studies that the resultant composite properties are sensitive to the internal fiber orientations. Three-dimensional orthogonal weaves contain fiber bundles which are parallel to orthogonal coordinate systems and are therefore rather easy to specify. The diagonal fibers in an Omniweave material are parallel to the diagonals of a parallelepiped, as shown in Figure 76. The fibers need not be orthogonal to one another or to an easily identified direction in the panel. Therefore, the identification of the true fiber orientations is somewhat difficult.

Since the fibers are parallel to the diagonals of a parallelepiped, the characteristics of the parallelepiped can be utilized to define the fiber orientations. In particular, the orientations of the face diagonals of the parallelepiped represent the orientation of the body diagonal direction projected to the faces of the parallelepiped. Definition of the orientations of the face diagonals on two planes also defines the complete shape of the parallelepiped. Since the nature of the Omniweave weaving process orients the parallelepiped parallel to the surfaces of the woven panel, the projected fiber angles on the surfaces of the panel identify the face diagonal directions. Therefore, the projected fiber angles should be utilized to define the fiber orientations within the panel.

The two projected fiber angles which are most readily obtainable are on the surface of the panel and on the side of the panel where, in both cases, the fibers reenter the panel. In order to avoid confusion, these angles should be measured relative to the weaving direction. Once defined, the projected fiber angles provide a description of the characteristic parallelepiped and hence the true fiber orientations can be determined, if necessary.

A word of caution is necessary relative to measuring the projected fiber angles on the surface of a panel. During the weaving process, as a fiber bundle exits the panel, it is reentered as a diagonal fiber entering the panel. Thus, small loops of fiber bundles exist on the surface of the panel which connect pairs of diagonals. These reentrant fiber loops make an angle on the surface of the weave which is not the projected fiber angle.

The above is illustrated in Figure 77. All of the bundles labelled with similar numbers are parallel to one another. Bundles "1" and "2" form a pair of diagonals which lie in the same plane. Figure 77 is taken as a slice of material just below the surface. In the actual weave,

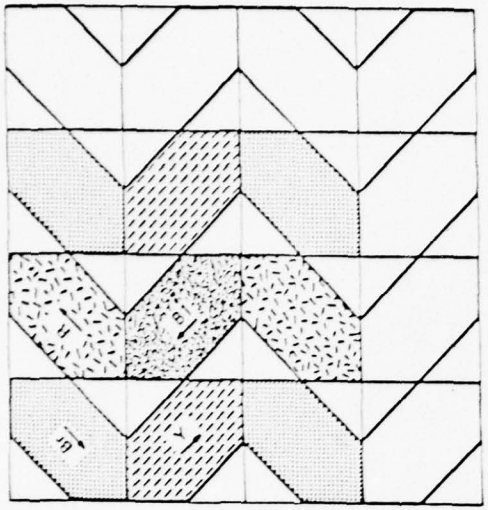

A) Typical Yarn Shapes Predicted for a 4-D Material

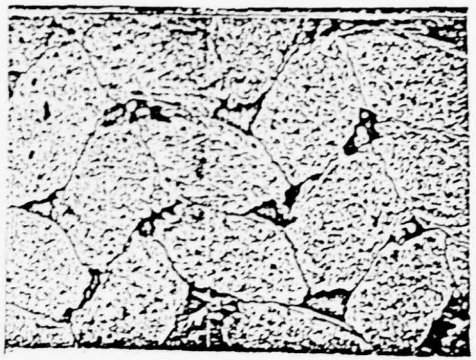

B) Surface of a 4-D (T-50) Composite Perpendicular to Weave Direction

Figure 75. Comparison of Predicted Fiber Bundle Cross Section with an Actual 4-D Cross Section

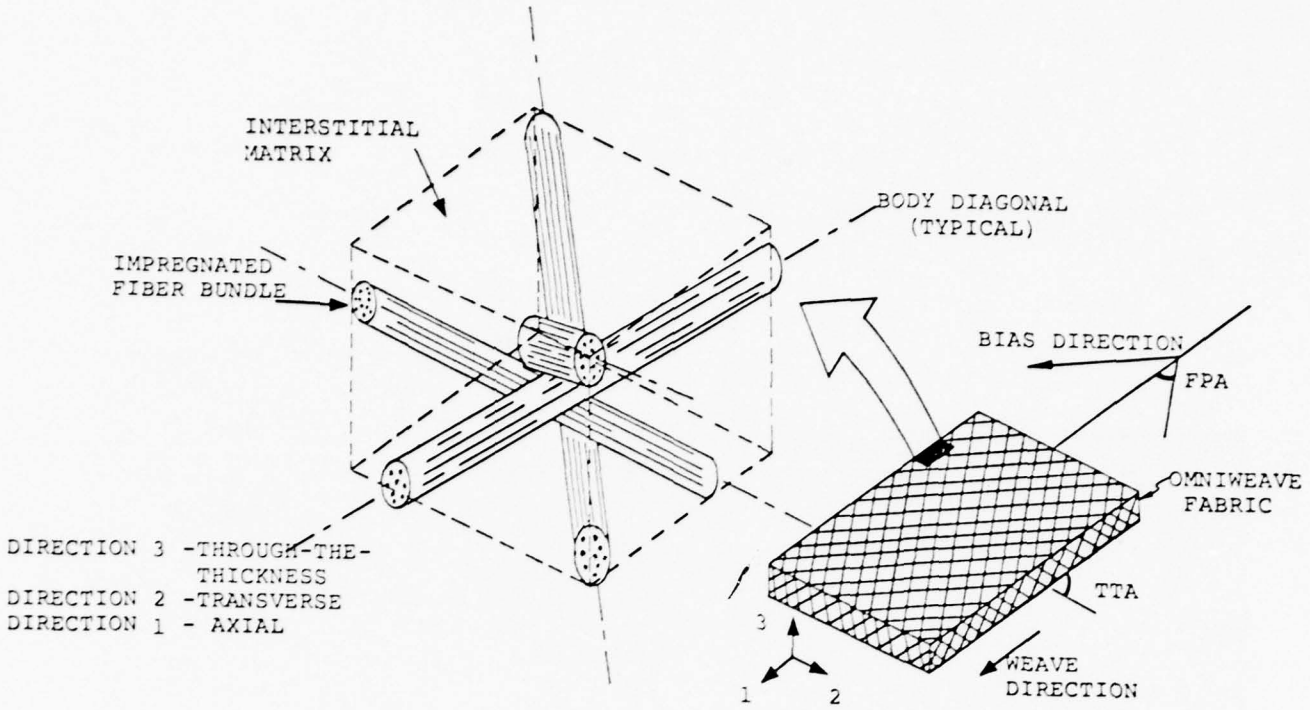

Figure 76. 4-D Unit Cell

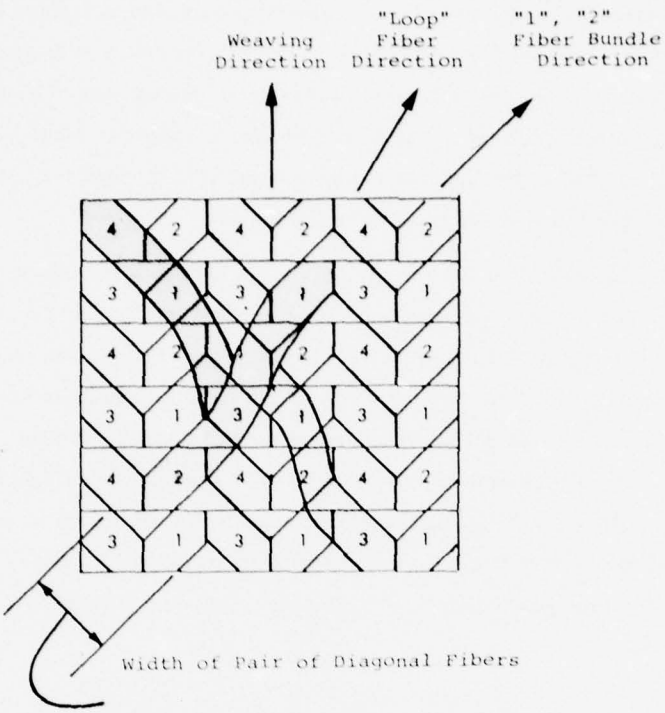

Figure 77. Cross Section of 4-D Weave Showing Fiber Path

the fibers in bundle "1" would reenter the panel in bundle"2" as shown by the "loop" formed on the surface. Clearly, the fiber projected angle for bundles "1" and "2" is measured as indicated in Figure 77 as the angle between adjacent bundle "2" and the weaving direction and not the angle made between the weaving direction and the fiber direction in the loop of the material.

It is believed that the line formed by sides of a row of surface loops is indeed the projected line of the diagonal fibers. This line should be utilized to define the fiber orientation. This point could be easily verified by measuring the projected fiber angles on the surface of a panel and then machining away the outer material loops and remeasuring the projected fiber angle using the line connecting the sides of the fiber bundles to define the orientation. It is suggested that this exercise be carried out on a small specimen of material to verify that one can indeed utilize surface measurements to define the internal fiber orientation.

4.5.3 DEFINITION OF THE COARSENESS OF WEAVE

In all multidimensional weaves the coarseness of the weave is an important parameter. Coarseness (usually termed unit cell size) defines the number of repeating volume elements which will exist over a given area. It is desirable to maintain a maximum number of unit cells in a test specimen cross section to minimize edge effects. Additionally, it is generally desirable to maintain a small unit cell dimension, fine weave, to provide a more uniform

surface under service recession conditions. However, cost of manufacture is a strong function of unit cell dimension and therefore, from a cost standpoint, it is desirable to maintain the weave as coarse as possible. In orthogonal materials the number of bundles which must be handled varies with the cube of the unit cell dimension. Since weaving costs are proportional to the number of fiber bundles which must be placed in the material, it is easy to see why cost is a strong function of the fineness of the weave.

In 3-D orthogonal materials the unit cell is readily defined by the weave spacing. A repeating volume element, or unit cell, is easily identified as shown in Figure 78. However, in 4-D materials it is not possible to remove a repeating volume element of simple dimensions. Examining Figure 73, it is clear that one cannot draw a simple rectangle which encompasses the four fiber bundles. As one follows the fiber bundles through the thickness, Figure 79, it is clear that if a simple rectangular shape were chosen to outline four fiber bundles, then as one penetrates the material, by the time the same bundle pattern is repeated, the top bundles would have exited the rectangular area and new bundles would have entered. Therefore, a simple description of the coarseness of a 4-D weave which corresponds to a unit cell description is not possible.

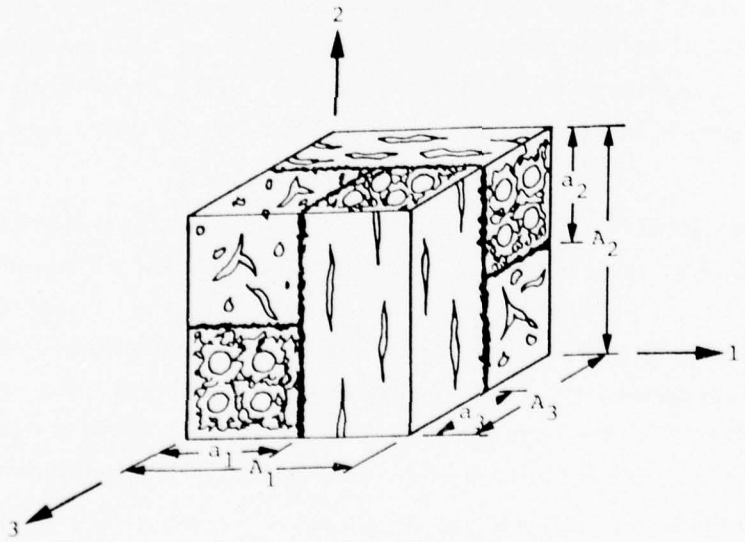

Figure 78. 3-D Unit Cell

4. The dielectric properties of standard and fine weave ADL-4D6 were measured at the Laboratory for Insulation Research of MIT in X-band (8.5 GHz) and in the millimeter wave band (24 GHz). The X-band measurements confirm the

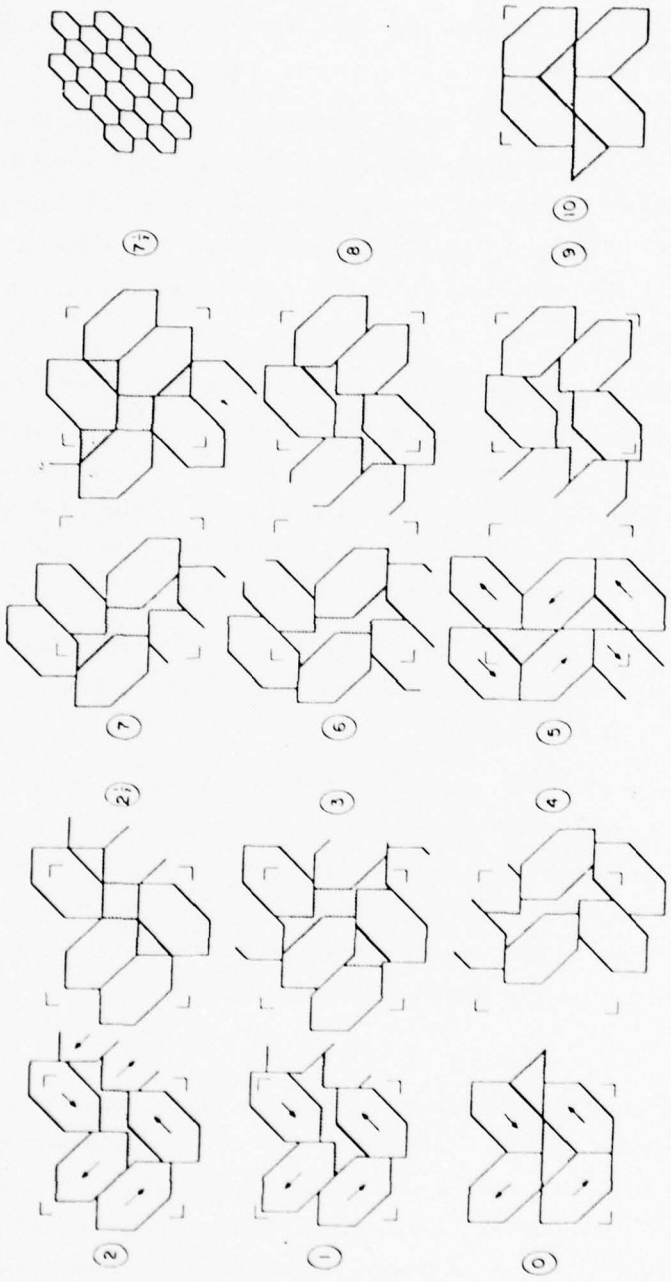

Figure 79. Typical Sections Through Model of Figure 73 Showing Shape of Matrix Region Between Hexagonal Rovings

As a minimum, this evaluation should include the DuPont 99 percent alpha-alumina fiber

It is necessary then to define a dimension which will be a characteristic dimension of the coarseness of the weave. Additionally, a dimension should be chosen such that it can be identified from the surface of the panel without requiring slicing of material. Several options exist which will be discussed below.

For the 5-D material shown in Figure 74, the dotted lines clearly indicate the characteristic dimensions of the weave. These dimensions would be a natural choice since they represent the Z to Z spacing. However, if the Z bundles were removed and replaced with diagonal fibers, without changing any bundle dimensions, one arrives at Figure 73. If the same characteristic dimension were applied to Figure 73, it is found that the resulting area contains two each of the diagonal fiber bundles, and not one.

It appears appropriate to utilize several characteristic dimensions, depending upon the type of weave. For a 4-D weave the dimension across a pair of diagonals is both easily identified and is a direct measure of the coarseness of the weave, see Figure 77. This dimension is, in fact, the dimension across the loops of yarn on the surface of the panel. Although a square of this dimension does not enclose all four fiber bundles, it is a direct measure of the size of the fiber bundles and is thus a measure of the coarseness of the weave.

In the case of panels reinforced in a fifth direction or more, the specifications should include the center to center spacing of the additional reinforcement bundles as well as the dimension across a pair of diagonal fiber bundles.

As in the case of measuring fiber orientations from the surface of a panel, there is some uncertainty relative to the relationship between the dimension across a surface loop and the actual dimension across a pair of diagonal fibers. The accuracy of measuring this dimension from the surface should be checked. This can be done at the same time as the angle measurements are checked by measuring the distance across the surface loops at the surface and then removing the surface material and remeasuring the dimension.

4.5.4 VARIABILITY

A complete understanding of the properties of Omniweave panels requires some knowledge of the variability of the weave. Ideally, the statistical properties of each of the pertinent parameters, fiber volume fraction, fiber orientation, and coarseness of weave should be known. For the current material development programs, perhaps the effort required to define the statistical variability of the various parameters is unwarranted. However, at a minimum, an attempt should be made to characterize each panel by defining the mean value and range of each parameter. This can be most easily accomplished in terms of fiber orientations and weave coarseness.

The weaving process sometimes results in a variation in fiber angles which is fairly uniform through the thickness, but varies across the panel. Some definition of this variation is required along with identification of the location where specimens are removed.

At the current stage of antenna window material development, it is important to identify the sources of material variability.

The 4-D and 5-D portions of preform No. 426 will be used as an example of how the Omniweave material should be specified. The preform densities have not yet been measured, but will be assumed to be 1.0 gm/cc for the purpose of illustration. Since the fiber density is 2.2 gm/cc, this implies that the preforms (A), (B), and (C) each contain a total of 45.4 percent fibers by volume.

The 4-D portion of this panel, 426-A, described in Table 2 contains one-fourth of the fibers in each of the diagonal directions, thus it is a balanced 4-D weave containing 45.4 percent fibers by volume. The through the thickness fiber angles were not determined in Table 2, thus the fiber orientation can only be described as having projected fiber angles on the panel surface of 38 percent.

The 5-D section, 426-B, contains 40 roving ends in each of the diagonal directions and 12 roving ends in the fifth direction. Thus, a repeating cell contains 172 yarn ends. This weave is defined by stating that it contains 45.4 percent fibers with a fiber distribution of 23.26 percent in each of the 4-D directions and 6.98 percent in the fifth direction. The diagonals have a projected angle on the surface of the panel of 31 percent. Again, the fiber orientation through the thickness of the panel is not given in Table 2.

The final 5-D section, 426-C, contains 40 roving ends in each diagonal direction and 20 roving ends in the fifth direction. Thus, the repeating cells contain 180 yarn ends. This weave is defined by stating that it contains 45.4 percent fibers with a fiber distribution of 22.22 percent in each of the 4-D directions and 11.12 percent in the fifth direction. The diagonals have a projected angle on the surface of 30 degrees. The fiber orientation through the thickness of the panel is not given in Table 2.

Along with the above data, these weaves should be further specified by defining the spacing across the diagonal pairs of fibers as well as the spacings between the fiber bundles in the fifth direction.

The above characterization data is tabulated in Table 41 along with the additional data required to fully characterize these weaves.

TABLE 41. CHARACTERIZATION OF OMNIWEAVE PREFORM NO. 426

Parameter	426 A	426 B	426 C
Weave Design	4-D	5-D	5-D
Fiber Type	Astroquartz® Type 552 Roving		
Roving End Count	40	40/12	40/20
Fiber Finish		Teflon	
Cell Size - Across Diagonals (mm)	3		
5-D Yarn Spacing (mm)	-	TBD/TBD	TBD/TBD
Woven Dimensions (mm)	1.3x4.5x12	1.6x4.5x10	1.8x4.5x4
Volume (cu. in.)	70	72	32
As Woven Bulk Density (gm/cc)	1.0*	1.0*	1.0*
Avg. Weave Face Half Angle (Deg.)	38°	31°	30°
Avg. Weave Through Thickness Half Angle	TBD	TBD	TBD
Total Fiber Volume Fraction (Vol %)	45.4	45.4	45.4
Fiber Orientation % 4-D (Total)/5-D	100%	93.02%/6.98%	88.88%/11.12%

4.6 OMNIWEAVE ANTENNA WINDOW MATERIAL MECHANICAL TESTING TECHNIQUES

The test methods currently being utilized to evaluate the antenna window materials have been reviewed. In particular, the usefulness of flexure testing has been addressed. Some differences between flexure and tensile test data have been reported for these materials, thus making it desirable to determine if the differences were real material differences or simply apparent differences which resulted from test techniques.

During material development programs it is advantageous to have simple test techniques which require small volumes of materials, yet can provide reasonable estimates of elastic properties and strengths. Early antenna window materials were brittle, with a very small strain to failure. Thus, flexure tests offer an economical means of obtaining modulus and strengths for this class of material. Therefore, flexure tests were initially utilized in place of tension tests in the early antenna window material studies (i.e. brittle materials). However, as the development of these materials progressed, the strength as well as the strain to failure has been continually improved.

It is appropriate at the current stage of material development to reexamine the material properties obtained through flexure tests in light of the improved strain to failure. A discussion of the use of the flexure test as an approximation (or substitute) to the tension test is discussed in the following paragraphs.

The ASTM flexure test (Ref. 10) originally developed for plastics, is becoming more and more commonly used to measure the flexure modulus and flexure strength of fiber reinforced composite materials which have different (and sometimes nonlinear) stress-strain curves under tension loads than under compression loads. Such materials are considered multimodulus materials. Key limitations of the ASTM flexure test are: a) applicable only to materials with the same modulus under both tension and compression loading, and b) limited to materials for which the stress is linearly proportional to strain up to the point of rupture and for which the strains are small. If the above two criteria are met, then the properties obtained from a flexure test can be related to tensile test results.

The standard ASTM flexure test for plastic materials (Ref. 10), is that of a rectangular cross section beam subjected to either a 3-point or a 4-point transverse load. If the tension and compression moduli are the same, then the flexure modulus is a redundant method for measuring the Young's modulus, and if the tension strength is equivalent to the compression strength, then the flexural strength is a redundant way of measuring the tensile strength of the material. If the moduli and/or strengths are different in tension and compression, then the flexural strength calculated with the ASTM equations is neither the compressive strength nor the tensile strength. Thus, the interpretation of the apparent flexural strength is difficult for many materials.

In a recent study by Jones (Ref. 19), the effects of applying an ASTM flexure test to a multimodulus fiber reinforced material were investigated and comparisons between predicted and measured properties were assessed. Results indicate that an apparent flexure modulus can be predicted (Equation 21) for the multimodulus material (if the tension and compression moduli are known) which agrees very well with test data. However, due to the restriction that the material must be linear elastic to failure, predictions of the flexural strength of multimodulus materials are in poor agreement with test data.

A plot of the normalized flexural modulus (E_f/E_c), along with the normalized, average modulus,

$$\frac{E_{avg}}{E_c}$$

and the normalized tension and compression moduli versus the multimodulus ratio (E_t/E_c) is shown in Figure 80. It can be seen from Figure 80 that:

1. E_f is always less than E_{avg}, and
2. E_f is always closer to the smaller of E_t and E_c.

In summary, it can be concluded that flexural modulus and flexural strength data for multimodulus materials cannot be utilized to extract tension and/or compression properties. Instead, properties obtained from flexure tests are a rough averaging of those two behaviors.

A comparison of predicted flexure modulus with that of actual test data from Reference 1 indicates that the predicted flexure modulus calculated by means of Equation (21):

$$E_f = \frac{4E_tE_c}{(E_t^{1/2} + E_c^{1/2})^2} \tag{21}$$

which includes both the tension and compression moduli, bounds the test data of Reference 1, (see Figure 81). This indicates that the properties being measured through tension, compression, and flexure tests are probably valid. The above indicates that one must be cautious in interpreting the meaning of flexural modulus since for the current materials one cannot expect to infer a tensile or compressive modulus from the flexure data.

No correlation between predicted flexure strength and actual test data could be made due to the nonlinearities of the material being tested. The flexure test cannot be utilized to measure tensile or compressive strength. As long as the flexure specimen geometry is not changed, however, the flexure test can be utilized as a means of comparative evaluation of different materials. The flexure test provides a good method for comparing various processing methods under the assumption that the modes of material failure do not significantly change from one material process to another.

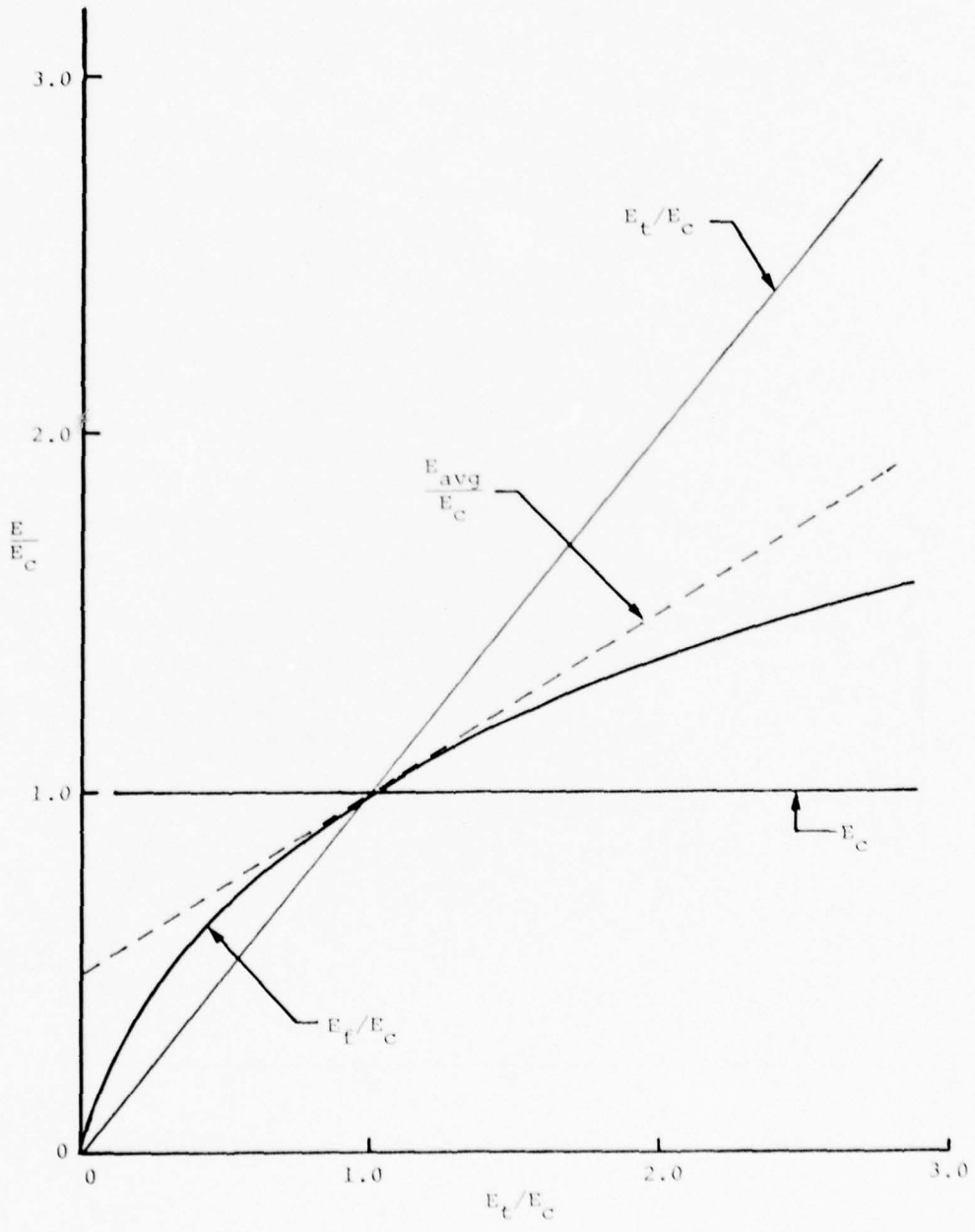

Figure 80. Normalized Flexure, Average, and Tension Moduli Versus E_t/E_c

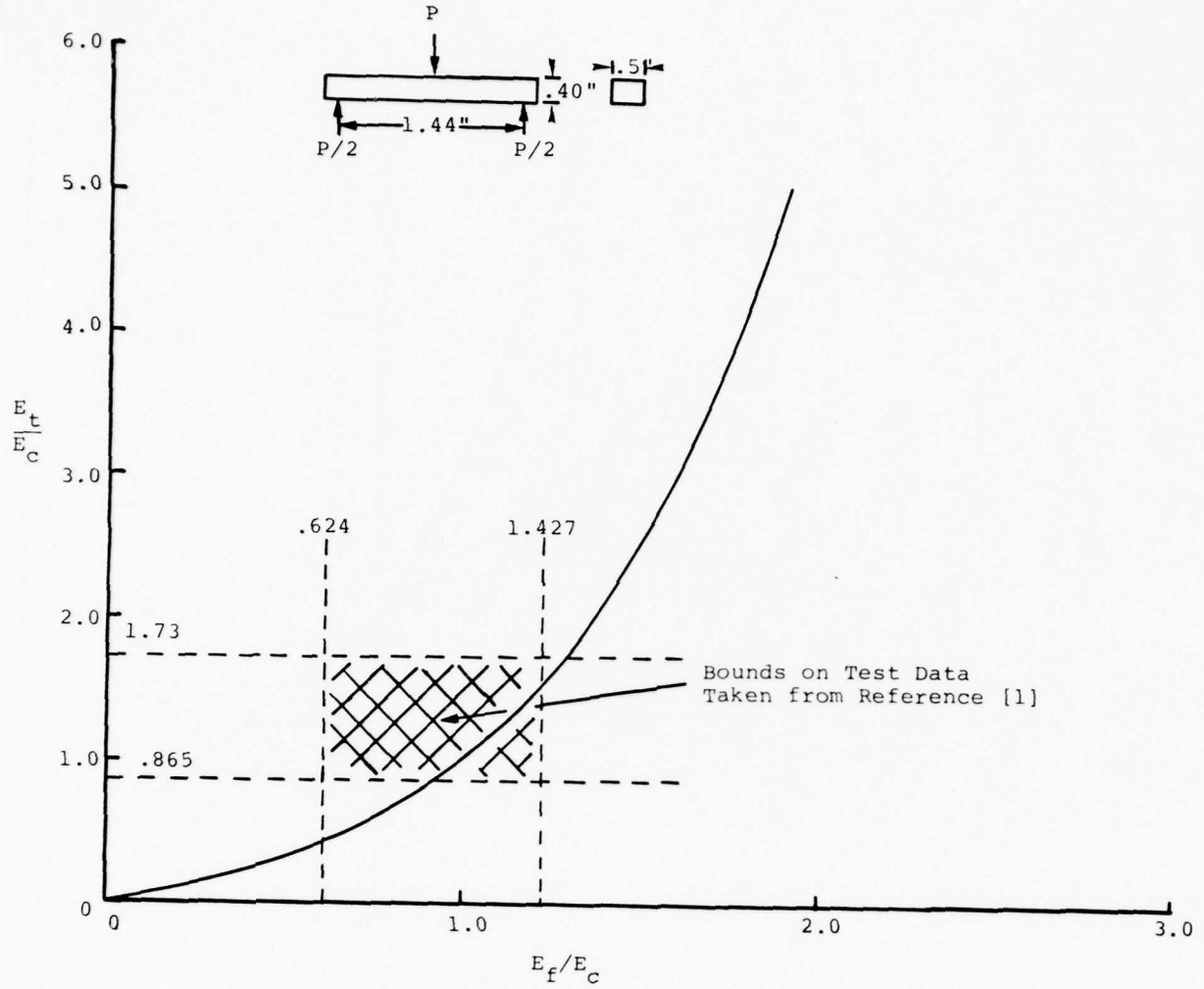

Figure 81. Comparison of Test Data Versus Predicted Flexure Modulus

Figure 74. Cross Section of 5-D Material

The current flexure specimen geometry has been analyzed to assess its validity for the following two cases:

1. Tension and compression moduli assumed equal and the stress is linearly proportional to strain up to the point of rupture; and

2. Tensile and compressive moduli assumed different, as well as nonlinear stress-strain response of the material.

To aid in the verification of the test specimen for the two cases mentioned above, a finite element model of the specimen was utilized (see Figure 82). Test runs using the SAAS finite element computer code were made using typical 4-D material properties. Results for the two cases are shown in Figure 83, as bending stress versus thickness at the center of the specimen cross section. It can be seen from Figure 83 that the maximum tensile stress predicted for either of the two cases were within ±15 percent of that calculated using beam theory (assuming equal tensile and compressive moduli). However, it should be noted that the material properties were assumed to be linear elastic to failure. Therefore, the results of Figure 83 are not too surprising. The major problem arises when the stress-strain response for the material is very nonlinear. For this case the equation used to calculate the modulus of rupture (σ_{mor}) no longer holds true. Since the current materials are not linear and behave differently in tension and compression, it is recommended that tension tests be utilized for the purpose of obtaining the tension modulus and strength while the flexure test be utilized as a quality control test for the evaluation of different densification processes. Flexure tests can be utilized to provide a qualitative ranking of the effects of different process cycles. However, once a densification process is selected, sufficient material should be fabricated to permit standard tension and compression test specimens to be utilized to obtain engineering properties of the material.

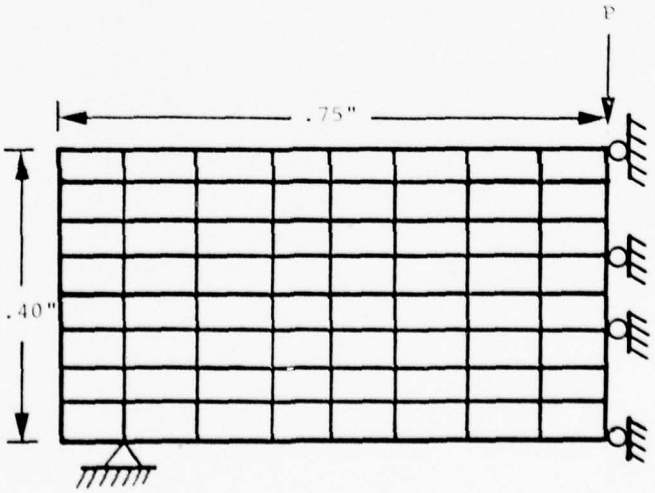

Figure 82. Finite Element Model of Test Specimen

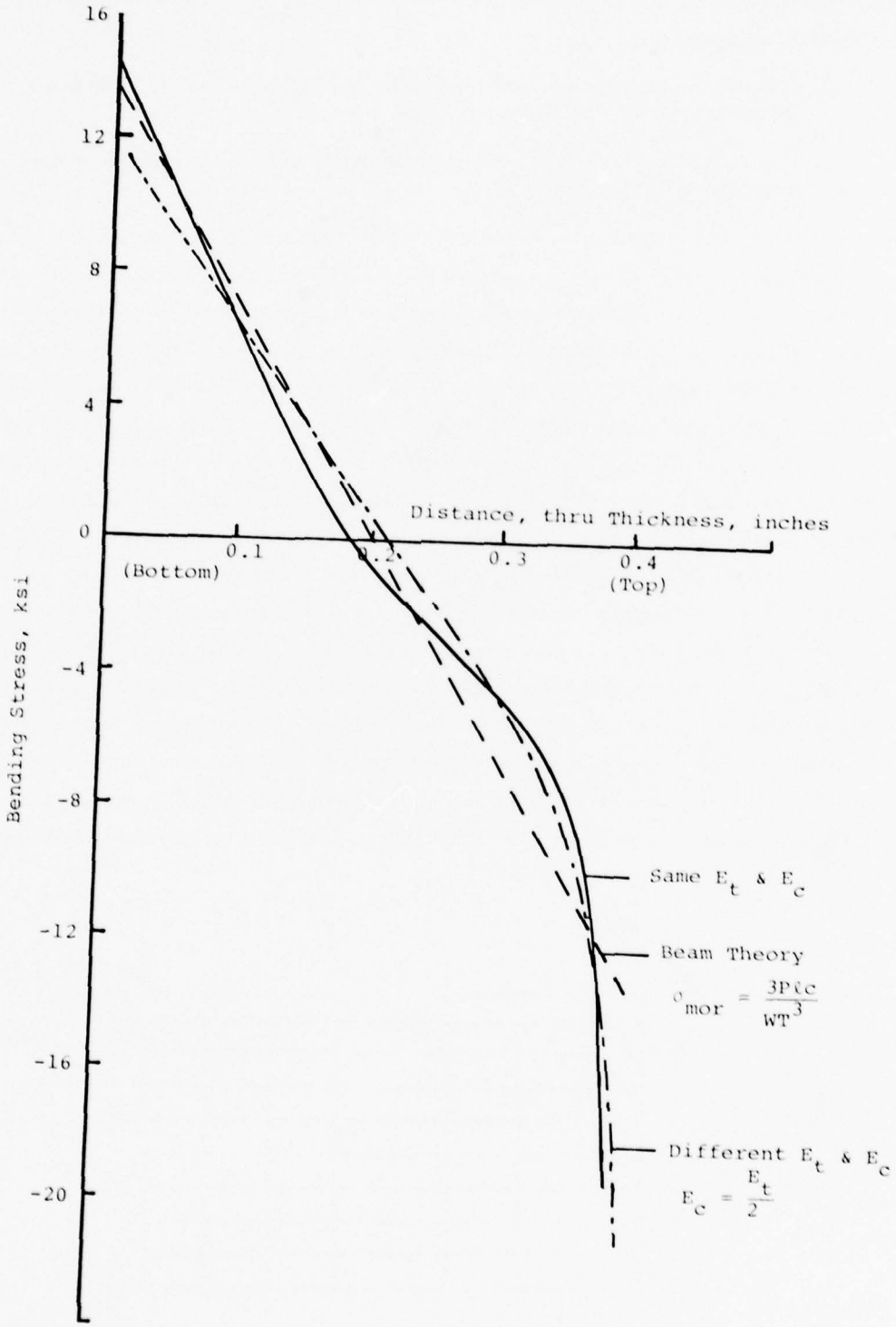

Figure 83. Stresses Through-the-Thickness of Flexure Specimen at Mid Span

4.7 CONCLUSIONS FROM MICROMECHANICS ANALYSIS

This study of test methods, constituent properties, and window material characteristics has yielded the following conclusions:

1. The differences between square and round cross section geometries which were thought to be significant in the previous program, were not. The differences in test data were due to processing differences of the specimen tested with only perhaps very small specimen geometry effects.

2. Data correlations with the previous ADL-4D6 specimens were reasonably consistent and resulted in a better definition of constituent matrix properties.

3. The strength parametric studies have provided a foundation from which various test data on composites can be utilized to define the individual constituent strengths. The available test data were utilized to estimate constituent strengths. The results indicate that improvements in composite axial strength can be achieved by improving the fiber bundle shear strength.

   The significant results of the strength parametrics which have been generated are that one can define relative amounts of constituent strength improvements which can effectively be utilized to increase composite strength.

4. The 4-D class of Omniweave configurations have been reviewed carefully and recommendations have been made for material specification which will permit a complete identification of the weave in terms of fiber content, orientation and weave coarseness.

5. The results of the evaluation of current testing techniques indicate that flexure tests should be utilized to qualitatively rank the effects of various densification processes when small amounts of material are available. Material design data and engineering properties should be obtained through the more conventional tensile and compression test specimens.

5. PART I: MULTIDIRECTIONAL REINFORCED FIBROUS COMPOSITES – CONCLUSIONS AND RECOMMENDATIONS

5. PART I: MULTIDIRECTIONAL REINFORCED FIBROUS COMPOSITES – CONCLUSIONS AND RECOMMENDATIONS

5.1 CONCLUSIONS

1. Particle impact tests with 0.5 and 1.0 millimeter glass spheres at 10 degree incidence have shown the standard ADL-4D6 silica-silica composite to have the highest erosion resistance in the 8 to 12 Kfps ENNK BMDI velocity range of any hardened antenna window material.

2. A "fine weave" version of the Astroquartz fused silica 4D preform has been produced by the Omniweave process. Fabrication of this fine weave with 12 end yarn in place of the standard 20 ends presented no disproportionate difficulty. Preforms with major cell dimension of 2mm (as compared to 3mm for the standard weave) were densified by the standard ADL-4D6 process.

Flexural strength tests showed equivalent mechanical strength and elastic properties compared to the standard weave material; while unaxial loading tensile tests showed an improvement of 40-60 percent in measured value, establishing a mean in excess of 5000 psi.

Flyer plate impact tests showed improved spall resistance, nominally 9,000 taps for the threshold of backface spall damage.

3. A comprehensive study of ADL-4D6 densification process variations has been carried out to assess the effect of fiber surface preparation, colloidal silica densifier particle size and chemistry, and heat treatment temperature. Using flexural strength tests as the primary discriminant, no improvement in strength has been demonstrated over the standard ADL-4D6 material.

However, the influence of several process variables on the strain-to-failure and composite fracture mechanism is evident:

- Deletion of the teflon coating step before initial colloidal silica infiltration resulted in composites with "ideal" fracture surfaces and a flexural tension surface strain-to-failure well in excess of 1.44 percent.

- A specimen densified by the acid-stabilized process had a flexural tension surface strain-to-failure which apparently exceeded 2.0 percent. A higher composite bulk density of 1.64, in contrast to the nominal 1.60, was also achieved.

These strain-to-failure and composite failure mechanism improvements have their greatest implication for environmental performance properties such as plate spall and particle impact. The effect of density on particle erosion of ADL-4D6 has also been demonstrated.

Figure 78. 3-D Unit Cell

4. The dielectric properties of standard and fine weave ADL-4D6 were measured at the Laboratory for Insulation Research of MIT in X-band (8.5 GHz) and in the millimeter wave band (24 GHz). The X-band measurements confirm the low loss properties found in previous work; i.e., loss tan less than 0.006. The 24 GHz measurements however show increased sensitivity to absorbed moisture, with loss tangent ranging from 0.008 to 0.010. This higher loss appears to be also intrinsically present in the high purity silica; but the principal contribution to raising the loss tangent value to the benchmark level of 0.01 is water absorption. Further development work for millimeter wave applications must address this problem.

5.2 RECOMMENDATIONS

1. The densification process variation study begun in this contract should be extended and completed. As a minimum it should:

- Confirm the effect of the acid pH stabilization process on a larger sample of material
- Study the effect of extended use of the silane coupler agent at each densification stage
- Examine a low cost, minimum process time densification process
- Develop an improved water desensitization process, with emphasis on properties in the millimeter wave band

The structural capability of the most promising of these densification process variations should be finally proven by uniaxial loading tensile tests.

2. An improved ADL-4D6 combination of Astroquartz 4D preform cell size and densification process should be selected. As necessary this selection should be implemented by a series of screening characterization tests. This optimum new ADL-4D6 formulation should then be characterized for design level properties.

These tests would include as a minimum:

- Mechanical and thermophysical properties to 1800^{o}F
- Spall threshold and equation of state.
- Particle impact testing for erosion resistance in the projected most probable BMDI environment
- Dielectric property and hot transmission tests at millimeter wave frequencies.

3. The potential of advanced refractory dielectric fibers should be evaluated for improved hardened BMDI millimeter wave composite antenna windows, with particular emphasis on structural, erosion resistance and electromagnetic transmission performance.

As a minimum, this evaluation should include the DuPont 99 percent alpha-alumina fiber "FP". Other candidate fibers to be considered should include silicon nitride and boron nitride.

Candidate matrices should include colloidal silica, colloidal alumina, aluminum nitride, silicon nitride, boron nitride and combinations of these.

4. Alternates to or improved versions of the state of the art 4D preform weaving processes should be examined, primarily for their potential as short production time, low cost sources of 4D Astroquartz preforms.

The worth of such alternatives shall be measured by production costs, production cycle and comparison of the mechanical properties of standard densification process ADL-4D6 composites produced from such preforms.

PART II: ULTRAHIGH PURITY NITRIDE-BASED CERAMICS

6. PROGRAM OVERVIEW

PART II: ULTRAHIGH PURITY NITRIDE-BASED CERAMICS

6. PROGRAM OVERVIEW

6.1 PROGRAM PLAN

Figure 84 illustrates the "roadmap" which was used to guide material development and evaluation of the four (4) nitride-based ceramics considered on this program. The solid lines shown indicate that the previous processing feasibility had been demonstrated in our laboratory. For these systems, process optimization focused upon the preparation of ultrapure forms of each material. Essentially, no process development was associated with the β'-Sialon and cubic boron nitride, both of which were made available to the program at no cost. The dotted-lines in Figure 84 represented new process research requiring initially exploratory studies to define experimentai parameters leading to the required material (free-standing plates of AlN, ultrahigh purity Si_3N_4 powder).

In the case of materials for which a process was already developed, the screening phase was bypassed and final characterization properties were immediately sought with the purpose of filling in gaps in existing properties which were critical to the millimeter wave antenna requirements. For other materials (such as CVD-Si_3N_4 and AlN), initial formulations were screened for highest chemical purity and density prior to final property characterizations. Again, these characterizations were primarily aimed at filling gaps in existing knowledge of each material which was pertinent to the millimeter wave application (e.g., radar transmittance behavior as a function of frequency and temperature).

6.2 SUMMARY OF RESULTS

Table 42 summarizes available property data on each candidate nitride-based ceramic, and also data on a commercial grade hot-pressed Si_3N_4. A thermal shock resistance figure-of-merit has been computed for each system at 1000°K. Although generalizations must be made with caution, cubic boron nitride is predicted to have a superior resistance to thermal shock compared to other candidates. However, size limitations (~1 cm diameter), imposed by the current state-of-the-art in super-pressure processing, would require its utilization as a mosaic antenna window. Its room-temperature radar transmittance properties are comparable to hot-pressed Si_3N_4 at 24 GHz. Also noteworthy is the microhardness level of cubic boron nitride which is second only to diamond.

Hot-pressed AlN, CVD Si_3N_4 and hot-pressed Si_3N_4 have comparable thermal shock resistance figures; however, the ultralow loss tangents for CVD Si_3N_4 exceed other materials by at least an order of magnitude. Also noteworthy is the insensitivity of loss tangent to temperature. β'-Sialon, while having comparable radar properties to other candidates (with the exception of CVD Si_3N_4), is predicted to have about one-half the thermal shock resistance because of its lower thermal conductivity.

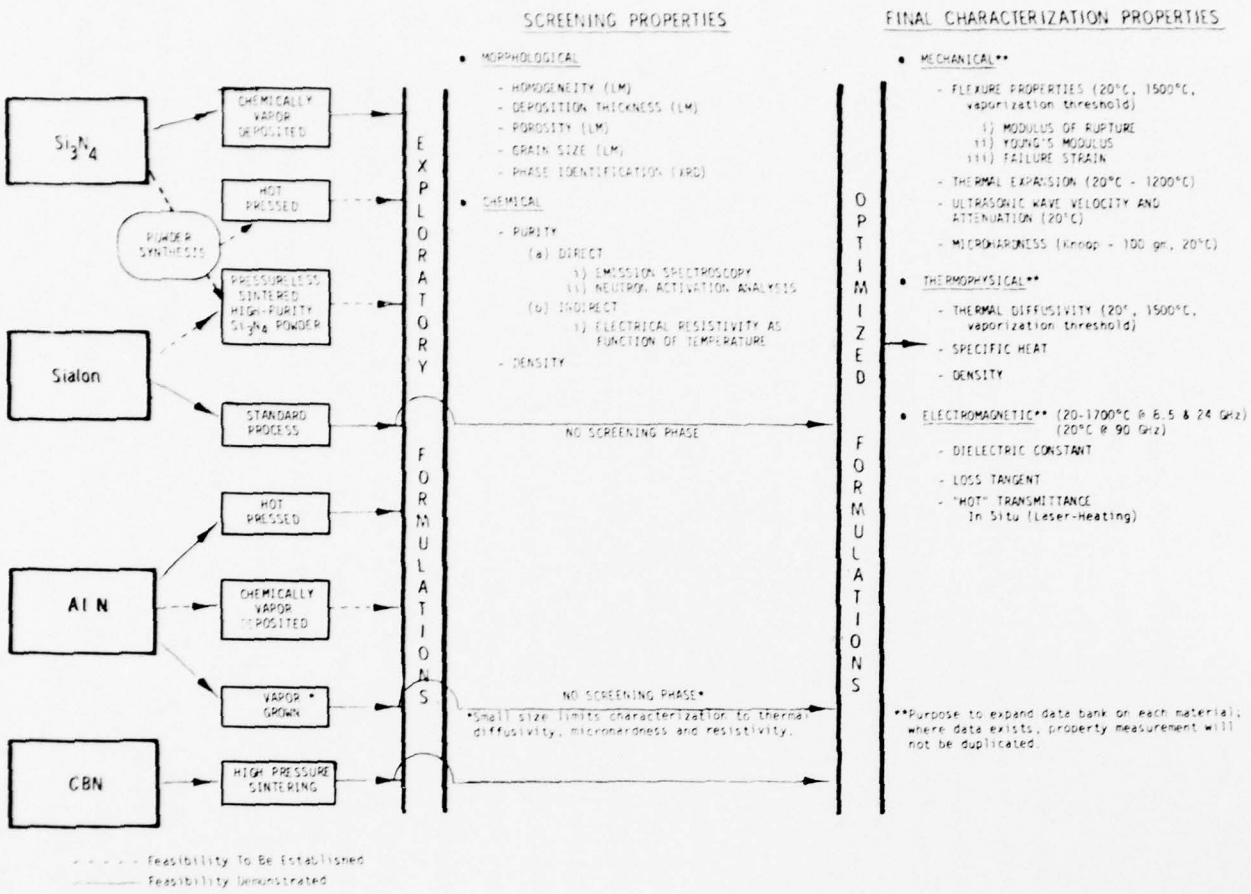

Figure 84. Process Development and Evaluation Roadmap for Nitride-Based Ceramics

TABLE 42. PROPERTY COMPARISONS FOR CANDIDATE NITRIDE-BASED CERAMICS. ALSO SHOWN ARE DATA FOR HOT-PRESSED Si_3N_4

Fabrication Process			CBN	AlN			Si_3N_4			$Si_4Al_2N_6O_2$	
			High. Press.*	Hot-Press.* (Vapor Gr*)			CVD*		(1)Hot-Press.**	**Sintered*	
$\bar{\alpha} \cdot 10^6$ (1/°C)RT-1000°K			5.8	6.0			3.5		3.0	3.0	
$E \cdot 10^{-6}$ (psi)			101	50			45		45	30	
k(W/cm-°C) @ 1000°K			3.3	0.32		(0.51)	0.18		0.17	0.05	
$(k/\bar{\alpha}E) \cdot 10^4$ @ 1000°K			56.0	10.7		(17.0)	11.0		11.3	5.8	
$Knoop_{100g}$ (kg/mm^2)			4700	1225			2570		1954	1660	
γ_E (J/m^2)			—	—			29.7		31.7	9.7	
K_{IC} ($MN/m^{3/2}$)			—	—			3.2-4.3 (Ref20)		4.7	2.2	
Radar		GHz	24	8.5	24	(24)	8.5	24	24	8.5	24
	RT	ϵ	7.0	6.04	5.99	(7.96)	7.64	7.65	8.25	7.67	7.65
		$\tan\delta$	0.0048	0.0011	0.0021	(0.0206)	<0.0003	<0.0006	0.0040	0.0014	0.0028
	800°C	ϵ	—	—	6.55	—	7.9	7.93	8.59	8.21	8.02
		$\tan\delta$	—	—	0.0044	—	<0.0003	<0.0006	0.0056	0.0017	0.0025
Ablation Morphology (After Laser Vaporization)				Oxidation (Al_2O_3); Evidence of Congruent vaporization.			Oxidation (SiO_2); Non-congruent vaporization. (Si melting observed)			Oxidation (Al_2O_3, SiO_2); Possibly Congruent Vapor. (No evidence of Al or Si Melting)	

*Candidates being developed and/or evaluated on this contract.

**Zero rain erosion in Hollomon M=5 Sled Test (14th Sym. EM Windows, Meyer/Letson).

(1) Typical of commercial hot-pressed Si_3N_4.

With regard to surface vaporization behavior, data collected to date indicate that both AlN and β'-Sialon may be able to transmit radar frequencies while vaporizing. Cubic BN will transform to the hexagonal form above 1600°C and should be a clean ablator. Conversely, CVD Si_3N_4 (and probably hot-pressed Si_3N_4) exhibit non-congruent vaporization behavior making them questionable in their ability to transmit radar frequencies while the surface is vaporizing (which may occur during a high velocity mission). Synergistic simulation experiments (e.g., combined ablation and radar transmittance), however, will be required to obtain conclusive data regarding the issue of "hot" transmittance capability.

More detailed discussions of each candidate's performance characteristics are given in the following sections.

7. SILICON NITRIDE

7. SILICON NITRIDE

7.1 INTRODUCTION

7.1.1 APPLICATION AS A MILLIMETER WAVE WINDOW

The more conventional forms of silicon nitride (hot-pressed (HP), reaction sintered (RS)) could exhibit serious deficiencies with regard to exhibiting acceptable transmittance levels of millimeter wave radar at temperatures approaching as well into the vaporization range of silicon nitride. This concern is based upon the fact that metallic impurity contents in the above commercially available modifications range from about 0.6 weight percent (w/o) for RSSN to over 2.3 w/o for HPSN (Ref. 21). In addition, non-metallic impurities, in particular, oxygen are present in both commercial modifications (Ref. 22).

7.1.2 CHEMICALLY VAPOR DEPOSITED SILICON NITRIDE

Silicon nitride (Si_3N_4), prepared by the chemical vapor deposition method, offers an alternative consolidation technique which produces theoretically-dense forms of Si_3N_4 of previously unattainable ultra-high purity levels. Under company and government sponsored research (Ref. 20), processing methods have been developed resulting in the formation of near-theoretically dense plate with negligible metallic impurity levels and oxygen impurity levels as low as 0.36 w/o. Room temperature radar measurements at 10 GHz on such deposits produce loss tangent levels at least an order of magnitude lower than commercially-available hot pressed Si_3N_4. As will be discussed in subsequent sections of this report, this trend of superior radar properties for CVD-Si_3N_4 (compared to commercial modifications) continues both at elevated temperatures and over a range of radar frequencies from 8.5 to 24 GHz.

7.2 CHEMICAL VAPOR DEPOSITION OF FREE-STANDING PLATE

7.2.1 PROCESS DESCRIPTION

The general procedure for forming CVD Si_3N_4 consists of passing a mixture of vapor-borne precursors into a chamber, hot wall or cold wall, within which the precursors react and form deposition species. These then adhere to the heated substrate and crystallize. The process is continued until desired thicknesses are achieved. The chemistry and detailed transformation processes (deammination, crystal growth, etc.) involved in formation of deposits of certain characteristics are at present inferred primarily through analysis of the materials and correlation with the deposition conditions (temperature, pressure, gas feed rate and concentration, gas flow dynamics, substrate characteristics, etc.).

Silicon nitride can be formed from the vapor phase by interaction of ammonia and a silicon halide (e.g., silicon tetrachloride, -fluoride or -bromide), a silane derivative (e.g., chlorosilane SiH_xCl_y ($x + y = 4$), or silane itself (SiH_4). Typical gross reactions are:

$$3\ SiCl_4 + 4NH_3 \longrightarrow Si_3N_4 + 12\ HCl$$

$$3\ SiF_4 + 4NH_3 \longrightarrow Si_3N_4 + 12\ HF$$

$$3\ SiH_4 + 4NH_3 \longrightarrow Si_3N_4 + 12\ H_2$$

In this work, α-Si_3N_4 plate was prepared using the $SiCl_4$ precursor since previous research (Ref. 20) had shown that this precursor provided the highest deposition rate, and largest as-deposited thicknesses thereby offering the potential for direct radar property measurement with minimal stacking of flat-plate specimens to achieve desired specimen thicknesses.

Ten (10) process runs were performed using a four (4) inch diameter hot-wall deposition furnace to define optimum conditions for forming thick, flat-plate, deposits of ultra-high purity. Process parameters explored in this series included: temperature, pressure, feed ratios of silicon and nitrogen, feed rate, mandrel geometry and deposition time.

The deposition system used for this study consisted of a resistively heated graphite furnace, 10 cm diameter by 25 cm high through which reacting gases passed at reduced pressure. The deposition occurred within a replaceable graphite chamber inserted into the furnace hot zone. This chamber was typically a four or six sided channel made of graphite plates, within which additional graphite plates are suspended to provide a larger deposition surface.

Figure 85 shows a typical deposition mandrel with a square cross-sectional area. Flow deflectors, such as that shown in Figure 85, were used to improve deposition uniformity.

Table 43 lists the experimental conditions used and tabulates results in terms of deposition rate, process efficiency and deposition microstructure. Initial experiments in this series provided amorphous deposits which were unsatisfactory for conducting material characterization studies. Previous evaluations indicated that this form of Si_3N_4 exhibits poor strength as the result of porosity and/or microcracked microstructure. The most satisfactory material prepared in this exploratory series was obtained from Run No. 191, which provided the thickest free-standing deposit (maximum thickness ~ 1.57 mm).

Figure 86 shows free standing α-Si_3N_4 plate after removal from graphite mandrels by oxidation. The translucency of as-deposited plate is clearly in evidence (Figure 86(a)). Also shown is the thickness profile for plate material which was removed by oxidation from the flow-deflector mandrel. Typical radar specimens extracted from the plate material are also shown (Figure 86(c)). In order to arrive at required radar specimen thicknesses, it was planned to stack these discs to arrive at optimum specimen configurations for measurement.

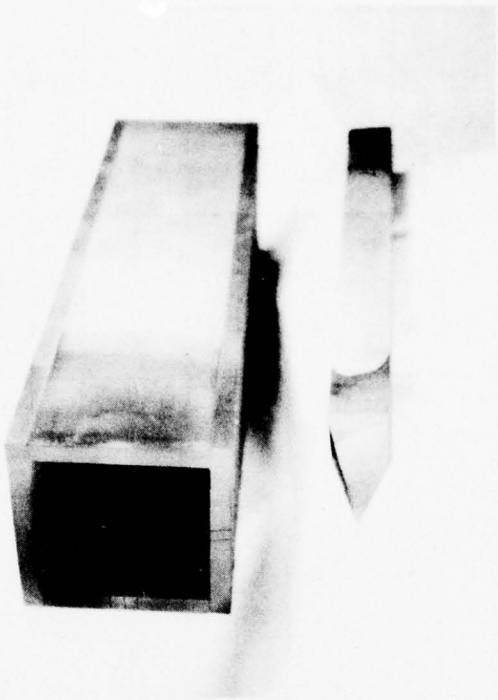

Figure 85. Graphite Deposition Mandrel for Forming CVD Flat-Plate Deposits. Also Shown Is Flow Deflector Rod—Centrally Located Within Mandrel During Deposition. Deposition Plate Area Per Side ~ 5.1 x 20.3 cm

7.2.2 PROPERTY CHARACTERIZATION

7.2.2.1 Screening Properties

Selection of the highest purity material from a given deposition experiment was based upon previously developed correlations relating deposition color to oxygen impurity content (Ref. 20) such as shown in Table 44. The highest purity material in this deposit was brown in color and did not fluoresce when exposed to ultraviolet radiation of wavelength 3360Å. On the basis of these earlier correlations, radar specimens from Run 191 were selected which were brown in color.

7.2.2.2 Radar Properties

Table 45 lists numerically the nine α -Si_3N_4 specimens (extracted from Run 191) which were submitted for radar property evaluations at 8.5, 24.0 and 90.0 GHz. Where possible, specimens were stacked to achieve optimum thicknesses for a given frequency. This stacking technique, however, presented handling problems for elevated temperature measurements and was not pursued. Good agreement was obtained between measurements on stacked discs and individual discs, however, at room temperature. Even though specimen thicknesses were not optimum,

TABLE 43. SILICON NITRIDE PLATE DEPOSITION RUNS

Run No.	Mandrel Geometry	Temp. (°C)	Pressure (torr)	Time (hrs)	Precursor Gas Flow Rate (cc/m)				N:Si Ratio	Residence Time (msec)	Velocity (m/sec)	Conversion (%)	Max. Depos. Rate (mm/hr)	Wt. Incr. of Set-up (gms)	Si Used (gms)	Deposit Characteristics
					$SiCl_4$	NH_3	H_2	N_2								
182	Hex. box	1500	1.5	13.0	275	300	2650	-	1.09	5.5	37.81	28.8	0.052	128.6	1624.6	Amorphous, flaky, blistered, white
183	Hex. box	1515	5.0	2.5	leak in line	-	2650	-	-	-	-	-	-	-	-	Aborted Run
184	Hex. box	1497	4.5-7.0	16.0	338	470	2650	-	1.39	17.8	11.70	68.0	-	460.7	2464	Amorphous, sooty, modular, white
185	Hex. box	1515	5.0	1.0	224	480	-	500	2.14	48.6	4.28	-	0.175	-	102	Amorphous, smooth, white
186	Hex. box	1465	5.0	1.0	207	480	-	500	2.32	50.8	4.10	-	0.200	-	94	Amorphous, smooth, white
187	Hex. box	1420	5.0	1.0	222	480	-	500	2.16	51.5	4.05	-	0.225	-	101	Amorphous, smooth, white
188	Hex. box	1490	5.0	1.5	107	1200	-	-	11.20	45.4	4.58	51.2	0.058	35.0	85	Crystalline/Amorphous white
189	Sq. box	1500	5.0	2.0	126	600	-	-	4.76	39.4	2.55	9.9	-	19.0	15	Amorphous, smooth white
190	Sq. box	1475	6.0	2.0	255	2400	-	-	9.40	13.1	16.2	20.4	0.363	13.0	232	Crystalline, brown white
191	Sq. box	1475	6.0-7.0	6.0	200	2400	-	-	12.00	14.4	14.6	58.5	0.204	87.7	546	Crystalline, brown to white

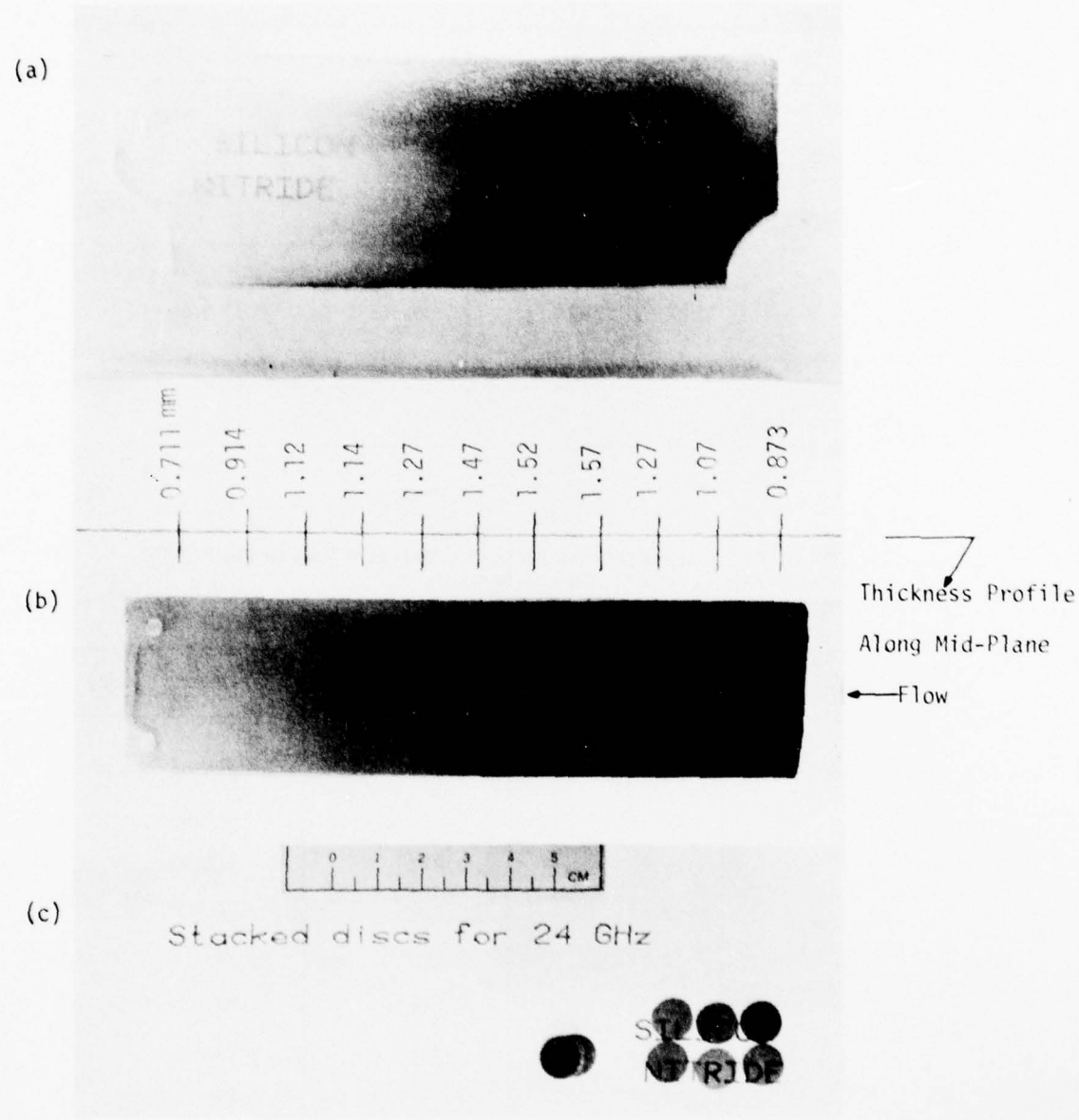

Figure 86. As-Deposited α-Si_3N_4 (Run 191) Plate After Removal of Graphite Mandrel by Oxidation (a). As-Deposited α-Si_3N_4 (Run 191) After Removal from Graphite Flow Deflector. Thickness Varies from 28 to 62 mils (b). Typical Radar Specimens Extracted from Deposition Plate (c).

TABLE 44. CORRELATION OF α-Si_3N_4 DEPOSIT COLOR WITH OXYGEN CONTENT AND DEGREE AND COLOR OF ULTRAVIOLET FLUORESCENCE

Specimen Designation	139-W1	139-G1	139-B5
Visual Color	White	Green	Brown
O2 Content,* W/O	1.40	0.92	0.40
Trace Impurities (Emission Spec.)			
ppm Mg	60	20	80
ppm Fe	300	180	380
ppm Al	60	40	30
ppm Cu	20	10	ND
Fluorescence to 3360 A			
Visually Observed	Yes	Yes	No
Color of Fluorescence	Pink	Yellow-green	Not observed
*Neutron Activation Analysis			

TABLE 45. LIST OF CVD α-Si_3N_4 SPECIMENS SUBMITTED FOR RADAR PROPERTY MEASUREMENT AT 8.5, 24.0 AND 90.0 GHz

Specimen Designation	Diameter (mm)	Thickness (mm)	Frequency (GHz)
191 - 1	25.40	0.483	8.5,90
191 - 2	25.40	0.508	8.5,90
191 - 3	25.40	0.813	8.5,90
191 - A	9.51	0.826	24
191 - B	9.51	0.965	24
191 - C	9.51	0.686	24
191 - D	9.51	0.965	24
191 - E	9.51	0.711	24
191 - F	9.51	0.838	24

sufficient measurement accuracy and precision was obtained to permit a meaningful assessment of the potential for CVD α-Si_3N_4 as a high-temperature millimeter wave antenna window.

Tables 46 and 47 list the radar property data on CVD α-Si_3N_4 at 8.5 and 24.0 GHz, respectively. Also, shown for comparison in Table 47 are data for a commercially-available hot-pressed silicon nitride measured at the same frequency over the same temperature range using identical equipment.

At 24 GHz (which is near the frequency of interest for this program) CVD α-Si_3N_4 has a significantly lower loss tangent than commercial-grade hot-pressed Si_3N_4 over the temperature range from 25 to 800°C. This order of magnitude spread in loss tangent is anticipated to widen as temperatures approach the intrinsic vaporization point of Si_3N_4. At temperatures near 1400°C, the sintering aids used to consolidate hot pressed Si_3N_4 become plastic resulting in large decreases in mechanical strength (>100%).

It is anticipated that this mobile second phase will adversely affect the dielectric properties of hot-pressed Si_3N_4 at temperatures beyond 1400°C. Conversely, it is anticipated that the ultra-low loss tangent of CVD α-Si_3N_4 will continue to show negligible temperature dependence up to the vaporization range of Si_3N_4 (~1700°C).

TABLE 46. RADAR TRANSMITTANCE PROPERTIES OF CVD α-Si_3N_4 AT 8.5 GHz FROM 25 TO 800°C

CVD α-Si_3N_4 @ 8.5 GHz			
Specimen Designation	Temperature (°C)	Dielectric Constant (K)	Loss Tangent (tan δ)
191-1	25	7.64	<.0003
	99	7.66	<.0003
	205	7.70	<.0003
	327	7.74	<.0003
	408	7.77	<.0003
	509	7.81	<.0003
	595	7.84	<.0003
	704	7.88	<.0003
	755	7.90	<.0003
	800	7.92	<.0003

TABLE 47. RADAR TRANSMITTANCE PROPERTIES OF CVD α-Si_3N_4 AND HOT-PRESSED SILICON NITRIDE

CVD α - Si_3N_4 @ 24 GHz			
Specimen Designation	Temperature (°C)	Dielectric Constant (K)	Loss Tangent (tan δ)
191-F	25	7.65	<.0006
	62	7.66	<.0006
	133	7.67	<.0006
	162	7.68	<.0006
	224	7.72	<.0006
	276	7.73	<.0006
	324	7.75	<.0006
	399	7.77	<.0006
	479	7.80	<.0006
	564	7.83	<.0006
	618	7.85	<.0006
	679	7.88	<.0006
	736	7.89	<.0006
	747	7.90	<.0006
	800	7.93	<.0006
Stack of 191-A,B,C,D,F	25	7.63	.00043
Hot-Pressed Si_3N_4 @ 24 GHz (Ref. 22) (Low Dielectric Constant Direction)			
NC-132	22	8.25	.0040
	100	8.26	.0042
	200	8.28	.0045
	300	8.31	.0047
	400	8.35	.0048
	500	8.39	.0049
	600	8.44	.0051
	700	8.51	.0054
	800	8.59	.0056

7.2.2.3 Other Physical Properties

Table 48 summarizes other pertinent thermophysical and thermostructural properties of CVD α-Si_3N_4 at its current stage of development.

7.2.2.4 Vaporization Characteristics

A qualitative investigation of the vaporization behavior of CVD α-Si_3N_4 was conducted in air using a 15KW CO_2 laser beam to create surface temperatures sufficiently high to induce surface vaporization. Four (4) specimens were evaluated at intensities ranging from 500 to 1000 W/cm^2 and exposure times of 4 to 15 seconds. Figure 87 shows a typical surface condition for specimens in this series. Evidence of non-congruent vaporization is conclusive, in that solidified droplets of silicon metal extensively cover the surface. Also, a white layer of SiO_2 is clearly in evidence. The potential problem of "hot" transmission while Si_3N_4 is vaporizing must be further investigated by subsystem simulation testing.

7.3 PREPARATION OF PURE SILICON NITRIDE POWDER

Two approaches have been considered in this program for preparation of pure, stable, finely divided silicon nitride powder. One is based on controlled thermal decomposition of the reaction intermediates that occur in chemical vapor deposition of silicon nitride from silicon tetrachloride-ammonia mixtures:

$$SiCl_4 + NH_3 \longrightarrow SiCl_4 \cdot x\,NH_3$$

$$Si_3N_4 \longleftarrow Si(NH)_x \text{ polymers}$$

The second approach is based on nitriding of finely divided, high purity silicon powder, a source for which has recently been found.* The particle size of this material, which is prepared by thermal decomposition of silane, averages 300 Å, which should be small enough to permit total nitridation rather than leaving unreacted silicon in the center of the particle. A laboratory-scale nitriding furnace system was designed and assembled on this phase of the program and will be used for Si_3N_4 powder preparation on the next phase of the program.

More directly, amorphous silicon nitride was prepared by reacting ammonia and silicon tetrachloride in the four inch chemical vapor deposition furnace used for fabricating CVD silicon nitride plate material. By increasing pressure and residence time of the gas mixture in the furnace, the formation of a monolithic deposit was prevented and a relatively large quantity of powdered white nitride: ammonia complex material was deposited in the downstream regions of the furnace. This was collected quickly under a nitrogen blanket to minimize hydrolysis, placed in the furnace hot zone on a graphite platform, and heat treated for 1.5 hours at 1180°C under a

*Callery Chemical Company, Callery, PA.

TABLE 48. THERMAL AND MECHANICAL PROPERTIES OF CVD α-Si_3N_4

Thermophysical		
• Density (g/cc)		3.18
• Specific Heat* $\left(\frac{cal}{(g-^oK)}\right)$,	300 ^oK	0.165
	600^o	0.224
	1000^o	0.276
	2000^o	0.326
• Thermal Conductivity $\left(\frac{W}{cm^oK}\right)$	300^{o}K	0.328
	553^o	0.241
	1103^o	0.158
	2000^o	0.118
• Hemispherical Emittance**	293^{o}K	0.590
	773^o	0.540
	1273^o	0.340
	1773^o	0.240
Thermostructural		
• Mean Thermal Expansion Coeff.	$(1/^oC)$, (RT-1000^{o}C),	3.07×10^{-6}
• Young's Modulus	(GNm^{-2}), RT	389.6
• Flexure Strength (3 pt., 10 specimens)	(MNm^{-2}), RT	223.2
• Failure Strain, (%)		0.06
• Fracture Toughness	$(MNm^{-3/2})$	3.2-4.3 (Ref. 20)
• Microhardness, Knoop, (Surface ⊥ to Deposit, 100 gm load)	$(kg\ mm^{-2})$	3780-4240

* Estimated from TPRC Data

** Computed from Specular Reflectance Data

$\underline{\text{CVD-Si}_3\text{N}_4}$

400-191

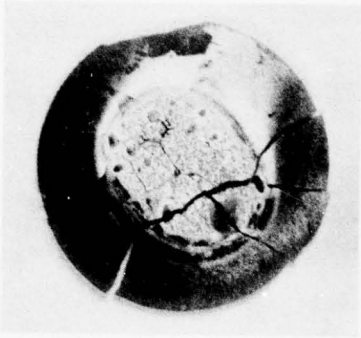

$\underline{1000\ \text{W/cm}^2,\ 4\ \text{Sec.}}$

Figure 87. Post-test Surface Condition of CVD α-Si_3N_4 After Vaporization. Point-loaded at 1000 W/cm^2, 4 sec With a Beam Diameter: Specimen Diameter = 0.50.

slow flow of nitrogen at 15 torr. The powder charge was reduced in volume considerably through loss of ammonium chloride, a co-by-product collected with the ammine complex, but remained white and powdery.

Future work will involve the consolidation of these ultra-high purity powders to form dense phase-pure silicon nitride, and also, the utilization of these powders to form higher-purity β'-Sialon plate.

AD-A076 769 GENERAL ELECTRIC CO PHILADELPHIA PA RE-ENTRY AND ENV--ETC F/G 17/5
MILLIMETER WAVE HARDENED ANTENNA WINDOW MATERIALS DEVELOPMENT.(U)
AUG 79 J P BRAZEL , R FENTON , J A ROETLING DAAG46-79-C-0047
UNCLASSIFIED AMMRC-TR-79-45 NL

3 OF 3
AD A076769

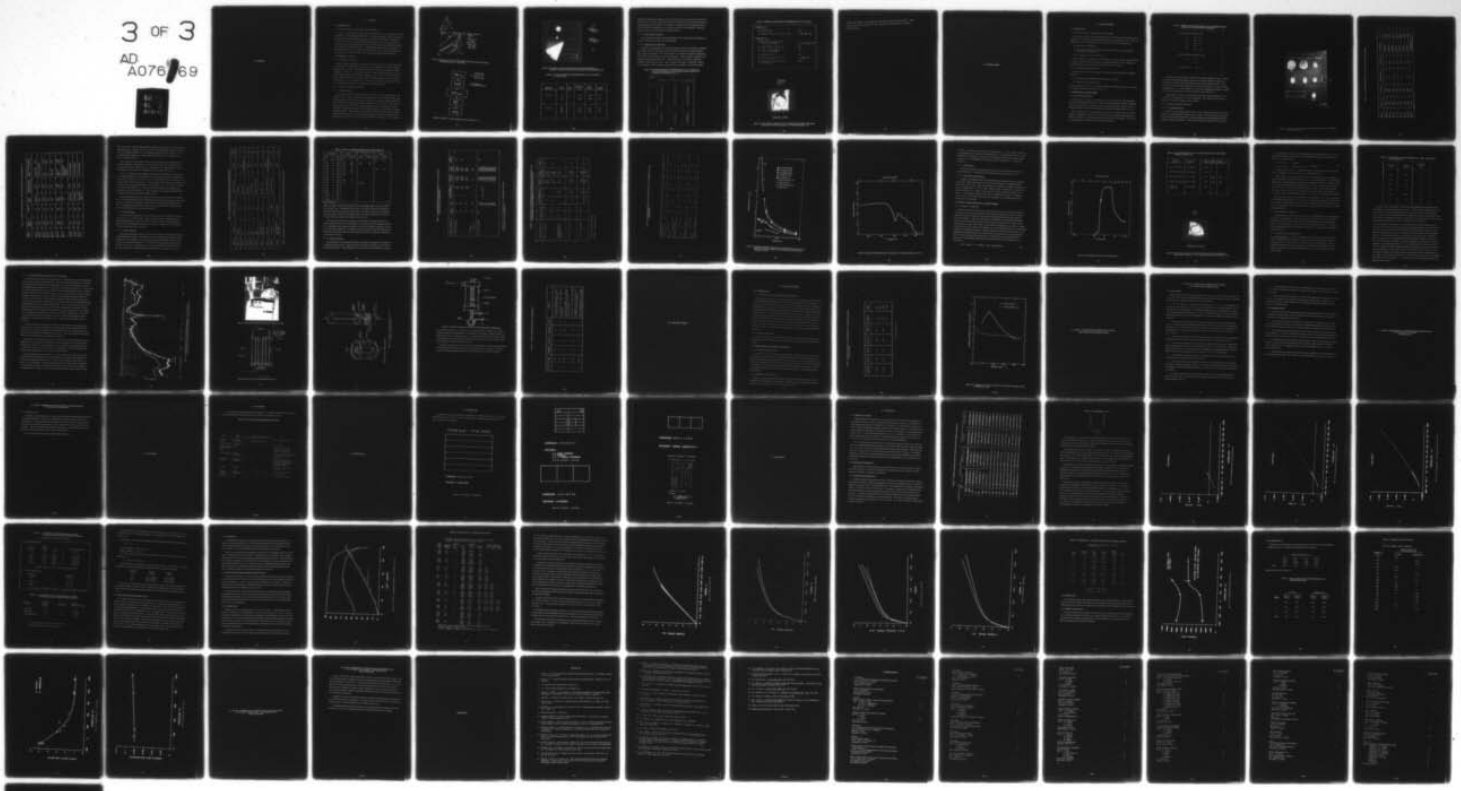

END
DATE FILMED
12-79
DDC

8. β'–SIALONS

8. β'–SIALONS

8.1 INTRODUCTION

8.1.1 APPLICATION AS A MILLIMETER WAVE WINDOW

Under a recently completed AFML-sponsored program (Ref. 23), a sintering process was developed for producing theoretically-dense β' - Sialon solid solutions. Radar property measurements on these solid solutions at 8.5 and 24 GHz indicate performance comparable to hot-pressed silicon nitride, but with the distinct advantages of lower cost processing and, also, the ability to form theoretically-dense complicated shapes using conventional pressureless-sintering consolidation procedures. Although its thermal shock-resistance figure is lower than that of hot-pressed silicon nitride (because of its lower thermal conductivity), it may still provide sufficient margins for the contemplated antenna window application.

8.2 SINTERABLE β'–SIALON

8.2.1 PROCESS DESCRIPTION

Figure 88 shows the isothermal quaternary section (1760° C) of the Si-Al-O-N phase diagram in which the β' single-phase region is located. The particular β'-Sialon evaluated on this program was the GE-128 modification which has the following stoichiometric formula: $Si_4Al_2N_6O_2$. Figure 89 is a schematic of the process used for synthesizing the GE-128 composition which consists of the following constituents: 50 m/o Si_3N_4, 25 m/o AlN and 25 m/o Al_2O_3. Figure 90 shows the specimens of GE-128 β'-Sialon prepared for radar property measurement at 8.5, 24.0 and 90.0 GHz. Also shown is a ground and polished GE-128 subscale radome illustrating the scale-up potential of the sintering process.

8.2.2 PROPERTY CHARACTERIZATION

8.2.2.1 Radar Properties

Table 49 lists radar transmittance properties of the GE-128 β'-Sialon measured on this program at 22° C. Elevated temperature data obtained on a recently completed AFML sponsored program (Ref. 21) is listed in Table 50. Both sets of data show a definite dependence of loss tangent on frequency, approximately doubling from 8.5 to 24.0 GHz. Since both sets of data were measured on identical equipment, differences in loss tangent and dielectric constant for nominally similar material is attributed to differences in the purity of starting constituent powders. This dependence will be further investigated on the next program phase. It is noteworthy that both sets of loss tangent data and their temperature dependence show significant improvements over commercially-available hot-pressed Si_3N_4. For example, the

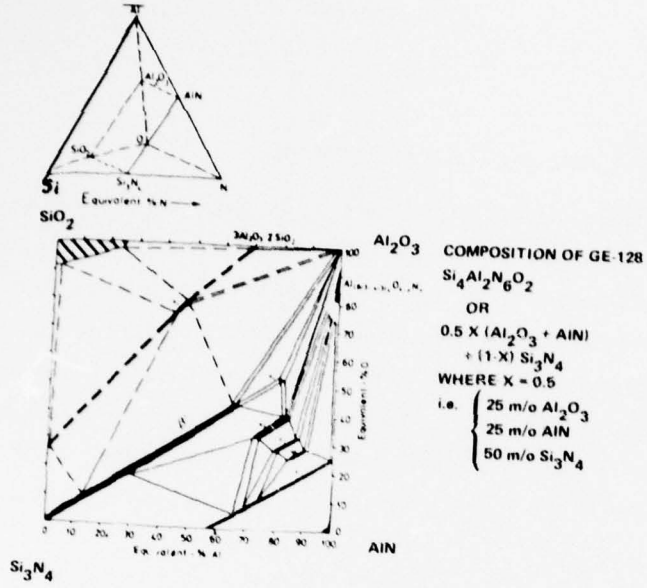

Figure 88. Subsection of the Si-Al-O-N Phase Diagram Showing a Si_3N_4-AlN-Al_2O_3-SiO_2 Isothermal Plane and the β'—Sialon Phase

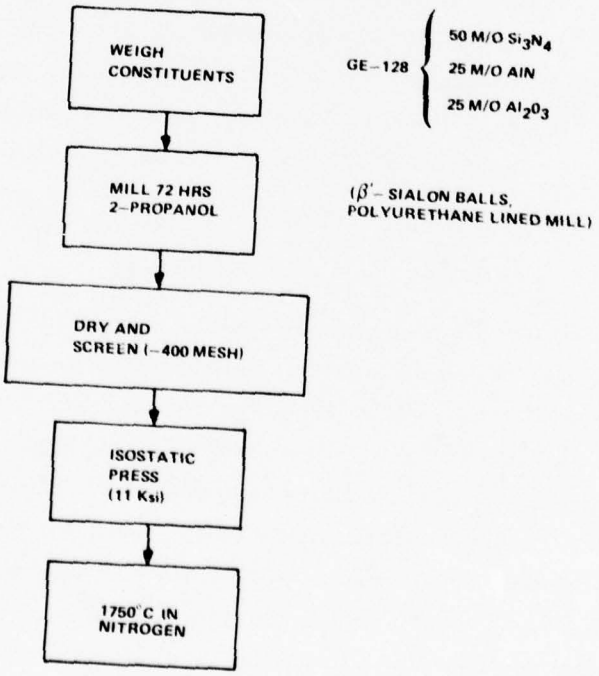

Figure 89. Schematic of Current Sintering Process for Forming GE-128

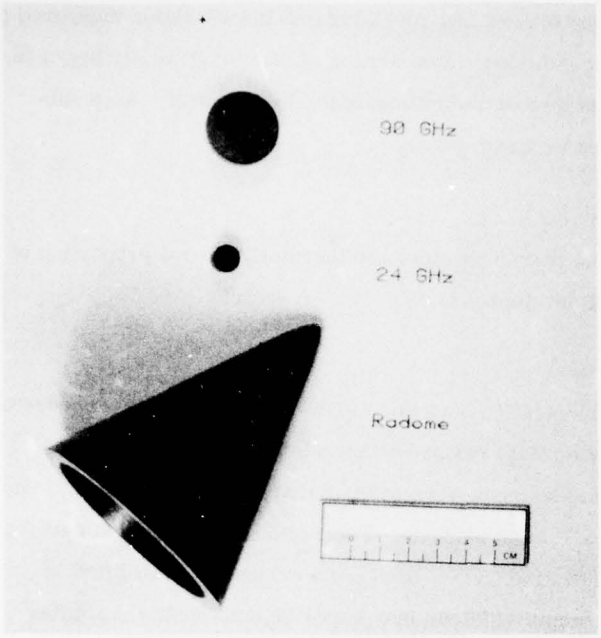

(A)

GE-128-1
(25.4mm dia. x
4.75 mm)

GE-128-2
(9.51 mm dia. x
4.78 mm)

(B)

Figure 90. Photograph Showing GE-128 Sialon Specimens for Radar Measurement (A). Also Shown is a Subscale Radome Fabricated Using the GE-128 Sintering Process (B).

TABLE 49. RADAR TRANSMITTANCE PROPERTIES OF GE-128 β'–SIALON AT 8.5 AND 24.0 GHz

Specimen Designation	Orientation	Temp. (^{o}C)	Dielectric Constant (K)	Loss Tangent (tan δ)	Frequency (GHz)
GE-128-1	0^{o}	22	7.907	.00305	8.5
	90^{o}		7.889	.00313	8.5
GE-128-2	70^{o}	22	8.470	.0067	24.0
	90^{o}		8.450	.0067	24.0

dielectric constant and loss tangent of commercial grade hot-pressed Si_3N_4 (NC-132) at 800° C and 24 GHz are 8.59 and 0.0056 compared to 8.02 and .0025 for GE-128 β'-Sialon measured on identical equipment under identical test conditions. Substitution of ultra-high purity Si_3N_4 in the β'-Sialon process should lead to even further reductions in the loss tangent. Such substitutions will be explored during the next program phase.

8.2.2.2 Other Physical Properties

Table 51 summarizes other pertinent thermophysical and thermostructural properties of GE-128 β'-Sialon at its current stage of development.

8.2.2.3 Vaporization Characteristics

A qualitative investigation of the vaporization behavior of GE-128 β'-Sialon was conducted in air using a 15KW CO_2 flat-top beam to create surface temperatures sufficiently high to induce surface vaporization. Three (3) specimens were evaluated at intensities ranging from 250 to 500 W/cm^2 and exposure times of 7 to 30 seconds. Figure 91 shows a typical surface condition for specimens in this series. Unlike CVD α-Si_3N_4, no evidence of solidified droplets of silicon metal was found. Thus, β'-Sialons may vaporize congruently. Similar to CVD α-Si_3N_4, a white oxide layer was found which is probably a mixed oxide (probably

TABLE 50. RADAR TRANSMITTANCE PROPERTIES OF GE-128 β'-SIALON AS A FUNCTION OF FREQUENCY AND TEMPERATURE MEASURED ON A PREVIOUS AFML PROGRAM (Ref. 21)

Specimen Designation	8.5 GHz		
	Temperature (°C)	Dielectric Constant (K)	Loss Tangent (tan δ)
GE-128-2-AF	25	7.67	.0014
	100	7.72	.0014
	200	7.78	.0015
	300	7.85	.0015
	400	7.91	.0015
	500	7.97	.0015
	600	8.05	.0015
	700	8.13	.0016
	800	8.21	.0017
	900	8.30	.0018
	1000	8.40	.0021
	1100	8.51	.0026
	1150	8.57	.0030
	1200	8.62	.0037
	1220	8.65	.0040
	1250	8.70	.0050
	1270	8.75	.0098
	24 GHz		
GE-128-2-AF	25	7.65	.0028
	100	7.67	.0022
	200	7.69	.0024
	300	7.73	.0025
	400	7.78	.0026
	500	7.84	.0027
	600	7.89	.0027
	700	7.95	.0026
	800	8.02	.0025

TABLE 51. THERMAL AND MECHANICAL PROPERTIES OF GE-128 β'–SIALON

THERMOPHYSICAL	
• Density (g/cc)	3.08
• Thermal Diffusivity (cm^2/sec.), 573°K	0.0195 (Ref. 24)
THERMOSTRUCTURAL	
• Mean Thermal Expansion Coeff. (1/°C), (RT-1000°C),	3.0×10^{-6} (Ref. 24)
• Young's Modulus (GNm^{-2}), RT	207.
• Flexure Strength (MNm^{-2}), RT (4 pt., 2 specimens)	216.
• Failure Strain, (%)	0.10
• Fracture Toughness ($MNm^{-3/2}$)	2.2 (Ref. 24)
• Microhardness, Knoop (kg mm^{-2}) (100 gm load)	1660

$Si_4Al_2N_6O_2$

GE-128

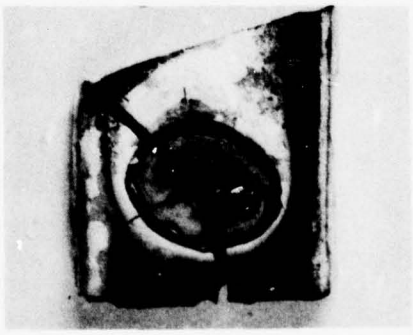

250 W/cm^2; 30 Sec.

Figure 91. Post-Test Surface Condition of GE-128 β'–Sialon After Vaporization. Point Loaded at 250 W/cm^2, 30 Seconds with a Beam Area: Specimen Area Ratio ~0.50

a mullite solid solution). Also evident in the rim of the specimen was a glassy phase. Thus, β'-Sialons may offer the potential for "hot" transmittance at temperatures exceeding its vaporization point.

9. ALUMINUM NITRIDE

9. ALUMINUM NITRIDE

9.1 INTRODUCTION

9.1.1 APPLICATION AS A MILLIMETER WAVE WINDOW

Recent processing research on aluminum nitride has produced material of unprecedented purity and size to permit measurement of intrinsic physical properties (Ref. 25). Three (3) characteristics (of ultrahigh-purity AlN) of particular interest to this program are:

(1) AlN vaporizes congruently

(2) Its thermal conductivity at 100° C exceeds most insulators, approaching that of copper (within a factor of 1.6)

(3) Its resistivity at 20° C is 10^{13} Ω-cm.

These properties could translate into a millimeter wave window with good thermal shock resistance, and with the added potential of transmitting millimeter radar at temperature levels approaching and beyond the vaporization range of AlN (~1700° C).

9.1.2 PROCESSING RESEARCH PLAN

Two (2) approaches have been followed for synthesizing theoretically dense ultrahigh purity AlN:

(1) Hot-pressing of ultrahigh-purity fine diameter AlN powder

(2) Chemical vapor deposition of AlN

Also, vapor-grown crystals were obtained to establish key intrinsic properties over temperature ranges previously not characterized (Ref. 25).

9.2 HOT-PRESSED ALUMINUM NITRIDE

9.2.1 PROCESS DESCRIPTION

The objective of this task was to synthesize near theoretically dense, ultrahigh purity AlN by consolidating the highest purity, commercially available powder using a combination of elevated temperature and external pressure to augment solid-state sintering. Table 52 lists the chemical analysis of the ultrahigh purity AlN powders obtained from Cerac, Inc.

Since AlN powders react readily with air, the powders were kept in a dry box to avoid moisture contamination. Before a hot press run, the dies were filled with the powders in the dry box enclosure and immediately transferred to the hot press apparatus. The system was rough pumped and then purged with a nitrogen atmosphere.

TABLE 52. CHEMICAL ANALYSIS (BY CERAC, INC.) OF ALUMINUM NITRIDE POWDER USED IN HOT-PRESSING EXPERIMENTS

- TRACE METALLIC IMPURITIES (w/o)

Cu :	.0005 - .005
Fe :	.001 - .01
Si :	.0005 - .005
Mn :	.001
Mg :	.0005 - .005

- TRACE NON-METALLIC IMPURITIES (w/o)

C :	.01 - .05
O :	.12

- ESTIMATED PURITY: 99.8 w/o

The powders were hot pressed according to the conditions outlined in Table 53. Future experiments should include additional variations in die material (BN liners) and type of sintering gas for further improving the purity and the density of hot pressed AlN. Also, recent hot pressing research by Sakai (Ref. 26) will be reviewed since a critical level of O_2 contamination (viz. ~2 w/o) was found to lead to improved densification and flexure strength at more moderate temperatures (~2000° C) than those used in this series.

A photograph of several of the hot-pressed specimens is shown in Figure 92. The specimens are arranged in order of increasing density. The temperature and pressure parameters of the hot pressing are listed in Table 53.

9.2.2 PROPERTY CHARACTERIZATION

9.2.2.1 Screening Properties

Table 54 lists screening properties (density, color, resistivity) used to assess the suitability of a given formulation for further characterization. Several of the hot-pressed specimens came out of the run black due to carbon contamination from the graphite dies and the graphite resistance heated furnace. Most often, the specimens could be renewed in air at

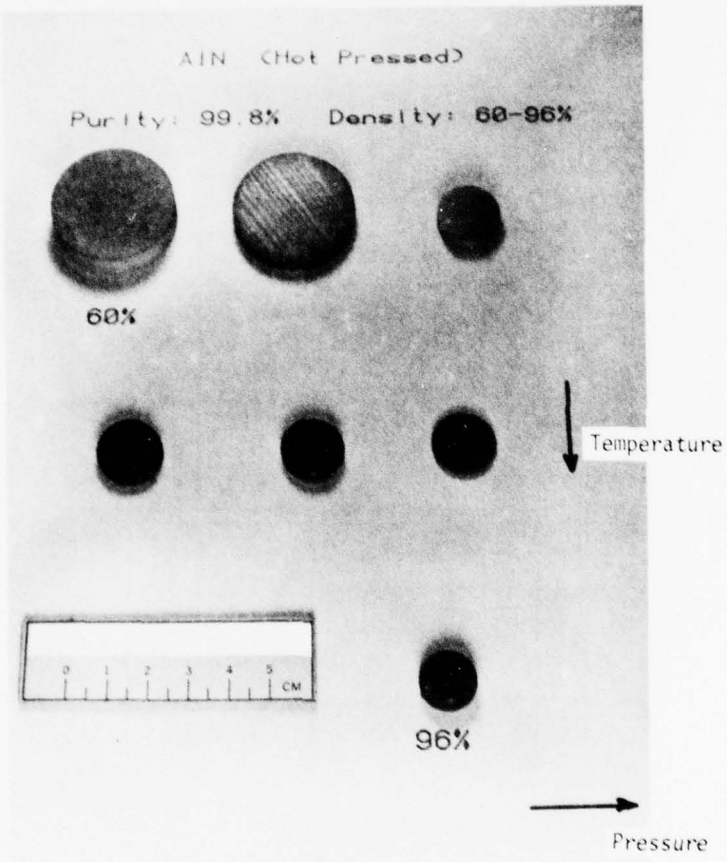

Figure 92. Photograph of Hot-Pressed AlN Specimens Illustrating Density Increasing With Temperature and Pressure

TABLE 53. HOT-PRESS EXPERIMENTS CONDUCTED ON ALUMINUM NITRIDE

Sample	Temp. (°C)	Press (psi)	Run Time (hr.)	Ambient gas	Die Material	Density (%)
HP-19	2000	2000	4	N_2	graphite	60
HP-20	2200	2000	4	N_2	graphite	82
HP-21	2200	3000	4	N_2	graphite	81
HP-22	2300	3395	.17	N_2	graphite	77
HP-24	2300	4000	1	N_2	graphite	94
HP-26	2200	5000	1	N_2	graphite	80
HP-27	2400	4000	.25	N_2	graphite	97
HP-30	2350	5000	.25	N_2	C-C polar weave with graphite liner	95

TABLE 54. CORRELATION OF DENSITY, COLOR AND RESISTIVITY OF HOT-PRESSED AlN

Sample	Density ρ(g/cc)	% dense	Visual Color	Electrical Resistivity ρ (Ω-cm)	Heat Treatment (990°C) Color	ρ (Ω-cm)
HP-19	1.95	60	light blue	$\sim 10^8$	lighter blue	$>10^8$
HP-20	2.68	82	blue	10^5	no heat treatment	
HP-21	2.64	81	black	$\sim 10^2$	blue	$>10^{10}$
HP-22	2.52	77	blue	$< 10^2$	blue	$>10^8$
HP-24	3.05	94	gray	$< 10^2$	light gray	$>10^9$
HP-26	2.35 2.61	72 80	blue black	10^{11} $< 10^2$	light blue blue	$\sim 10^{11}$ $\sim 10^9$
HP-27	3.15	97	black	10^2	dark gray with some clear crystals	10^9
HP-30	3.08	95	light gray	$< 10^2$	no heat treatment	
W-154	3.26	100	dark amber	$> 10^{12}$	no heat treatment	
W-167	3.26	100	clear, light amber	$> 10^{12}$	no heat treatment	

990° C for an hour. The color after the heat treatment varied from blue to gray depending on the oxygen content. The blue color is due to Al_2OC contamination which results from a reaction of AlN with the graphite die. It is known that Al_2OC is soluble in AlN (Ref. 27). The post-anneal heat treatments were found to significantly improve room-temperature resistivity, as shown in Table 54.

Also in Table 54, the properties of two vapor-grown polycrystals of ultrahigh purity are listed for comparison. Since pure AlN is water clear, the amber or brown color of the vapor-grown specimens could be due to N_2 vacancies (Ref. 28). High resistivities have also been found by Yim, et al (Ref. 29), obtaining values greater than 10^{13} Ω -cm.

Table 55 is a summary of the qualitative fluorescence data obtained from samples that were irradiated with light of wavelength 3360 Å. The hot-pressed specimens containing O_2 impurity (blue-colored) fluoresced yellow, whereas the high purity, low O_2 content vapor-grown specimens show almost no fluorescence. Since oxygen has a high affinity toward aluminum, it enters the lattice as $Al_{0.67}O$ substituting for AlN molecules, i.e., Al vacancies are formed one per three O_2 atoms (Ref. 30). Deep levels due to these impurities contribute to the luminescence spectra of AlN (Ref. 28). Thus, the fluorescence data when quantified could be indicative of the type and quantity of impurity present.

Phase identification of hot-pressed and vapor-grown AlN was checked by X-ray diffraction. Table 56 lists the analysis for the highest density hot-pressed AlN and the vapor-grown crystals. Also shown for comparison are the data for the ASTM standard polycrystalline AlN. Varying degrees of preferred orientation are present being smallest in hot-pressed AlN and extreme in the case of vapor-grown crystals.

9.2.2.2 Radar Properties

Three (3) hot-pressed and two (2) vapor-grown specimens were submitted for radar measurements at 8.5, 24.0 and 90.0 GHz. Table 57 lists data on those formulations which exhibited the highest purity. Conversely, Table 58 lists data on those formulations which exhibited some contamination (carbon in the case of HP-27, probably free Al and possibly carbon for vapor-grown W-184 and W-185).

9.2.2.3 Thermal Properties

The thermal conductivity of hot pressed AlN was determined as a function of temperature by the flash diffusivity method. Table 59 lists the thermal diffusivity and computed thermal conductivity for each modification. Figure 93 compares these data with other hot-pressed and single crystal data in the literature. The theoretical value of thermal conductivity for pure AlN is 3.2 W/cm-°K at 300°K (Ref. 30). The values of thermal conductivity for the vapor-grown materials are slightly different with specimen W-154 having a lower level

TABLE 55. FLUORESCENCE OF HOT-PRESSED AND VAPOR-GROWN AlN

Sample	Sample Color	Fluorescence (3360 Å)	Fluorescent (Color)	ρ (Ω-cm)	Density (%)
HP-19	light blue	yes	dark yellow	$>10^8$	60
HP-20	blue	yes	bright yellow	(10^5) no heat treatment	80
HP-21	blue	yes	dim yellow	$>10^{10}$	81
HP-22	blue	yes	yellow-orange	$>10^8$	77
HP-26	blue black	yes no	bright greenish yellow	$\sim 10^{11}$	72 80
HP-27	some clear areas dark gray	yes	dim yellow areas	$\sim 10^9$	77
HP-30	mostly gray	yes	few yellow-orange areas	($<10^2$) no heat treatment	95
HP-154*	dark amber*	slightly	very few yellow spots	$>10^{12}$	100
W-167*	clear-transparent light amber	did not fluoresce		$>10^{12}$	100

*NOTE: Vapor-grown polycrystals were provided from recently completed AFOSR research (Ref. 25).

TABLE 56. X-RAY DATA FOR HOT-PRESSED AND VAPOR-GROWN AlN

ASTM 8-262			HP-27		W-167		W-154	
d (Å)	I/I_1	hkl	d (Å)	I (relative)	d (Å)	I (relative)	d (Å)	I (relative)
2.7	100	100	2.7	25			2.7	83
2.49	60	002	2.49	>100	2.49	100		
2.372	70	101	2.37	60				
1.829	20	102	1.83	30			1.83	60
1.557	30	110	1.55	20				
1.414	20	103	1.41	75				
1.348	6	200						
1.320	18	112	1.32	18				
1.301	8	201	1.30	6	1.245*	15		
1.186	4	202						
1.047	6	203						
1.019	4	210						
.9984	6	211						
.9345	6	105						
.8684	6	213						

*unaccounted line

which is probably related to the smaller grain size and slightly higher N_2 vacancy content (darker amber color). Sample HP-27 has a lower level than the vapor-grown modification but higher than previously hot-pressed specimens. The lower oxygen content of the HP-27 specimen probably accounts for the higher thermal conductivity compared to previous hot-pressings which used comparatively impure powder (Ref. 31).

The thermal conductivity data on hot-pressed AlN made on this program (HP-27) is already comparable to CVD SiC, indicating that a CVD form of AlN when synthesized should have a significantly higher thermal conductivity than CVD SiC (probably comparable to vapor-grown AlN shown in Figure 93). It should be noted that the achievement of this high thermal conductivity will improve the thermal shock figure of merit for AlN making it comparable or even superior to CVD SiC.

9.2.2.4 Optical Properties

The availability of a transparent vapor-grown crystal (W-167) suggested its evaluation as a multimode window material. Figure 94 shows the specular transmittance of AlN in the infrared frequency range. The absorption band at 5.05 microns has been identified by Collins,

TABLE 57. RADAR PROPERTIES OF HOT-PRESSED AlN AS A FUNCTION OF FREQUENCY AND TEMPERATURE

Specimen Designation	Frequency (GHz)	Temp. (°C)	Orientation Face-Up	Orientation Rotation	Dielectric Constant (K)	Loss Tangent (tan δ)	Sample* Position
HP-20 (82% Dense)	8.5	24	1	0°	6.183	.00238	BH
			2	90°	6.046	.00223	
	8.5	24	1	0°	6.040	.0025	OP
				90°	6.044	.0011	
	8.5	24	2	0°	6.271	.0022	
				90°	6.317	.0026	
Literature (Ref. 31)	8.5	20	-	--	8.5	.0035	
HP-21 (81% Dense)	24.0	28	one orientation		5.963	.00216	BH
		85			5.996	.00224	
		136			6.038	.00243	
		222			6.090	.00275**	
		311			6.144	.00239	
		408			6.202	.00234	
		507			6.285	.00276	
		607			6.380	.00320	
		708			6.457	.00372	
		738			6.492	.00395	
		800			6.549	.00435	

* See Section 3.5.1 for description of measurement technique
**Probably due to H_2O absorption.

TABLE 58. MILLIMETER WAVE ELECTROMAGNETIC PROPERTIES OF HOT-PRESSED AND VAPOR-GROWN AlN WHICH EXHIBITED CONTAMINATION EFFECTS

Specimen Designation	Frequency (GHz)	Temp. (°C)	Orientation		Dielectric Constant (K)	Loss Tangent (tan δ)	Sample Position
			Face-Up	Rotation			
HP-27 (97% Dense)	24.0	22	1		10.1	.363	BH
			2		19.9	.123	
			1		20.7	.219	
	24.0	22	1		6.96	.296	OP
			2		16.0	.340	
			1		15.	.386	
Re-measurement of HP-27 after Regrinding Face 1	24,0	24	1	0°	17.2	.334	
				90°	16.8	.345	
W-184 (100% Dense)	24.0	22	1	0°	8.00	.0619	BH
			1	90°	8.35	.0441	
			2[a]	0°	9.36	.082	
W-185 (100% Dense)	24.0	22	1	0°	7.96	.0206	BH
				90°	7.90	.0168	
			2[b]	0°	10.50	.0015	BH
				90°	8.00	.0173	

[a] Face 2 is the blacker face.

[b] Face 2 is the glossy face.

TABLE 59. THERMAL DIFFUSIVITY AND CONDUCTIVITY OF AlN (HOT-PRESSED AND VAPOR-GROWN)

Temperature (°K)	357	475	735	1314	1843
HP-27 α (cm^2/sec)	0.256	0.193	0.119	0.0618	0.0391
HP-27 K(watts/cm°K)	0.707	0.618	0.423	0.247	0.167
Thickness = 0.146 in.					
W-167 α (cm^2/sec)	0.593	0.356	0.191	0.088	0.051
W-167 K	1.652	1.159	0.694	0.359	0.224
Thickness = 0.065 in.					
W-154 α (cm^2/sec)	———	0.327	0.178	0.076	0.051
W-154 K		1.068	0.645	0.310	0.223
Thickness = 0.128 in.					

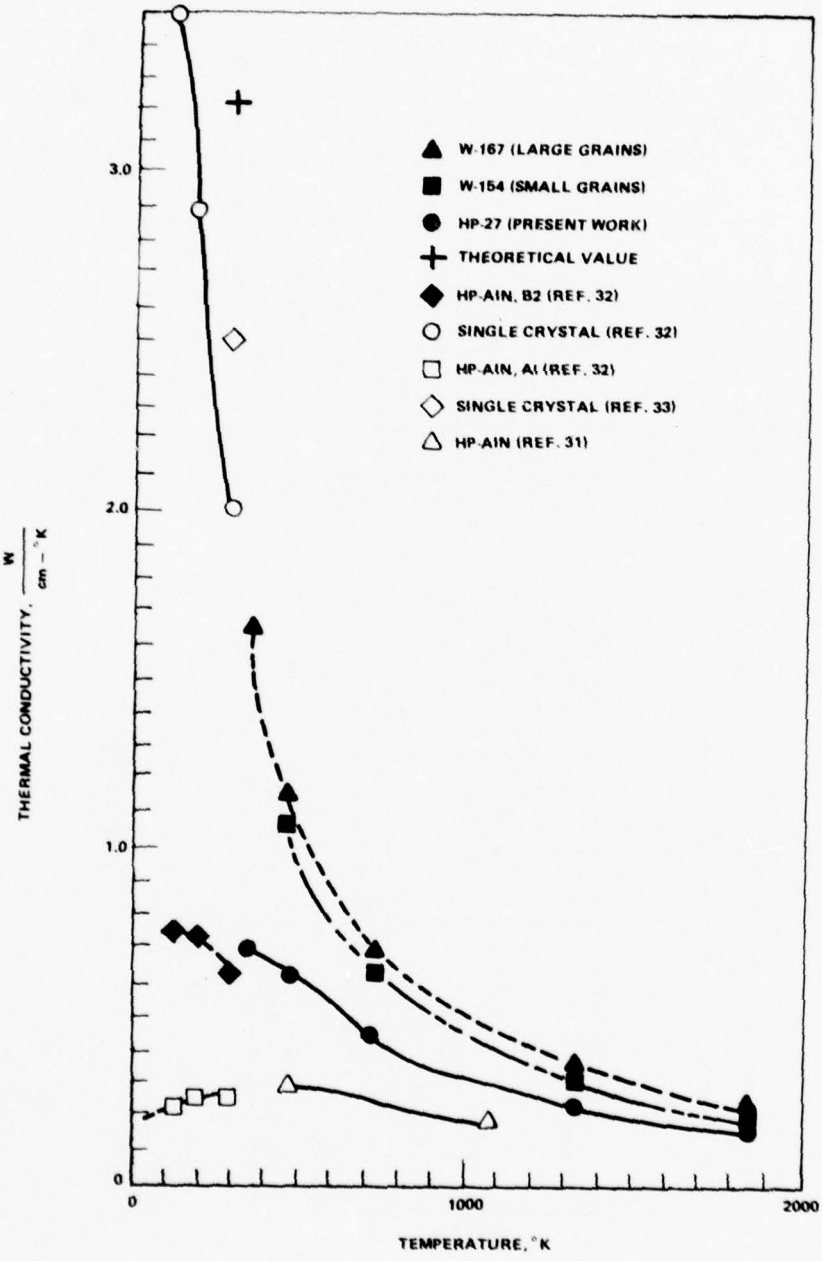

Figure 93. Comparison of Thermal Conductivity Versus Temperature Data for Several AlN Specimens Fabricated by Different Methods and Having Various Grain Size and Impurity Content

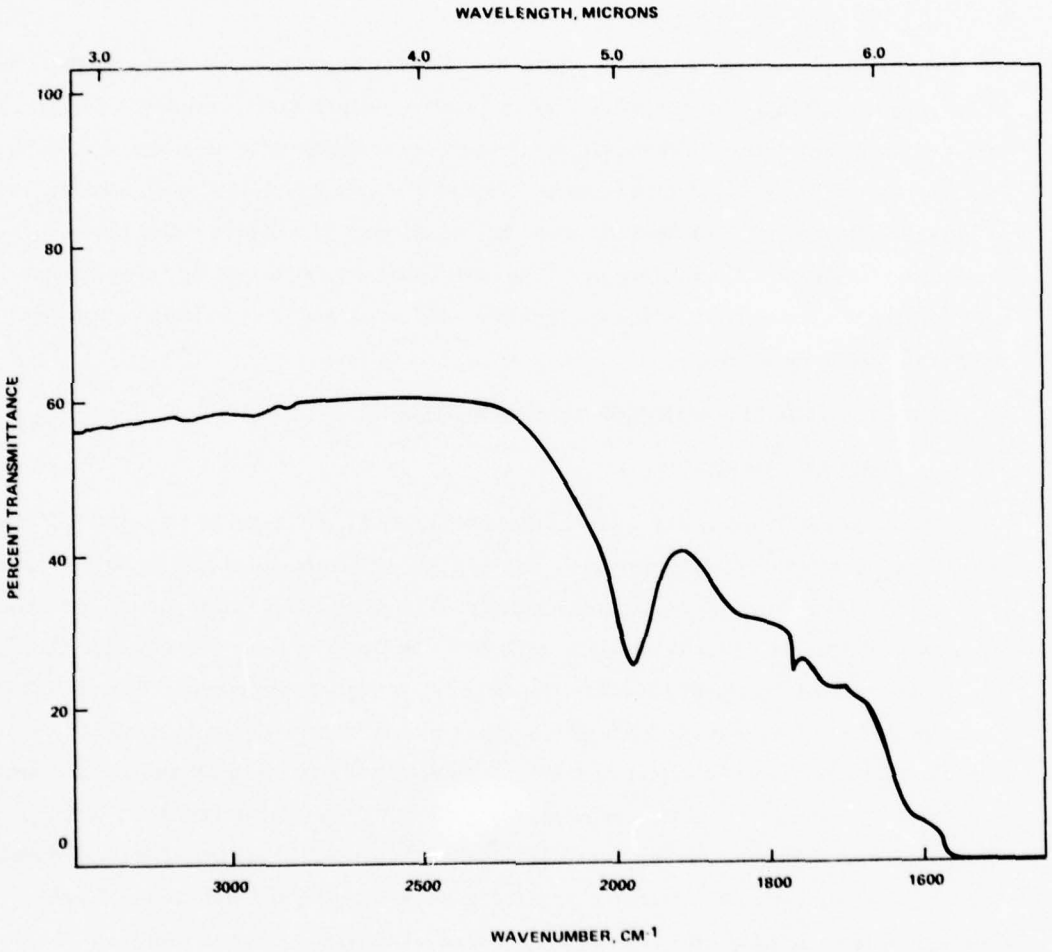

Figure 94. Infrared Transmission Spectrum of AlN Sample W-167. Specimen Thickness = 1.65 mm

et al (Ref. 28), as three times the transverse optical mode (i.e., 3TO). Figure 95 shows the corresponding specular reflectance of vapor-grown AlN. The Reststrahlen reflectance region is bounded by wavelengths of 10.9 and 15.0 microns which correspond according to Collins, et al (Ref. 28), to the longitudinal and transverse optical frequencies (i.e., LO and TO), respectively.

9.2.2.5 Microhardness

Table 60 lists Knoop microhardness data measured on selected hot-pressed and vapor-grown modifications. Also shown are literature data on hot-pressed AlN (Ref. 31).

9.2.2.6 Vaporization Characteristics

A qualitative investigation of the vaporization behavior of hot-pressed AlN was conducted in air using a 15KW CO_2 flat-top beam to create surface temperatures sufficiently high to induce surface vaporization. Three (3) specimens were evaluated at an intensity of 1000 W/cm^2 for times ranging from 2.3 to 15.0 seconds. Figure 96 shows a typical surface condition for specimens in this series. Unlike CVD α-Si_3N_4, no evidence of a molten cation (Al) was found. As reported in the literature (Ref. 34), AlN exhibited visual evidence of congruent vaporization, a characteristic which could enable millimeter wave transmission while the antenna window is vaporizing.

9.3 CHEMICAL VAPOR DEPOSITION OF ALUMINUM NITRIDE

9.3.1 TECHNICAL APPROACH

While most refractory nitrides (e.g., those of Si, B, Ti, etc.) can be prepared from the vapor phase by reaction of the appropriate metal halide with ammonia at temperatures between about 800 and 1500°C or higher, the preparation of aluminum nitride by the direct approach offers some obstacles. This is due principally to the difficulty of reducing aluminum chloride directly to form the intermediate species required by the deposition process. Silicon, boron and titanium for example can be reduced from the chloride by hydrogen to form either a reduced chloride such as $SiCl_2$ or $BHCl_2$ which continues to react to form the metal species or ammoniated complexes, from which the nitride is eventually produced at the heated deposition surface. The high stability of aluminum chloride prevents this direct approach, however, and the deposition species is usually prepared externally from the reaction of $AlCl_3$ and ammonium chloride (Reaction 1) in small quantities and vaporized onto a heated disc to form a film (Ref. 35) as shown below:

$$AlCl_3 + NH_4Cl \longrightarrow AlCl_3 \cdot NH_3 + HCl \quad \text{(Reaction 1)} \qquad (22)$$

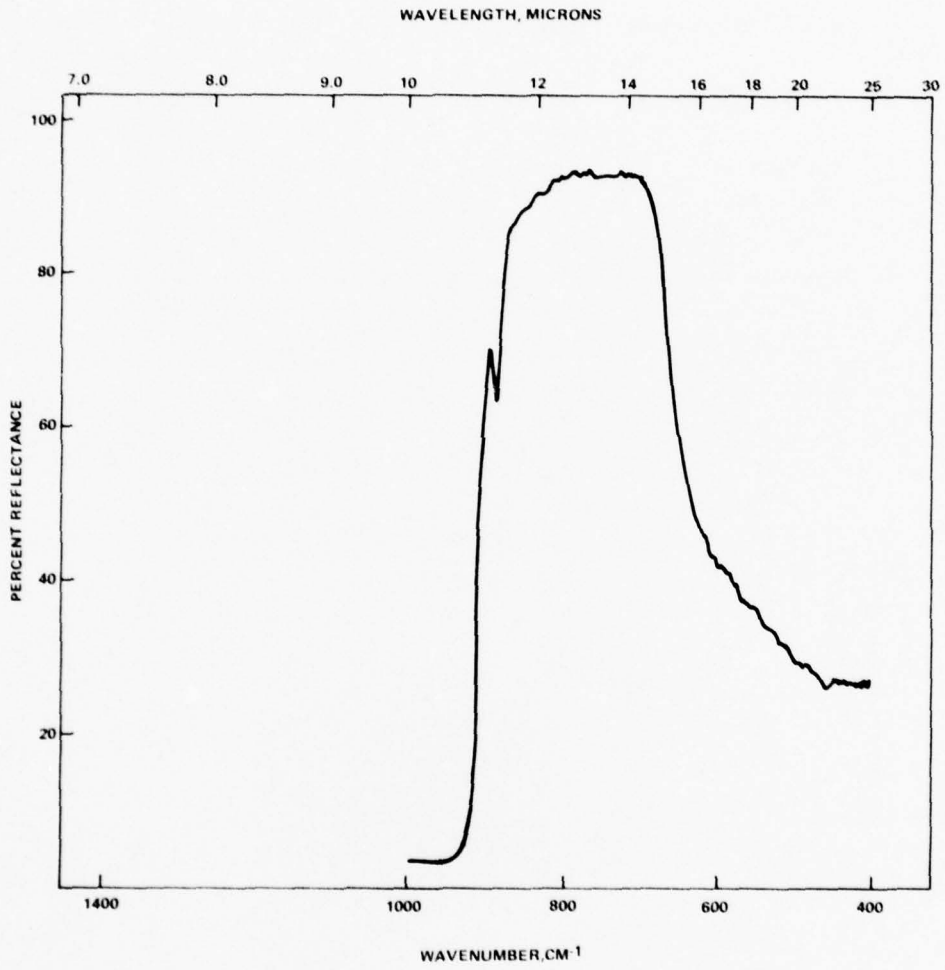

Figure 95. Infrared Reflectance Spectrum of AlN Sample W-167

TABLE 60. KNOOP MICROHARDNESS DATA ON HOT-PRESSED AND VAPOR-GROWN MODIFICATIONS OF AlN

Specimen Designation	Consolidation Method	Knoop Hardness ($kg\ mm^{-2}$)		
		100 g	200 g	500 g
HP-27 (97% Dense)	Hot Pressed	1492		
HP-20 (82% Dense)	Hot Pressed	1275		
W-167 (100% Dense)	Vapor-Grown	1217	1089	1128
W-154 (100% Dense)	Vapor-Grown	1124	1009	1097
AlN (98%) (Ref. 31)	Hot-Pressed	1225		

AlN

HP-22

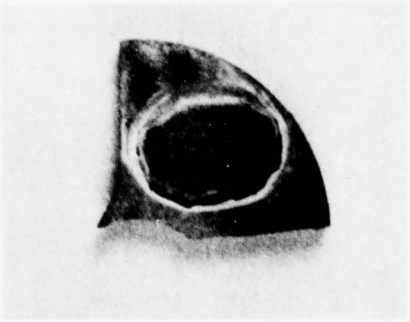

1000 W/cm^2, 2.3 Sec.

Figure 96. Post-Test Surface Condition of Hot-Pressed AlN (Spec. HP-22) After Vaporization. Point-Loaded at 1000 W/cm^2, 2.3 sec. with a Beam Area: Specimen Area Ratio ~0.80

A second approach consists of reacting aluminum metal with aluminum chloride vapor to form the reduced halide, and subsequently reacting that with ammonia to form the nitride (Ref. 36), as described below:

$$\text{a.}\quad 2Al + AlCl_3 \longrightarrow 3AlCl$$

$$\text{b.}\quad AlCl + NH_3 \longrightarrow AlN + HCl + H_2 \qquad \text{(Reaction 2)} \qquad (23)$$

As shown in Table 61 (Ref. 37), aluminum chloride is readily reduced to form the monochloride, with higher conversion at low pressure and high temperature.

A third approach consists of ammoniation of a previously deposited layer of aluminum metal at temperatures between 800 and 1150° C (Ref. 35); deposit thicknesses are limited by the diffusion rate of nitrogen through the surface layer of aluminum nitride formed on first contact, or by reaction of the aluminum layer with the substrate, silica. Thicknesses were limited to 0.05 to 1.0 μm. It was also reported that thicker layers, prepared at the higher temperatures, were yellow in contrast to those deposited at lower temperatures where white layers were formed. It was concluded that the yellow color was due to silicon monoxide in the deposit.

Other approaches such as evaporation (Ref. 38), glow discharge (Ref. 39), and deposition from aluminum trimethyl (Ref. 40) do not appear to be suitable for formation of relatively large area deposits of useful thickness. Direct reaction of aluminum vapor and nitrogen has been used for forming single crystals and whiskers (Ref. 31), but again does not seem to be suitable for extended deposits.

9.3.2 EXPERIMENTAL APPROACH

Two approaches were taken in order to prepare reasonably thick plates of aluminum nitride by chemical vapor deposition. The first consisted of formation of the reactive intermediate (Reaction 1) so that it could be vaporized into a deposition furnace and decomposed to the nitride. The second consisted of formation of the reduced chloride in situ, i.e., in the gas feed system immediately before entering the deposition zone, and reacting it with ammonia at a heated substrate.

9.3.2.1 Separate Precursor Preparation

A. Reaction with NH_4Cl. A charge of aluminum metal, in the form of aluminum needles as well as cut aluminum 1100 welding rod, was mixed with dry aluminum chloride and heated slowly under a stream of dry ammonia. Reaction occurred at approximately 350-400° C, usually with sufficient vigor to prevent control and collection of a useful product. Several efforts at dilution of the charge with alumina powder were made, but with equally unsatisfactory results.

TABLE 61. FORMATION OF ALUMINUM MONOHALIDE VAPOR: TRICHLORIDE CONVERSION DATA

Temperature (°C)	Pressure (Torr)	Conversion of $AlCl_3$ (%)
800	152	1
800	0.6	50
1000	190	10
1000	5.4	90
1200	266	50
1200	21.3	99

A further effort to moderate the reaction rate on decomposition of ammonium chloride involved the use of an experimental hot wire reactor. In this approach, radiant energy from the wire heats an aluminum-ammonium chloride charge located directly beneath the wire. The expectation was that the aluminum chloride ammine would vaporize and decompose on the wire to form an alumimum nitride deposit. Again, however, initiation of the reaction occurred with sufficient gas evolution to prevent a controlled reaction at the hot wire.

B. Reaction Between $AlCl_3$ and NH_3. A second approach to separate preparation of the amine precursor consisted of reacting ammonia and freshly formed aluminum chloride vapor. The latter was prepared by reaction of aluminum metal and hydrogen chloride gas at 180° C, with the latter having been generated by dropping concentrated sulfuric acid on dry sodium chloride. The product consisted of a small amount of a gray, glassy mass, identified by infrared spectroscopy as containing aluminum chloride-ammonia complexes as shown in Figure 97 and described as a mixture of complexes containing varying amounts of ammonia complexed to aluminum chloride (Ref. 41). The complex mixture was then heat treated at 250° C to decompose the higher ammoniates to the monoammoniate which is useful for vaporization into the furnace for deposition of aluminum nitride. The yields for this process were somewhat discouraging in view of the fact that relatively thick deposits of aluminum nitride were sought. In view of this, the approach was deferred for the present, and it was concluded that the use of the second method, i.e., formation of the reduced aluminum chloride in situ offered the most promise.

9.3.2.2 In Situ Intermediate Formation and Vapor Deposition

Since the reduction of aluminum trichloride can be accomplished by reaction with aluminum vapor as shown in Table 61 and Equation (23), deposition of aluminum nitride was accomplished by carrying out the reduction in the deposition furnace in the presence of ammonia. This was accomplished using the laboratory scale deposition system shown in Figure 98. A cross-sectional view of the deposition furnace is shown in Figure 99 and the aluminum metal charge receptacle is shown in Figure 100. The furnace hot zone is 2.5 cm x 20 cm., and has a relatively uniform temperature profile. Hence, the only control over the aluminum temperature and hence its vapor pressure is its location. Placement of the aluminum container directly above the gas inlet zone as shown in Figure 100(B) provides a temperature several hundred degrees below that of the deposition target, also shown in Figure 100(B). Loss of heat both to the water-cooled jacket and the incoming gases provides the differential, although it is not possible to control deposition temperature and aluminum vaporization temperature independently. The container for the aluminum is a graphite cup, provided with a gas passage along the axis. These cups were pyrolytically infiltrated with carbon to prevent permeation of the aluminum into the graphite pores and formation of aluminum carbide. Capacity is approximately 5-6 gm of aluminum.

Aluminum chloride was contained in a flask below the furnace and was carried up to the furnace inlet by a slow stream of nitrogen passing through the flask as shown in Figure 101. Temperature in the flask was maintained at approximately 200° C and a heating tape was provided to prevent premature condensation in the gas lines. In the early runs, there were problems associated with clogging and maintenance of gas flows.

During the course of deposition runs at lower temperatures where the aluminum was only slightly above the melting point, the buildup of a gray, glassy deposit was observed around the upper edge of the cup. Some of this material was collected on the assumption that it was the aluminum chloride amine, and used for one deposition run. Table 62 summarizes the results of the deposition runs carried out thus far in the program.

The deposit obtained in Run 1 consisted of a canary yellow material found directly above the feed gas inlet on the downward face of the deposition target, yellow-white whiskers halfway up the rod supporting the target, and a relatively thick crystalline black deposit elsewhere. All were identified as containing aluminum nitride, with a high content of aluminum carbide in the black deposit. The material from Run 6 which was white was also identified as aluminum nitride. Literature references mention both white and yellow deposits as being

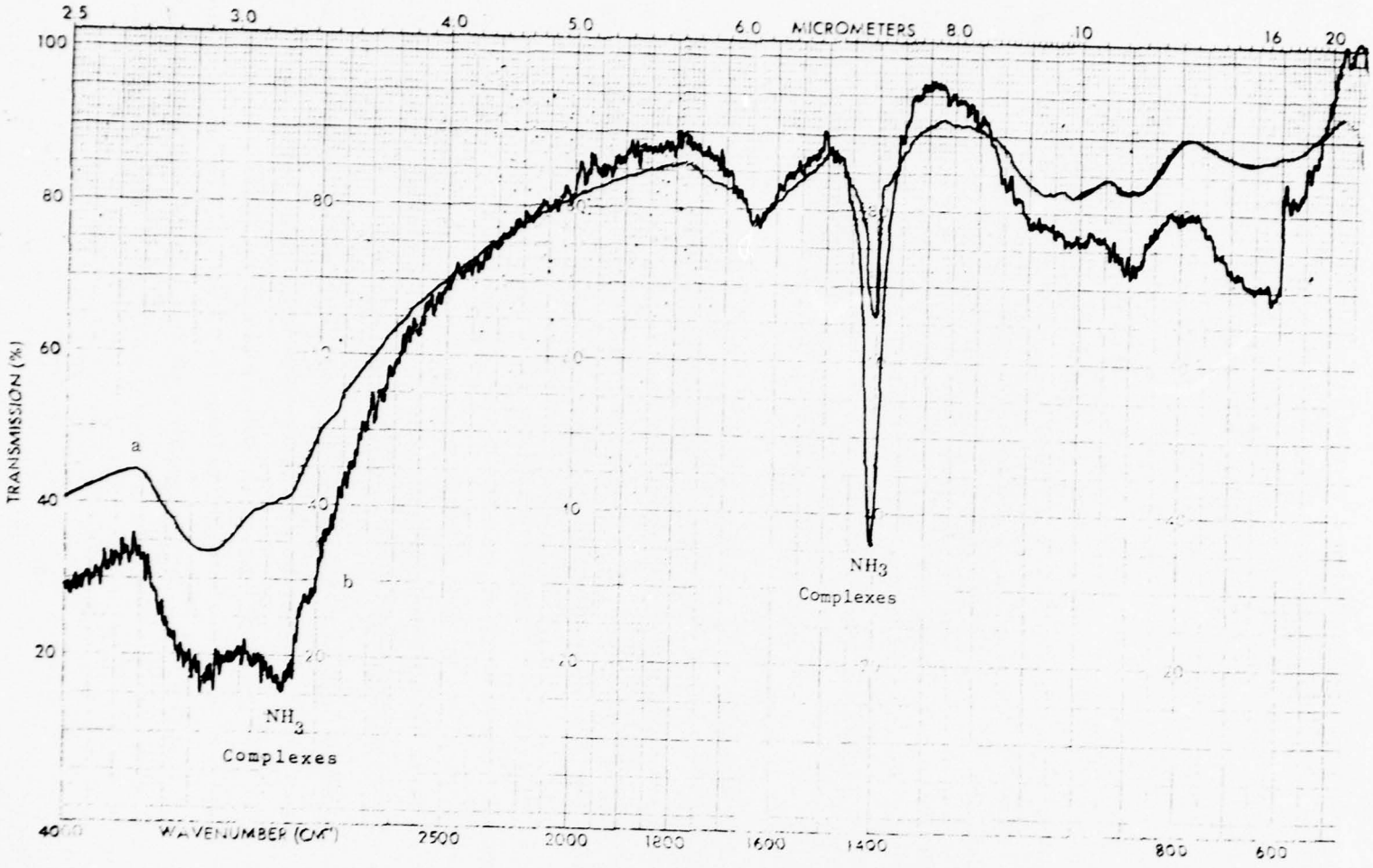

Figure 97. Infrared Spectrum of $AlCl_3 \cdot NH_3$ (KBr Pellet Technique). Curve (a) is for a less concentrated mixture of the ammine with the KBr matrix as compared with curve (b).

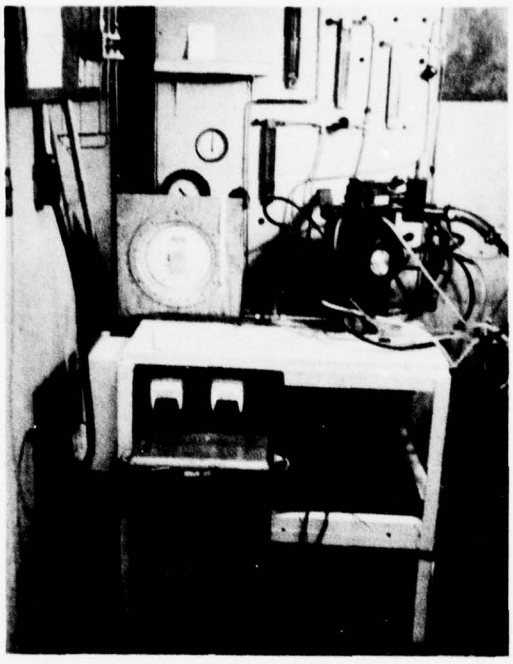

Figure 98. Photograph of Deposition System Used to Prepare CVD-AlN

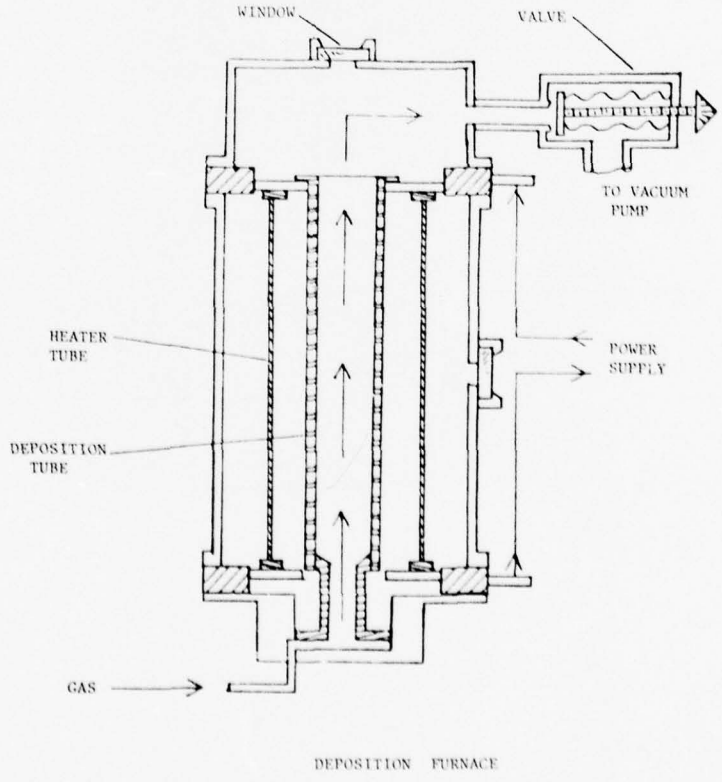

Figure 99. Schematic of Experimental Deposition Furnace

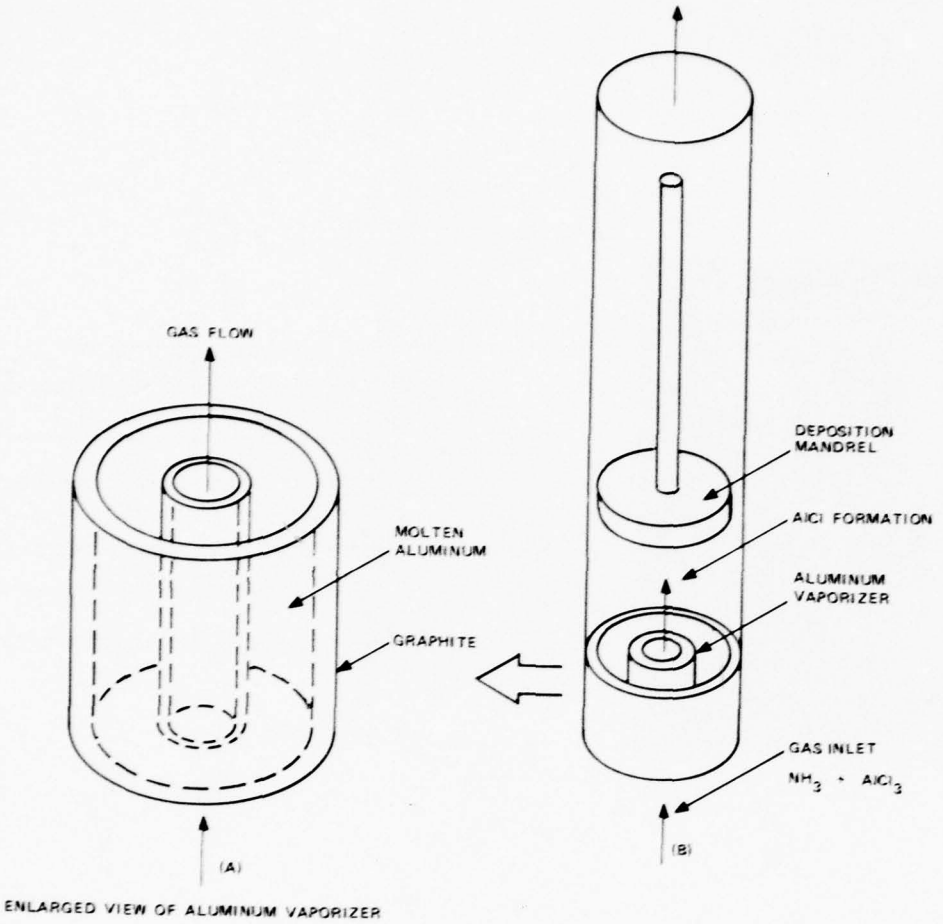

Figure 100. Enlarged View of Aluminum Vaporizer (A) and Schematic of Deposition Tube (B)

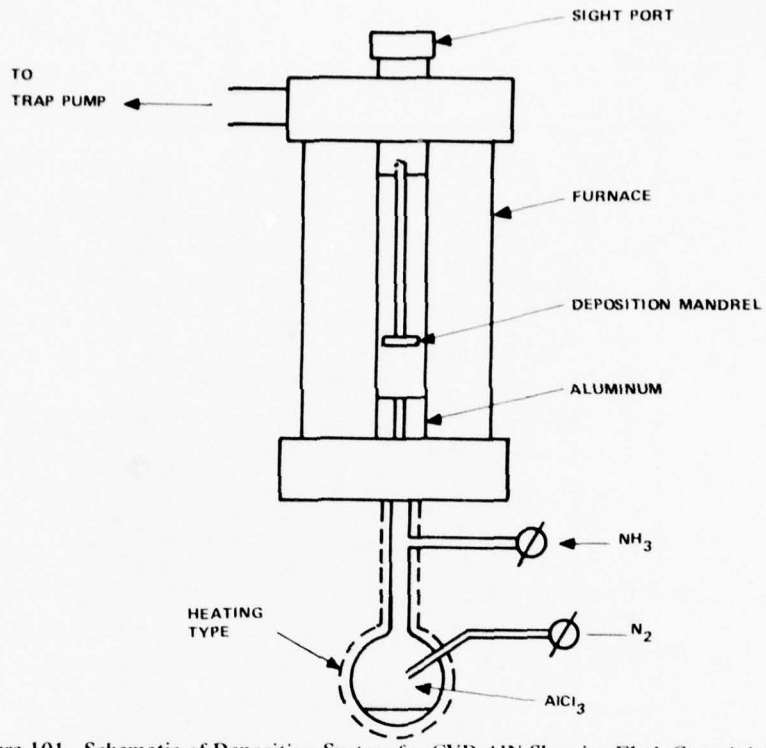

Figure 101. Schematic of Deposition System for CVD-AlN Showing Flask Containing $AlCl_3$

characteristic of pure AlN. The yellow color is attributed in one case (Ref. 35) to silicon monoxide impurities formed through reaction with the silica substrate. Single crystals prepared under very pure conditions, however, were light yellow in several cases (Ref. 38, 39). The possibility is always present that contamination of the deposit by traces of oxygen could lead to aluminum oxynitride which may be white.

Experience with the above runs indicates that aluminum nitride can be prepared by chemical vapor deposition, but also that if reasonably thick deposits are to be made, a separate control for vaporizing aluminum at known and reproducible pressures will be required.

TABLE 62. ALUMINUM NITRIDE DEPOSITION EXPERIMENTS

Run No.	Temp. (°C)	Pressure (Torr)	NH_3 Flow (cc/min.)	N_2 Flow (cc/min)	Time (hrs.)	Comments
1	1500	1.5	37	75	4	Aluminum completely used - yellow AlN and black AlN + Al_4C_3 dep.
2	1225	0.5	37	65	3.5	Aluminum temp. low (above nozzle). No deposit.
3	1825	0.5	37	269	1.5	Aluminum container 1 in. into furnace - excessive vaporization and electrical short.
4	800	0.5	37	37	4	No deposit. $AlCl_3$-HN_3 line clogged.
5	1750	0.5	37	37	2	Intermediate $AlCl_3 \cdot NH_3$ from Run 3 vaporized - very thin deposit.
6	1260	1	75	75	2	White matte AlN deposit on target; gray white deposit on Al container.

10. CUBIC BORON NITRIDE

10. CUBIC BORON NITRIDE

10.1 INTRODUCTION

10.1.1 APPLICATION AS A MILLIMETER WAVE WINDOW

Hexagonal boron nitride is currently being considered as a radar transmitting window for several high-performance DoD missile systems. Another modification of boron nitride, viz. cubic boron nitride, has not been considered to date as a potential radar window, although it may provide certain advantages. Recent processing research at the Specialty Materials Department (SMD) of the General Electric Company has resulted in the synthesis of translucent, theoretically-dense, cubic boron nitride with purity-levels previously unattainable. The material in this form has a measured "super" thermal conductivity only excelled by diamond, being almost double that of metallic copper at 100°C and comparable to copper at about 600°C. Thus, its thermal shock figure is unexcelled by currently known insulators and its microhardness is second only to diamond. It has been introduced into this program primarily to assess its potential for transmitting radar and could be used in a mosaic antenna window configuration.

10.1.2 PROCESS RESEARCH

The two (2) specimens evaluated on this program were provided from existing Specialty Materials Department inventory. Processing details for these specimens are company proprietary.

10.2 CHARACTERIZATION OF PHYSICAL PROPERTIES

10.2.1 RADAR TRANSMITTANCE

Table 63 lists the room temperature radar properties of two differently processed cubic boron nitride specimens at 24 GHz. Although similar dielectric constants were obtained, loss tangent data showed significant variability between specimens. It is suspected that this variability may be traceable to different lots of precursor material used to synthesize each specimen. As was the case for other nitride-based ceramics being evaluated on this program, improved or comparable dielectric properties have been obtained compared to commercial-grade hot-pressed Si_3N_4.

10.2.2 THERMAL CONDUCTIVITY

Figure 102 compares the thermal conductivity of cubic boron nitride (Spec. No. 1025-3) with high purity metallic copper. Only single crystal high purity diamond has a thermal conductivity at room temperature greater than cubic boron nitride.

TABLE 63. RADAR TRANSMITTANCE PROPERTIES OF CUBIC BORON NITRIDE (CBN) AT 24 GHz

Specimen Designation	Density (g/cc)	Thickness (mm)	Processing Temp. (°C)	Frequency* (GHz)	Dielectric Constant (K)	Loss Tangent
1139 (2)	3.50	3.33	2440	24.0	7.01	.0089
					7.00	.0091
1025 (3)	3.50	1.60	2275	24.0	7.02	.00481
					7.00	.00476

*Cavity Position - BH

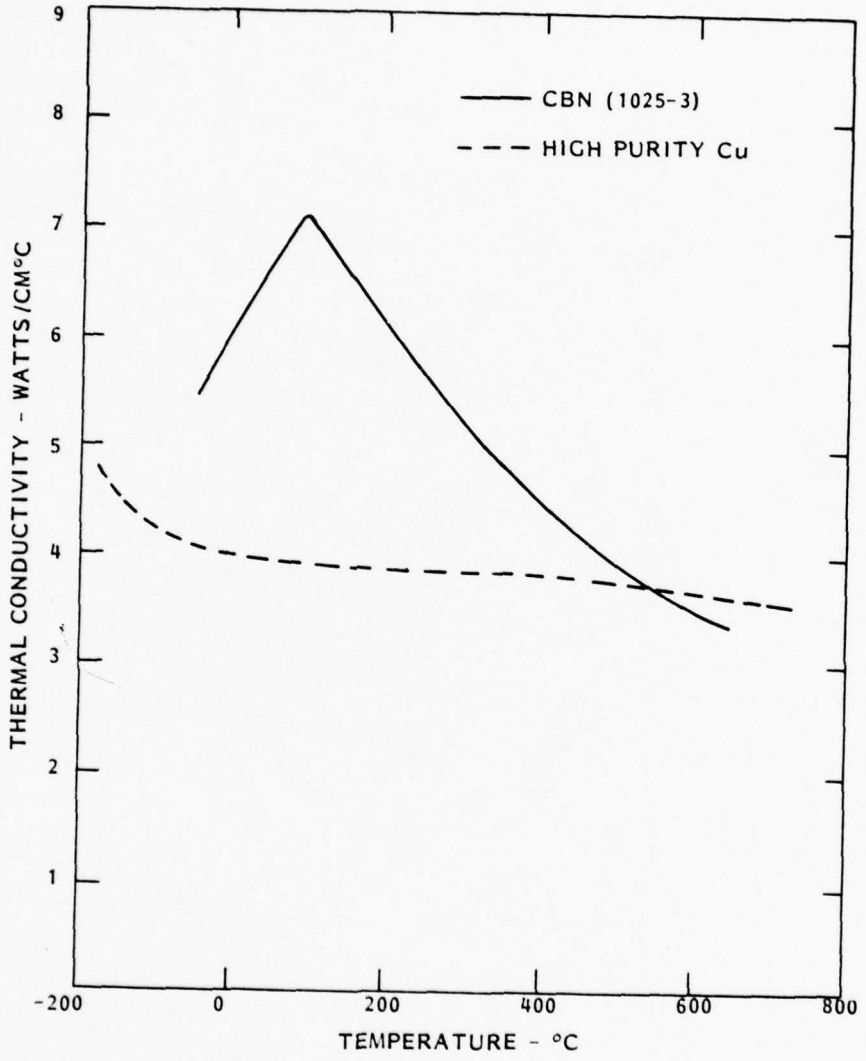

Figure 102. Comparison of the Thermal Conductivity of Cubic Boron Nitride (Spec. 1025-3) with High Purity Copper

11. PART II: ULTRAHIGH PURITY NITRIDE-BASED CERAMICS CONCLUSIONS AND RECOMMENDATIONS

TABLE 66. KNOOP HARDNESS (50 g)

11. PART II: ULTRAHIGH PURITY NITRIDE-BASED CERAMICS CONCLUSIONS AND RECOMMENDATIONS

11.1 CONCLUSIONS

Experimental work on this contract during the past year has provided several alternative millimeter wave window materials with potentially superior performance than state-of-the-art materials. Some of the more significant conclusions are summarized below.

1. Over the temperature range (20-800°C) and frequencies (8.5 - 24.0 GHz) investigated, CVD α-Si_3N_4 has been found to have at least an order of magnitude lower loss tangent than commercial grade hot-pressed modifications. It is anticipated that this advantage will continue up to temperatures approaching the vaporization level (~1700°C) for stoichiometric Si_3N_4) where non-congruent vaporization characteristics of both modifications could limit their capability to transmit mm wave frequencies.

2. Hot-pressed AlN, prepared on this program, exhibits a 40 percent lower loss tangent (20°C, 8.5 GHz) than currently reported literature data on AlN prepared by the hot-pressing technique (Ref. 31). At 24 GHz, hot-pressed AlN, prepared on this program has an 85 percent lower loss tangent at 20°C and a 30 percent lower loss tangent at 800°C than commercial-grade hot-pressed Si_3N_4.

3. The thermal conductivity of hot pressed AlN, prepared on this program, is approximately double that of currently reported data on AlN prepared by the hot pressing method (Ref. 31).

4. The thermal conductivity of vapor-grown AlN, evaluated on this program, is significantly higher than hot-pressed AlN reported in the literature (factor of 3.7 higher at 200°C, factor of 2.5 higher at about 800°C). Thus, AlN prepared by the chemical vapor deposition method, should also exhibit improved thermal conductivity levels compared to hot-pressed modifications.

5. The feasibility of synthesizing AlN by the chemical vapor deposition technique has been demonstration on a laboratory-scale deposition system.

6. Vaporization experiments conducted on hot-pressed AlN confirm literature observations regarding its congruent vaporization behavior. This congruent vaporization characteristic suggests the potential of AlN for transmitting millimeter wave radar frequencies while surface vaporization is occurring.

7. β'-Sialon is a viable alternative to hot-pressed Si_3N_4 from a cost and fabricability viewpoint. Its lower thermal conductivity (compared to Si_3N_4) will result in a lower thermal shock resistance figure, however.

8. β'-Sialon exhibits relatively "clean" vaporization kinetics compared to Si_3N_4, and therefore may offer the advantage of being able to transmit radar frequencies while surface vaporization is occurring.

9. Cubic boron nitride, while limited to mosaic window configurations because of size limitations (~1 cm diameter), has an unexcelled thermal shock resistance figure compared to other nitride-based candidate antenna windows. Its room temperature dielectric properties are comparable to hot-pressed Si_3N_4.

11.2 RECOMMENDATIONS

An assessment of the current status of nitride-based ceramic millimeter-wave antenna window developments in this laboratory (as a result of the first year's contract activity) has resulted in the following recommendations for future work:

1. Processing research should continue on the chemical vapor deposition of Si_3N_4 and AlN since property characterizations to date indicate that ultrahigh purity forms of each material will better satisfy the stringent millimeter wave radar transmittance requirements of BMI systems.

2. Concurrently, other processing methods such as hot-pressing and pressureless sintering should continue to be evaluated, especially for AlN and β'-Sialons. Utilization of ultrahigh purity precursor powders will be the key to improved millimeter wave radar transmittance properties.

3. Both analytical and experimental sub-scale simulation studies should be initiated on future programs as material synthesis tasks begin to produce antenna window materials of sufficient size and quality to lead to meaningful assessments of thermostructural and "hot" radar transmittance performance.

4. Limited resources should be expended assessing the feasibility of a mosaic antenna window configuration utilizing "super" thermal shock resistance candidates such as cubic boron nitride.

12. PART III: THERMOPHYSICAL AND MECHANICAL CHARACTERIZATION OF "RAYTRAN" ZINC SELENIDE

12. INTRODUCTION

12. PART III: THERMOPHYSICAL AND MECHANICAL CHARACTERIZATION OF "RAYTRAN" ZINC SELENIDE

12.1 INTRODUCTION

The objective of this test program was to provide mechanical and thermophysical characterization data on Raytheon's "Raytran" zinc selenide infrared window material over a range of temperatures. This material is produced by chemical vapor deposition (CVD) whereas earlier ZnSe plates were produced by hot pressing. Hence, much of the earlier data are not strictly applicable. Since ZnSe sublimes rather rapidly at temperatures above about 1000°C, measurements were limited to the range -250°F (-157°) to 1800°F (982°C).

The ZnSe used in this work was government furnished material.

TRANSMISSION (%)

13. TEST MATRIX

Figure 99. Schematic of Experimental Deposition Furnace

13. TEST MATRIX

The test matrix for this program is given in Table 64. The testing was intended to provide some basic mechanical and thermophysical data over a fairly wide temperature range.

TABLE 64. ZINC SELENIDE CHARACTERIZATION MATRIX

Property	Test Direction	Measurement Temperatures (°F) -250	-100	RT	100	250	500	750	1000	1800	Notes
Thermal Expansion	In-Plane Perpendicular	2 2	Continuous to 1000°C (1832°F)								"Theta" differential Dilatometer
Hardness (Knoop)	Perpendicular	-	-	5	-	-	-	-	-	-	50 gm. indenter
Flexure (Strength, Modulus, Poisson's Ratio)	In-Plane	3	-	6	-	3	3	3	3	3	Poisson's Ratio to 500°F only. R.T. Tests: 3 as-Received, 3 After 1800°F Exposure. Check Tensile vs. Compressor Behavior.
Tensile Properties	In-Plane Perpendicular	-	-	3 3	-	-	-	-	-	-	For elastic Constants Only (Modulus, Poisson's Ratios), check for anisotropy
Ultrasonic Wave Velocity	In-Plane Perpendicular	-	-	6 6	-	-	-	-	-	-	For determination of Elastic Constants under Dynamic Conditions. 3 tests each. Direction will be Uniaxial Stress Condition and 3 Uniaxial Strain Condition.
Cold Flow	In-Plane	-	-	3	-	-	-	-	-	-	Flex Loading - Various Hold Times - Measure Set
Thermal Conductivity	In-Plane Perpendicular	- -	2 2	- -	2 2	2 2	- -	2 2	2 2	- -	Gradient Guarded Comparative Rod - LN_2 Heat Sink
Specific Heat	Any	-	2	-	2	2	-	2	2	-	Differential Scanning Calorimeter

14. CUTTING PLANS

14. CUTTING PLANS

The plates used for characterization were obtained in five different thicknesses. Nominal plate thicknesses were 0.125, 0.250, 0.500, 0.750 and 1.00 inch. Cutting plans for these plates are shown in Figures 103 through 107.

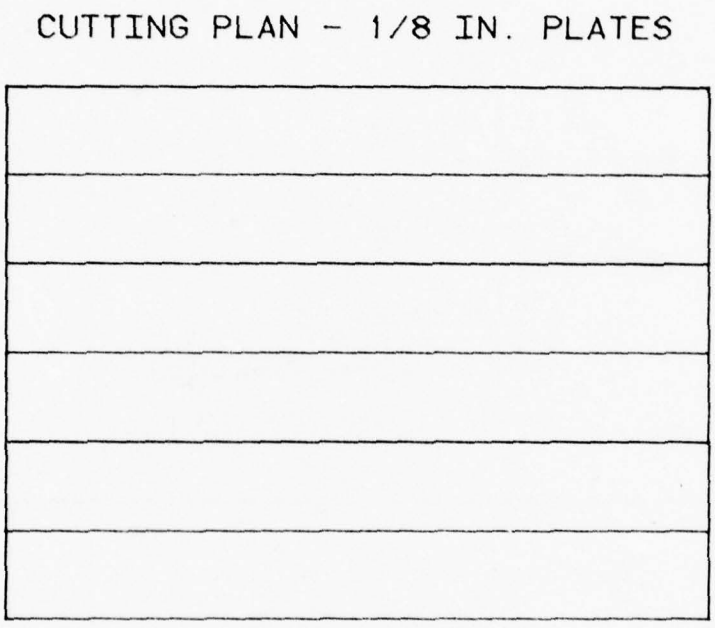

Figure 103. Cutting Plan – 1/8 Inch Plates

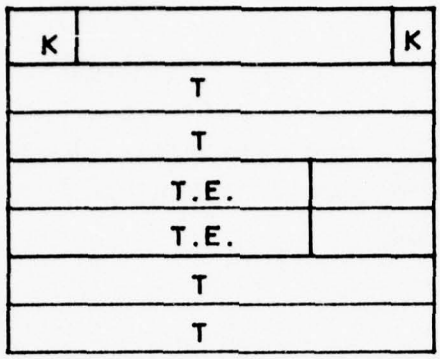

DIMENSIONS: 1/4 X 2.5 X 3.1

SPECIMENS:

K = KNOOP HARDNESS
T = TENSILE
T.E. = THERMAL EXPANSION

Figure 104. Cutting Plan – 1/4 Inch Plate

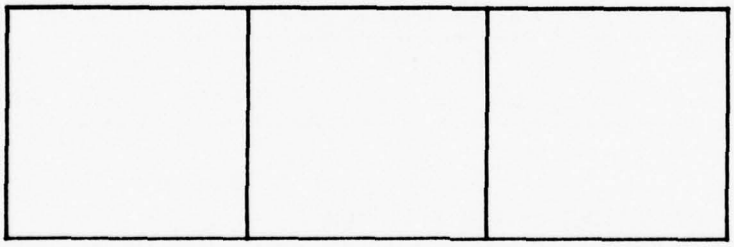

DIMENSIONS: 1/2 X 1.6 X 5.0

SPECIMENS: ULTRASONIC

Figure 105. Cutting Plan – 1/2 Inch Plate

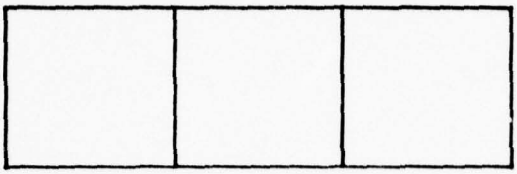

DIMENSIONS: 3/4 X 1.1 X 3.5

SPECIMENS: THERMAL CONDUCTIVITY

Figure 106. Cutting Plan — 3/4 Inch Plate

CUTTING PLAN - 1.0 IN. PLATE

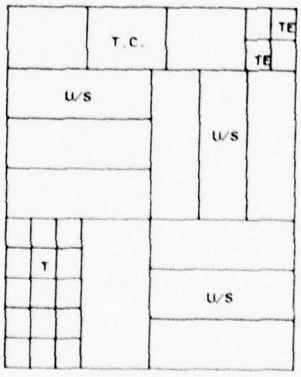

DIMENSIONS: 1.0 X 4.0 X 5.0

SPECIMENS:

T.C. = THERMAL CONDUCTIVITY (3)
U/S = ULTRASONIC (8)
TE = THERMAL EXPANSION (4)
T = TENSILE (15)

Figure 107. Cutting Plan — 1.0 Inch Plate

ductivity at room temperature greater than cubic boron nitride.

15. TEST RESULTS

15. TEST RESULTS

15.1 THERMAL EXPANSION

Thermal expansion measurements were made from -250°F to 1800°F using two dilatometers. In the region from -250°F to 200°F, a quartz tube dilatometer was employed. This dilatometer was calibrated against an NBS certified fused silica standard. The specimens were then run in a "Theta" differential dilatometer against an NBS certified sapphire standard. Two in-plane (X) and two perpendicular to the plane (Z) specimens were tested. The in-plane or X-direction specimens were cut from a 1/4 inch thick plate and measured 1/4 x 1/4 x 2.00 inches. The Z-direction or perpendicular specimens were cut from a 1.0 inch thick plate and consisted of two pieces, each 1/4 x 1/4 x 1.00 inch, which were stacked to form a two-inch long specimen.

The results of the measurements are shown in Figures 108 and 109 for the two test directions. There is no significant difference between the two sets of data, which are shown combined in Figure 110. The two sets of data were each regression-fitted using a cubic polynomial. Ninety-nine data points were employed for the X-direction data and 130 points for the Z-direction. The resultant equations were then used to calculate expansion (dl/l) or thermal strain and the slope of the curve, which is the coefficient of thermal expansion, at several temperatures. These results are given in Table 65.

15.2 HARDNESS MEASUREMENTS

Knoop hardness (50 g) measurements were made at five points on each of two plates. Results are given in Table 66. The mean is only slightly lower than the value of the 100 given in vendor data and the difference is probably not significant.

15.3 ULTRASONIC MEASUREMENTS

Ultrasonic velocity measurements were made to determine the elastic constants of the material under dynamic conditions. Initial measurements were made in the longitudinal mode at several frequencies on specimens from a 0.500 inch thick plate. Three specimens were employed, each approximately 1.65 inches square by 0.500 inch thick. The direction of measurement was perpendicular to the plane of the plate. Measured density of the specimens was 5.26 g/cm^3, determined by water immersion. The ultrasonic measurements were made by the bufferblock method, using the sweep delay of a "Tektronix" oscilloscope to measure transit time. This delay was calibrated using a crystal-controlled time mark generator to assure accuracy. The results of the initial measurements are given in Table 67.

TABLE 65. THERMAL EXPANSION ESTIMATES FROM CUBIC POLYNOMIAL FIT OF DATA

TEMPERATURE (^{O}C)	THERMAL STRAIN (m/m)		COEFFICIENT OF EXPANSION (m/m/^{O}C)	
	IN-PLANE	PERPENDICULAR	IN-PLANE	PERPENDICULAR
= -150	-0.0010970407115	-0.00106884608287	5.516393549E-6	5.497093703E-6
= -100	-8.102835378E-4	-7.83675106E-4	5.950240282E-6	5.906688699E-6
= -50	-5.023819948E-4	-4.784828804E-4	6.362168322E-6	6.297943653E-6
= 0	-1.744320171E-4	-1.54186408E-4	6.752177669E-6	6.670858567E-6
= 50	1.724704605E-4	1.882973089E-4	7.120268321E-6	7.025433439E-6
= 100	5.372295034E-4	5.480512685E-4	7.466440281E-6	7.36166827E-6
= 150	9.18749177E-4	9.241584686E-4	7.790693545E-6	7.67956306E-6
= 200	0.00131533354651	0.00131570190709	8.093028119E-6	7.979117808E-6
= 300	0.00215291263471	0.00214142949131	8.631941183E-6	8.523207182E-6
= 400	0.00303939929064	0.00301789800467	9.083179473E-6	8.993936391E-6
= 500	0.00396662603689	0.0039377714397	9.44674299E-6	9.391305435E-6
= 600	0.00492582539698	0.00489371375293	9.722631732E-6	9.715314315E-6
= 700	0.00590822989081	0.0058783889549	9.9108457E-6	9.96596303E-6
= 800	0.00690507204369	0.00688446102012	1.001138489E-5	1.014325158E-5
= 900	0.00790758437731	0.00790459393212	1.002424932E-5	1.024717997E-5
= 1000	0.0089069394143	0.00893145167444	9.949438962E-6	1.027774819E-5

TABLE 66. KNOOP HARDNESS (50 g)

#1	#2
93	96
96	94
95	91
93	87
100	83
95	92

Mean = 94
S = 3.4

Considering the wave velocity data, it is doubtful that any real change in velocity occurs over the range of frequencies employed. The higher frequency data tend to be more precise since the wave peaks are more sharply defined. This tendency is reflected by the decrease in the estimated standard deviation (S) with increasing frequency.

Following these initial measurements, more extensive velocity measurements were made in the X, Y (both in-plane) and Z (perpendicular to plane) directions. The X and Y direction specimens were cut from a 1.0 inch thick plate, whereas the Z-direction specimens were those previously cut from a 0.5 inch thick plate. Measurements were made at 10.0 Megahertz and each specimen was measured four times. Results of these measurements are given in Table 68.

Although the wave velocity perpendicular to the plane (Z) was only slightly less than the in-plane velocity (X, Y), the difference is significant at the 99 percent confidence level. At first it was thought that this indicated a slight anisotropy, but additional Z-direction measurements on a specimen from the 1.0 inch (2.54 cm) thick plate gave a velocity of 4.41 km/s. It was therefore concluded that the material is isotropic but that a small plate-to-plate difference in elastic constants exists.

Since the elastic stress-strain behavior of an isotropic material requires only two elastic constants for its description, an attempt was made to determine the long bar wave velocity to obtain the second constant. The specimens initially employed for this purpose were 0.25 x 0.25 x 3.00 inches and were cut from a 0.25 inch thick plate. The cross-section of these specimens proved to be too large for long-bar measurements, particularly at the higher frequencies. Attempts were also made to measure long-bar velocity on a specimen which was 0.125 x 0.50 x 6.00 inches in size, at frequencies as low as 0.20 MHz, but the results were not satisfactory (i.e., they were questionable). It appears at this time that a shear velocity measurement would probably be the best way to obtain the second elastic constant.

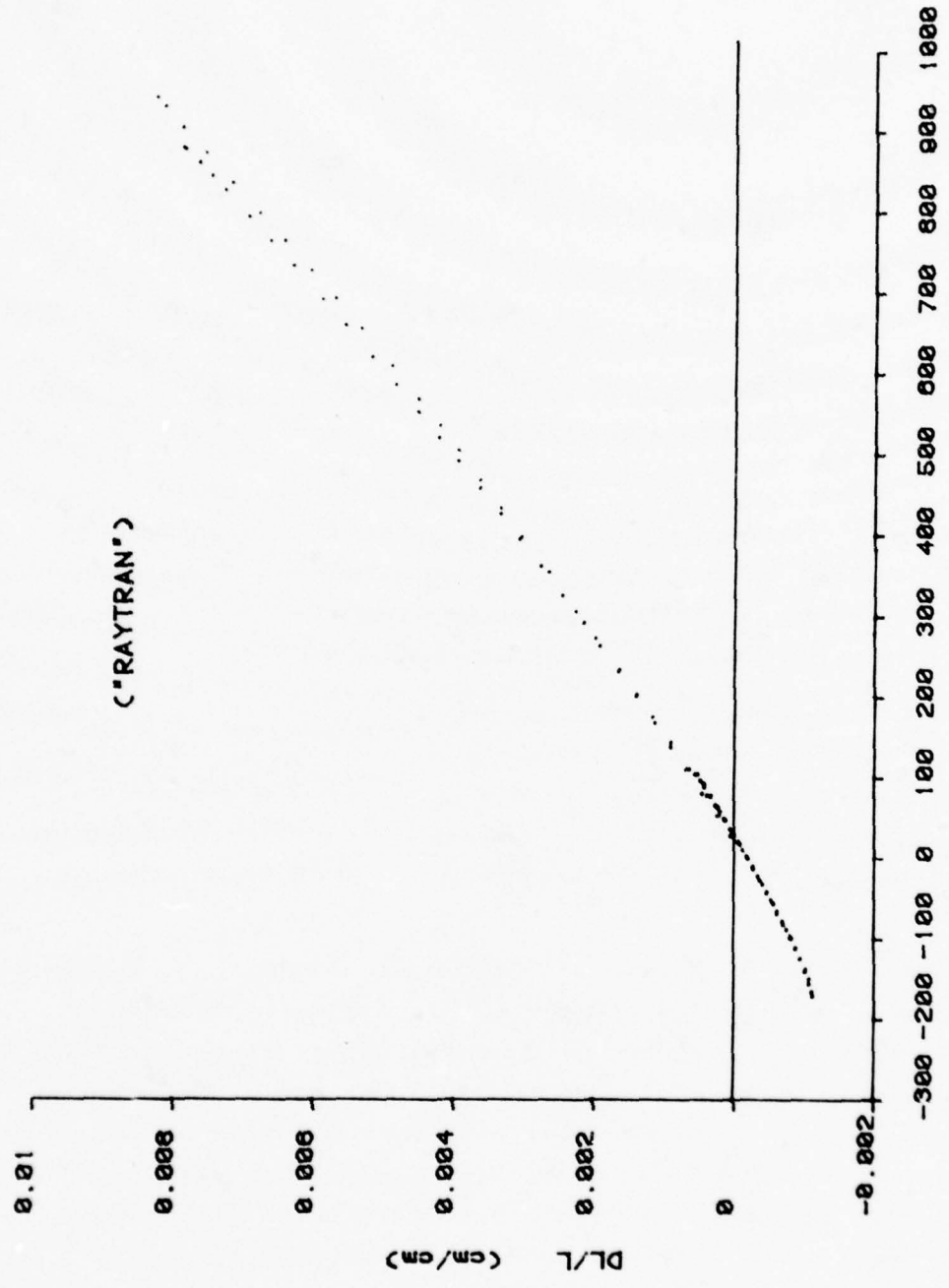

Figure 108. Zinc Selenide, X Direction, Thermal Expansion

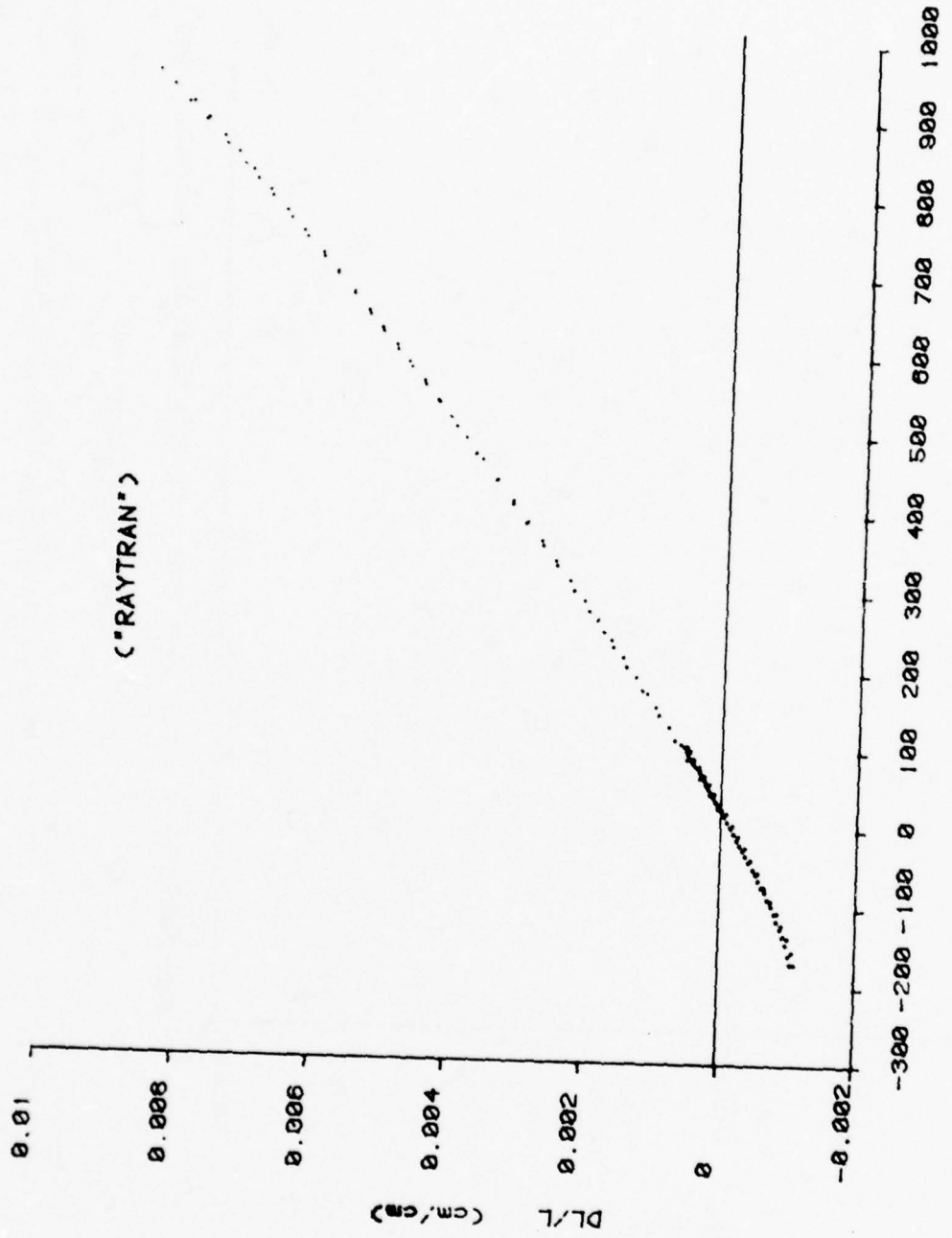

Figure 109. Zinc Selenide, Z Direction Thermal Expansion

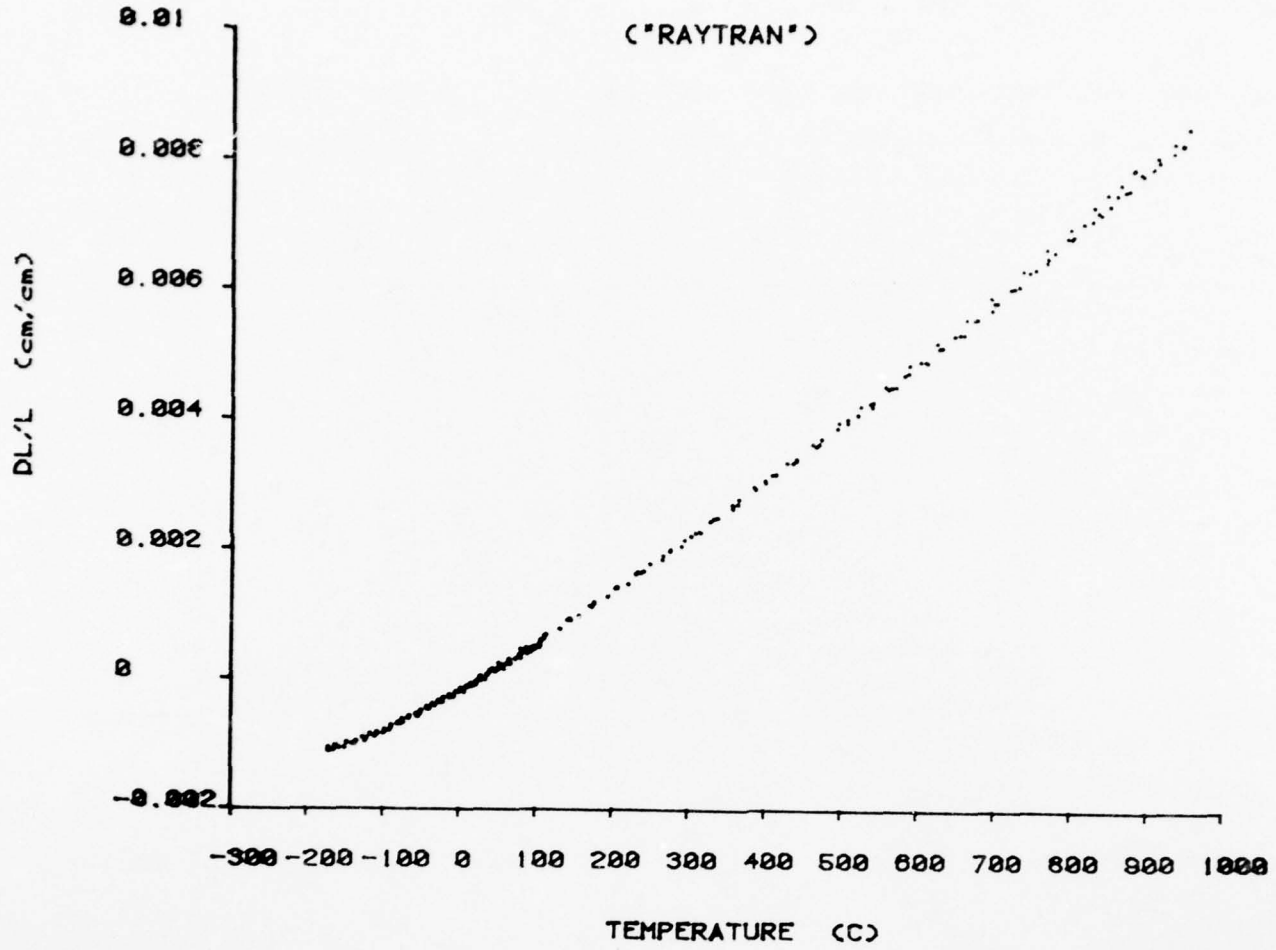

Figure 110. Thermal Expansion – ZnSe Combined In-Plane and Perp. Data

TABLE 67. ULTRASONIC MEASUREMENTS ON ZINC SELENIDE (LONGITUDINAL WAVE, UNIAXIAL STRAIN CONDITIONS)

(Perpendicular to the Plane of the Plate)

A. Wave Velocity Data

Frequency (MHz)	Mean Velocity (km/s)	S (km/s)	N	Elastic Constant, C_{11} ($=\rho C^2$)
0.20	4.31	0.032	10	14.2×10^6
0.69	4.36	0.038	2	14.5×10^6
1.00	4.45	0.021	3	15.1×10^6
2.25	4.38	0.015	3	14.6×10^6
5.00	4.39	0.016	5	14.7×10^6
10.00	4.38	0.006	5	14.6×10^6

(Density of Specimen = 5.26 g/cm^3, by Water Immersion)

B. Wave Attenuation Data

Frequency (MHz)	N	Attenuation (db/cm)
0.69	2	2.2 ± 1.1
5.00	2	2.9 ± 2.3
10.00	2	7.5 ± 1.5

N = Data Points; $S = \left[\Sigma (X_i - \bar{X})^2 / (N-1) \right]^{1/2}$ the Estimated Standard Deviation

TABLE 68. ULTRASONIC VELOCITY MEASUREMENTS AT 10.0 MHz (LONGITUDINAL WAVE, UNIAXIAL STRAIN CONDITION)

Test Direction	Mean Wave Velocity (km/s)	No. of Data Points	Estimated Standard Deviation
X (in plane)	4.40	12	0.00319
Y (in plane)	4.40	12	0.00417
Z (perpendicular)	4.38	12	0.00392

X, Y specimens (3 ea.) from a 1.0 inch thick plate.

Z specimens (3) from a 0.5 inch thick plate

In regard to the elastic constants for an isotropic material, these are often given as Lames' constants, λ and G. G is the shear modulus. In terms of λ and G, other elastic constants are (Refs. 42, 43):

The constant C_{11}, which can be calculated from the density and the ultrasonic wave velocity:

$$C_{11} = \lambda + 2G$$

Young's Modulus, $E = G(3\lambda + 2G)/(\lambda + G)$.

Poisson's Ratio, $\nu = \lambda/2(\lambda + G)$.

For a wave velocity of 4.39 ±0.01 km/s and a density of 5.26 g/cm^3, the value of the elastic constant C_{11} is

$$C_{11} = 14.70 \pm 0.07 \times 10^6 \text{ psi.}$$

Using this value for C_{11} and assuming various Poisson's ratios, we can calculate corresponding values of Young's modulus and shear modulus. Doing this we obtain the following:

Poisson's Ratio	Young's Modulus	Shear Modulus
0.29	11.22×10^6 psi	4.35×10^6 psi
0.30	10.92×10^6 psi	4.20×10^6 psi
0.31	10.61×10^6 psi	4.05×10^6 psi

As will be seen in later sections, flexure and tensile data give a Poisson's ratio of about 0.29 and a Young's modulus of about 10.2 Msi. Thus the above calculation gives a Young's modulus which is about 10 percent higher than that obtained from the other tests (assuming Poisson's ratio is 0.29).

15.4 HIGH TEMPERATURE EXPOSURE EFFECTS

The original test plan called for flexure testing of three specimens at room temperature after exposure to 1800°F. When the flexure specimens were received after machining, three were exposed to high temperature while the remaining were being tested. These three were placed inside an alumina tube, approximately 1.5-inch in diameter and 18 inches long, and heated at 9°F (5°C) per minute to 1800°F (982°C), then allowed to cool. The atmosphere was air, but as the system was closed, the quantity of oxygen was limited. At the end of this heating-cooling cycle, it was found that two of the specimens had shattered and the third had deteriorated to the extent that it was pointless to proceed with flexure testing. Prior to this temperature exposure, it had been understood from vendor data that the material had a sublimation temperature somewhere between 1100 and 1200°C (2000 to 2200°F); but the condition of the specimens after 1800°F exposure prompted us to run a TGA to determine the extent of weight loss as a function of temperature.

15.5 TGA RESULTS

A thermogravimetric analysis (TGA) was run at an average heating rate of about 12°C per minute in a nitrogen atmosphere. It was found that the material starts to lose weight at about 150°C and that the weight loss becomes very rapid at about 1000°C. The results of the TGA are given in Figure 111, together with Differential Thermal Analysis (DTA) results.

The TGA was not included in the original test matrix, but it is unfortunate that it was not run prior to starting the other tests. Hindsight, resulting from the TGA, suggests several changes that should have been made in the program, but the information came too late. Not only would the high temperature exposure have been limited to lower temperatures, but one must question even intermediate temperature tests. For example, at 500°F it is probable that the surfaces of the flexure specimens lost material in areas not protected by the strain gages (and adhesive) and hence, probably developed stress concentrations adjacent to the gages.

15.6 COLD FLOW TESTS (ROOM TEMPERATURE CREEP TESTS)

Three flexure specimens were loaded to 2000 psi stress and held under load (at room temperature) for periods of 16 to 72 hours. At the end of the load periods, they were unloaded and checked for any permanent set. This was done by means of strain gages, the resistances of which were checked before and after loading. No detectable changes in strain was observed and it was concluded that cold flow was negligible at this stress level.

In regard to cold flow, it should be noted that such flow is usually most rapid immediately after loading and then slows down. Hence, there did not appear to be much reason for extending the loading periods unless one were to hold the load for several months. Also, it did not seem reasonable that the material would be held at much higher stress levels for any extended period of time in end-use applications.

15.7 FLEXURE TESTS

Flexure tests were run at temperatures from -250°F to 1000°F. A self-aligning four point fixture was employed with a support span of 5.0 inches and a load span of 2.5 inches. The specimens of the original set were six inches long with nominal width and thickness of 0.625 and 0.130, respectively. The faces of the specimens were polished to the optical finish condition, as supplied. The cut edges were ground to a 25 microinch finish. Strain gages were used for strain measurements at temperatures up to and including 500°F but a deflectometer was employed for the higher temperature measurements.

Results of the tests are given in Table 69. At temperatures of 500°F and below, strain measurements were made on both the tension and compression sides of the specimen and both

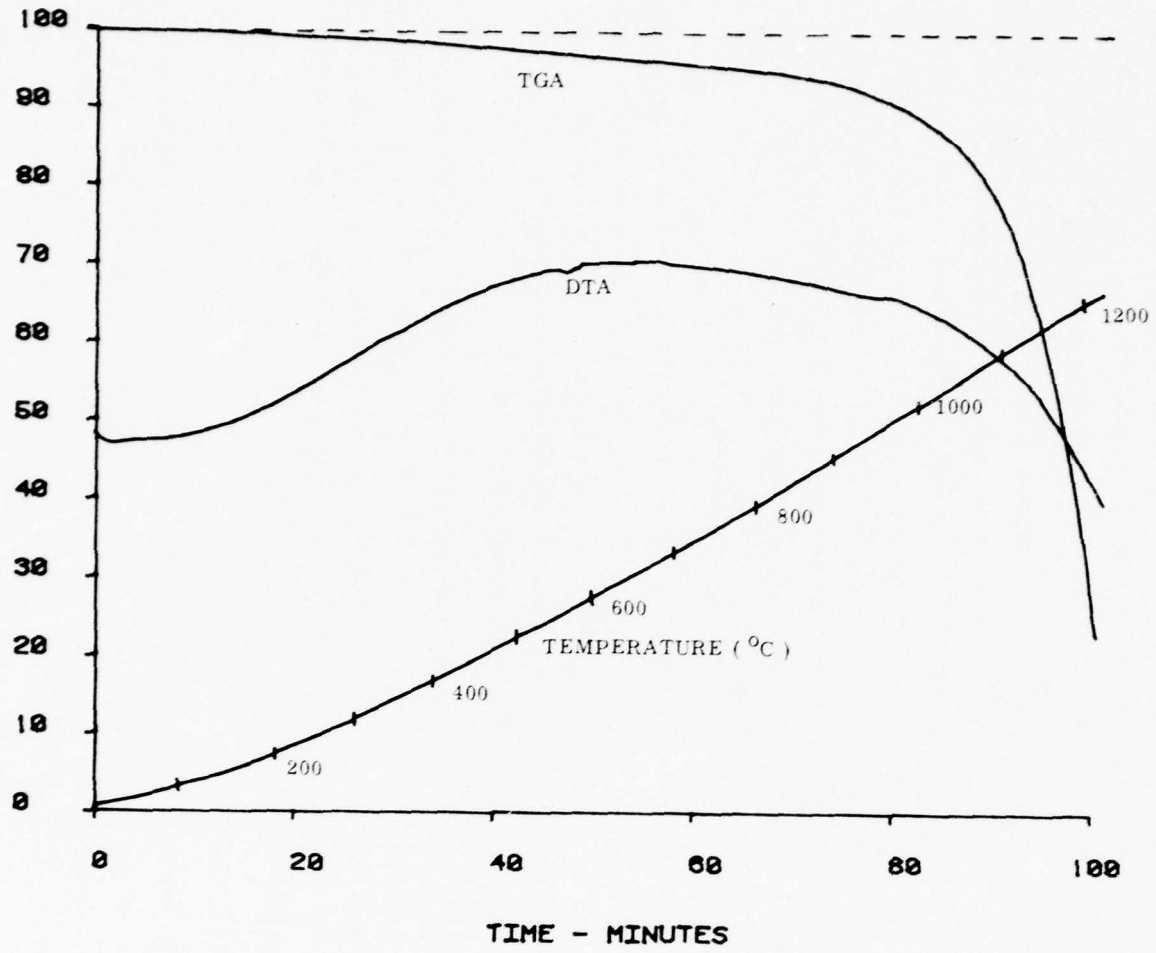

Figure 111. TGA/DTA – Zinc Selenide, Atmosphere: 0.15 Liters/Min. – Nitrogen

TABLE 69. FLEXURE TESTS – RAYTRAN ZINC SELENIDE

(Specimens with top and bottom surfaces in optically polished condition, sides ground to 25 microinch finish.)

Test Temp. (°F)	Specimen Number	Tension or Comp.*	M.O.R. (psi)	Ultimate Strain (%)	Modulus (Msi)	Poisson's Ratio At Strain Indicated 0%	0.05%	0.10%
-250	1-1	T	2460	0.024	10.1	--	--	--
-250	2-3	T	3320	**	--	--	--	--
-250	3-5	T	2780	0.028	9.9	--	--	--
			2850	0.026	10.9			
-250	1-1	C	2460	0.024	10.1	--	--	--
-250	2-3	C	3320	0.034	9.9	--	--	--
-250	3-5	C	2780	0.027	10.1	--	--	--
			2850	0.028	10.0			
R.T.	2-1	T	3520	0.034	10.4	0.31	--	--
R.T.	3-3	T	3860	0.038	10.2	0.29	--	--
R.T.	4-1	T	3320	0.033	10.1	0.29	--	--
			3570	0.035	10.2	0.30		
R.T.	2-1	C	3520	0.035	10.0	0.28	--	--
R.T.	3-3	C	3860	0.038	10.1	0.31	--	--
R.T.	4-1	C	3320	0.033	10.0	0.29	--	--
			3570	0.035	10.0	0.29		
250	1-2	T	6850	0.082	10.5	0.32	0.33	--
250	2-4	T	5590	0.055	10.5	0.32	0.33	--
250	3-6	T	5690	0.059	10.6	0.32	0.32	--
			6040	0.065	10.5	0.32	0.33	
250	1-2	C	6850	0.081	10.6	0.33	0.34	--
250	2-4	C	5590	0.054	10.7	0.33	0.34	--
250	3-6	C	5690	0.057	10.8	0.32	0.33	--
			6040	0.064	10.7	0.33	0.34	
500	3-4	T	6100	0.32	10.0	0.29	0.35	0.41
500	4-2	T	6220	0.26	10.6	0.35	0.34	0.37
			6160	0.29	10.3	0.32	0.34	0.39
500	3-4	C	6100	0.29	10.4	0.29	0.35	0.39
500	4-2	C	6220	0.27	9.9	0.26	0.31	0.35
			6160	0.28	10.1	0.28	0.33	0.37
700	1-3	-	6970	0.35	7.4	--	--	--
700	2-5	-	6190	0.49	8.0	--	--	--
700	4-3	-	7370	0.52	7.8	--	--	--
			6840	0.51	7.7			
1000	1-4	-	6090	0.52	7.3	--	--	--
1000	4-4	-	5700	0.56	(15.7)	--	--	--
			5890	0.54	7.3			

*The side of the specimen on which strain measurements were made.
**Defective gage; no strain reading.
M.O.R. - Modulus of Rupture (strength based on linear, elastic analysis).

sets of readings are given in the table. At room temperature and -250°F the stress-strain curves were linear to failure and so are readily reproduced from the strength (Modulus of Rupture) and ultimate strain data. At 250°F the material showed a slight ductility which increased with increasing temperature and therefore, the stress-strain curves for the higher temperatures are reproduced in Figures 112 through 115. The specimens tested at 700°F and 1000°F did not fail, the tests being terminated when the specimens had deflected to the limit of travel imposed by the test fixture.

Poisson's ratio measurements were made from room temperature to 500°F. An attempt was also made to obtain Poisson's data at -250°F, but the outputs of the Poisson gages were too erratic at this temperature to provide reliable data.

Considering the modulus of rupture data, it will be noted that the strength increases rather suddenly between room temperature and 250°F, where the material is beginning to become ductile. It was suspected that this was an indication that the low temperature (i.e., R.T. and -250°F) strengths were low, probably as a result of the ground finish on the edges of the specimens. We therefore contacted Mr. Robert Donadio of the Raytheon Research Division to seek his advice. Mr. Donadio was quite certain that the ground edges were contributing to the low strengths and kindly provided us with six bars of the size we had already tested plus three small bars in order that we might check for possible size effects. These bars were polished on all faces and edges and the corners (of the cross section) were slightly beveled to minimize possible nicks.

Since we had already acquired the necessary modulus and Poisson's data, it was decided to run these nine specimens without strain gages in order to avoid any possible surface damage from such additional handling.

The three small specimens were tested in four point flexure at room temperature using spans of 1.50 and 0.75 inches. Two each of the large specimens were tested at -250°F, room temperature, and +250°F. The spans used in testing were 5.0 and 2.5 inches. The results are given in Table 70.

Comparing the large and small specimens, it is seen that the small specimens gave strengths which averaged over 2000 psi higher than the large specimens, but even the large specimens gave strengths equal to those listed for the material (i.e., 7500 psi) in Raytheon literature (Ref. 44).

All of the large specimens had strengths which were significantly higher than those obtained in the earlier tests. The difference is illustrated in Figure 116 and is attributed to the ground edges on the earlier specimens.

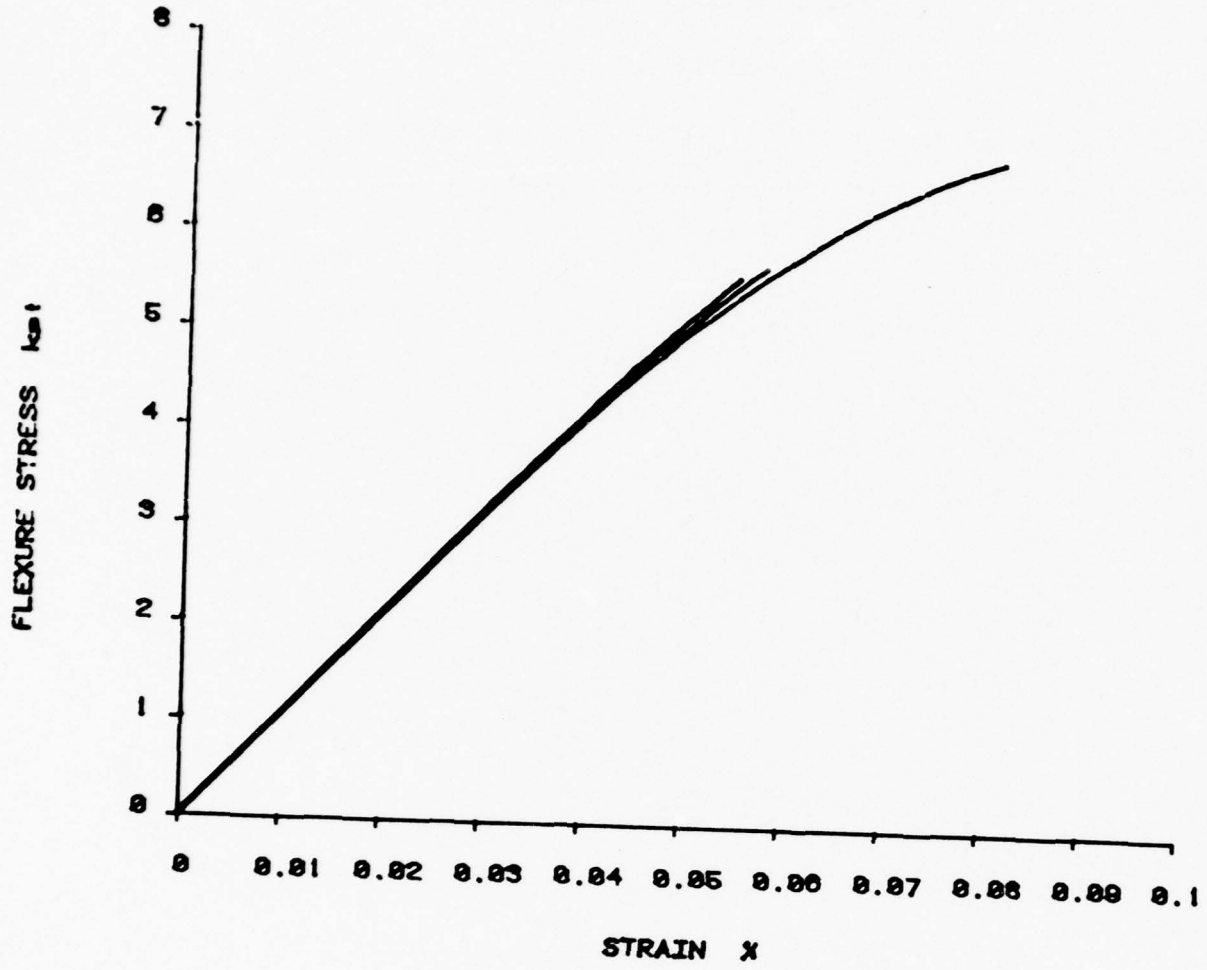

Figure 112. Flexure Test, ZnSe, 250°F

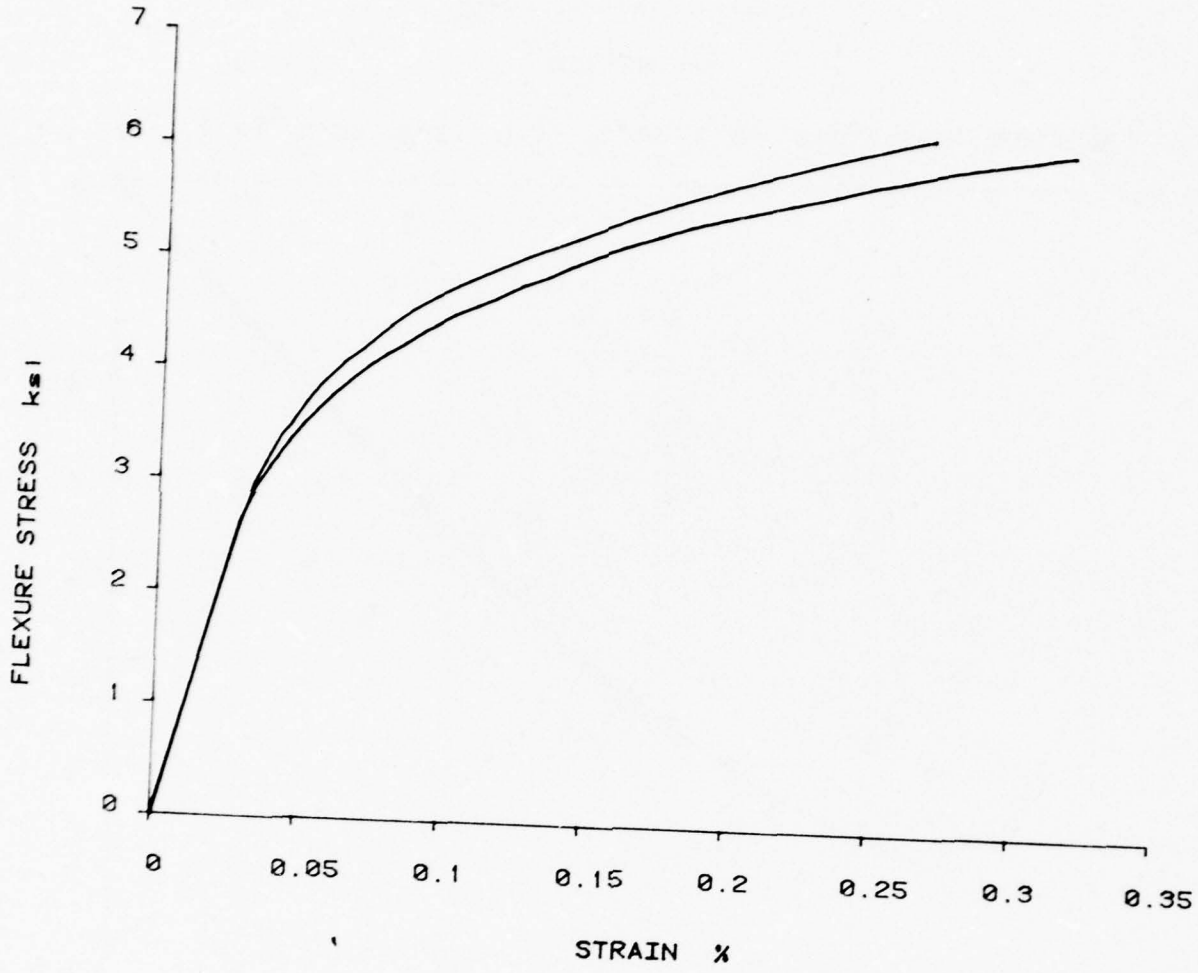

Figure 113. Flexure Test – ZnSe, 500°F

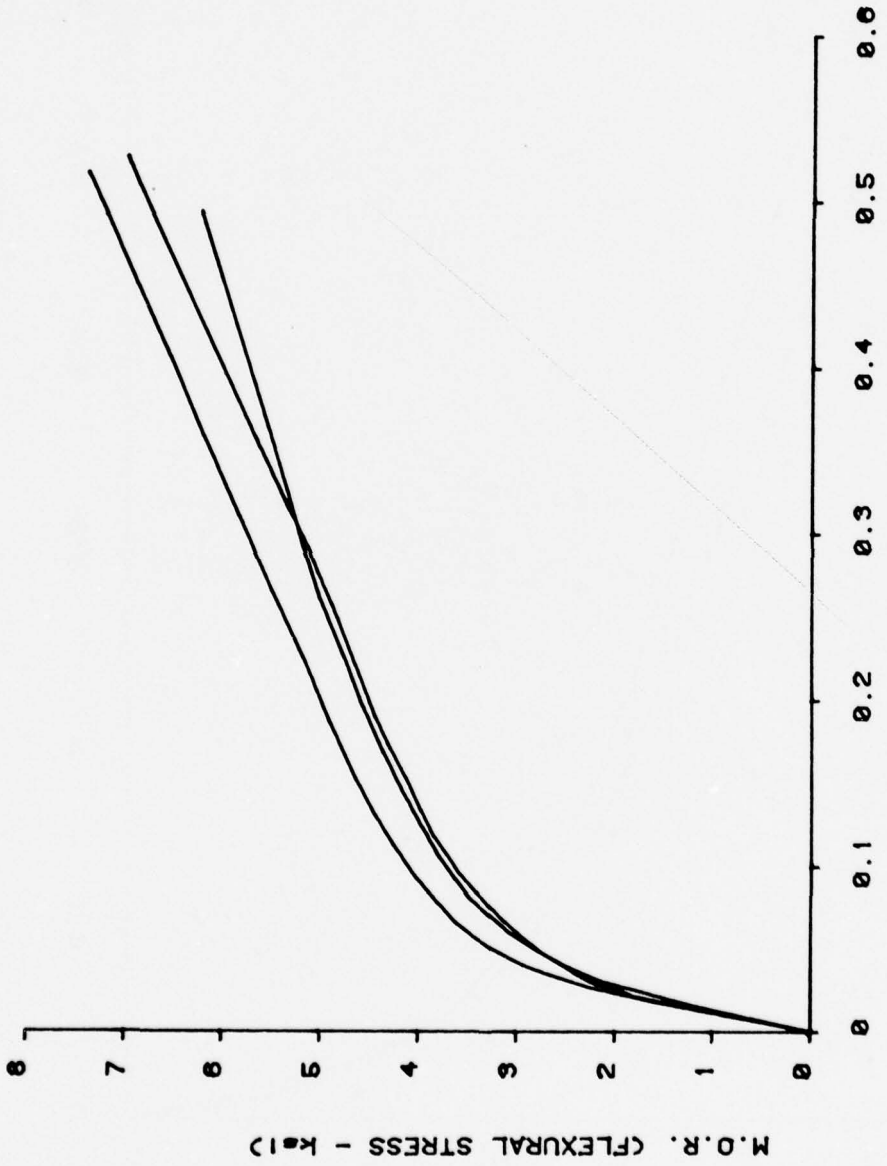

Figure 114. Flexure Test – ZnSe, 700°F

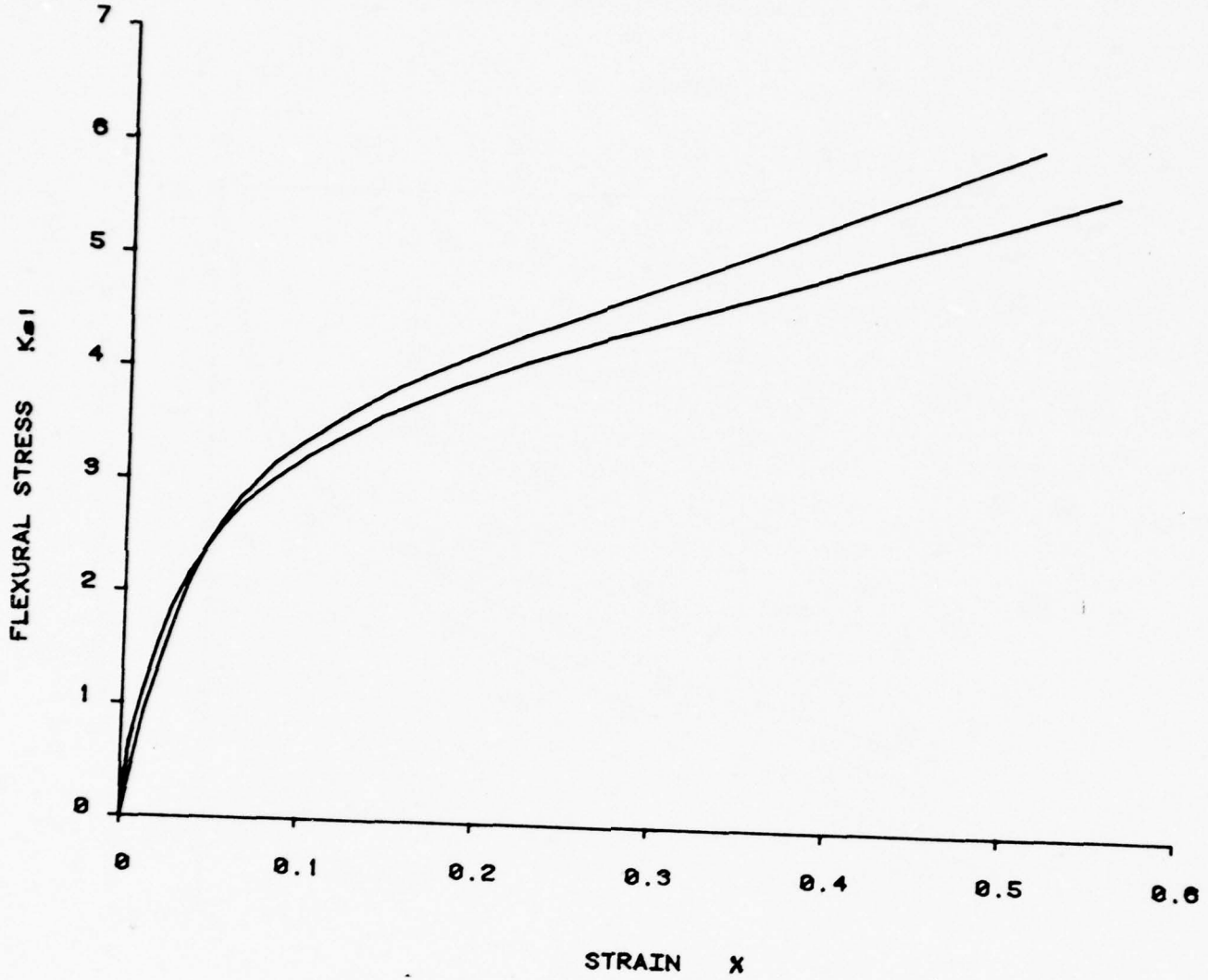

Figure 115. Flexure Test – ZnSe, 1000°F

TABLE 70. RAYTRAN ZnSe – FLEXURE TEST RESULTS (FOUR POINT LOADING)

[Specimens with Polished Faces and Sides, Bevelled Edges.]

Number	Temperature (°F)	Width (in.)	Thickness (in.)	Flexure Strength (psi)	Notes
S-1	+ 75	0.2702	0.1476	11,050	(1)
S-2	+ 75	0.2703	0.1481	9,260	(1)
S-3	+ 75	0.2704	0.1480	9,250	(1)
L-1	+ 75	0.6110	0.1150	7,470	(2)
L-2	+ 75	0.6113	0.1132	7,760	(2)
L-3	- 250	0.6115	0.1148	7,960	(2)
L-4	- 250	0.6100	0.1132	8,440	(2)
L-5	+ 250	0.6100	0.1141	9,630	(2)
L-6	+ 250	0.6120	0.1151	9,020	(2)

(1) Spans = 1.5 and 0.75 inch

(2) Spans = 5.0 and 2.5 inch

15.8 TENSILE TESTS

Since a flexure test specimen experiences tension and compression stresses, tensile measurements of the elastic constants were made as a check on those obtained in the flexure tests. These results are given in Table 71 and in general, are comparable to those obtained from the flexure tests.

15.9 THERMAL CONDUCTIVITY

Thermal conductivity measurements were made using a one-inch diameter cut-bar comparator. These results are tabulated in Table 72 and are shown graphically in Figure 117. It is seen from the figure that the in-plane and perpendicular to plane conductivities are essentially the same, further indicating that the material is isotropic.

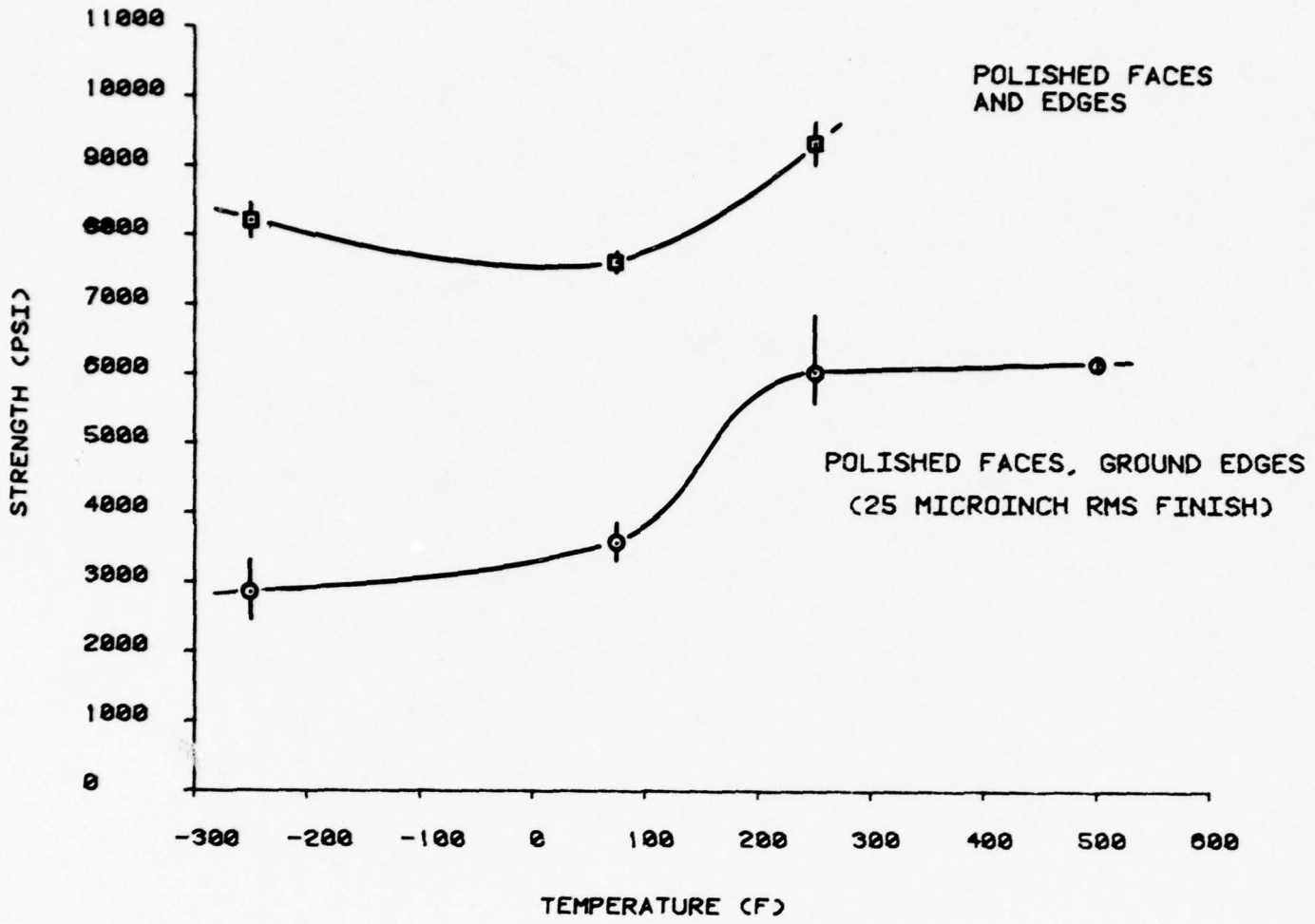

Figure 116. Zinc Selenide Flexure Strength Finish Effects

15.10 SPECIFIC HEAT

Specific heat measurements were made using a Perkin-Elmer Model DSC-II differential scanning calorimeter. Results of the measurements were as follows:

	Specific Heat (BTU/lb-°F)			
	100°F	250°F	750°F	1000°F
	0.080	0.081	0.088	0.090
	0.084	0.0815	0.086	0.095
Mean:	0.082	0.081	0.087	0.092

These data are shown in Figure 118.

TABLE 71. ZnSe ELASTIC CONSTANTS FROM TENSILE TESTS (ROOM TEMPERATURE)

	In Plane		Perpendicular	
Number	Modulus (psi)	Poisson's Ratio	Modulus (psi)	Poisson's Ratio
1	10.7	0.28	10.3	0.29
2	10.5	0.28	9.8	0.30
3	10.5	0.27	9.9	0.29
Mean	10.6	0.28	10.0	0.29

TABLE 72. THERMAL CONDUCTIVITY DATA

(One Inch Diameter Cut-Bar Comparator)

Temperature (°F)	Thermal Conductivity (10^{-3} BTU/ft-sec-°R)	
	In Plane	Perpendicular
- 112	4.92	--
- 108	--	4.61
- 108	--	4.64
- 102	5.05	--
96	3.02	--
109	--	2.68
199	2.19	--
260	--	2.81
416	1.80	--
604	1.26	--
734	1.19	--
758	--	1.30
763	--	1.28
778	--	1.29
993	--	1.27
1000	1.15	--
1002	--	1.28

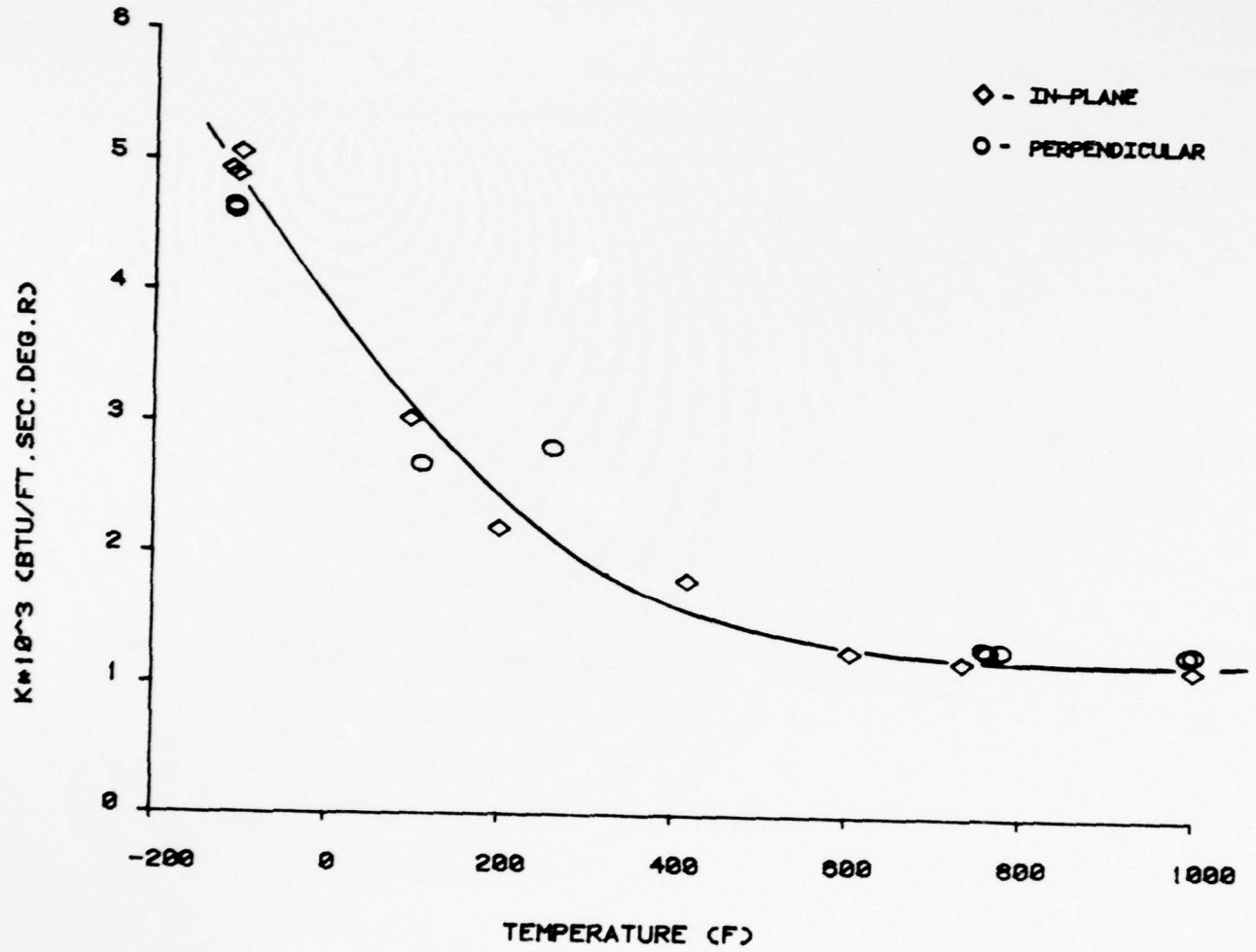

Figure 117. Thermal Conductivity – Zinc Selenide

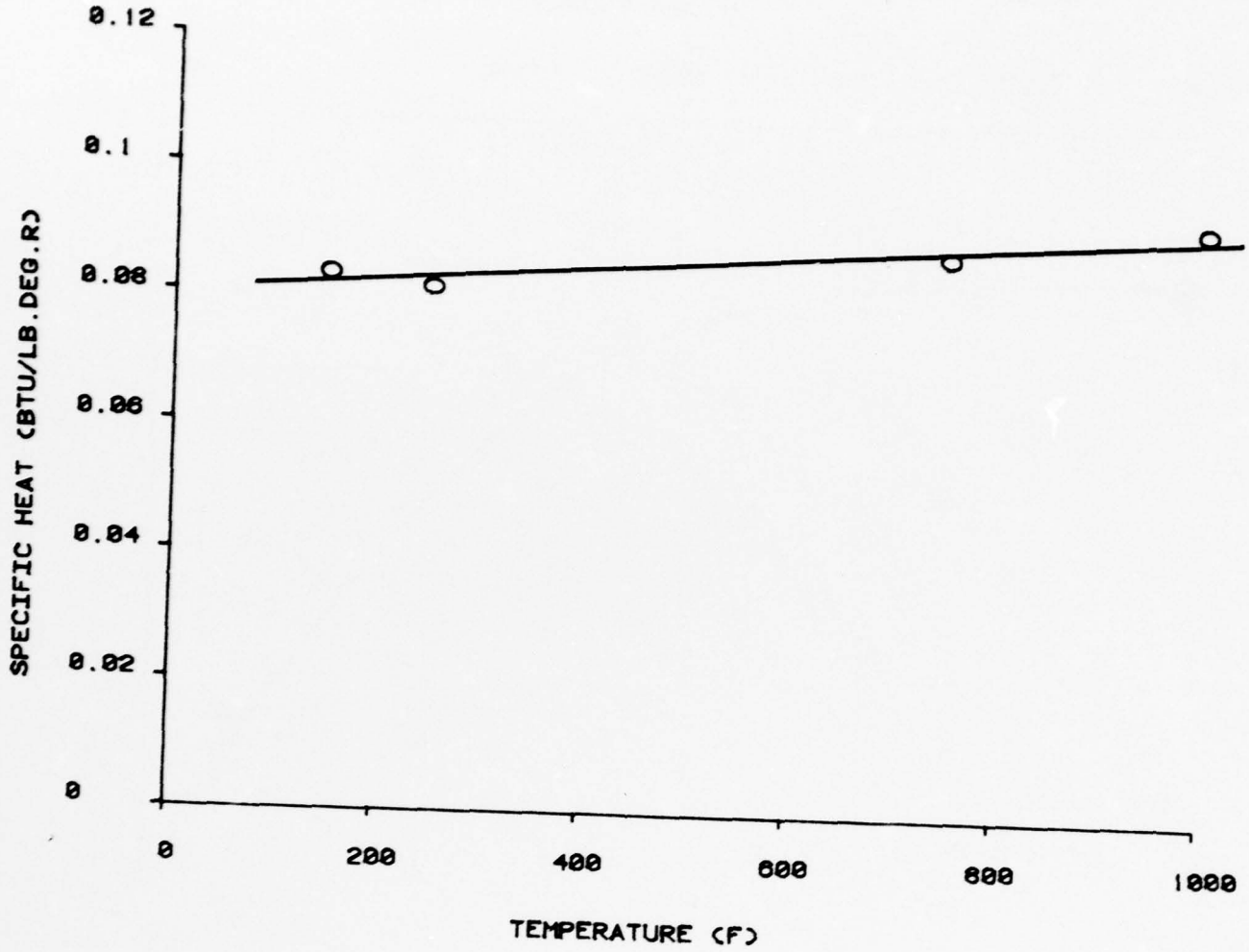

Figure 118. Specific Heat – Zinc Selenide

16. PART III: THERMOPHYSICAL AND MECHANICAL CHARACTERIZATION OF "RAYTRAN" ZINC SELENIDE – RECOMMENDATIONS FOR FUTURE WORK

16. PART III: THERMOPHYSICAL AND MECHANICAL CHARACTERIZATION OF "RAYTRAN" ZINC SELENIDE – RECOMMENDATIONS FOR FUTURE WORK

In the present work the range of temperatures involved was considerably greater than the ZnSe IR window was expected to experience in end use and the number of tests conducted at each temperature was therefore, very limited. It is recommended that a more detailed study be made over the narrower end-use temperature range. This would include flexure tests with at least six to ten specimens per temperature to provide a better statistical basis. These should be taken from several lots of material. Dynamic determination of elastic constants over this limited temperature range should also be included.

In regard to cold flow or creep, the present work showed no detectable effect at room temperature and 2000 psi after 72 hours exposure. However, if window clamping stresses are applied over a period of years, some measureable flow or relaxation could occur.

It is understood that Raytheon currently has an experimental, higher strength version of the "Raytran" ZnSe and it is recommended that this be included in future work, if available.

REFERENCES

REFERENCES

1. Brazel, J. P., "Advanced Hardened Antenna Window Materials Study IV", Final Report, AMMRC CR 76-4, February 1976.

2. Brazel, J. P., "Advanced Hardened Antenna Window Materials Study III", AMMRC CTR 73-26, July 1973.

3. J. P. Stevens Product Bulletin 310-53, April 1973.

4. J. P. Stevens Product Bulletin 310-66, October 1975.

5. Thuss, R., Brazel, J., and Fenton, R., "Silica Study Investigation for Reflective Heat Shield Applications", Final Report for NASA/Ames, Contract NAS-2-9361, August 1977.

6. Matijevic, E., Surface and Colloid Science, Vol. 6, Figure 12, Wiley and Sons, 1973.

7. Letter from W.O. Roberts, E.I. duPont DeNemours and Company, to R. Fenton, GE-RESD, June 22, 1978.

8. Gebhardt, J.J., "Proceedings of the Third Int. Conf. on Chemical Vapor Deposition", Boston, MA., October 1973.

9. Callery Chemical Co., Callery, Pa.

10. "Standard Methods of Test for Flexural Properties of Plastics", ASTM D790-71, American Society of Testing and Materials, 1971.

11. Graham, Marlyn E., John D. Carlyle, and Thomas L. Menna, "Facility for High-Speed Particle Impact Testing," Review of Scientific Instruments, Vol. 46, No. 9, September 1975.

12. McHenry, Michael R., "Design Technology-E Program, Vol. II. Erosion Model for Hypervelocity Impacts" (U). Effects Technology, Inc., ETI-78-2668, SAMSO-TR-79-82, October 1978. (Confidential).

13. McHenry, M.R., and M.E. Graham, "Design Technology-E, Vol. III. Erosion Testing Results, 1978," (U). Effects Technology, Inc., ETI-78-2687, SAMSO-TR-79-82, December 1978. (Confidential).

14. Graham, Marlyn E., "Particle Impact Testing of ADL-4D6 Hardened Antenna Window Material" (U). Addendum to AMMRC-TR-79-45, Effects Technology, Inc., November 1979 (Confidential).

15. Westphal, W.B., "Permittivity in Distributed Circuits in Dielectric Materials and Applications", A.R. Von Hippel, Ed., Wiley & Sons, New York, 1954.

16. "The Microwave Engineer's Handbook and Buyer's Guide", Horizon House, Microwave, Inc. (Pg. 72), 1961-1962

17. Thuss, R., Brazel, J.P. Fenton, R., "Silica Study Investigation for Reflective Heatshield Application", Prepared under Contract NAS-2-9361 for Ames Research Center National Aeronautics and Space Administration.

18. Kibler, J.J., Derby, E. and Dow, N., "Study of Three-Dimensional Reinforcements for Impact Resistant Composite FAN Blades", Materials Sciences Corporation Final Report in preparation for General Electric Company, Atomic Energy Commission.

19. Jones, R.J., "Apparent Flexural Modulus and Strength of Multimodulus Materials", Journal of Composite Materials, October 1976.

20. R. Tanzilli et. al., "Potential for Chemically Vapor Deposited Silicon Nitride as a Multimode Electromagnetic Window (VIS, IR, RF)", Proceedings of the Fourteenth Symposium on Electromagnetic Windows, June 21-23, 1978, Georgia Institute of Technology, pp. 13-20.

21. P.L. Land et. al., "Evaluation of β-Sialon for Radome Application", AFML-TR-78-79, July, 1978, p. 6.

22. Personal Communication, Dr. Peter L. Land, AFML, May 1979.

23. A. Gatti, M.J. Noone, "Methods of Fabricating Ceramic Materials", AFML-TR-77-135, Nov., 1977.

24. R.R. Wills et. al., "Intrinsic Thermal and Mechanical Properties of Reaction-Sintered $Si_4Al_2N_6O_2$ Sialon", Ceramic Bulletin, Vol. 55, 1976, pp. 975-978.

25. G.A. Slack, T.F. McNelly, "Research on Aluminum Nitride Materials", Report SRD-78-051, March, 1978.

26. T. Sakai, "Effect of Oxygen Composition on Flexure Strength of Hot-Pressed AlN", J. Am. Ceram. Soc., Vol. 61, Sept.-Oct. 1978, pp. 460-461.

27. G. Long, L.M. Foster, J.Am. Ceram. Soc., 42, 2,53 (1959).

28. A.T. Collins, E.C. Lightowlers, P.J. Dean, Phys. Rev. 158, 3,833 (1967).

29. W.M. Yim, E.J. Stofko, P.J. Zanzucci, J. I. Pankove, M. Ettenkerg, S.L. Gilbert, J. Appl. Phys., 44, 1,292 (1973).

30. G.A. Slack, J. Phys. Chem. Solids, 34, 321 (1973).

31. K.M. Taylor, C. Lenie, "Some Properties of Aluminum Nitride", J. Electrochem. Soc., Vol. 107, April, 1960, pp. 308-314.

32. M.P. Boron, G.A. Slack, J.W. Szymaszek, "Studies on Aluminum Nitride, a Non-Metallic Solid with a High Thermal Conductivity, I. Evaluation of Commercial Material", Technical Information Series, Corporate Research and Development, General Electric Co., Report #72CDR072, 1972.

33. G.A. Slack, T.F. McNelly, "Research on Aluminum Nitride Materials", Final Technical Report for AFOSR Contract #F44620-76-C-0039, March, 1978

34. D.L. Hildenbrand, W.F. Hall, "The Vaporization Behavior of Boron Nitride and Aluminum Nitride", J. Phys. Chem., 67, 888 (1963).

35. B.E. Samorukov, A.M. Zykov, D.M. Demidov, Tranl. from Zhurnal Prikladnoi Khimii 47, (3) 564-568 (1974); Consultants Bureau, Plenum Press.

36. "Chemical Vapor Deposition" ed. by C.F. Powell, J.H. Oxley and J.M. Blocher, pp. 278-281, J. Wiley, NY, 1966.

37. A.S. Russell et.al., J. Am. Chem. Soc., 73, 1466 (1951).

38. G.A. Slack, T.F. McNelly, "Research on Aluminum Nitride Materials", Final Report, AFOSR Contract No. F44620-76-C-0039, March, 1978

39. G.A. Cox et.al., J. Phys. Chem. Solids, 28, 543-548 (1967).

40. H.M. Manasevit, F.M. Erdmann, W.I. Simpson, J. Electrochem. Soc., 118, 1864 (1971).

41. T.V. Renner, Z. Allqem u. Anorg. Chemie 292, 22 (1959).

42. Love, A.E.H., "A Treatise on the Mathematical Theory of Elasticity", Dover Publications, 1944. (Reprint of the Fourth [1972] edition).

43. Kolsky, H., "Stress Waves in Solids", Dover Publications, 1963.

44. Raytheon data sheet entitled, "Raytran ZnSe", January 1977.

DISTRIBUTION LIST

	No. of Copies
Commander U.S. Army Materiel Development and Readiness Command ATTN: DRCLDC, R. Zentner 5001 Eisenhower Avenue Alexandria, VA 22333	1
Ballistic Missile Defense Program Office ATTN: DACS-BMT 5001 Eisenhower Avenue Alexandria, VA 22333	1
Director Ballistic Missile Defense Advanced Technology Center Attn: ATC-R, F. King ATC-M, J. Papadopoulis ATC-M, M. Whitfield P.O. Box 1500 Huntsville, AL 35807	 2 1 1
Ballistic Missile Defense Systems Command ATTN: W. Graves E. Martz N.J. Hurst P.O. Box 1500 Huntsville, AL 35807	 1 1 1
Commander U.S. Army Missile Research and Development Command ATTN: DRDMI-EAM, W.K. Patterson Redstone Arsenal Huntsville, AL 35809	1
Director Defense Nuclear Agency ATTN: SPAS, J.F. Moulton, Jr. Washington, DC 20305	1
Office of Deputy Under Secretary of Defense for Research and Engineering (ET) ATTN: J. Persh, Staff Specialist for Materials and Structures The Pentagon, Room 3D1089 Washington, DC 20301	1
Office of Deputy Chief of Research Development and Acquisition ATTN: DAMA-CSS-D, J. Bryant The Pentagon, Room 3D424 Washington, DC 20310	1

	No. of Copies
Commander Harry Diamond Laboratories ATTN: DRXDO-NP, F. Wimenitz DRXDO-NP, J. Gwaltney 2800 Powder Mill Road Adelphi, MD 20783	 1 1
Commander Air Force Flight Dynamics Laboratory ATTN: AFFDL/FBC, H.A. Wood Wright-Patterson Air Force Base, OH 45433	 1
Commander U.S. Army Combat Development Command Institute of Nuclear Studies ATTN: Technical Library Fort Bliss, TX 79916	 1
Commander Air Force Materials Laboratory Air Force Systems Command ATTN: W. Kessler R. Farmer H. Materne D. Schmidt Wright-Patterson Air Force Base, OH 45433	 1 1 1 1
Commander Space and Missile Systems Organization ATTN: DYSE, Cpt. J. Sikra P.O. Box 92960, Worldway Postal Center Los Angeles, CA 90009	 2
Commander Naval Sea Systems Command ATTN: ORD-03331, M. Kinna Washington, DC 20360	 1
Commander Naval Surface Weapons Center ATTN: W.Carson Lyons C. Rowe W. Messick Silver Springs, MD 20910	 1 1 1
Los Alamos Scientific Laboratory ATTN: GMX-6, J.W. Taylor P.O. Box 1663 Los Alamos, NM 87544	 1

	No. of Copies
Sandia Laboratories ATTN: J.K. Cole P.O. Box 5800 Albuquerque, NM 87115	1
Aerospace Corporation ATTN: W. Riley R. Myers L. Rubin P.O. Box 92957 Los Angeles, CA 90009	1 1 1
AVCO Systems Division ATTN: P.G. Rolincik 201 Lowell Street Wilmington, MA 01887	1
Institute for Defense Analysis ATTN: S. Channon 400 Army-Navy Drive Arlington, VA 22202	1
Boeing Aerospace Company ATTN: M. Kushner W.A. Symonds P.O. Box 3999 Seattle, Washington 98124	1 1
Effects Technology, Inc. ATTN: M. Graham J. Greene R. Parisse 5383 Hollister Avenue Santa Barbara, CA 93111	1 1
Fiber Materials, Inc. ATTN: L. Landers G. Williams R. Burns M. Subilia Biddeford Industrial Park Biddeford, ME 04005	1 1 1 1
General Dynamics Corporation Convair Division ATTN: J. Hertz H. McCutcheon, Jr. R. Adsit W. Weisinger 5001 Kearny Villa Road San Diego, CA 92138	1 1 1 1

	No. of Copies
General Electric Company, RESD	
Advanced Materials Development Laboratory	
ATTN: J.P. Brazel, Room 4466	1
B. McGuire	1
P. Gorsuch, Room 4466	1
3198 Chestnut Street	
Philadelphia, PA 19101	
General Electric Company, RESD	
Valley Forge Space Center	
ATTN: R. Tanzilli, Rm U7025	1
R. Fenton, Rm U8614	1
J. Gebhardt, Rm U7025	1
K. Bleiler, Rm U8417	1
J. D'Andrea, Rm U8614	1
R. Kreitz, Rm U8630	1
J. Roetling, Rm U8630	1
B. Kennedy, Rm. U8425	1
C. Dulka, Rm U7025	1
P.O. Box 8555	
Philadelphia, PA 19101	
General Electric Company, HMED	
ATTN: D. Kuhn	1
K. Olsen	1
P.O. Box 1122	
Syracuse, NY 13201	
Georgia Institute of Technology	
Engineering Experiment Station	
ATTN: J.W. Fuller	1
J.D. Walton	1
S. Bomar	1
25 North Avenue, NW	
Atlanta, GA 30332	
Hughes Aircraft Company	
ATTN: R.W. Jones	2
Culver City, CA 90230	
Martin Marietta Corporation	
ATTN: D. Easter	1
J. Madden	1
R. Hewitt	1
J. Potts	1
W. Spencer	1
P.O. Box 5837	
Orlando, FL 32855	

	No. of Copies
MIT/Lincoln Laboratory ATTN: Carl Blake P.O. Box 73 Lexington, MA 02173	1
McDonnell Douglas Corporation ATTN: L. Cohen G. Eykholt I. Richman 5301 Bolsa Avenue Huntingdon Beach, CA 92647	1 1 1
New Technology, Inc. Research Park P.O. Box 5245 Huntsville, AL 35805	1
Prototype Development Associates ATTN: J. Schutzler N. Harrington 1740 Garry Avenue, Suite 201 Santa Ana, CA 92705	1 1
Polytechnic Institute of New York ATTN: Prof. A. Hessel Route 110 Farmingdale, Long Island, NY 11735	1
Raytheon Corporation ATTN: R. Donadio 28 Feyon St. Waltham, MA 02154	1
R&D Associates ATTN: A. Field P.O. Box 9695 Marina del Rey, CA 90291	1
RCA Government and Commercial Systems ATTN: Walter Beck Missile & Surface Radar Division Morristown, NJ 08057	1
Science Applications, Inc. ATTN: I. Osofsky One Continential Plaza, Suite 310 101 Continental Blvd. El Segundo, CA 90245	1

	No. of Copies
Southwest Research Institute ATTN: A. Wenzel 8500 Culebra Road San Antonio, TX 78206	1
Sperry Gyroscope ATTN: John Strangel Great Neck, Long Island, NY 11020	1
Terra Tek, Inc. ATTN: A.H. Jones University Research Park 420 Wakara Way Salt Lake City, Utah 84108	1
TRW Defense and Space Systems ATTN: L. Berger P.O. Box 1310 San Bernardino, CA 92402	1
U.S. Polymeric ATTN: C.K. Mullen 700 East Dyer Road Santa Ana, CA 92707	1
University of California Lawrence Livermore Laboratory ATTN: T.T. Chiao E.M. Wu P.O. Box 808 Livermore, CA 94550	1 1
Defense Documentation Center Cameron Station, Bldg. 5 5010 Duke Station Alexandria, VA 22314	10
Director Army Materials & Mechanics Research Center ATTN: DRXMR-H, J.F. Dignam DRXMR-H, L.R. Aronin DRXMR-H, S.C. Chou DRXMR-H, D.P. Dandekar DRXMR-H, J.A. Hofmann DRXMR-H, R. Lewis DRXMR-EO, R. N. Katz DRXMR-AP DRXMR-PL DRXMR-PR Watertown, MA 02172	 1 1 1 1 1 1 1 1 2 1

Army Materials and Mechanics Research Center
Watertown, Massachusetts 02172
MILLIMETER WAVE HARDENED ANTENNA WINDOW MATERIALS DEVELOPMENT
James P. Brazel, Richard Fenton,
John Roetling and Richard Tanzilli
General Electric Company, RESD
3198 Chestnut Street
Philadelphia, PA 19101
Technical Report AMMRC TR 79-45
Contract No. DAAG46-79-C-0047
D/A Project: 1X363304D215, AMCMS Code 633304.21500.07
Final Report, July 1978 - April 1979

AD _____

UNCLASSIFIED
UNLIMITED DISTRIBUTION

Key Words
Antenna Windows, Silicon nitride,
Aluminum nitride, Silica-silica composites,
Sialons, Boron nitride, Raytran,
zinc selenide, Hardened radar materials

A materials development and characterization program has been conducted with the goal of developing hardened antenna window materials for application to millimeter wave and infrared sensors for ballistic missile defense intercector (BMDI) applications.

Three distinct classes of materials were studied. The ADL-4D6 multidirectionally reinforced silica-silica composite developed in previous BMD work was tested for particle erosion resistance and dielectric properties in the mm wavelength region. A comprehensive study was also performed on the effects of constituent properties and weaving and composite densification variations on the mechanical properties of this material.

A second class of refractory dielectrics, ultrahigh purity nitrides of silicon and aluminum, were also examined for their ultimate potential in the BMDI environment. Specimens were prepared by chemical vapor deposition and hot pressing of powders. These were variously tested for mechanical and thermal properties, chemical purity and dielectric properties in X and millimeter wavelength bands. The CVD Si_3N_4 material in particular showed a decade lower loss tangent than previously reported versions of this ceramic.

A third material, "Raytran" zinc selenide, an infrared window material candidate, was characterized for its thermophysical and mechanical properties from -150°C to 1000°C.

Army Materials and Mechanics Research Center
Watertown, Massachusetts 02172
MILLIMETER WAVE HARDENED ANTENNA WINDOW MATERIALS DEVELOPMENT
James P. Brazel, Richard Fenton,
John Roetling and Richard Tanzilli
General Electric Company, RESD
3198 Chestnut Street
Philadelphia, PA 19101
Technical Report AMMRC TR 79-45
Contract No. DAAG46-79-C-0047
D/A Project: 1X363304D215, AMCMS Code 633304.21500.07
Final Report, July 1978 - April 1979

AD _____

UNCLASSIFIED
UNLIMITED DISTRIBUTION

Key Words
Antenna Windows, Silicon nitride,
Aluminum nitride, Silica-silica composites,
Sialons, Boron nitride, Raytran,
zinc selenide, Hardened radar materials

A materials development and characterization program has been conducted with the goal of developing hardened antenna window materials for application to millimeter wave and infrared sensors for ballistic missile defense intercector (BMDI) applications.

Three distinct classes of materials were studied. The ADL-4D6 multidirectionally reinforced silica-silica composite developed in previous BMD work was tested for particle erosion resistance and dielectric properties in the mm wavelength region. A comprehensive study was also performed on the effects of constituent properties and weaving and composite densification variations on the mechanical properties of this material.

A second class of refractory dielectrics, ultrahigh purity nitrides of silicon and aluminum, were also examined for their ultimate potential in the BMDI environment. Specimens were prepared by chemical vapor deposition and hot pressing of powders. These were variously tested for mechanical and thermal properties, chemical purity and dielectric properties in X and millimeter wavelength bands. The CVD Si_3N_4 material in particular showed a decade lower loss tangent than previously reported versions of this ceramic.

A third material, "Raytran" zinc selenide, an infrared window material candidate, was characterized for its thermophysical and mechanical properties from -150°C to 1000°C.

Army Materials and Mechanics Research Center
Watertown, Massachusetts 02172
MILLIMETER WAVE HARDENED ANTENNA WINDOW MATERIALS DEVELOPMENT
James P. Brazel, Richard Fenton,
John Roetling and Richard Tanzilli
General Electric Company, RESD
3198 Chestnut Street
Philadelphia, PA 19101
Technical Report AMMRC TR 79-45
Contract No. DAAG46-79-C-0047
D/A Project: 1X363304D215, AMCMS Code 633304.21500.07
Final Report, July 1978 - April 1979

AD _____

UNCLASSIFIED
UNLIMITED DISTRIBUTION

Key Words
Antenna Windows, Silicon nitride,
Aluminum nitride, Silica-silica composites,
Sialons, Boron nitride, Raytran,
zinc selenide, Hardened radar materials

A materials development and characterization program has been conducted with the goal of developing hardened antenna window materials for application to millimeter wave and infrared sensors for ballistic missile defense intercector (BMDI) applications.

Three distinct classes of materials were studied. The ADL-4D6 multidirectionally reinforced silica-silica composite developed in previous BMD work was tested for particle erosion resistance and dielectric properties in the mm wavelength region. A comprehensive study was also performed on the effects of constituent properties and weaving and composite densification variations on the mechanical properties of this material.

A second class of refractory dielectrics, ultrahigh purity nitrides of silicon and aluminum, were also examined for their ultimate potential in the BMDI environment. Specimens were prepared by chemical vapor deposition and hot pressing of powders. These were variously tested for mechanical and thermal properties, chemical purity and dielectric properties in X and millimeter wavelength bands. The CVD Si_3N_4 material in particular showed a decade lower loss tangent than previously reported versions of this ceramic.

A third material, "Raytran" zinc selenide, an infrared window material candidate, was characterized for its thermophysical and mechanical properties from -150°C to 1000°C.

Army Materials and Mechanics Research Center
Watertown, Massachusetts 02172
MILLIMETER WAVE HARDENED ANTENNA WINDOW MATERIALS DEVELOPMENT
James P. Brazel, Richard Fenton,
John Roetling and Richard Tanzilli
General Electric Company, RESD
3198 Chestnut Street
Philadelphia, PA 19101
Technical Report AMMRC TR 79-45
Contract No. DAAG46-79-C-0047
D/A Project: 1X363304D215, AMCMS Code 633304.21500.07
Final Report, July 1978 - April 1979

AD _____

UNCLASSIFIED
UNLIMITED DISTRIBUTION

Key Words
Antenna Windows, Silicon nitride,
Aluminum nitride, Silica-silica composites,
Sialons, Boron nitride, Raytran,
zinc selenide, Hardened radar materials

A materials development and characterization program has been conducted with the goal of developing hardened antenna window materials for application to millimeter wave and infrared sensors for ballistic missile defense intercector (BMDI) applications.

Three distinct classes of materials were studied. The ADL-4D6 multidirectionally reinforced silica-silica composite developed in previous BMD work was tested for particle erosion resistance and dielectric properties in the mm wavelength region. A comprehensive study was also performed on the effects of constituent properties and weaving and composite densification variations on the mechanical properties of this material.

A second class of refractory dielectrics, ultrahigh purity nitrides of silicon and aluminum, were also examined for their ultimate potential in the BMDI environment. Specimens were prepared by chemical vapor deposition and hot pressing of powders. These were variously tested for mechanical and thermal properties, chemical purity and dielectric properties in X and millimeter wavelength bands. The CVD Si_3N_4 material in particular showed a decade lower loss tangent than previously reported versions of this ceramic.

A third material, "Raytran" zinc selenide, an infrared window material candidate, was characterized for its thermophysical and mechanical properties from -150°C to 1000°C.